Peat, David T. (2015) Magnetic resonance relaxation at ultra low temperatures. PhD thesis, University of Nottingham.

Magnetic Resonance Relaxation at Ultra Low Temperatures

David Peat MSci

Thesis submitted to the University of Nottingham for the

degree of

Doctor of Philosophy.

Dedicated to Mum and Dad

Abstract

The focus of this thesis is to produce highly polarised Nuclear Magnetic Resonance (NMR) samples for use in vivo applications. This work focuses on using the brute force method to polarise relevant molecules, for example, ^{13}C labelled pyruvic acid and ^{13}C labelled sodium acetate. The brute force method uses the Boltzmann distribution to polarise a sample by exposing it to large magnetic fields, 15 T, and ultra-low temperatures, ~20 mK. The disadvantage of using this method is the long polarisation time. To counteract the long relaxation times, two sets of relaxation agents were assessed: paramagnetic lanthanides and nanoparticles.

Chelated gadolinium is routinely used as a spin-lattice, T_1, contrast agent in clinical Magnetic Resonance Imaging (MRI). It is known that when the electron spin flip time is similar to the Larmor frequency, the T_1 time of the nuclei is reduced. Each lanthanide has a different electron spin flip time, therefore, one lanthanide may be effective at low temperatures. Unfortunately the lanthanides do not prove to be efficient in the millikelvin regime, where the brute force method is at its most effective, so the lanthanides are of limited use.

Metals are known to have short T_1 times in the millikelvin regime due to the Korringa effect. The conduction electrons of the metal can contribute or absorb energy from nuclei, resulting in a reduction of the T_1 of relevant molecules. By having a strong interaction between conduction electrons and the nuclei of interest, it could be possible to reduce the T_1 of any nuclei of interest. To maximise the contact between the metals and the nuclei, metal nanoparticles were used. Copper and platinum nanoparticle samples are shown to enhance the relaxation rate of nearby protons, however, aluminium and silver nanoparticle samples, which are also expected to be effective, are not. This contradicts the idea that the Korringa effect is the only relaxation mechanism which relaxes the nuclei.

The magnetic properties of nanoparticles can be different from their bulk counterpart, therefore, could be contributing to the relaxation of nearby nuclei. It would therefore be advantageous to study the nanoparticle's magnetisation in a Superconducting Quantum Interference Device (SQUID). Unfortunately, the interpretation of the magnetisation becomes very complicated, as the nanoparticles can react with the solvents. These reactions can result in a 1000-fold increase in the magnetisation of the sample. With the limited

magnetic data collected in this work, it is difficult to correlate the nanoparticles magnetic properties with their effectiveness as a T_1 relaxation agent.

Publications

Peat, D. T., Horsewill, A. J., Köckenberger, W., Linde, A. J. P., Gadian, D. G., Owers-Bradley, J. R. Achievement of High Nuclear Spin Polarization Using Lanthanides as Low-Temperature NMR Relaxation Agents. *PHYSICAL CHEMISTRY CHEMICAL PHYSICS* **15 (20)**, 7586-7591 (2013).

Owers-Bradley, J. R., Horsewill, A., Peat, D. T., Goh, K. S. K., Gadian, D. G. High Polarization of Nuclear Spins Mediated by Nanoparticles at Millikelvin Temperatures. *PHYSICAL CHEMISTRY CHEMICAL PHYSICS* **15 (25)**, 10413-10417 (2013).

Acknowledgements

Contents

~ x ~

Table of Figures

$\sim$ xvii $\sim$

~ xviii ~

~ xix ~

~ xx ~

Abbreviations

Ac	Acetic acid
ATP	Adenosine TriPhosphate
Ce-DTPA	Cerium-DTPA
CS	Citrate synthase
DNP	Dynamic Nuclear Polarisation
DTPA	Diethylene Triamine Pentaacetic Acid
Dy-DTPA	Dysprosium-DTPA
Dy-EDTA	Dysprosium-EDTA
EDTA	Ethylene Diaminete Traacetic Acid
ESR	Electron Spin Resonance
FID	Free Induction Decay
FT	Fourier Transform
FUM	Fumarase
FWHM	Full Width Half Maximum
G	Glycerol
Gd-DTPA	Gadolinium-DTPA
Ho-DTPA	Holmium-DTPA
ICDH	Isocitrate dehydrogenase
JJ	Josephson Junctions
MDH	Malate dehydrogenase
MRI	Magnetic Resonance Imaging
NaAc	Sodium Acetate
NaPh	Sodium Phosphate (monobasic)
NaPyr	Sodium Pyruvate
NMR	Nuclear Magnetic Resonance
ODHC	2-Oxoglutarate dehydrogenase complex
P or Pyr	Pyruvic acid
PDHC	Pyruvate dehydrogenase complex
RF	Radio Frequency
RMS	Root Mean Square
SCS	Succinate-CoA synthetase
SDH	Succinate dehydrogenase
SQUID	Superconducting QUantum Interference Device (magnetometer)
SNR	Signal to Noise Ratio
W	Water
WG	Water Glycerol

Chapter 1. Introduction

Nuclear Magnetic Resonance (NMR) and Magnetic Resonance Imaging (MRI) are routinely used for chemical analysis, determination of protein structure and in vivo applications (1,2,3). There has been interest in increasing the signal-to-noise ratio (SNR) of these techniques by using hyperpolarised samples. A hyperpolarised sample is a sample that has a higher polarisation than its thermal equilibrium.

This research focuses on hyperpolarising samples for in vivo applications, therefore the hyperpolarisation method should be able to polarise a large quantity of ^{13}C labelled metabolites. This research has been conducted on three key metabolites: sodium acetate (NaAc) pyruvic acid (Pyr) and sodium pyruvate (NaPyr).

Several hyperpolarisation techniques exist, each with its own limitation. When producing hyperpolarised samples, it would be advantageous to produce large quantities of material. There are two methods of producing a large throughput of sample, either polarise small quantities of samples in a short period of time, which is analogous to Dynamic Nuclear Polarisation (DNP) or polarising a larger quantity of samples over a longer period of time, the latter is analogous to the brute force method.

DNP is a method of hyperpolarising nuclei for use in NMR (3,4,5). S. Nelson, et al have proven the effectiveness of using DNP to hyperpolarise ^{13}C labelled pyruvate for in vivo applications. The focus of their research is to use the hyperpolarised pyruvate to identify prostate cancer in human subjects. The results of Nelson's work were promising; however, it is believed that alternative methods of producing the hyperpolarised sample could be developed.

DNP has several limiting factors, which include being nuclei specific and with limited sample volume. These limitations mean that DNP can only produce a limited number of samples in each batch and that only one nucleus, usually ^{13}C, in the sample is hyperpolarised. Though DNP has been proven to be effective at increasing the signal-to-noise ratio, SNR, its short polarisation time would be much more suited to a research environment where testing many different samples is desired.

Chapter 1. Introduction

The brute force method of hyperpolarisation is another method of achieving large polarisation enhancement factors and is the method employed in this research. One of the key points of this research is to consider the feasibility of brute force hyperpolarisation as an alternative to DNP in a clinical environment (6,7,8). The principle idea of brute force polarisation is based on using the Boltzmann distribution to achieve high levels of polarisation, by polarising the sample at low temperatures and high magnetic fields. The brute force method has two advantages over DNP, it can polarise all of the nuclei within a sample simultaneously and the sample size is much larger.

The brute force method does come with one limitation, which is long polarisation times for key metabolites at ultra-low temperatures and high magnetic fields. To combat this limitation, three strategies can be implemented. These include the addition of relaxation agents, the use of a technique called thermal mixing and staggering the production of samples. The ideal relaxation agent would decrease the T_1 time of the sample while it is under polarisation conditions, but should be ineffective at the higher temperatures. Thermal mixing is useful as it allows for the spin temperatures of nuclei within a sample to equilibrate, therefore, a thermal bath of nuclei with a short T_1 time can be used to polarise nuclei with a longer T_1 time.

Within this thesis, two types of relaxation agents will be tested under the polarisation conditions required by the brute force method. Chapter 3 contains the first type of relaxation agent, which is a selection of metals from the lanthanide group. The use of lanthanides as a relaxation agent was inspired by the use of gadolinium as a T_1 contrast agent in MRI (9,10).

Lanthanides are well known relaxation agents within the imaging community and have been routinely used since the 1980's in clinical settings (9,11). In this work, lanthanides will be used as a T_1 relaxation agent to achieve a hyperpolarised state, rather than as a contrast agent for imaging. The lanthanides are effective relaxation agents due to their paramagnetic properties. The underlying theory behind the enhanced relaxation rates due to paramagnetic impurities has been expressed by I. Solomon (12). At a later time, R. Lauffer gave an overview of many aspects of using paramagnetic metal complexes in a clinical environment (11).

Chapter 1. Introduction

Lanthanides have proven to be effective relaxation agents down to ~ 4 K. However, this limits the level of polarisation that can be achieved and is therefore of minimal use unless moderate levels of polarisation enhancement are acceptable.

Chapter 4 describes the use of various metallic and non-metallic nanoparticles as relaxation agents. The initial motivation for using the nanoparticles was the known short T_1 times exhibited by metal in the millikelvin regime (13,14). The nanoparticles have shown much more potential, than the lanthanides, as an effective relaxation agent. This is mainly due to their effectiveness at temperatures as low as 10 mK.

Nanoparticles are an example of a new type of relaxation agent, as such it is important to develop an understanding of how the nanoparticles cause relaxation of the nuclear spin system. Knowledge of the relaxation mechanism will allow the nanoparticles to be optimised. The conduction electrons in metals are known to enhance the relaxation of the metal's own nuclei through the Korringa effect (7). This logic was extended, by suggesting that the conduction electrons from metals will also enhance the relaxation of other nearby nuclei. Work in this thesis shows that copper nanoparticles are effective relaxation agents in the millikelvin regime, as predicted by the extended use of the Korringa effect. However, it was also shown in this work that nanoparticles, which do not have conduction electrons, can also act as effective relaxation agents, the main example is copper oxide. This suggests that another relaxation mechanism can reduce the T_1 times of the sample.

In an attempt to understand the relaxation enhancement from the nanoparticles, various magnetic measurements were conducted in a Superconducting Quantum Interference Device (SQUID) magnetometer. These studies were prompted by various reports in the literature, which state that nanoparticles can display non-intuitive behaviour in respect to their bulk counterpart (15,16,17). The magnetic measurement of the nanoparticles presented in this thesis gives some of the groundwork required in understanding an alternative relaxation mechanism and has also yielded several interesting results. The most interesting observation was that the magnetisation of some samples depends upon whether the nanoparticles are dissolved in a solvent. In the most extreme case, the magnetisation of the sample is 1000-fold larger than the dry nanoparticle equivalent. The magnetic properties of the nanoparticles used in this work are discussed in Chapter 5.

Chapter 1. Introduction

A topic, which is mentioned and used in both Chapter 3 and 4 is thermal mixing. Initially thermal mixing was explored by A. Abragam and W. Proctor in a lithium fluorine crystal (18,19). They explained that at lower fields, it is possible to modify the lithium spin system in the crystal by applying a pulse at the fluorine's Larmor frequency. This idea is extended further by suggesting that at lower magnetic fields, the spin temperature of the lithium and fluorine in the crystal can become equal. Thermal mixing was probed by creating various magnetic states in the lithium and fluorine in the crystal, before allowing the crystal to experience a low field environment for a short period of time, which allowed the spin temperature of the sample to reach equilibrium. Work on thermal mixing has been conducted more recently on a glassy sample by D. Gadian, et al showing that thermal mixing can occur in frozen solutions (20). This becomes of interest, as it proves that thermal mixing is a general technique which can be used to transfer polarisation between nuclear spin systems in solid samples. It is now possible to introduce the idea that thermal mixing can be used to polarise nuclei with large T_1 values, by transferring polarisation from a thermal bath of nuclei with a shorter T_1 value. Although this thesis is not considering the ejection and dissolution process of the frozen sample, it is important to note that thermal mixing will occur between the polariser and scanner, as the sample is likely to experience a low field during transported between the devices. This means that no extra experimental setup is required to take advantage of thermal mixing.

Chapter 2. NMR Theory

This chapter of the thesis focuses on the theory of the NMR and contains an overview of hyperpolarisation methods. In NMR, atomic nuclei are studied by rotating the magnetic moments of the nuclei, so they are perpendicular to an external magnetic field, the external field is often chosen to be in the *Z*-direction. The magnetic moments then precess about the Z-axis and can be measured with a detection coil. Only nuclei that have a spin greater than zero can be measured using NMR, otherwise they are classed as being NMR silent.

Non-NMR silent nuclei have multiple energy levels in an external magnetic field. The number of energy levels depends upon the spin of the nucleus and is equal to *2S+1*, where *S* is the spin of the nucleus. The energy difference between the energy levels can be calculated by considering Zeeman splitting. For simplicity we will assume a nucleus with a spin of ½ (21,22).

$$E = -\mu B \tag{1}$$

Where *E* is the energy, *B* is the magnetic field and μ is the magnetic moment. If the energy difference between the energy levels is known, it is possible to supply that energy to the spin system and change the number of spins in each energy state. The energy required to change the populations can be supplied by a photon of a particular a frequency. Thus, in the field of NMR, it is common to think in terms of a frequency rather than energy. The frequency required to match the energy difference between two energy levels is known as the Larmor frequency.

$$E = \hbar\omega = hf \tag{2}$$

Where $\hbar$ is the reduced Planck constant and ω is the angular frequency. NMR can be thought of in both a classical and quantum mechanical way. In a classical view of NMR, the total magnetisation of the sample is the sum of all of the magnetic moments within the sample. The net magnetisation of a sample is rotated into the XY-plane and over time it aligns back towards the external magnetic field, which is in the Z-direction. The quantum mechanical view of NMR is based on the idea that nuclei can only exist in defined energy levels. If we assume a sample contains spin ½ nuclei, they can either be aligned parallel or

anti-parallel to the external field. The occupancy of the lower energy level, *N+*, is align with the external magnetic field, while the occupancy of the higher energy level, *N-*, is aligned anti-parallel to the external field. The population of these energy levels is governed by the Boltzmann distribution.
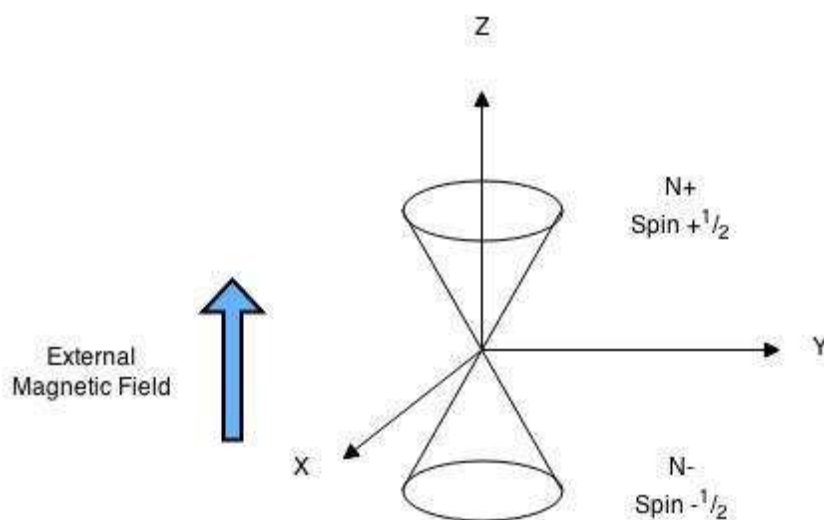
Figure 1: The two possible states for spin ½ nuclei. The exact direction of the magnetic moment for a single nucleus can be anywhere around the edge of the cone, but its length, (the amplitude of the magnetic moment), has a fixed value. On average the magnetisation points in the Z direction.

Classically, the net magnetisation of the system is rotated into the *XY*-plane by applying a second magnetic field, B_1 (in the form of a radio frequency, RF, pulse at the Larmor frequency). The RF pulse tips the magnetisation from the *Z*-direction towards the *XY*-plane. The angle of rotation of the magnetisation, α, is determined by the amplitude of B_1 and the length of the pulse, τ (22).

$$\alpha \propto B_1 \tau$$

The nuclei are then left to relax to their equilibrium state. If the timing and angles of the RF pulses are set correctly various properties about the sample can be measured, for example, the spin lattice relaxation time, T_1. The RF pulse, from a quantum viewpoint, is a method of changing the populations of the energy levels, forcing higher energy states to become more occupied. In either case, the observed signal is produced only from the excess spins in the lower energy state i.e. the net magnetisation. This is because the magnetisation of the spins in the higher energy level cancels with the magnetisation from the spins in the

lower level. The lower energy level tends to have a small excess which forms the net magnetisation. It should be noted that at room temperature and 3 T, standard conditions for an MRI machine, only about 1 in 10^5 spins in a proton sample are responsible for the signal. The fact that only a small percentage of the sample is responsible for the signal is counteracted by the fact that a typical system contains Avogadro's number of protons, (6 x 10^{23}) (8,22). Equation (3) is used to determine the number of spins in any given energy level and is useful for determining the magnetisation for a system in a given state.

$$Population = \frac{N}{Z} \exp\left(\frac{-E}{kT}\right) \tag{3}$$

N is the number of spins in a system, k is the Boltzmann constant, T is the temperature and Z is the partition function to normalize the result.

$$Z = \sum_{m=-j}^{j} \exp\left(\frac{-E}{kT}\right)$$

By considering the populations of the higher and lower energy levels, a value for the polarisation of the sample can be obtained, as seen in equation (4).

$$P = \frac{N_+ - N_-}{N_+ + N_-} \tag{4}$$

From equation (4), we can find an expression for the polarisation of the sample in terms of the temperature and external field, B_0, by combining equations (3) and (4).

$$P = \tanh\left(\frac{E}{kT}\right) = \tanh\left(\frac{\gamma \hbar m B_0}{kT}\right) \tag{5}$$

γ is the gyromagnetic ratio and m is the spin of the nucleus. The gyromagnetic ratio is a measure of nuclei precess rate in the external magnetic field. The value of the gyromagnetic ratio is dependent on the nuclei being measured. Another central equation in NMR is equation (6). This combines the equations for Zeeman splitting and photon energy and is used to find the resonance condition of a system.

$$\omega = -\gamma B_0 \tag{6}$$

2.1. *Rotating Magnetisation Using RF Pulses*

When an oscillating magnetic field is applied, from an RF source, the magnetisation of the sample can be rotated towards the XY-plane (22). For many applications of NMR, it is useful to rotate the magnetisation 90^0 from the Z-direction into the *XY*-plane or 180^0 into the negative *Z*-direction. This is known as a π/2 or π pulse respectively. The use of these pulses makes manipulating the sample practical. After a given pulse, the magnetisation vectors are coherent, but over time this coherency is lost due to spin-spin interactions making the signal decay with a characteristic relaxation time, T_2, which will be discussed later.
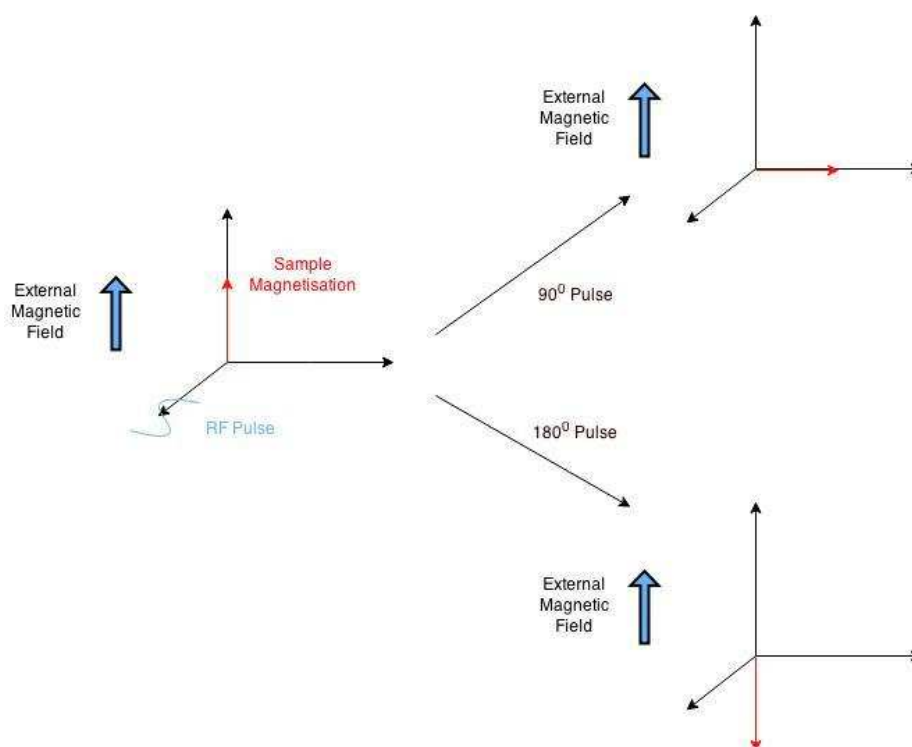
Figure 2: The effects of a 90^0 pulse and a 180^0 pulse

Another useful set of pulses is a saturation sequence. This is a set of pulses which rotates all of the magnetisation into the XY-plane; however, there is no coherence in the magnetisation, this means that there is no net nuclear magnetisation. This is a repeatable starting point and is useful for many experiments. There are several ways to saturate a

system, one example would be to apply a series of 90^0 pulses, with a time delay between them that is several times longer than the T_2 time of the nuclei. The reason for using several pulses, instead of just one, is to ensure the magnetisation is in the XY-plane. Alternatively a longer series of shorter pulses can be used.

Another important tipping angle which is commonly used in the imaging community is the Ernst angle, θ_E. This is the tipping angle that should be used to gain the maximum signal in a given amount of time, when signal averaging. This angle depends upon the T_1 of the sample and the repetition time of the experiment, T_R (23).

$$\theta_E = \mathrm{acos}\left(e^{-T_R/T_1}\right)$$

Finally, there are some situations where the magnetisation of a sample is large enough that it is possible to use very small tipping angle pulses, ~5^0, and still produce a signal large enough to measure. This is useful for measurement of long relaxation processes in real time, as discussed in Section 3.3.2.1.

2.2. Signal Measurement

After the magnetic moments are rotated from the *Z*-axis to the *XY*-plane, the magnetic moments are all in phase. A signal is then produced via induction in a detector coil. It is possible to use the same coil to produce the RF pulse and collect a signal from induction, as the frequency is the same, therefore, the probe only needs one tuned circuit. A duplexer is used to control the signals going into and out of the NMR coil.

The signal collected by the coil, known as a free induction decay, FID, has the same shape as one, or multiple, damped oscillators. The FID is Fourier transformed to produce a spectrum of peaks at characteristic frequencies of the damped oscillators. The frequency depends on the nuclei studied and the local chemical environment for that nuclei. An example would be that protons in a CH_3 group would produce a peak at a different frequency than protons in a COOH group. This is due to the protons in each case experiencing a slightly different magnetic field, this equates to a different Larmor frequency. The equipment being used in this work is not sufficient to measure chemical shifts, as we are

working with solid state samples without shims or magic angle spinning, so the line shapes which are acquired are very broad.

2.3. *Bloch Equations*

The Bloch equations are a set of equations that can be used to calculate the magnetisation of the sample, in a given direction, over time (21). There are three Bloch equations (see below) one for each direction, relating to the magnetisation, $\boldsymbol{M}(t) = (\boldsymbol{M}_x(t), \boldsymbol{M}_y(t), \boldsymbol{M}_z(t))$, the magnetic field, $\boldsymbol{B}(t) = (\boldsymbol{B}_x(t), \boldsymbol{B}_y(t), \boldsymbol{B}_0 + \Delta \boldsymbol{B}_z(t))$, and the relaxation times, T_1 and T_2. It should be noted that the $\boldsymbol{B}_z$ component of $\boldsymbol{B}(t)$ is broken into two parts: the static $\boldsymbol{B}_0$ field and $\Delta \boldsymbol{B}_z(t)$, which is the perturbation in $\boldsymbol{B}_z$ over time.

$$\frac{d\boldsymbol{M}_x(t)}{dt} = \gamma (\boldsymbol{M}(t) \times \boldsymbol{B}(t))_x - \frac{\boldsymbol{M}_x(t)}{T_2}$$

$$\frac{d\boldsymbol{M}_y(t)}{dt} = \gamma \left(\boldsymbol{M}(t) \times \boldsymbol{B}(t)\right)_y - \frac{\boldsymbol{M}_y(t)}{T_2}$$

$$\frac{d\boldsymbol{M}_z(t)}{dt} = \gamma (\boldsymbol{M}(t) \times \boldsymbol{B}(t))_z - \frac{\boldsymbol{M}_z(t) - \boldsymbol{M}_0}{T_1}$$

These equations can only be used at a macroscopic level (22). It can be seen from these equations that the T_1 time is a time constant that controls how the magnetisation returns to equilibrium in the Z direction. If it is assumed that the T_1 time is large, then the time taken for a sample to reach equilibrium is long. The T_2 time is associated with the coherency of the magnetisation the X and Y directions. If the value of T_2 is large, it can be seen that the sample will remain coherent for a long period of time after an RF pulse.

In the field of hyperpolarisation, the value of T_1 in various conditions is one of the most important parameters to know. This is because the T_1 time is an effective measure of how long a hyperpolarised state can be maintained. The T_1 time is even more important in this research as the brute force method relies upon spin-lattice relaxation to achieve the highly polarised state. Before giving a more formal introduction to the T_1 and T_2 times it can be useful to understand and invoke the rotating frame of reference.

2.4. *Rotating Frame of Reference*

When considering a system with elements of rotation or precession, it is usually useful to invoke a rotating frame of reference, for example, when thinking about pulse sequences. In the case of NMR, the speed of rotation in this rotating frame is set to match the precession of the magnetic moments. For simplicity the T_1 and T_2 times will be set to infinity to remove the effects of relaxation.

If we imagine that we are at the origin of the rotating frame of reference, with the magnetisation facing radially outwards, as time passes the direction of the magnetisation would not change as both the reference frame and the magnetisation are precessing at the same frequency. If we were in the lab frame and watched the precessing magnetisation, it would appear to precess at the Larmor frequency.

2.5. *Relaxation*

Over time the magnetisation of the system will move towards its minimum energy, based on the Boltzmann distribution. The process of the magnetisation moving towards its minimum energy is called spin-lattice relaxation, this has a time constant associated with it called T_1. Below is an equation showing the relaxation after a 90^0 RF pulse (22).

$$M_z = M_0(1 - e^{t/T_1})$$ (7)

M_z is the component of magnetisation in the *Z*-direction after a time *t*. M_0 is the equilibrium magnetisation in the *Z*-direction at the current polarisation conditions.
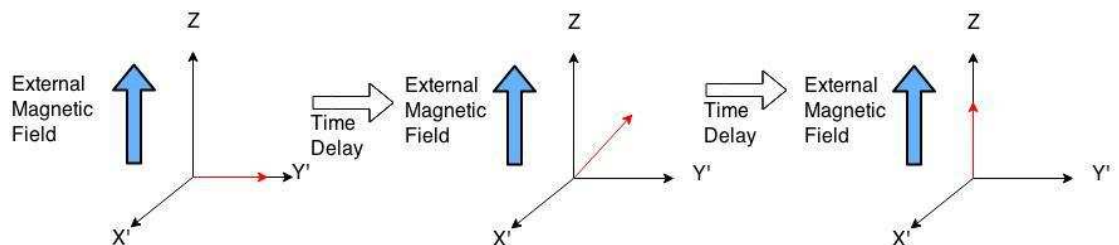
Figure 3: The Spin-lattice relaxation of a system in the rotating frame.

Although the magnetisation recovery tends to follow equation (7), this is not always the case. In samples which are inhomogeneous, the magnetisation might follow a multi-exponential recovery. A cause of inhomogeneity might be due to the addition of a relaxant into a sample.

The T_2 time is a measure of the coherence between nuclei in the sample (12). Spins in a higher magnetic field precess faster than those in lower magnetic fields, as predicted from equation (6). A cause of the variance in the magnetic field can be the molecular motion of other nearby nuclei. Over time, the magnetisation in the XY plane loses coherency because the difference in orientation between the faster precessing nuclei and slower precessing nuclei increases.

It is easier to imagine the decoherency by invoking the rotating reference frame. We can think of the sample as having fast precessing nuclei, slow precessing nuclei and an average set of precessing spins. As the rotating frame matches the average precession speed we only have to be concerned with the fast and slow components. In the rotating reference frame it can be seen that, as time passes, the angle between the fast and slow components increases. In doing so the average magnetisation decreases as the components oppose one another. One can now imagine reintroducing the spins of each precession frequency, in doing so it can be seen that eventually all the spins will cancel with one another.

The loss of coherence in a system can occur in a shorter time than that of T_2. This decrease in the coherence time is due to inhomogeneity of the external magnetic field. The dephasing rate of the nuclei, following a single pulse, is defined as $1/T_2*$ and contains the contribution from molecular motion of the nuclei and the inhomogeneity of the external field.

$$\frac{1}{T_2{}^*} = \frac{1}{T_2} + \frac{1}{T_{Inhomo}} \qquad (8)$$

The dephasing of the magnetisation normally happens on a shorter time scale than the T_1 relaxation (22). Below is an equation which will always hold true for NMR relaxation times:-

$$2\ T_1 \geq T_2 \geq T_2* \qquad (9)$$

~ 12 ~
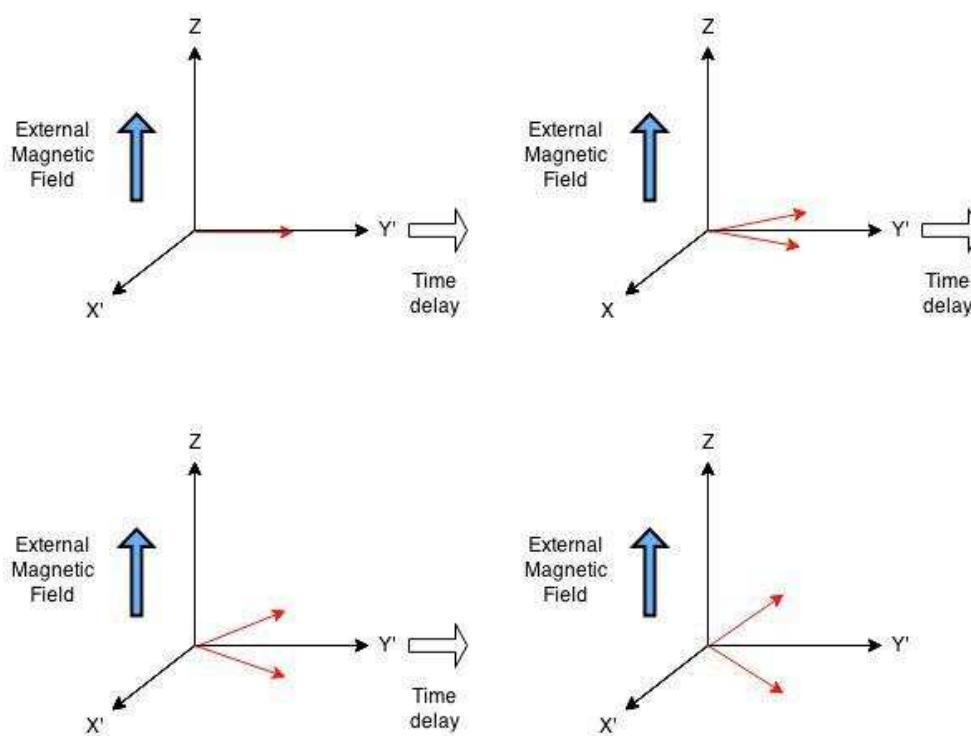
Figure 4: A Schematic of the progression of the T_2 relaxation as a function of time. The red arrows in show the fastest and slowest precessing nucleus in the rotating frame of reference. Only these two nuclei are shown for simplicity. The average magnetisation would be pointing in the Y' direction and would be the vector sum of all of the nuclei in the sample

Combining T_2 relaxation, with the idea that the precessing magnetic moments can induce a voltage in a detection coil, via Lenz's law, it becomes straight forward to see that the FID's shape is an exponentially decaying oscillating wave.

$$\varepsilon_x \propto M_0 \omega_0 \sin(\alpha) \cos(\omega_0 t) \ \exp\left(-\frac{t}{T_2}\right) \tag{10}$$

The FID can be Fourier transformed to produce an NMR spectrum which may have several peaks. Each of these peaks represents a frequency of the FID whose amplitude represents how much of the FID is associated with that frequency. The full width half maximum, FWHM, of each peaks can also be related to the T_2 time of the sample, applying the uncertainly principle.

$$FWHM = \frac{1}{\pi T_2} \tag{11}$$

$\sim 13 \sim$

2.6. *Relaxation Enhancement*

The rate of relaxation depends on several factors, including the magnetic fields that the nuclei experience and the fluctuations in these fields. It was appreciated by I. Solomon that adding a paramagnetic material to a sample would enhance the relaxation rate of the other nearby nuclei through dipole-dipole interactions (12).

2.6.1. *Correlation Function and Spectral Density*

The correlation function is a way of looking at random fluctuations in a system over time and is an important mathematical tool when considering molecular motion. Over large time scales, the average fluctuation of a randomly fluctuating system, is zero, while the mean squared average of the system is greater than zero. The autocorrelation function is a function which quantifies of how rapidly the field is fluctuating (22).

$$G(\tau) = < F(t)F(t + \tau) > \neq 0 \tag{12}$$

$G(\tau)$ is the autocorrelation function, τ is a small time step and F is the randomly fluctuating parameter. The angular brackets represent the average value. If $F(t)$ is varying slowly and τ is very short, $F(t)$ and $F(t+\tau)$ are likely to have the same sign and therefore, $F(t)F(t + \tau)$ >0. As τ is increased, the bias between the signs of $F(t)$ and $F(t+\tau)$ is reduced, this means that half of the time $F(t)$ and $F(t+\tau)$ will have the same sign and half of the time they will have opposite signs. This means that, on average, $G(\tau)$ will approach zero. It is also common to assume that $G(\tau)$ follows a single exponential (22).

$$G(\tau) = < F^2 > e^{-|\tau|/\tau_c} \tag{13}$$

τ_c is the correlation time of a randomly fluctuating function. Rapid fluctuations have a small value of τ_c and slow fluctuations have a large value of τ_c. In the case of rotating molecules in a liquid, the value of τ_c can be between 10-1000 ps, while in solids it will be longer. Figure 5 is a visual representation of how the size of τ can change $G(\tau)$.
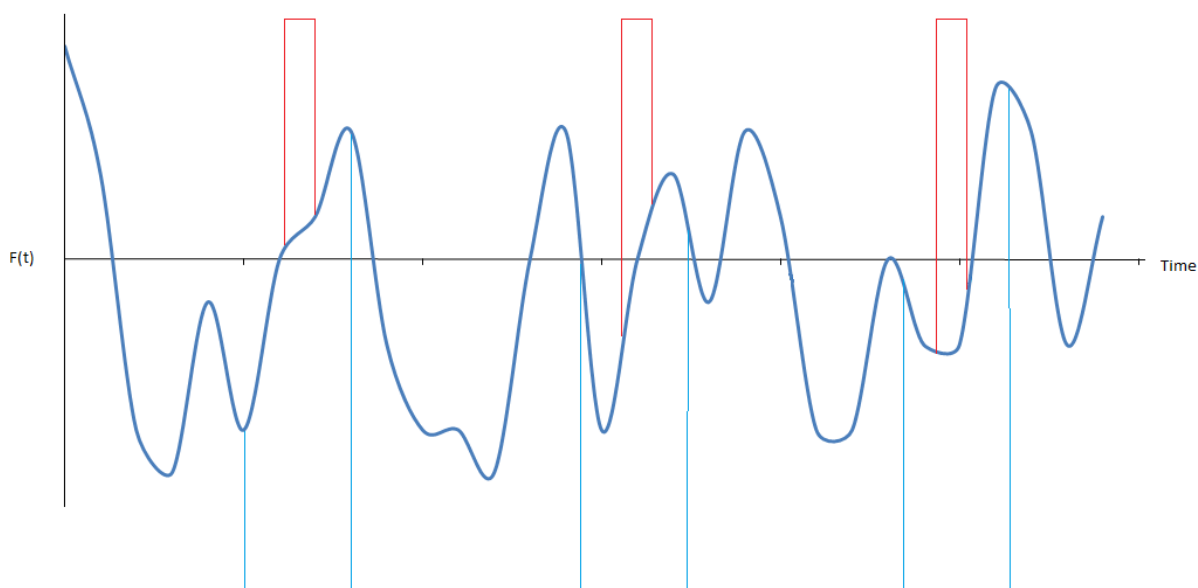
Figure 5: Graph of randomly varying 'data'. The red and blue boxes represent a data point for *G(τ)*, where the red assumes a small value of *τ* and the blue represents a larger value. For the small values of *τ* it is more likely that *t* and *t+τ* have the same sign, meaning *G(τ)* will be very positive, while for larger values of *τ* there is less to no correlation between the values at *t* and *t+ τ*, therefore, *G(τ)* tends towards zero.

The spectral density, *J(ω)*, is the Fourier transform of the correlation function, as seen in equation (14). This transformation allows us to convert the correlation time into a frequency. A system that has a short correlation time will have a broad spectral density and vice versa. This is intuitive, as rapidly tumbling molecules will sample a larger set of frequencies than slower molecules, therefore more rapidly tumbling molecules will have a broader spectral density.

$$J(\omega) = 2\int_0^\infty G(\tau)e^{-i\omega\tau}d\tau \tag{14}$$

The relaxation of nuclei is fastest when the value of the spectral density matches the Larmor frequency. The maximum of $J(\omega_0)$ occurs when the correlation time is $\tau=1/\omega_0$. In a case where multiple spins are in the system, not only is the spectral density at ω_0 important, but also the spectral density that corresponds to the summation and difference between the Larmor frequencies of the other nuclei in the system. These frequencies correspond to the

double quantum and zero quantum transitions respectively (18). In the case of like spins the spin-lattice relaxation rate has the form:-

$$\frac{1}{T_1} \propto J(0) + J(\omega_0) + J(2\omega_0) \tag{15}$$

The form of equation (15) matches that of derived by Solomon (equation (16)). Where there is dipolar coupling between two spins, the relaxation induced follows the square of the coupling (18). By considering the spectral density function in equation (15), I. Solomon formulated two equations which can calculate the T_1 and T_2 times of a sample (12).

$$\frac{1}{T_1} = \frac{\hbar^2 \gamma_I^2 \gamma_S^2}{10r^6} \left[\frac{\tau_c}{1 + (\omega_I - \omega_S)^2 \tau_c^2} + \frac{\tau_c}{1 + \omega_I^2 \tau_c^2} + \frac{\tau_c}{1 + (\omega_I + \omega_S)^2 \tau_c^2} \right] \tag{16}$$

$$\frac{1}{T_2} = \frac{\hbar^2 \gamma_I^2 \gamma_S^2}{20r^6} \left[4\tau_c + \frac{\tau_c}{1 + (\omega_I - \omega_S)^2 \tau_c^2} + \frac{3\tau_c}{1 + \omega_I^2 \tau_c^2} + \frac{6\tau_c}{1 + \omega_S^2 \tau_c^2} + \frac{6\tau_c}{1 + (\omega_I + \omega_S)^2 \tau_c^2} \right] \tag{17}$$

Where γ_I and γ_s and the gyromagnetic rations for spin I and spin S and r is the distance between spin I and spin S. From equation (16) it should also be noted that if two protons were at a fixed distance, then the relaxation would be 16 times stronger than if two ^{13}C were at the same separation. Equation (16) can be useful in determining which properties are desirable in a relaxation agent as it considers the interaction between two spins.

2.7. *Thermal Mixing*

It has been shown in various papers that polarisation can be transferred between nuclei using a method known as thermal mixing (7,20,24). Initially thermal mixing was explored by A. Abragam and W. Proctor in a lithium fluorine crystal (18,19). They realised that at low fields, the spin temperature of the lithium and fluorine in the crystal come to an equilibrium. This idea was probed by setting the polarisation of the lithium and fluorine to 1, 0, or -1 relative to their own equilibrium polarisation. The crystal was then exposed to a low field by physically removing the sample from the external field for a short period of time. This allowed the spin temperature, T_s, of the spin systems in the sample reach a common equilibrium.

The spin temperature is a measure of the populations of each energy level. If the spin system was not polarised, i.e. both states are equally populated, its spin temperature would be infinity. If the spin system is polarised to unity, i.e. all of the nuclei are in the lower energy state, then the spin temperature is zero. The spin temperature can be calculated by using equation (18).

$$\frac{N_-}{N_+} = exp\left(\frac{-\gamma\hbar B}{k_b T_s}\right)$$ (18)

Consider a system of highly polarised protons and unpolarised ^{13}C, it should be possible to transfer the proton polarisation to the ^{13}C, by transiently reducing the magnetic field of the system. The transfer will occur when B_0 is of the same order of magnitude as the local field of the sample, B_{loc}. The time spent at this very low field is normally of the order of milliseconds, as it takes time for the polarisation transfer to occur. However, if the time spent at the low field is long, compared to the T_1 time at the low field, the entire polarisation is lost. This method of polarisation transfer is potentially useful, as the T_1 for protons is shorter than that of ^{13}C or ^{31}P; therefore this should allow high levels of polarisation in ^{13}C or ^{31}P to be achieved in a shorter period of time.

The principle ideas that makes using thermal mixing possible in this way is that the "specific heat" of the faster relaxing nuclei can be arranged to be much larger than that of the slower relaxing nuclei (19). The specific heat of the ith nuclei e.g. ^1H or ^{13}C can be calculated with:-

$$C_i = p_i I_i(I_i + 1)\gamma_i^2$$ (19)

Where C_i is the spin specific heat, p_i is the ratio of the number of spins and I_i is the spin of the nuclei i. The spin temperature will be distributed across the spin system allowing for the spins to reach a common spin temperature (19). Protons have the highest specific heat of the nuclei in the sample, they are also the most common nuclei, meaning they are the equivalent of a heat reservoir. They also have a short T_1, meaning their spin temperature will reach equilibrium with the lattice in the shortest time. These properties are ideal for using protons to polarise the other nuclei in the sample.

2.8. *Hyperpolarisation*

A hyperpolarised state is one where the magnetisation of the sample is greater than its thermal equilibrium. There are many methods of achieving this state, the most common method, DNP, cross-polarises electron polarisation to the nuclei of interest (8).

The progression to thermal equilibrium, from any magnetisation, normally follows an exponential curve with a time constant of T_1. The T_1 value varies as a function of field and temperature, this is an important consideration when using hyperpolarisation techniques as a temperature change normally occurs prior to measurement.

The aim of the research is to make a contrast agent that can be used in MRI, by making a hyperpolarised sample, which can highlight an area of interest. To accomplish this, a sample should be easy to polarise in favourable conditions, high fields and low temperatures, and maintain its polarisation while at 300 K and 3 T, the standard conditions for MRI. The problem with the brute force method is the very long T_1 at low temperatures. The long polarisation times can be combated with the use of relaxation agents (7,24,25).

Once a sample has been polarised at low temperatures, it will need to be quickly heated to room temperature and measured whilst ensuring the smallest amount of polarisation is lost. This is likely to be done by injecting warm water into the sample (3,26). An ideal relaxation agent would work like a switch, i.e. only decrease the T_1 at the very low temperatures, while at temperatures, near 300 K, the T_1 value is unaffected.

At the higher temperatures the hyperpolarised state will only last for a short duration as the sample begins to equilibrate with its new surroundings. As a general rule of thumb, spending $5*T_1$ in an environment means the sample has reached its new equilibrium. Once the sample is polarised and is ready for measurement, it is warmed. As the sample is warming, it starts relaxing to its new equilibrium polarisation. The loss of polarisation can be seen in Figure 6. Therefore, it is ideal to reduce the time between warming the sample and the measurement so that the largest polarisation is maintained for measurement.
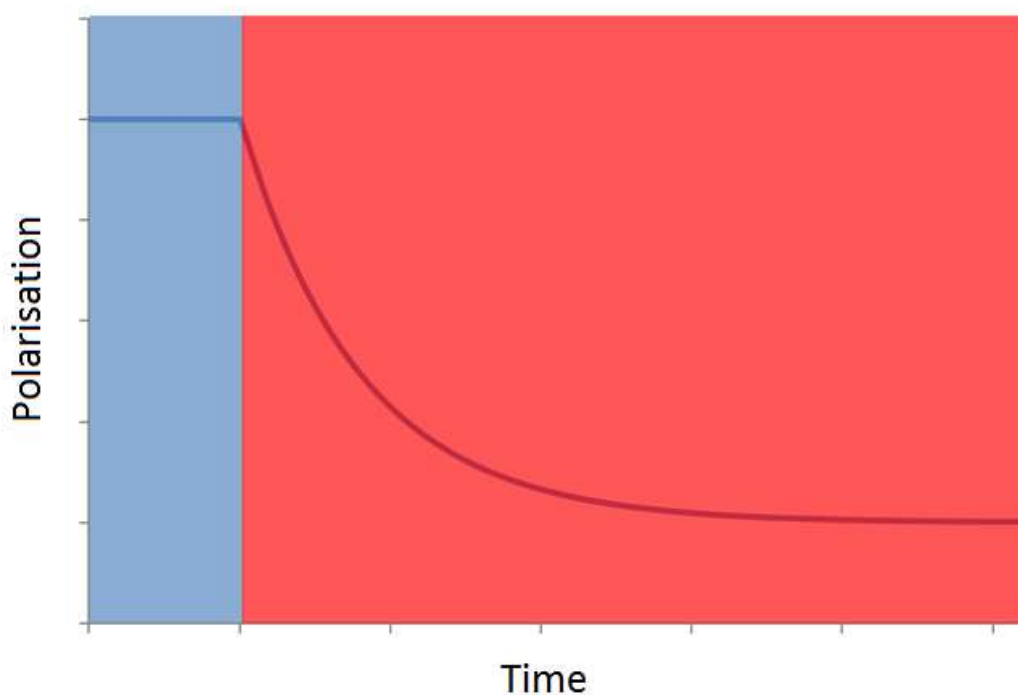
Figure 6: Schematic of the magnetisation of the sample during a warming routine. The blue section indicates that a sample is in its polarised state. The red section indicates that the sample has been warmed to conditions suitable for measurement. It can be seen that the magnetisation decays rapidly from a highly polarised state to its new equilibrium.

Hyperpolarisation Methods

Although the research conducted in this thesis is focused on using the brute force method to achieve high levels of polarisation, it is by no means the only way in which hyperpolarised states can be achieved. It is fitting to have an overview of these other methods highlighting the benefits and drawbacks of each (8,27).

2.8.1. *Dynamic Nuclear Polarisation (DNP)*

Dynamic nuclear polarisation was first considered by Overhauser (28). The concept was based on increasing the nuclear polarisation by using the electron polarisation of unpaired electrons in the sample, usually in the form of a free radical additive. Electron-nuclear interactions, which can be used in solid state DNP, include the solid effect and the cross

~ 19 ~

effect. The solid effect works by irradiating the zero or double quantum transition with a microwave source, which offsets the populations of the energy levels and enhances the nuclear signal (27). As these transitions are forbidden, a powerful microwave source is required. The transitions between energy levels can be seen in Figure 7. It should be noted that the solid effect has a strong B_0 dependence.
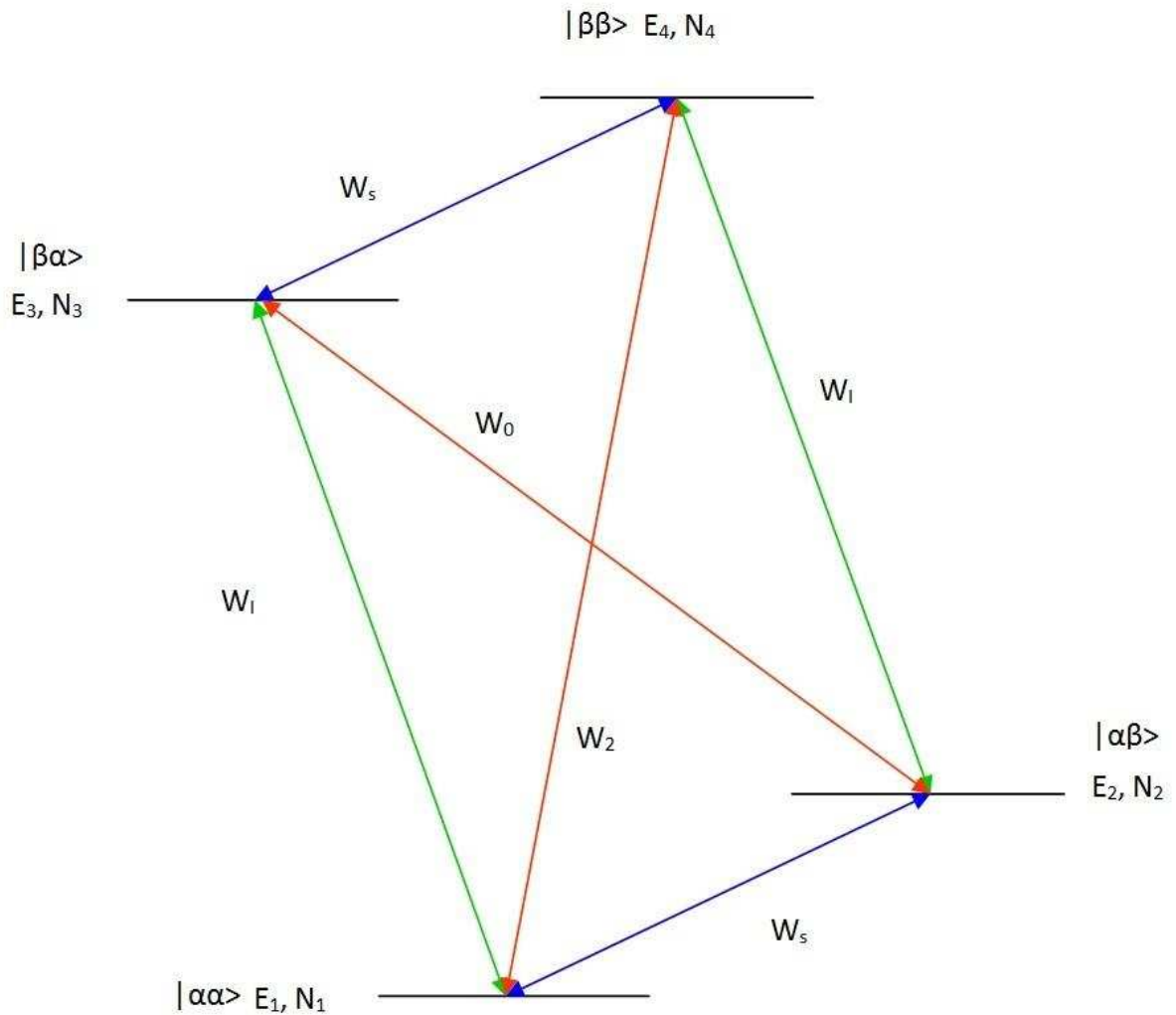
Figure 7: Energy level diagram showing the four available energy levels for a electron-nuclear system. It also shows all the available transitions that can occur. The W_I and W_s transitions are single quantum transitions of a spin with a larger and smaller gyromagnetic ratio respectively. The W_0 and W_2 transitions are the forbidden transitions. W_0 is the zero quantum transition or a flip-flop, while W_2 is a double quantum transition or a flip-flip.

The cross effect requires two unpaired electrons which are dipolar coupled and whose resonance frequencies are separated by the Larmor frequency of the nuclei of interest (29,30). The microwave source is tuned to the allowed single quantum transition which means the microwave source can be much weaker than in the solid effect.

Many DNP experiments also operate at low temperatures, in the order of 1 K; this ensures that the electrons can be fully polarised. The sample is then warmed up through a dissolution step before a being used in NMR or MRI; this is known as dissolution DNP (3,4). The development of dissolution DNP means that technologies for rapid heating of a sample already exist, and with some modifications, could be used in conjunction with the brute force method. However, dissolution technology was not available for the brute force experiments in this thesis.

2.8.2. *Para-Hydrogen Induced Polarisation (PHIP)*

PHIP is a chemical route used to hyperpolarise a sample (4,27,31). Dihydrogen has forms called spin isomers; in one form, known as orthohydrogen, the protons spins align to one another and in the other form, known as parahydrogen, the hydrogen spins align in opposition. The total spin in the ortho- state is 1 and therefore have three states, with M_I=1, 0, -1. Alternatively the para- state has a total spin of 0 and therefore is only a singlet state. Parahydrogen has a lower energy state due to symmetry arguments. Therefore, at low temperatures, around 4 K, dihydrogen will be almost completely in the para- state, however, at room temperature only 25% of the dihydrogen is in the para- state. A para- to ortho- state conversion is very slow, in the order of months.

In PHIP, parahydrogen is mixed with a sample that contains a double bond, which can be broken in a process called hydrogenation. For the polarisation to occur, the parahydrogens must then end up in non-equivalent positions in a molecule whilst remaining coupled. Note they can end up in equivalent positions so long as in the intermediate steps they are not equivalent. The measured spectrum will consist of a pair of antiphase doublets if the hydrogenation is done at high field. The energy levels in the system can be thought as being the same as that seen in Figure 7; the parahydrogen fills up energy levels E_2 and E_3, so we can see the signal contribution from the E_3-E_4 transition is a positive enhancement, while the

E_1-E_2 transition is a negative enhancement (27). The polarised state can then be transferred to other nuclei, e.g. ^{13}C, however, the signal will still be antiphased (32). This can be corrected either with field cycling or by using a pulse sequence. Normally a catalyst is used to increase the reaction rate with the parahydrogen; this would have to be removed if this method of hyperpolarisation is used for in vivo applications.

2.8.3. *Spin-Exchange Optical Pumping*

This method of hyperpolarisation is only achievable with noble gases (8,33). Noble gas, normally ^3He or ^{129}Xe, is placed in a glass container with an alkali metal, normally rubidium, with some quenching gas, usually nitrogen. A circularly polarised light source is then used to excite the electrons in the alkali metal. The noble gas then collides with the alkali metal and the angular momentum is transferred from the electrons of the metal to the nuclei of the noble gas. The quenching gas stops the polarised alkali metal from fluorescing, which would otherwise depolarise the noble gas.

Another important point is that the cross-section of the collision between the noble gas and the alkali metal is very small, it is only because of large numbers of atoms that such collisions occur. (34) To make the process more efficient potassium is usually added. The polarisation is now passed from rubidium to potassium before going to the ^3He. This is known as a hybrid system and as long as there is more potassium than rubidium, this can become a more efficient method of transferring the polarisation from the rubidium to ^3He (35).

2.8.4. *Haupt Effect*

The Haupt effect occurs when a compound with a quantum rotor, normally a methyl group, undergoes a temperature jump (36,37). The quantum rotor has various rotational levels and the effect occurs when a sample, which is below 50 K, is rapidly warmed by a few degrees. The sample has to have relaxed at the low temperature before the temperature jump can take place. This temperature jump allows for transitions in the rotational levels and over the course of several minutes the sample gains dipolar polarisation, though its

Zeeman polarisation experiences little change. Various pulse sequences can be used to transfer the dipolar polarisation into Zeeman polarisation. It is also possible to use cross polarisation to polarise ^{13}C and ^{15}N (38).

The rotational levels are known as the A and E states, which have spin 3/2 and 1/2 respectively. Transitions from A states to A states or E states to E states are very easy, as this can be done without the need of a magnetic transition, however, when transferring between A and E states a dipolar interaction is also required. The result of transitioning between the A and E states is the cause of the dipolar polarisation (36,39).
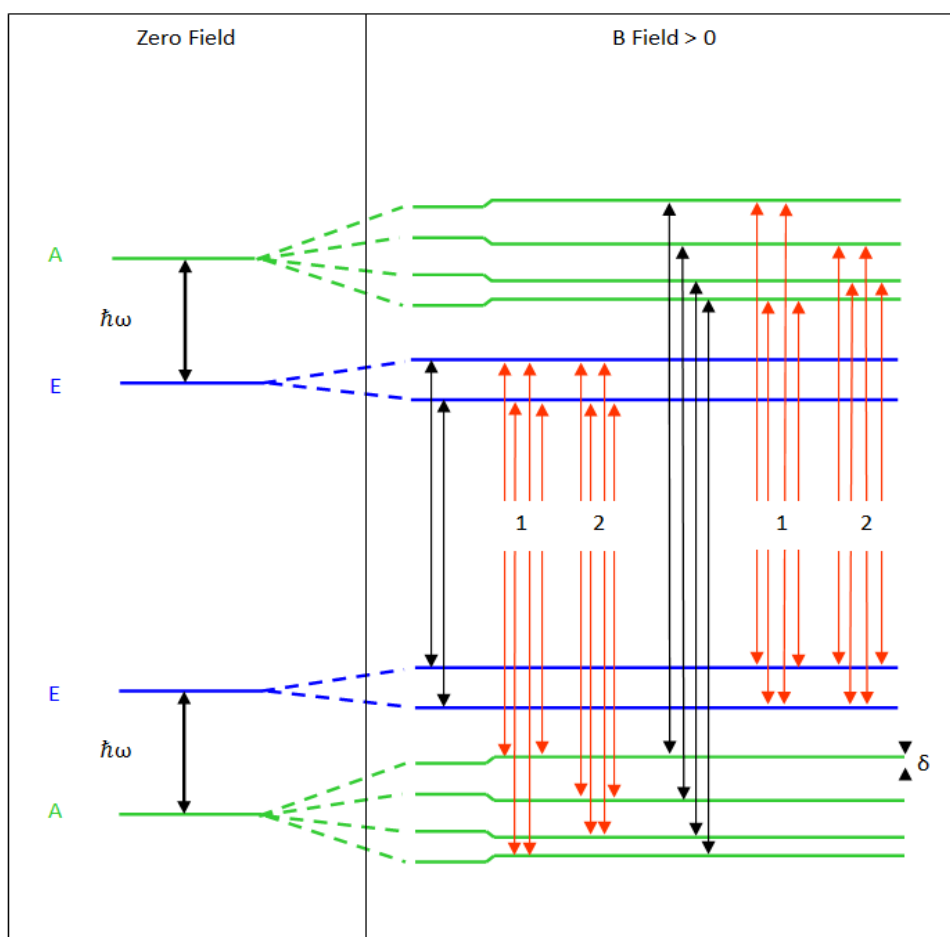
Figure 8: The energy levels of A and E states are separated by the tunnelling frequency $\hbar\omega$. The ordering of A and E alternates with each successive torsional level. The black transitions are the faster A-A or E-E transitions, while the red transitions are the slower A-E transitions. These red transitions are also broken down to group 1 or group 2, where group 1 are transitions to and from upward shifted levels and group 2 is to and from downwards shifted levels. The δ shift is due to the dipole interactions.

~ 23 ~

2.8.5. *Advantages and Disadvantages of the Brute Force Method Compared to Other Hyperpolarisation Methods*

The first point which should be made is that regardless of how a sample is polarised, as soon as it has left the polariser it will start decaying towards its new equilibrium point at the rate of its T_1, similar to that shown in Figure 6. The most important value, when considering hyperpolarisation, is not the magnetisation of the sample while it is being polarised, but the magnetisation of the sample in the scanner.

The level of polarisation achieved in a DNP system is greater than the polarisation achieved using the brute force method, while the sample is in its respective polariser. This generally means that the samples from DNP will enter the scanner with a higher level of polarisation. However, samples which are polarised via the brute force method can have longer T_1 times during transport between the polariser and the scanner, if the samples are stored in a magnetic field at liquid helium temperatures. Therefore, more polarisation is maintained for the measurement. Hence, even though DNP can reach higher levels of polarisation it might be possible to have similar levels of signal during measurement.

Some polarisation methods are limited as to which samples they can polarise, as well as the final polarisation enhancement. For the intended application of in vivo studies, only two methods of hyperpolarisation are suitable. These are DNP and the brute force method as they can produce high levels of polarisation in samples that are liquids at room temperature.

The rate of production as a central issue for in vivo studies. If a method is to be successful, a high throughput is required. The brute force method has an advantage here, as it is very easy to scale production. DNP is scalable in the sense that it requires a short polarisation time, although the volume of sample is limited to the absorption of the microwave irradiation (40,41).

The cost associated with buying and running a polariser is also an important factor when considering which polarisation method to use. The brute force method's hardware is in some aspects a little crude, for example, the magnetic field does not have to be uniform; it just has to be strong. A large portion of the funds would go towards buying the ^{3}He to run the fridge, in order to achieve the lowest temperatures. The cost associated with running a

brute force system is mainly for cooling the system; cryogens in a wet cryostat or electricity to run the pumps in a dry cryostat. A DNP system has similar running costs to the brute force method as it too has to be cooled and will be running a microwave source. The initial cost of equipment for DNP is expected to be higher as the magnet has to be more uniform than a magnet used for brute force polarisation, a DNP system also requires a microwave source which has to be purchased.

Both of these hyperpolarisation methods have their merits and the aim of this research is to determine if the brute force method is more beneficial than DNP for some intended purposes.

Chapter 2. NMR Theory

Chapter 3. Lanthanides

In Chapter 2, the basic theory of NMR was introduced along with hyperpolarisation. It was mentioned that the brute force method required a long time to reach high levels of polarisation. It is possible to decrease the polarisation time by adding a relaxation agent to the sample. This chapter is focused on using lanthanides as an additive to decrease the T_1 of samples at low temperatures (≤ 4 K). These low temperatures are where the brute force method becomes effective. If the lanthanides prove to be effective at decreasing T_1, it would allow for high levels of polarisation to be achieved in a practical time scale.

Gadolinium is a lanthanide which is routinely used as a relaxation agent in MRI. This lanthanide is effective at reducing T_1 near room temperature, as at room temperature the electron spin flip time matches the resonance conditions of protons in a conventional MRI scanner. More details about this mechanism are given in Section 3.1.1. The lanthanides used in this chapter have a shorter electron spin flip time than gadolinium at room temperature and are therefore expected to be effective relaxation agents at much lower temperatures. This is due to the spin flip time increasing as the temperature decreases.

The way lanthanides are used in this work will be different from how gadolinium is used in a clinical environment. When taking a MRI image, a pulse sequence is used to highlight areas of interest, commonly based on their T_1 or T_2 times. The gadolinium changes the T_1 of nearby protons so that areas of interest can be more easily distinguished, i.e. increasing the contrast. The lanthanide in this research will instead be used to decrease the T_1 times of the nuclei at ideal conditions for brute force polarisation. The samples will be polarised in a separate polariser at low temperatures and high fields, before being warmed to room temperature for a "single shot" experiment. In this case, the contrast comes from the highly polarised state of the injected sample. The drawback of this type of NMR is that once the hyperpolarised state has been used, it cannot be recovered.

The gadolinium, which is currently used as a contrast agent in MRI, comes in a chelated form; this is to reduce its toxicity and enhance its solubility at pH 7 for clinical use. As the other lanthanides are chemically similar, it would be expected that the lanthanides used in

this chapter will also have to be in a chelated form, so that they have the potential to be used in clinical studies (9,42).

The aim of this research is to supply candidate samples which can be used for clinical studies, therefore, it is important to obtain high levels of polarisation in nuclei within molecules of biological importance. Although protons could be used in principle, the T_1 time at room temperature is too short to reap the benefits of using a hyperpolarised sample (between 1 and 10 s) (43,44). The time between dissolution and measurement is too long, so the hyperpolarised state is lost. Nuclei such as ^{13}C are of interest as they tend to have a longer T_1 time than protons (26). Using nuclei with long T_1 times has the drawback that the sample needs longer to achieve a suitably large polarisation. A method of overcoming this long polarisation time is to transfer polarisation from nuclei with a short T_1 to nuclei with a longer T_1 (in these samples, from protons to ^{13}C) effectively replacing the ^{13}C T_1 with the proton T_1 (20). Thermal mixing is a method of transferring polarisation between nuclei and is detailed in section 2.7.

The full cycle of a sample would be as follows:-

1. The sample is loaded into a polariser with suitable settings for temperature and field, such that high levels of proton polarisation are achieved and in an acceptable time scale.

2. Once the protons have been polarised, a thermal mixing step that transfers the polarisation to ^{13}C should take place. This can either be by changing the B_0 field of the polariser, or more likely, transporting the sample through the low magnetic field between the polariser and the scanner. Thermal mixing should be done before the dissolution step so that the maximum polarisation maintained for measurement.

3. The sample is then brought to room temperature and filtered, if necessary, so it is ready for use.

4. A new sample is loaded into the polariser.

Step 1 in this process is the rate limiting step. The long polarisation step could be effectively overcome by allowing multiple samples to be polarised simultaneously and using the samples sequentially. This allows for some samples to polarise while other samples are ready for use.

3.1. *Theory*

3.1.1. *Relaxation Enhancement*

An effective relaxation agent for this research has three criteria which need to be satisfied. The first is that the relaxation agent is effective in the low temperature regime. If this is not the case the T_1 of the sample will be too long to be practical. The second criterion is that the T_1 times at the high temperatures, 300 K, are suitably long, tens of seconds. If this is not the case, the polarisation will be lost before a measurement can be obtained. The final criterion, although beyond the scope of this work, is that the final sample is non-toxic to the extent that it is acceptable for clinical applications.

The addition of paramagnetic materials in solution contributes to the relaxation rate of nuclei in the solvent. The observed relaxation rate is formed from the addition of diamagnetic and paramagnetic contributions (11).

$$(^1/_{T_1})_{Obs} = (^1/_{T_1})_d + (^1/_{T_1})_P \tag{20}$$

Where $T_{1\,Obs}$ is the observed T_1, $1/T_{1d}$ and $1/T_{1p}$ are the diamagnetic and paramagnetic relaxation rates respectively. If the solute-solute interactions are small, the relaxivity, *R1=1/T$_{1p}$*, is linearly related to its concentration, *[M]* (11).

$$(^1/_{T_1})_{Obs} = (^1/_{T_1})_d + R1[M] \tag{21}$$

As stated in Section 2.6., the local fluctuations in magnetic field increases the relaxation rate of the nuclei, if the fluctuations occur at a frequency similar to the nuclear Larmor frequency. The magnetic interactions are only effective over very short distances, *r*, as they have a dependence on r^{-6}, as seen in equation (22). Equation (22) is the Solomon-Bloembergen equation and gives a value for T_{1M} of nuclei, as a function of distance, by considering the dipole (through space) and contact (through bonds) contributions between spins (12,45).

$$\frac{1}{T_{1M}} = \frac{2\gamma_I^2 g^2 (S(S+1)\beta^2}{r^6} \left(\frac{7\tau_c}{1 + \omega_S^2 \tau_c^2} + \frac{3\tau_c}{1 + \omega_I^2 \tau_c^2} \right) \qquad (22)$$
$$+ \frac{2}{3} S(S+1) \left(\frac{A}{\hbar} \right)^2 \left(\frac{\tau_e}{1 + \omega_S^2 \tau_c^2} \right)$$

Where γ_I is the proton gyromagnetic ratio, g is the electronic g-factor, S is the total electron spin of the metal ion, β is the Bohr magneton, r is the proton-metal ion distance, ω_S and ω_I are the electronic and proton Larmor precession frequencies respectively. τ_c and τ_e are correlation times and $A/\hbar$ is the electron-nuclear hyperfine coupling constant. The dipolar and contact contributions each have their own correlation time, and they are the sum of the reciprocals of the electron spin-lattice relaxation time and of the bound time of the water to the metal.

From equation (22), multiple T_1 times could be associated with a sample containing a paramagnetic centre. This is because the distance between each nuclei and the paramagnetic centre varies. There are several mechanisms which allows for systems with multiple T_1 times to appear to have a single averaged T_1 time. Examples of these mechanisms are chemical exchange and spin diffusion.

In a liquid sample, chemical exchange can occur, meaning that the molecules can move around and therefore the T_1 times are essentially averaged. Relaxation in liquid samples is more conveniently broken down into two effects. The first interaction is the "inner-sphere relaxation", the other effect is known as "outer-sphere relaxation". A schematic of the inner sphere (red) and outer sphere (blue) can be seen in Figure 9.
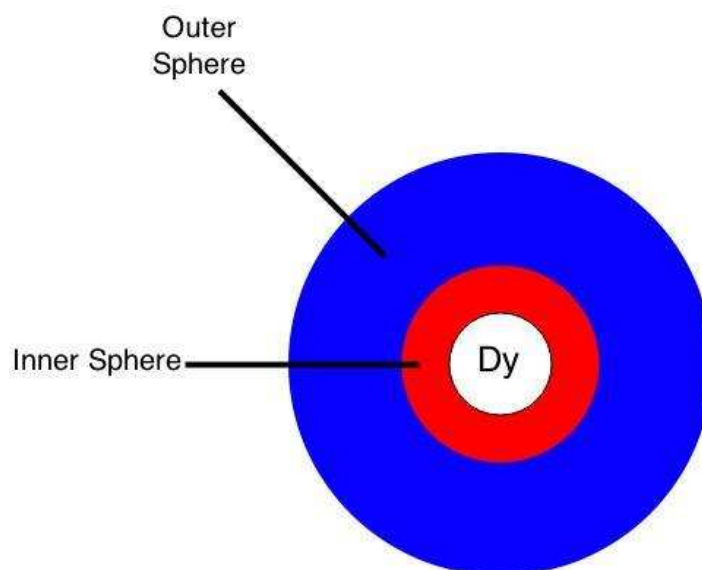
Figure 9: Schematic of inner and outer sphere relaxation in samples containing paramagnetic impurities

The paramagnetic relaxation rate can be rewritten as:-

$$(^1/_{T_1})_P = R1[M] = (^1/_{T_1})_{inner\ sphere} + (^1/_{T_1})_{outer\ sphere} \tag{23}$$

The idea of inner and outer sphere relaxation can only be applied to liquid samples and details can be found in work by R. Lauffer (11).

This research is primarily focused on the solid state, as the samples will be frozen during polarisation. In the solid state, there is no chemical exchange. The only possible way that the polarisation can be transferred between nuclei, therefore averaging the T_1 time of the sample, is via spin diffusion (46,47). Spin diffusion is only effective if the local magnetic field experienced by the two nuclei is similar. Nuclei near a paramagnetic centre are unlikely to experience spin diffusion, as the local magnetic field is very strongly related to the distance from the paramagnetic centre. Without a polarisation transfer technique, it would be expected that the T_1 time of the protons would be dependent upon the distance from the paramagnetic centre. With spin diffusion present, two T_1 times might be expected, one from the nuclei close to the paramagnetic centre, where there will not be spin diffusion and another from the nuclei in the rest of the sample. Experimentally, only one T_1 value is observed, this is because the nuclei near the paramagnetic centres are rendered invisible as detailed in Section 3.5.1. (46). It is noted in Section 3.4.1. that the linewidth of the spectra increase due to the sample is closer to the paramagnetic centre.

3.1.2. *Correlation Time*

At low temperatures, around 10 K, the electron spin flip time of some lanthanides, for example dysprosium, is in the order of the inverse of the Larmor frequency of the protons at 2 T. The electron spin relaxation time is approximately 10^{-9} s at 8K, this was derived by using the uncertainty principle on the linewidth of the EPR spectrum (24,48). Due to the electron spin flip time and the inverse Larmor frequency being similar, the conditions of the system are effective for T_1 relaxation of protons. If the temperature is increased or decreased the electron spin relaxation time will decreased or increased respectively; therefore, the proton relaxation times will be prolonged. This is due to a larger discrepancy in the electron spin flip time and the inverse Larmor frequency. This limits the effective temperature range of the lanthanides and allows for the fulfilment of the second criterion of being an effective relaxation agent.

3.2. *Hardware*

These experiments are based on measuring the T_1 times of protons, with fields and temperatures focused at around 2 T and 10 K. Two spectrometers were used to try to explore the full range of temperatures and fields. The first is a field cycling system that can be cooled down to 4 K and can run at temperatures of up to 200 K, while achieving a maximum field of 2.5 T. The field cycling system allows thermal mixing experiments to be conducted. The second system is a dilution fridge system that can be cooled to 10 mK and obtain a maximum field of 15.5 T. The dilution fridge was used to find the lowest temperatures whereby the lanthanides are still effective relaxation agents.

3.2.1. *Field Cycling System*

The field cycling system is a wet cryostat that can be cooled to 4.2 K with liquid helium, it can also cycle up to field strengths of 2.5 T at a rate of 10 T/s. The temperature can be reduced further by using a pump; however the stability of the system at these lower temperatures is unknown. The system has a PID which allows the temperature to be

stabilised to within 0.1 K of a set temperature, except at temperatures below around 10 K where it is a less stable. PID stands for proportion, integral and differential, these are a set of mathematical operations which looks at the temperature of the system and calculates the power required to achieve the target temperature in the shortest amount of time, without overshooting. The sample can be heated to around 200 K while running an experiment; this is useful for monitoring the T_1 evolution in a warming process. This is useful for calculating how much polarisation would be lost during dissolution.

The system is top loading and can use any one of three available probes at a time. The resonance frequencies of the probes are 14.63 MHz, 21.7 MHz and 38.88 MHz. These probes allow for the resonance frequency of different nuclei to be at the upper limit of the magnet. The 21.7 MHz probe is the most frequently used probe, as it can detect both ^{13}C and protons at 2 T and 0.5 T respectively. The rapid field cycling allows for samples to polarise at various B_0 fields in the same probe, permitting T_1 estimates to be made over a range of B_0 values. This is only valid if the field cycling is slow compared to T_1 as the field needs to return to resonance for measurement. The rapid field cycling also allows for thermal mixing experiments to be conducted.

3.2.2. *Dilution Fridge*

The dilution fridge uses ^3He to lower the temperature below 4.2 K which is set by liquid ^4He at atmospheric pressure. A purely schematic representation of a dilution fridge is shown in Figure 10 with key components labelled. To achieve lower temperatures the cryostat has various stages. The first stage is referred to as the 1 K Pot; however, its actual temperature is closer to 1.5 K. This stage involves transferring ^4He into a chamber which is evacuated by a pump. The decrease in pressure in the Pot increases the evaporation rate of the ^4He, resulting in a decrease in temperature. The 1 K Pot is then used to condense a mixture of ^4He and ^3He. Once the Mixing Chamber and Still are filled, a pump is used to decrease the pressure in the Still which starts the cooling process. When the temperature of the helium in the Mixing Chamber is approximately 0.8 K the helium separates into two phases, the lower phase being a mixture of ^3He and ^4He while the upper phase is pure ^3He. In the Still, the ^3He evaporates more readily than the ^4He because ^3He has a higher vapour pressure, this causes a concentration gradient between the Mixing Chamber and the Still. ^3He is drawn across the

phase boundary in the Mixing Chamber, due to osmotic pressure, which cools the Mixing Chamber. The ^{3}He is purified by being passed through a cold trap which freezes out the impurities. After this cleaning process, the ^{3}He is condensed again by going through the 1 K Pot and the Impedance. To get to the lowest temperatures a roots pump is normally used as it creates a stronger vacuum. This allows for further evaporation of ^{3}He in the Still, resulting in a minimum temperature of around 10 mK.
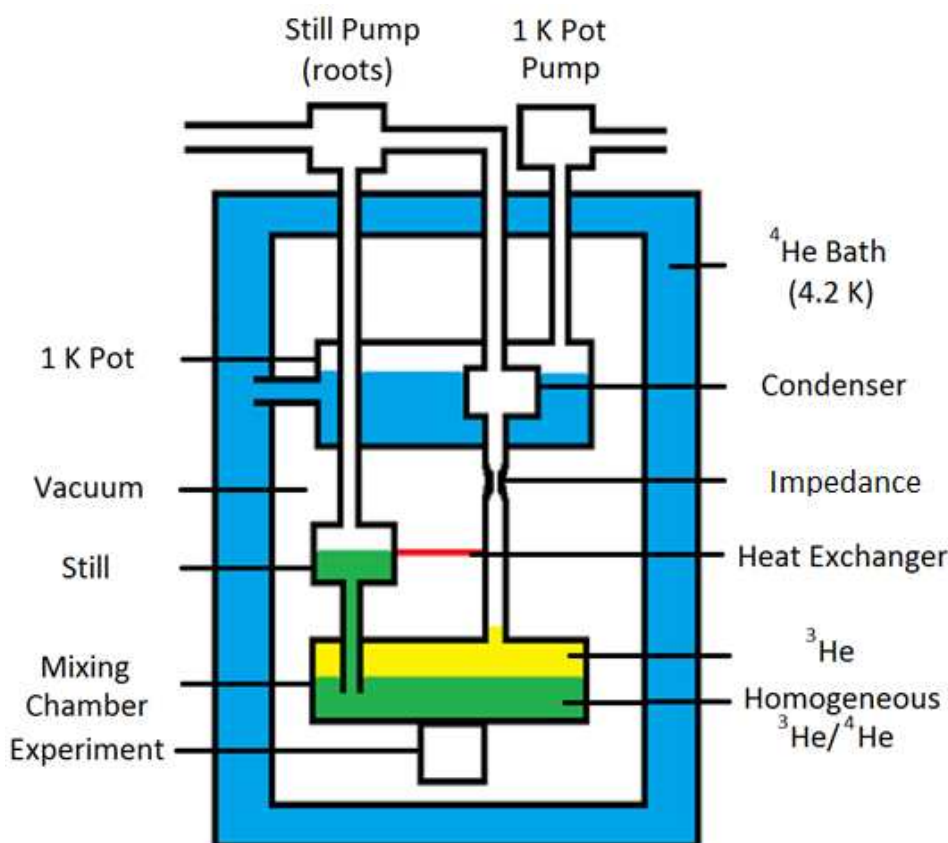
Figure 10: Schematic of Dilution Fridge

This NMR probe is tuned to 104.5 MHz; this means the resonance field of protons is about 2.45 T, ^{13}C is approximately 9.73 T and ^{31}P is around 6.06 T. The maximum field of the magnet is 15.5 T, which allows for a higher ratio of field to temperature, hence a higher absolute polarisation, over 90% for protons in principle. The disadvantage of the dilution fridge is that the maximum ramping speed of the magnetic field is much slower than the field cycling apparatus. The reason for this is that the inductance of the magnet is higher, creating a proportionally higher induced voltage. The persistent superconducting switch used can only tolerate a limited voltage, therefore limiting the rate the field in the magnet

can be changed. Also, a rapid change in field will induce eddy current heating in the probe. This heat can warm the sample and therefore can disrupt measurements. It is still possible to achieve thermal mixing in the dilution fridge as the T_1 of the sample is long in comparison to the time required to change the B_0 field.

3.3. *Methods*

3.3.1. *Sample Preparation*

The samples used in this chapter were lanthanides dissolved in a solution of 50:50 water and glycerol (WG) by volume. The samples form a glass-like phase which allows for a uniform distribution of the lanthanide within the sample. Some of the samples also contain [^{13}C-1] sodium acetate and monobasic sodium phosphate. These compounds are added to allow measurements on ^{13}C and ^{31}P. The lanthanides tested include dysprosium, cerium, holmium and gadolinium. These come as a standard compound of lanthanide (III) chloride. The chelate used in these experiments was Diethylene Triamine Pentaacetic Acid (DTPA). The pH of the sample was set by adding calculated quantities of HCl or NaOH and then checked with a digital pH meter. All of these chemicals were supplied by Sigma Aldrich, (Sigma-Aldrich Company Ltd, The Old Brickyard New Road, Gillingham, Dorset, SP8 4XT, UK).

3.3.1.1. *Paramagnetic material with DTPA in WG*

The use of DTPA is important as free lanthanides are toxic (49). In all of the samples that contain DTPA, the molar concentration of the DTPA is 10% greater than that of the lanthanide; this is to ensure that all of the lanthanide in the sample is contained within a DTPA chelate.

3.3.1.2. Table of Tested Solutions

Table 1 lists the samples used in this chapter. It should be noted that all of these samples were run on the field cycling machine, with the exception of the 6mM Dy-DTPA sample, which was run in the dilution fridge system.

Lanthanide	Concentration (mM)	DTPA	Contains sodium acetate and sodium phosphate	W:G Ratio	pH
Dysprosium	0.1	Y & N	N	50:50	5.3
Dysprosium	1	Y & N	N	50:50	5.3
Dysprosium	2	Y & N	N	50:50	5.3
Dysprosium	5	Y & N	N	50:50	5.3
Dysprosium	10	Y & N	N	50:50	5.3
Dysprosium	0.1	Y	Y	50:50	5.3
Dysprosium	10	Y	Y	50:50	5.3
Dysprosium	0.1	Y	N	50:50	7.1
Dysprosium	1	Y	N	50:50	7.1
Dysprosium	2	Y	N	50:50	7.1
Dysprosium	5	Y	N	50:50	7.1
Dysprosium	6	Y	N	50:50	7.1
Dysprosium	10	Y	N	50:50	7.1
Dysprosium	1	Y	N	40:60	1.25
Dysprosium	1	Y	N	50:50	1.25
Dysprosium	1	Y	N	60:40	1.25
Holmium	1	Y	N	50:50	1.25
Holmium	1	Y	N	50:50	5.2
Cerium	1	Y	N	50:50	5.9
Gadolinium	1	Y	N	50:50	6.7

Table 1: A list of all of the lanthanide samples tested in this chapter

3.3.1.3. Loading the Samples for the Field Cycling Machine

At room temperature all of these samples are liquid, so they were loaded into a sample tube with a pipette and sealed with a small wad of Teflon. The sample tubes were sealed in a way that minimised the quantity of air between the liquid and the Teflon. Samples with a

high water content do have an air bubble to compensate the expansion of water upon freezing. The sample tube was then inserted into the probe and wrapped in Teflon to hold it in place. The probe is then inserted into the inner chamber of the field cycling machine exposing the sample to liquid ^{4}He allowing the sample to freeze rapidly. Teflon is used in the probe as it does not contain any protons and therefore will not contribute to the proton signal.
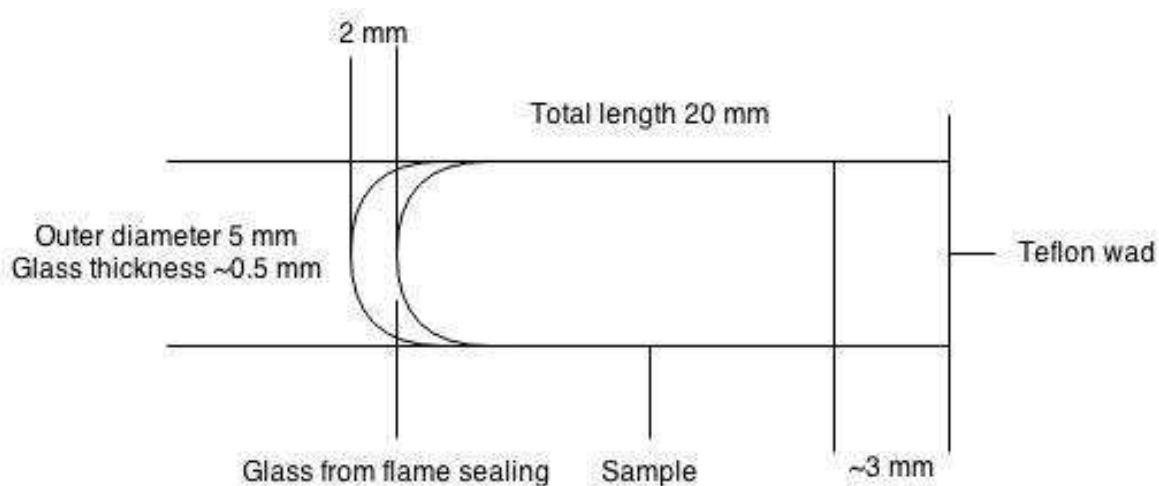
Figure 11: Dimensions of the sample tube

3.3.1.4. Loading the Sample into the Dilution Fridge

The procedure of loading a sample into the dilution fridge is very similar to the field cycling machine with one small exception. The sample size in the dilution fridge is smaller than that of the field cycling machine, this means that surface tension plays a larger role in the filling step. If a flame sealed tube is used, it can become problematic to remove air bubbles in the tube when filling it with a syringe. To overcome this factor the tube is not flame sealed, thus leaving both ends open. This is not a problem as the surface tension is enough to ensure that the sample does not leak from the tube while Teflon wads are attached to each end to secure the sample. The dimensions of the dilution fridge sample tube are 20 mm in length and an outer diameter of 2 mm. The inner diameter is 1.2 mm.

3.3.2. *Experimental Procedure*

All of the samples underwent a saturation recovery experiment to measure the T_1 of the protons. For some of the samples that contained [^{13}C-1] sodium acetate and sodium phosphate, T_1 experiments were conducted on the ^{13}C. These samples also underwent thermal mixing experiments to test the efficiency of polarisation transfer from the proton bath to the ^{13}C (20).

The samples in the field cycling system were generally cooled down to ~40 K, where tip angle calibrations were carried out. The sample was then cooled to 4.2 K and the pulse sequences, described below, applied. The sample can then be set to a new temperature and be repeated until all the necessary data is acquired. In some cases, the sample was cooled from a higher temperature to a lower temperature to check for hysteresis within the experiments, but none were found.

For the dilution fridge experiments, it takes a much longer time to change temperature, therefore, moving between temperatures should be minimized. Experiments run in the dilution fridge would typically start at 1.5 K. At this temperature a $T_{1/2}$ value will be collected instead of a T_1 value. The $T_{1/2}$ is the time required for a sample to reach 50 % of its equilibrium magnetisation, also referred to as the infinity value. The reason $T_{1/2}$ is used instead of T_1 is explained in Section 4.1.9.

As we are now only concerned with knowing the time required to obtain 50 % of the infinity value, the experimental time is shorter as the infinity values, at a given temperature, can be calculated by scaling results from another, usually higher, temperature by using equation (5). Several infinity points are taken at temperatures around 1-1.5 K so they can be cross referenced if required. As the temperature is lowered, the $T_{1/2}$ time increases, however, if the $T_{1/2}$ is suitably short, more infinity points can be taken to reduce our calculated errors. At the lowest temperatures the $T_{1/2}$ times become extremely long, so waiting for the infinity is impractical; therefore the calculated infinity values are used instead. A schematic of a full experiment using the dilution fridge can be seen in Section 3.3.2.2.

3.3.2.1. Pulse Sequence

These experiments are concerned with measuring the T_1 and $T_{1/2}$ of various nuclei using conventional methods. These methods are described below, along with how thermal mixing experiments are conducted.

3.3.2.1.1. Saturation Recovery – Field Cycling Machine

This sequence is used to measure the T_1 value of a sample. The first pulses in the sequence saturate the target nuclei in the sample at its resonance field; the field is then ramped to a higher magnetic field, usually 2 T, to polarise for a given time. The field is ramped back to the resonance field and a 90^0 pulse is to acquire an FID, as seen in Figure 12. This process is repeated, using longer polarisation times, until a full recovery curve has been produced. The increase in polarisation time is chosen to follow a geometric series, as this is a more time efficient way of sampling the recovery curve, compared to a linearly sampled curve with the same number of points. It is intuitive that a denser collection of measurements should be taken when the derivative of a function is very large. From differentiating equation (7) it is easy to see that the derivative is largest at small times and therefore this portion of the curve should be most densely sampled. An adequate set of data points should include an infinity point, which is generally accepted to be a point taken after a polarisation time that is five times longer than T_1 and have a total of around twenty points with geometric spacing.
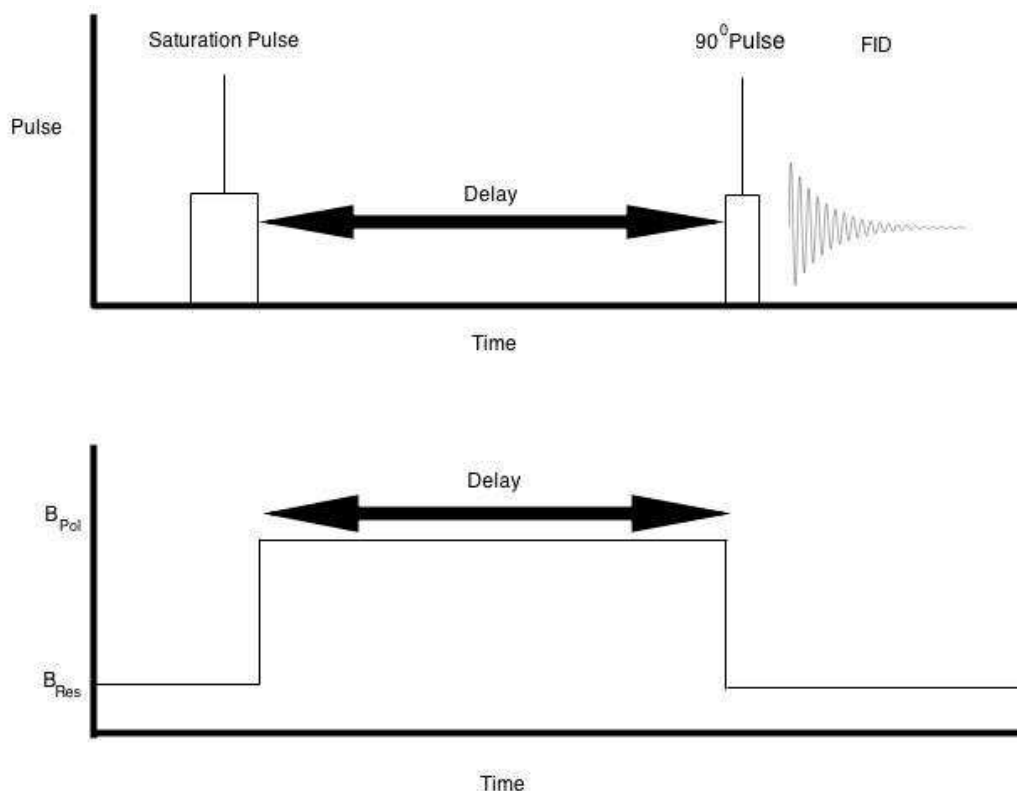
Figure 12: Pulse sequence used to determine T_1 in the field cycling machine

The FID is Fourier transformed and the area under the resulting peak is plotted against the polarisation time to obtain a polarisation recovery curve. If it is assumed that there is a single T_1 component, the recovery curve will follow equation (7). Since the field cycling machine is not shimmed and the samples are solid, the peaks produced are broad and any details in the lineshape are generally lost.

3.3.2.1.2. Thermal Mixing – Field Cycling Machine

In most cases the T_1 value of ^{13}C is much longer than those of protons (20,24). The aim of this work is to decrease the T_1 times of the sample to obtain larger ^{13}C polarisation. Thermal mixing is a method of rapidly polarising all of the nuclei in the sample by transferring polarisation from the protons to the other nuclei (20,24).

It is typical to start a thermal mixing experiment from an unpolarised or very low polarised state. This is achieved by leaving the sample in the earth's field for several times longer than the T_1 of the sample. With all the spins in a low polarised state a magnetic field

can now be applied. This is the polarisation field. As the ramping rate of the magnet is faster than the relaxation rates of the nuclei, saturation is not required. The polarisation field is left on for a set time to allow the whole sample to polarise, before the magnetic field is then set to the resonance of the target nuclei, at which point a saturation pulse is applied to remove any polarisation from the target nuclei. The magnetic field is then lowered to only a few gauss, for a short amount of time, which allows the spin temperatures of the system to equate. As protons tend to have the shortest T_1, they tend to have the lowest spin temperature; they also have the largest spin specific heat (19). This can be calculated from equation (19). This means that when the thermal mixing step occurs, the spin temperature of all of the spins in the system equilibrate to a point which is heavily weighted towards the proton's initial spin temperature. This does assume that the proton polarisation is not lost while at the low field. The field is then set to the resonance frequency of the target nuclei where a 90^0 pulse is applied and an FID acquired. This experiment is repeated with a range of polarisation times which is then used to build an effective T_1 time of the target nuclei. In an efficient thermal mixing experiment, the magnetisation recovery of all of the nuclei should match the T_1 curve of the thermal bath in the polarisation condition, usually 2 T and 4 K. The pulse sequence can be seen in Figure 13.
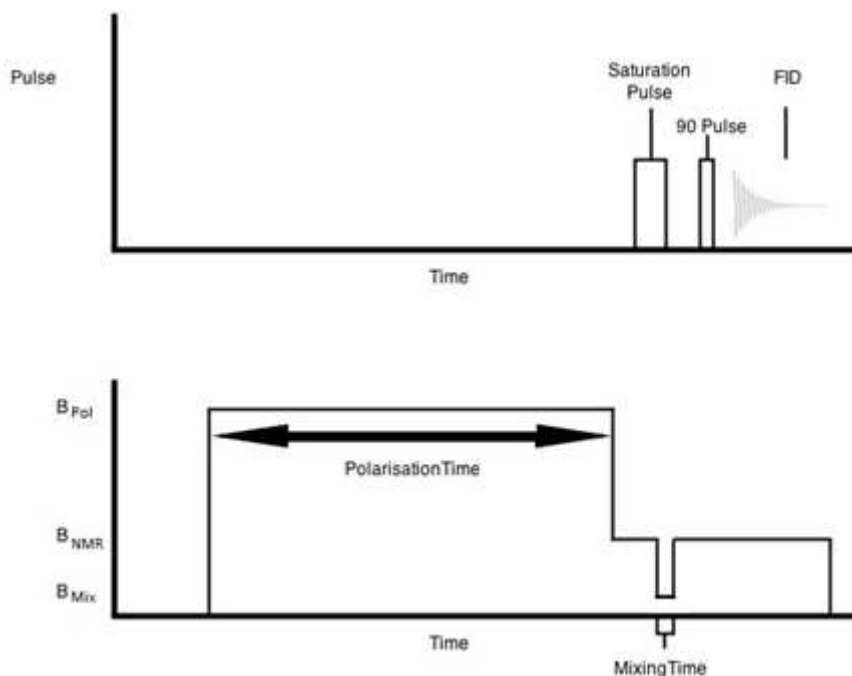
Figure 13: Pulse sequence used for thermal mixing in the field cycling machine

3.3.2.2. Saturation Recovery – Dilution Fridge

The saturation recovery experiment, used in the field cycling machine, does have a drawback. The time required to make one measurement is, to the first approximation, the length of the delay between saturation and measurement. Therefore, the time required to get a full recovery curve is the sum of each measurement, which is many times longer than the $T_{1/2}$. When entering the millikelvin regime the $T_{1/2}$ times become very long, tens of hours is common. This means making $T_{1/2}$ measurements, using the pulse sequence of the field cycling machine, become impractical as it could take several days to finish. Therefore, another way to conduct a saturation recovery experiment is needed.

The following method can only be used when the signal is sufficiently large that it is distinguishable from noise when small tip angles are applied to the sample. Samples in the very low temperature regime fulfil this criterion. This method of measuring $T_{1/2}$ makes the assumption that the tip angle of the pulses is sufficiently small to not affect the relaxation of the nuclei. A tip angle of 5^0 or less was used in these experiments. The pulse sequence starts with a saturation pulse followed by small pulses at various intervals. Each pulse gives a measure of magnetisation of the sample, without destroying a significant proportion of that magnetisation. As a result, the $T_{1/2}$ times can be measured in real time, which drastically decreases the length of the experiment; this is because only one saturation pulse is applied. Similarly to the previous saturation recovery pulse sequence, the timing between the small pulses is spaced geometrically to try to minimize the number of pulses applied while still getting a well sampled curve, as seen schematically in Figure 14.
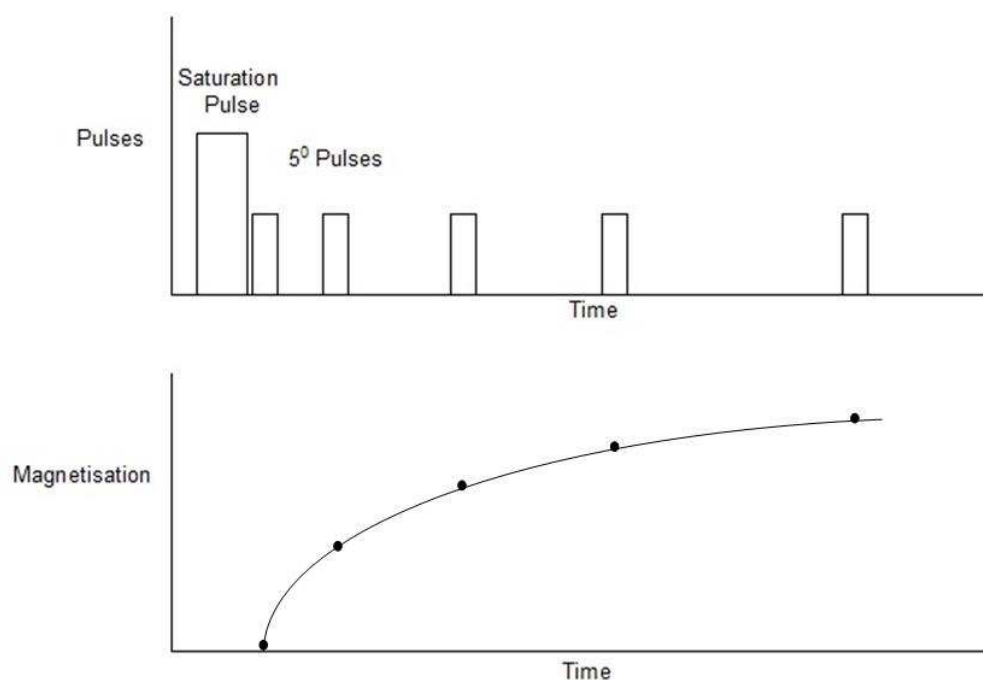
Figure 14: Saturation recovery experiment used in the dilution fridge system with small tipping angles

It is normal for several saturation recovery experiments to be conducted on a sample, each at a different temperature. Changing the temperature of the sample usually takes several hours, therefore, if the $T_{1/2}$ time of the sample is short, in comparison to the time required to change temperature, a measurement pulse can be used, before saturation, to get an estimate of the infinity point. An example of a full set of experiments can be seen schematically in Figure 15. The red shaded areas are points where a measurement is made prior to saturation, the blue areas represents a recovery curve measurement using the pulse sequence displayed in Figure 14.
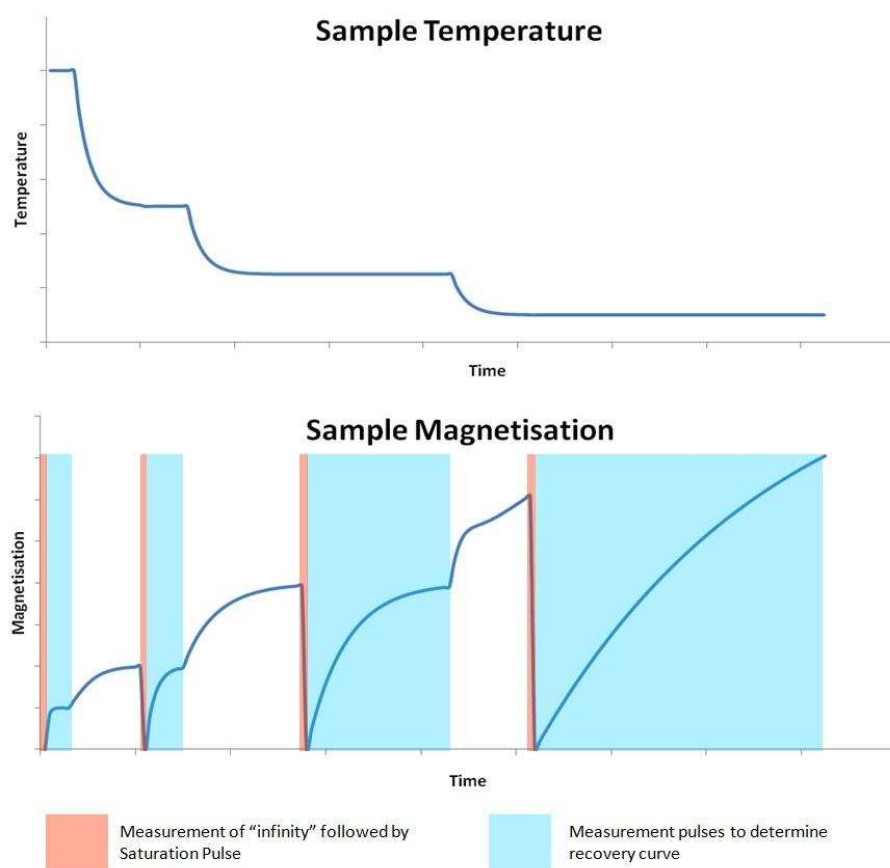
Figure 15: Schematic of a full set of experiments on the dilution refrigerator system. At high temperatures the measured point, before saturation, is indeed an infinity point. As the temperature decreases and the $T_{1/2}$ time becomes longer than the time required to cool the sample, the measured point is no longer an infinity point. This allows for an estimate of the $T_{1/2}$ compared to the cooling time prior to running a saturation recovery experiment.

The infinity point for a particular experiment is calculated by taking the ratio of the infinity point from a known temperature and scaling it using equation (5). If the measurement prior to saturation is the same as this calculated infinity, then a short $T_{1/2}$ time is expected, however, if the measurement is much smaller than the calculated infinity, a much longer $T_{1/2}$ time is expected. When long $T_{1/2}$ times are expected, the pulse sequence is only run to approximately 50-60 % of the calculated infinity, which is enough to give a value for $T_{1/2}$. In the case that this estimate is very long, days to weeks, there is no point in measuring the $T_{1/2}$ as it does not fulfil the goals of the thesis, which is having practical $T_{1/2}$ times at the lowest temperatures. More details about measuring $T_{1/2}$ in the dilution fridge can be found in Section 4.1.9.

3.4. *Results*

This section will be broken down into several subsections which focus on the dependence of T_1 for a particular parameter. These parameters include:-

1. Lanthanide concentration,
2. pH,
3. Lanthanide studied,
4. Water:glycerol ratio,
5. Magnetic field strength,
6. Thermal mixing.

Dysprosium was used for the majority of these experiments. Most of these experiments focus on investigating the T_1 time of protons, as it has been shown in previous work that the polarisation can be passed to the ^{13}C by thermal mixing (20,24). This means that reducing the proton T_1 time should lead to a reduced ^{13}C polarisation time.

3.4.1. *Lanthanide Concentration*

The T_1 times of samples containing various concentrations of Dy and Dy-DTPA were measured in the field cycling system at 4.2 K, with a polarisation field of 2 T. Increasing the lanthanide concentration should decrease the T_1 as there are more paramagnetic centres which act as a relaxant. Figure 16 shows a plot of $1/T_1$ as a function of the concentration of lanthanide. It can be seen that there is a linear relationship between the relaxation rate and concentration, as predicted in equation (21). The Dy-DTPA has a modest reduction in relaxivity compared to the free dysprosium.
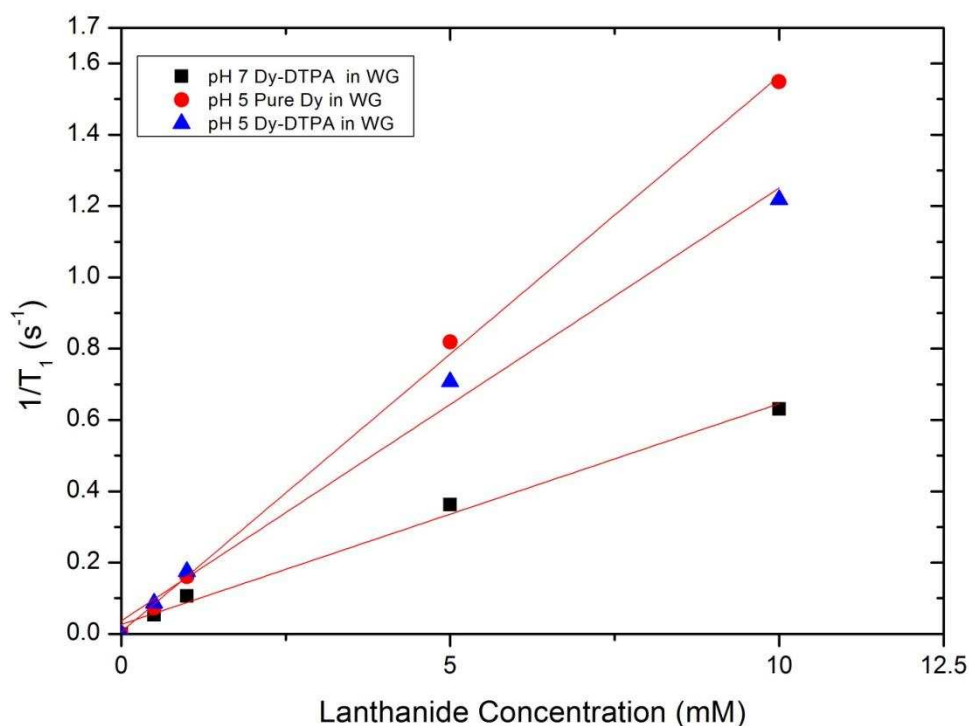
Figure 16: Increasing the concentration of the lanthanide increases the relaxation rate of the protons with a linear dependence. It can be seen that the Dy-DTPA (blue triangles) has a slower relaxation rate than the pure Dy (red triangles).

Figure 16 has been normalized to remove the background WG component, so that the effect due to the dysprosium is highlighted. The background subtraction allows for the data to intersect the origin of the graph. The T_1 times for a lanthanide free sample can be found in Figure 20; under these conditions the $1/T_1$ value for the lanthanide free sample is 0.0142 s^{-1}. The source of the offset can be seen in equation (20), where $1/T_{1d}$ is the relaxation rate of the WG.

When the samples were initially prepared the pH of the samples was not neutralized. As this would not have been appropriate for in vivo use, a second set of samples were made, in doing so it was noticed that the pH affected the T_1 times. The effects of pH are discussed further in Section 3.4.2.

It was also observed that the proton line broadened as the dysprosium concentration increased. Over the range of 0.5-10 mM of dysprosium, it was observed that there was an increase in the FWHM from 120 KHz to 133 KHz. The FWHM of the NMR peak can be related to the T_2 of the sample through equation (11). A shorter T_2 time means that a larger

proportion of the proton signal is lost within the dead time of the spectrometer. Figure 17 shows the effect of increasing the concentration of the relaxant on the signal integral for solutions containing Dy (black) and Dy-DTPA (red). As more relaxant is added to the sample, more nuclei are near a paramagnetic centre; this decreases the T_2 of those nuclei and therefore the signal. It is not known why the equilibrium magnetisations of equivalent pure Dy and Dy-DTPA samples differ from one another.

Equation	y=A*exp(-x/B)+C		
Reduced Chi-Sqr	16.86615	234.15454	
Adj. R-Square	0.98921	0.90702	
		Value	Standard Error
	A	163.52903	15.35127
Dy Signal	B	0.86571	0.11537
	C	26.79447	2.93897
	A	144.05663	23.4644
Dy-DTPA Signal	B	2.43881	1.20508
	C	70.25816	17.64826
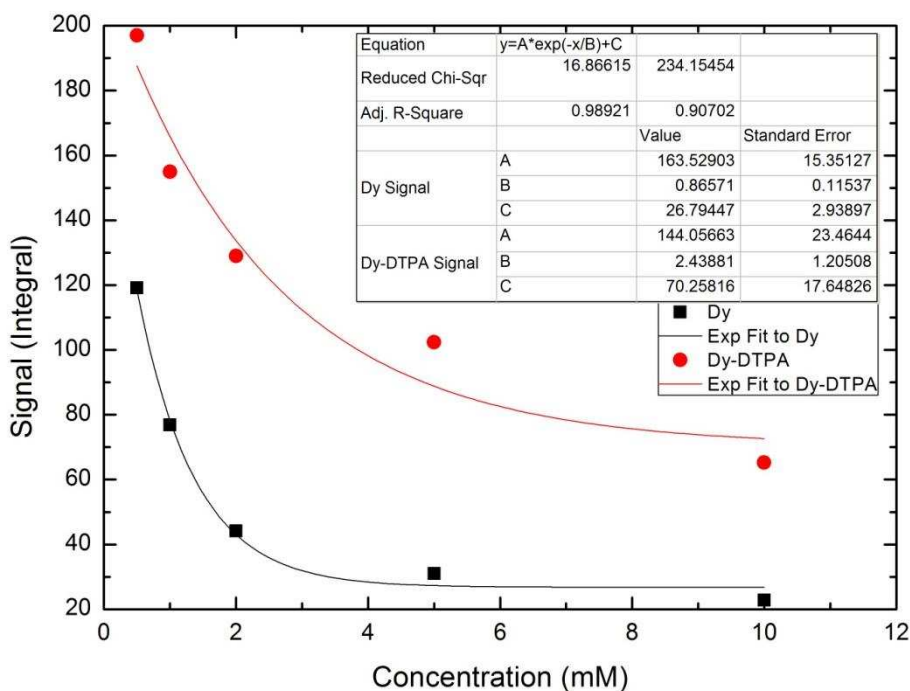
Figure 17: Equilibrium signal produced as a function for concentration for Dy and DY-DTPA at polarising conditions of 4 K and 2 T.

3.4.2. *pH Effects*

The initial experiments showed that the pH of the sample seems to affect the relaxation rate of the protons. This lead to further studies to determine the relationship between the pH of the sample and the T_1 value over a given temperature range. When the pH is higher than 7 the solution becomes a translucent white gel, this means that the sample cannot be directly compared with the neutral or acidic samples, which are clear liquids at room temperature. As a result, relaxation measurements were only undertaken on neutral and acidic samples.

These experiments were carried out on samples containing 1 mM Dy-DTPA at three pH values (1.24, 5.08 and 7.10). The polarisation field for these experiments was 2 T. Figure 18 shows that the pH 1.24 sample had the shortest T_1 at the lowest temperature. The T_1 minimum had also shifted to the lower temperatures, which is preferable for maintaining polarisation during dissolution.
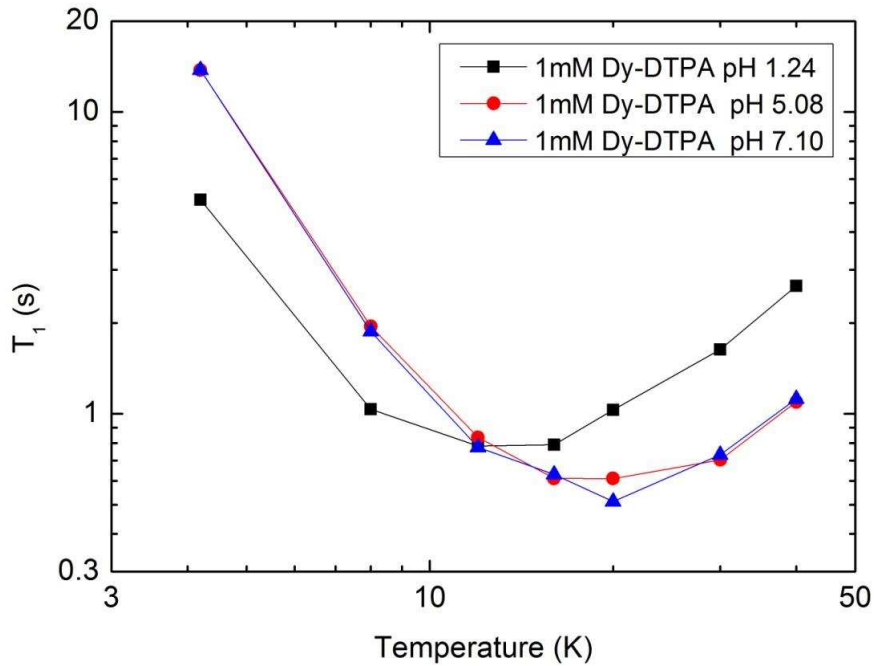
Figure 18: Proton T_1 values as a function of temperature for 1mM Dy-DTPA samples at three different pH values.

Making use of the fact that T_1 values go through a minimum, the data from Figure 18 can be processed to give correlation times of the protons at each temperature. This can be done by assuming that equation (16) can be approximated as:-

$$\frac{1}{T_1} \propto \frac{\omega \tau_c}{1 + \omega_S^2 \tau_c^2} \tag{24}$$

At the T_1 minimum, $\omega \tau_c = 1$, and when substituting into equation (24), a scaling constant to be calculated. This can then be used to calculate the correlation times for the nearby temperatures, as seen in Figure 19. This plot shows the calculated correlation times of the protons, at various temperatures, for each of the three 1 mM Dy-DTPA sample. The

correlation times for the samples in this temperature range are close to the expected value of 10^{-9} s at 8 K for Dy-EDTA (24,48).
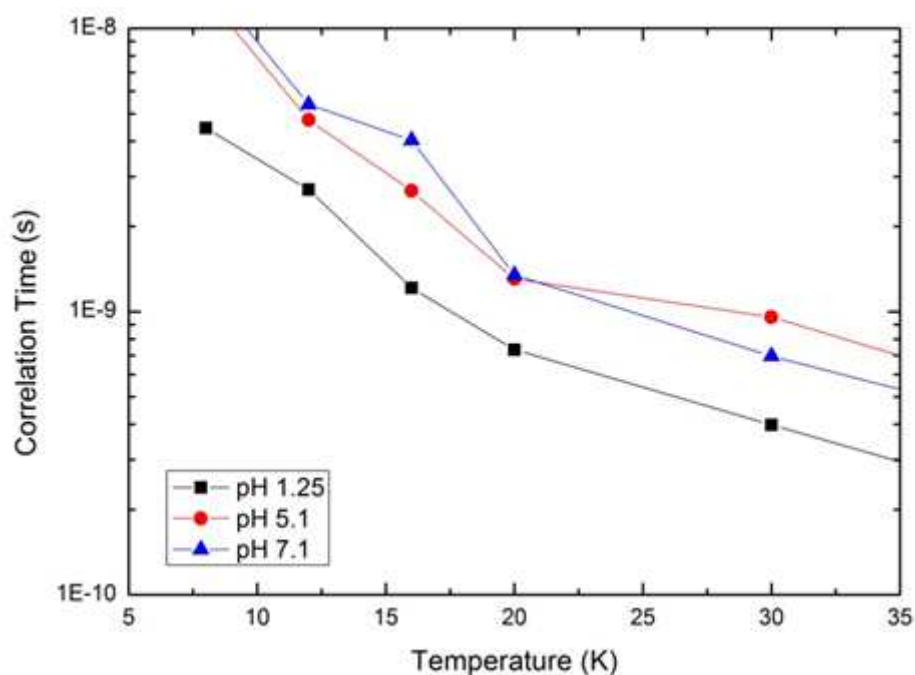
Figure 19: Correlation time of protons as a function of temperature at various pH values.

3.4.3. *Relaxivity Effects with Different Lanthanides*

3.4.3.1. 4 K to 200 K

A temperature study was conducted on four 1 mM lanthanide DTPA samples to determine which would make the best relaxation switch. The lanthanides used were dysprosium, holmium, cerium and gadolinium. A control, lanthanide free, sample was also measured. The pH of the samples were set to 7 and the polarisation field was 2 T. The gadolinium is expected to be an effective relaxant at ~300 K as its electron spin flip time matches the inverse of the Larmor frequency; however, at the lower temperatures, there will be a large mismatch between the Larmor frequency and the electron spin flip time, meaning that the gadolinium will be an ineffective relaxant. The other three lanthanides have much shorter electron spin flip times, thus it would be expected that their T_1 minima will occur at lower temperatures (~10 K) (50,51,52).
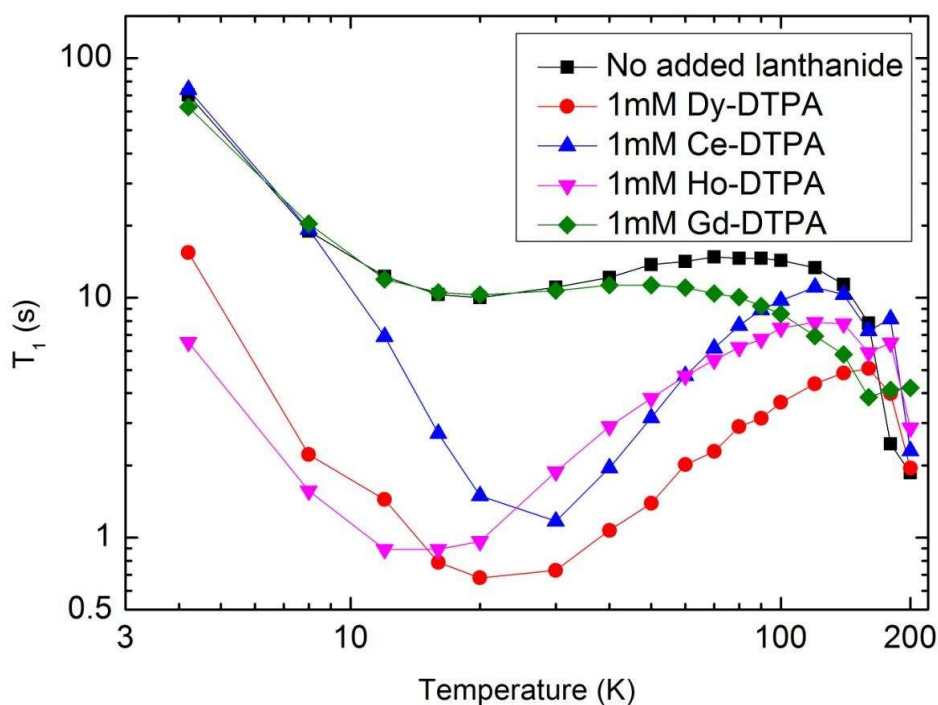
Figure 20: T_1 of protons over the full temperature range of the field cycling machine for various lanthanides

Figure 20 shows T_1 values as a function of temperature for the four lanthanides. An ideal relaxation switch would have a short T_1 at the lowest temperatures, while having a long T_1 at the higher temperatures. It can be seen that gadolinium and cerium are not very effective at 4 K as they have similar T_1 values to the lanthanide free sample, therefore are not useful for this study. Both holmium and dysprosium have short T_1 values at the lowest temperatures, however, the dysprosium has a shorter T_1, compared to holmium, at the higher temperatures, around 200 K; this means that dysprosium will lose its polarisation faster than holmium in the time between warming and measuring the sample.

From these measurements it has been shown that holmium is the most effective relaxation agent, however the temperature dependence between 200 and 300 K is still required to determine if holmium is truly the best relaxant tested. Dysprosium will still be used during other experiments in the chapter for consistency, allowing for easier cross referencing between data points. It should be noted that above 160 K the T_1 values of all of the samples drop; this is believed to be due to the WG going through its liquid-glass phase transition (53).

3.4.3.2. Ultra Low Temperature

Part of a data set was taken prior to my involvement in this research. A 6 mM Dy-DTPA was investigated with a dilution fridge system to observe the T_1 times down to 30 mK at 2.45 T. I have since run a control experiment of a lanthanide-free sample to clarify if there is any relaxation enhancement, due to the Dy-DTPA, at millikelvin temperatures. These measurements were carried out using the dilution fridge at a field of 2.45 T, as this matches the resonance frequency of the probe (104.5 MHZ). The time constant quoted in this data will be $T_{1/2}$ as this reminds the reader that the sample might not relax via a mono exponential, it also has the benefit of making the measurement time shorter if a calculated infinity point is known. The $T_{1/2}$ is the time taken to reach half of the equilibrium polarisation as stated in Section 3.3.2.
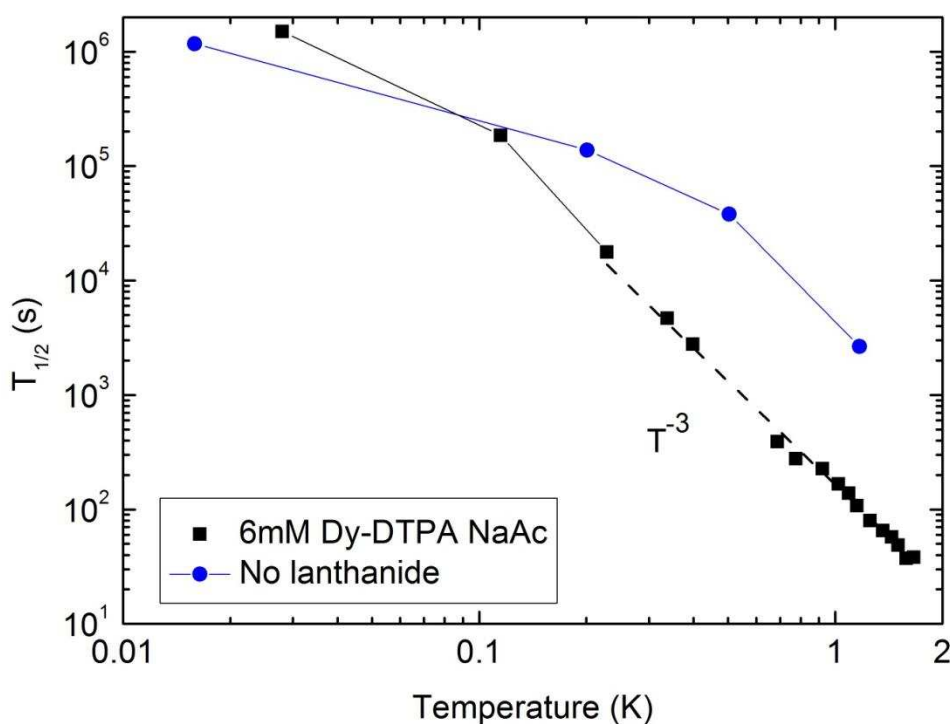
Figure 21: Ultra low temperature proton T_1 data for dysprosium and lanthanide free sample

The dysprosium was found to enhance the relaxation rate at temperatures above 0.1 K. At 0.1 K the $T_{1/2}$ time is 30 hours, and on the edge of a practical time scale for the desired purpose. It should also be noted that between 0.2 K and 2 K the $T_{1/2}$ relationship follows a

cubic relationship. The reason why this is a cubic dependence is not known, but this observation will be used in Chapter 4.

3.4.4. *Water:Glycerol Ratio*

The samples in this chapter have one final sample preparation parameter which can be optimised. This is the ratio of water to glycerol, which will change the glassiness of the sample and the liquid-glass transition temperature (53). The T_1 values of lanthanide-free solutions were first measured for pure water, pure glycerol and for a 50:50 mixture of WG at a range of temperatures with a polarisation field of 2 T. The results are shown in Figure 22.
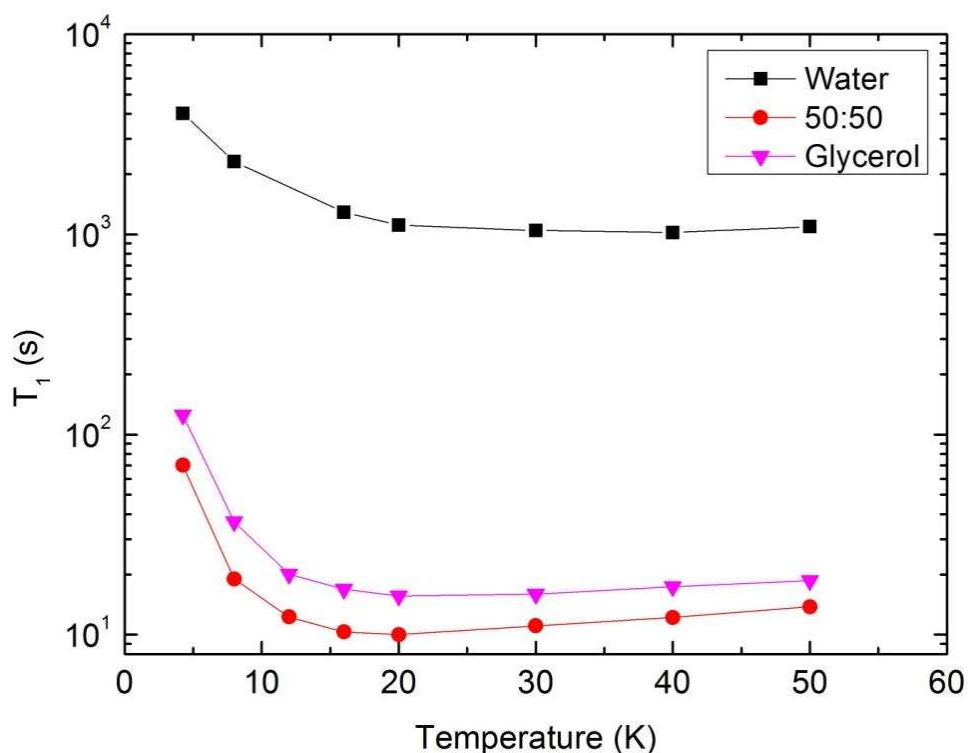
Figure 22: Proton T_1 values at various water:glycerol ratios

Figure 22 shows that a 50:50 mixture of WG has a shorter T_1 time than either pure water or pure glycerol, thus suggesting, at least for a lanthanide free sample, that a mixture of water and glycerol is optimal.

Several solutions of WG containing 1 mM Dy-DTPA were run over a range of temperatures to map out the T_1 minima, again with a polarisation field of 2 T. This test was

done at a pH of 1.25, as this was shown to give shorter T_1 times in Figure 18. The compatibility of the low pH with the sample was also checked, i.e. the sample did not seem to show any chemical reactions to the low pH. The results are shown in Figure 23.
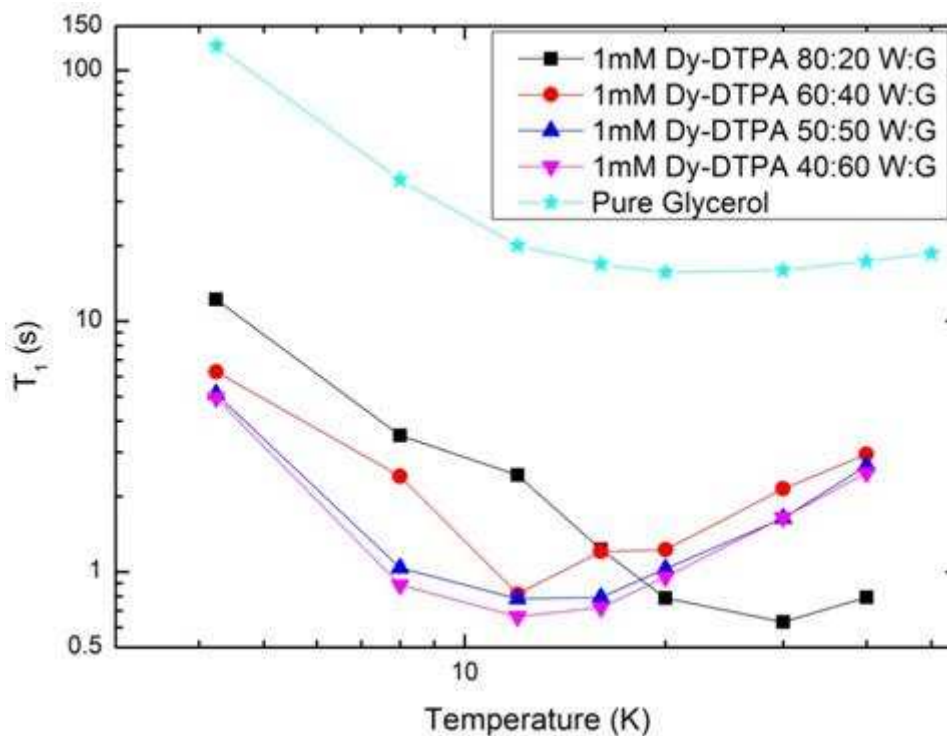
Figure 23: Proton T_1 values for 1 mM Dy-DTPA samples with various water:glycerol ratios

The T_1 times of the samples do not vary much as a function of WG ratio until there is a strong bias away from an equal mixture of water to glycerol. The T_1 times of the sample become noticeably longer, with the T_1 minima shifting to higher temperatures when there is a large bias towards water in the sample.

3.4.5. *Field Dependence*

The brute force method relies on both low temperatures and high fields. Selecting the right combination of field and temperature to polarise a sample is of key importance. If the T_1 is more dependent on temperature than field, for example, then it becomes favourable to polarise at higher temperatures and stronger fields. The T_1 of a 0.5 mM Dy-DTPA sample was measured at 4 K using various polarisation fields. Figure 24 shows that the T_1 is linearly dependent with respect to the polarisation field over the range of field strengths used.
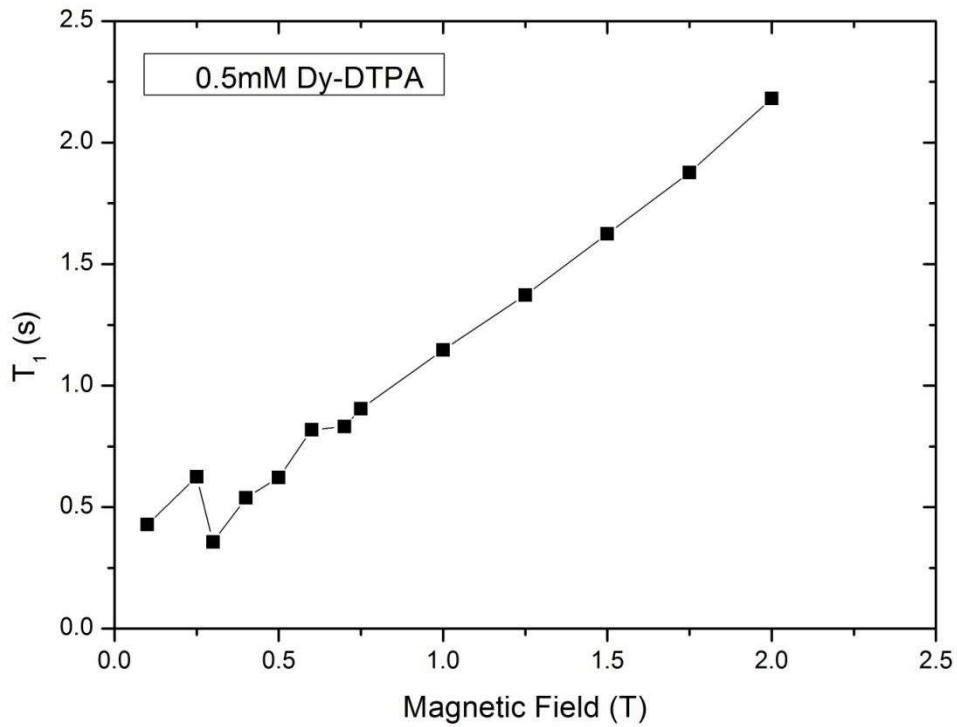
Figure 24: Proton T_1 dependence on field strength at 4 K

It is possible to simulate the polarisation build-up for set conditions using equations (5) and (7) as T_1 (T = 4 K, B_0) is now known. Figure 25 is a simulation of the polarisation recovery curves at a fixed temperature, across various field strengths. The time and polarisation axes are scaled to the T_1 time and equilibrium polarisation for a sample at 0.5 T.
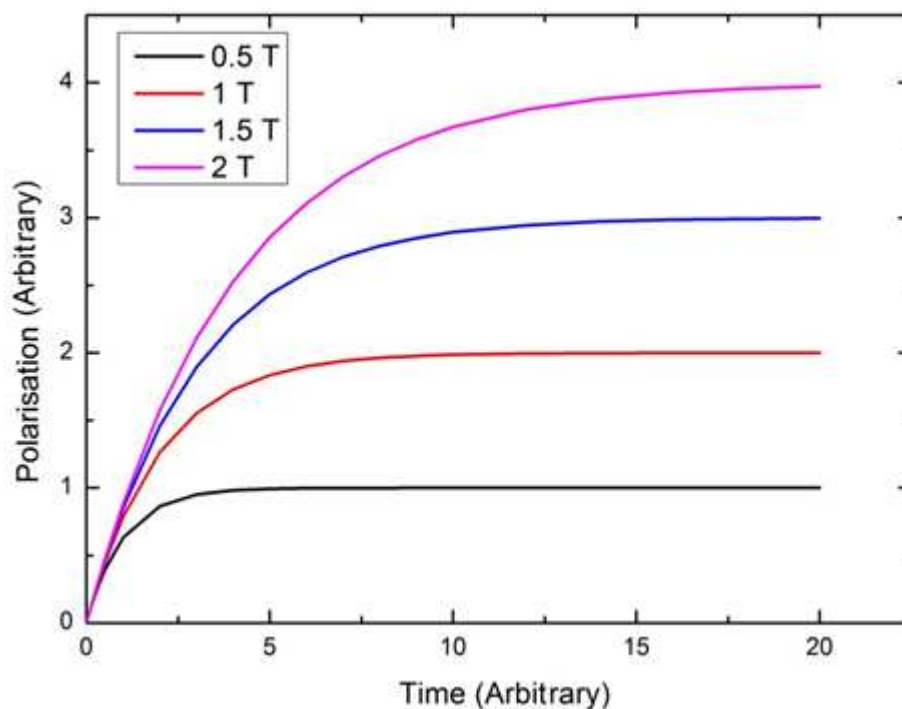
Figure 25: Simulation of T_1 recovery for a sample in various magnetic fields

The data shown in Figure 25 can be used to form polarisation strategies. The polarisation time must first be calculated before a strategy can be considered. The upper limit to the polarisation time can be calculated by considering the number of samples that can be polarised simultaneously and the rate at which the samples are required. If it is assumed that a polariser can hold 10 samples and 5 are required each day, this gives a polarisation time of 48 hours. The field dependence is not well known as a function of temperature; at 4 K the field dependence is linear, but at 1.5 K the field dependence has been shown to be cubic (24). It is hard to simulate the best combination of field and temperature to get the maximum polarisation in a fixed time, unless assumptions about the T_1 dependence are made.

3.4.6. *Thermal Mixing*

Studying ^{13}C with NMR is more challenging than studying protons, as ^{13}C is less sensitive due to its smaller gyromagnetic ratio and a lower natural abundance (1.1 %). Carbon is important in many chemical and biological processes and thus is the ability to detect ^{13}C is also important for many areas of research. Since ^{13}C is hard to measure in its natural form,

samples are prepared in a way to maximise their signal. In NMR this is done by using ^{13}C-enriched samples and by increasing ^{13}C polarisation. Thermal mixing can increase the ^{13}C polarisation by passing the polarisation from highly polarised protons to the ^{13}C nuclei (20,24). This means the protons are a surrogate for the [13]C. To see the benefits of thermal mixing, the T_1 time of ^{13}C, without using thermal mixing, needs to be known and compared to the thermal mixing data.

3.4.6.1. [13]C T_1 Data

The [13]C T_1 data was taken in a similar manner to the proton data, but with the B_{NMR} adjusted to account for the difference in the gyromagnetic ratio between protons and [13]C. Figure 26 shows the ^{13}C recovery curves of 2 M [1-^{13}C] NaAc in WG with various quantities of Dy-DTPA at 4 K and a polarisation field of 2 T.
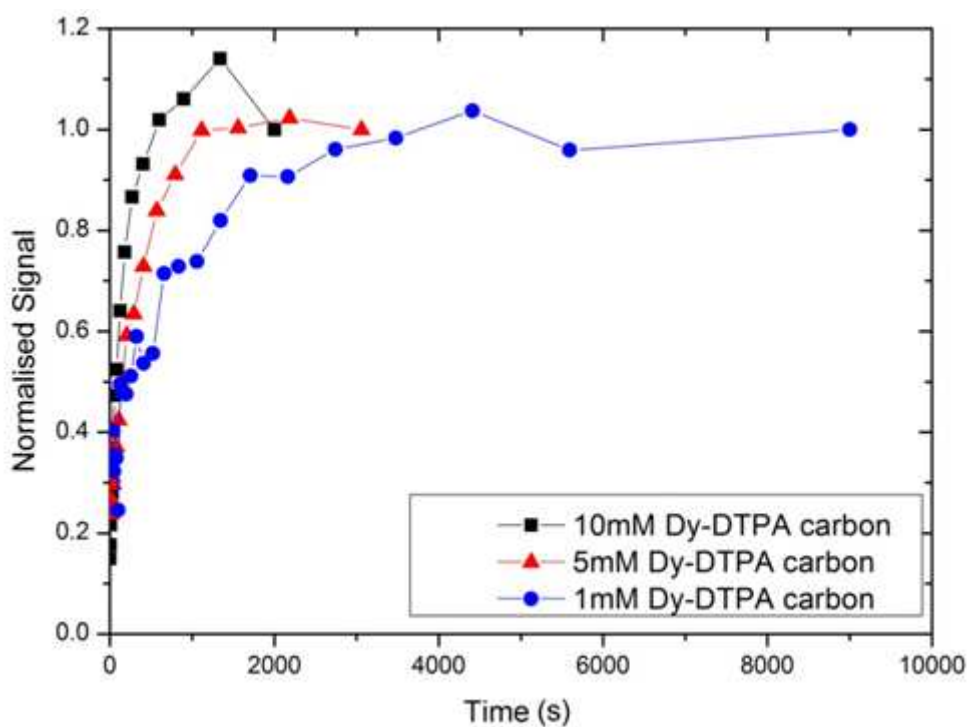
Figure 26:[13]C T_1 recovery curves at three different concentrations of lanthanide at 4 K and 2 T. Each curve is normalised to its equilibrium magnetisation

As expected, the sample with the higher concentration of lanthanide relaxes faster than the sample with less lanthanide and follows equation (21).

Concentration (mM)	T_1 (s)
1	919
5	381
10	171

Table 2: Carbon T_1 times at various concentrations

Assuming that thermal mixing is 100 % efficient, the ^{13}C T_1 should match the proton T_1. This would decrease the polarisation time of ^{13}C by a factor of ~60, taking the T_1 times of protons from Figure 20.

3.4.6.2. Thermal Mixing Enhancement

Thermal mixing was conducted on a 1 mM Dy-DTPA sample. The sample was allowed to polarise at 2 T and 4 K for various lengths of time before performing the mixing step, 0.004 T for 0.1 s and then taking a measurement at the ^{13}C resonance field. Figure 13 shows a schematic of the pulse sequence. The effective ^{13}C T_1 can be plotted by plotting the ^{13}C magnetisation against the polarisation time prior to the thermal mixing step. If thermal mixing is efficient, then the effective ^{13}C T_1 should match the proton T_1. Figure 27 shows the effective recovery curve of the ^{13}C when thermal mixing is used.
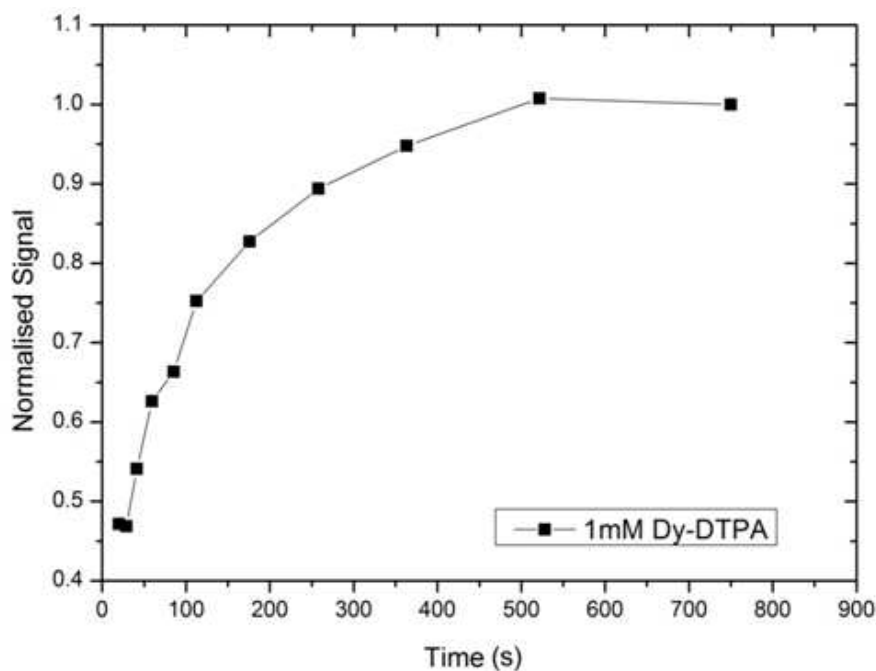
Figure 27: T_1 curve of ^{13}C with the use of thermal mixing

The effective T_1 for ^{13}C is 133.4 s. This is a factor of 7 faster than the T_1 without using thermal mixing, however, much longer than the proton's T_1 time (15 s). This means that the thermal mixing step used was not as effective as expected. Further optimisation of the thermal mixing step was conducted on pyruvic acid as seen in Section 4.5.3.

3.5. *Discussion*

3.5.1. *Lanthanide Concentration*

Figure 16 shows that Dy-DTPA samples have a weaker relaxation enhancement than pure dysprosium samples. The reason for this is not known, however, it could be that the electron spin flip time has changed with the introduction of the DTPA chelate.

Upon reviewing the signal produced by each sample, it is clear in Figure 17 that the increase in relaxant decreases the signal. Each paramagnetic ion has a sphere of influence, where the nuclei within this space will have an enhanced T_2 relaxation, as seen in the broader NMR peaks. The signal, which would be produced from these nuclei, is lost in the dead time of the spectrometer, as its FID is shorter. The volume around the paramagnetic centre, where the nuclei cannot be detected, will be known as the exclusion zone (46). As the concentration of the lanthanide increases, the detectable signal will decrease because more of the nuclei will be within an exclusion zone. As the concentration of the paramagnetic centre increases, the probability that exclusion zones overlap increases. If the exclusions zones are overlapping, then less new nuclei are entering an exclusion zones, the effect of which is the loss of signal tails off at higher concentrations.

3.5.2. *Relaxation with Respect to pH*

Figure 18 shows that decreasing the pH of the samples lowered the value of the T_1 minima of the sample and also shifts the minima to the lower temperatures. These changes allow the sample to become polarised faster and could help to maintain the polarisation during dissolution and measurement. The most likely explanation for the shift in T_1 minimum, is a change in the correlation time, therefore suggesting that the pH of the sample

influences the electron spin relaxation time of the lanthanide. An ionisation state change in Dy-DTPA could be the source of the electron spin flip time change; this would be expected to occur at around pH 2 and would also explain why the pH 5 and 7 data are similar to one another (24,54).

3.5.3. *Lanthanides Studied*

3.5.3.1. *4-200 K*

At the lowest temperatures, ~4 K, the T_1 time of protons is around ten times shorter for samples that contain dysprosium or holmium, than the control sample, as seen in Figure 20. This means they could make promising relaxation switches depending on how long the T_1 is at 300 K.

The cerium is not effective at the lowest temperatures; however, does show a relaxation enhancement at around 30 K. As cerium's T_1 minimum is at such a high temperature than ideal for the brute force method, it is not recommended as a relaxation agent.

The gadolinium behaves as expected, it only shows a relaxation enhancement near the higher temperatures (300 K) where the electron spin flip time matches the inverse Larmor frequency. The gadolinium was only used as a secondary control sample in this work to prove the electron spin flip time is the mechanism of relaxation.

It should be noted that at around 160 K the T_1 time for all of the samples rapidly decreases; the cause of this decrease is probably due to the glass liquid transition of the WG (53). These short T_1 times should be taken into consideration when designing the final samples as it will have a large impact on the measured signal after polarising.

3.5.3.2. *Ultra-Low Temperatures*

Above 0.2 K the $T_{1/2}$ of the dysprosium sample follows a cubic relation with temperature, as seen in Figure 21, this means that the $T_{1/2}$ time of the sample is growing faster than the equilibrium polarisation. By combining equations (5) and (7) it is possible to calculate the optimal polarisation conditions for a dysprosium sample. The data used to create Figure 28

was taken from Figure 21. In this simulation a fixed polarisation time, 200 s, was set so that the conditions of the best polarisation conditions could be found for a fixed polarisation time.
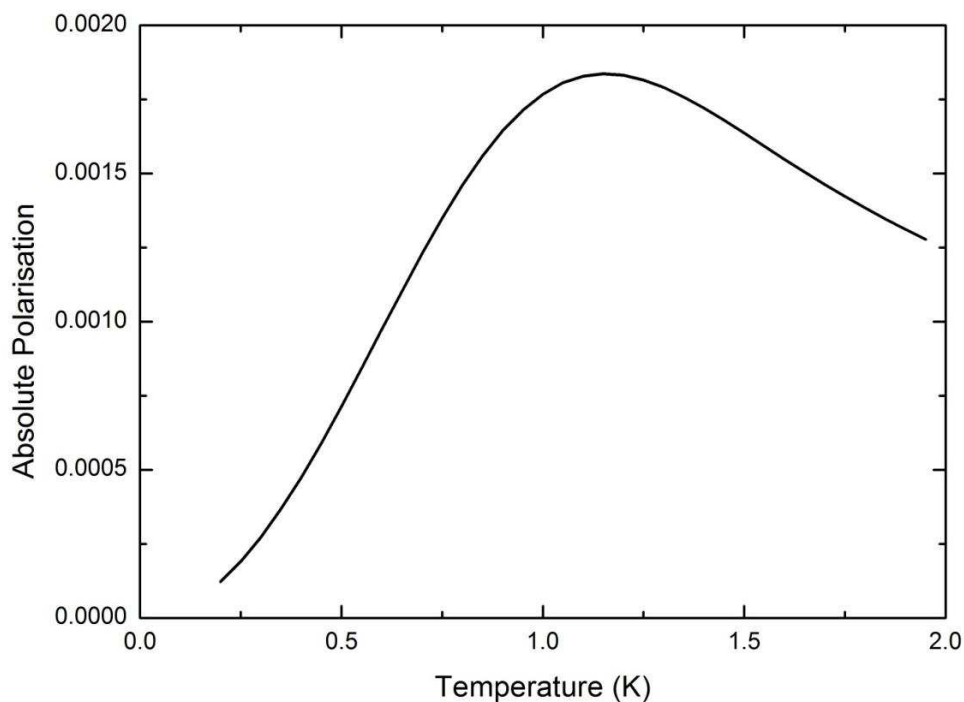
Figure 28: Simulation of the polarisation curve as a function of temperature for a 200 s polarisation time

The curve in Figure 28 represents the theoretically achieved polarisation after 200 s of polarising; to the left of the maxima the achieved polarisation is limited by the T_1 time of the sample, while to the right of the maxima the polarisation is limited by equilibrium polarisation. By varying the allowed polarisation time, it has been empirically observed that the best polarisation temperature, provided that T_1 has a cubic dependence on temperature, is when the T_1 time is around half of the polarisation time. The mathematics would work out the same for the magnetic field, if the T_1 time has a cubic dependence on magnetic field, as it has shown to be at 1.5 K (20). The cubic temperature dependence on $T_{1/2}$ only occurs between 0.2 and 2 K. Below 0.2 K the $T_{1/2}$ of the lanthanide sample starts to follow a weaker temperature dependence. This means that the simulation in Figure 28 is not valid below 0.2 K.

The $T_{1/2}$ of protons at 2.45 T and 15 mK for 2M NaAc WG sample, with or without Dy-DTPA, is around 200 hours and therefore the highest absolute proton polarisation possible in 48 hours, using the brute force method in these conditions, would be around 2 %. This is much smaller than the levels of polarisation achieved using DNP, yet is still an enhancement of ~2000 when compared to polarising a sample at 300 K and 3T.

3.5.4. *Water:Glycerol Ratio*

The first interesting point which can be seen from Figure 22 is that a mixture of water:glycerol has a shorter T_1 than either pure water or pure glycerol; this suggests that having a mixture of water and glycerol is desirable. When various samples of WG were tested with 1 mM Dy-DTPA, as seen in Figure 23, the T_1 times of 40:60 W:G, 50:50 W:G and 60:40 W:G were very similar at the low temperatures. When a large bias towards water is used (80:20 W:G) there was an increase in the T_1 time. This means that the most advantageous solution is when the water and glycerol is in roughly equal quantities, this gives the shortest T_1 times at 4 K. The exact ratio of water and glycerol can be altered to move the liquid-glass phase transition temperature as desired (53).

3.5.5. *Field Dependence*

Knowing the field dependence of T_1 is just as important as knowing the temperature dependence, as this makes it possible to calculate the optimal polarisation conditions of a sample. If, for example, the T_1 is less dependent on the field, then it would be beneficial to polarise at a higher field than lower temperatures.

To find the optimal polarising conditions, the allowed time for polarisation also has to be known. A polarisation time of 48 hours was assumed by considering the number of samples that can be polarised simultaneously and the demand for samples per day, as seen in Section 3.4.5. It is possible to simulate the polarisation growths of a sample by combining equation (5), which calculates the equilibrium polarisation, with equation (7), which is a mono exponential recovery curve. To calculate the polarisation a given set of conditions, a temperature and field map of T_1 has to be known.

Data in this thesis would suggest that there is a linear relationship between B_0 and T_1, however, from previous work from the group, the B_0 dependence of T_1 follows a cubic at temperatures around 1.5 K (24). Again, using the result from Figure 28, one could find the optimal field to polarise a sample by setting the $T_{1/2}$ to be half the allowed polarisation time, if the temperature is fixed at 1.5 K. There is not currently enough data to determine the best polarising conditions, as the B_0 dependence of the sample is not known over a large enough range of temperatures.

3.5.6. *Thermal Mixing*

The thermal mixing did show a large improvement to the effective T_1 time of the ^{13}C; however, the factor was smaller than expected. Work on a similar Dy-DTPA sample was conducted by Gadian, et al whereby they reduced the effective T_1 time of ^{13}C to match the proton T_1 time (20). The ^{13}C T_1 in this work does not match the proton T_1 times because of inefficiency in the mixing step.

For thermal mixing to occur, the B_0 field has to be dropped to almost 0 T for a short period of time. As seen from Figure 24, this reduces T_1 time of the protons and ^{13}C, resulting in polarisation being lost during the thermal mixing step. To maintain this polarisation, one could increase the mixing field strength, however, this weakens coupling between the proton and the ^{13}C, therefore the mixing step has to be longer to allow for the spin temperatures equate. It is easy to see that the mixing time and the mixing field have to be selected carefully to get an efficient polarisation transfer.

In this work the thermal mixing parameters were set to give the largest final signal. To do this, the spin temperatures of the ^{13}C were not allowed to reach equilibrium with the proton spin temperature. This is due to the proton relaxation rate being fast, compared to the time required for the spin temperatures of the nuclei to equilibrate. As seen schematically in Figure 29, the ^{13}C reaches a minimum spin temperature before the ^{13}C and protons spin temperatures equilibrate.
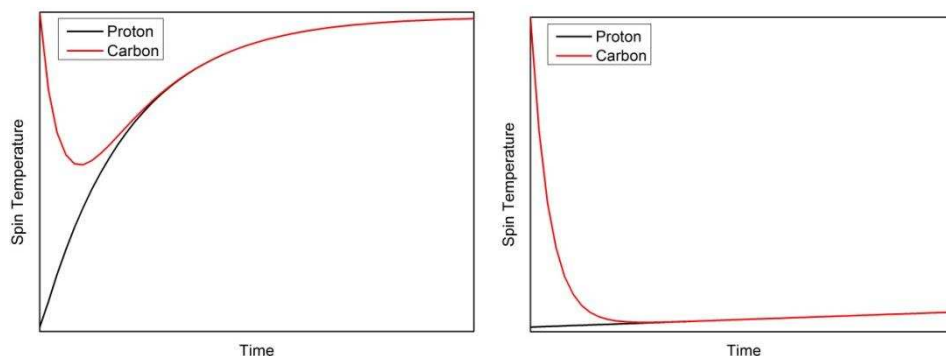
Figure 29: Schematic representation of the spin temperatures of a sample during thermal mixing. The graph to the left is a case when the T_1 time of the protons is short compared to the time require for thermal mixing, while the graph to the right is when the T_1 of the protons is long compared to the required mixing time.

The result of the short T_1 time of the proton's means that the thermal mixing process was not efficient and the effective T_1 time of the carbon is longer than the proton T_1 time at 2 T; however, the final signal produced by the carbon, after thermal mixing, is larger than the what would have been produced if the sample were to relax in a fixed field. If the T_1 time of the protons was long compared to the mixing time, then allowing the nuclei to reach equilibrium is beneficial. A thermal mixing optimisation study has been conducted on a pyruvic acid sample in Section 4.5.3. where the effects of changing the mixing time and field are demonstrated.

3.5.7. *Overview*

The effectiveness of the lanthanides can be attributed to the electron spin flip times matching the inverse Larmor frequency of the protons. Both dysprosium and holmium have a short electron flip time of around 10^{-12} s at room temperature (51,52). This flip time lengthens as the lanthanide is cooled. The inverse Larmor frequency of the protons match the electron spin relaxation time, as denoted by their T_1 minima in Figure 20, at 10 K and 20 K for Ho-DTPA and Dy-DTPA respectively. Below these temperatures the lanthanides become less effective. Dy-DTPA becomes ineffective at 0.1 K, while the lower temperature limit for the Ho-DTPA is not known. Contrasting gadolinium with either dysprosium or

holmium, the gadolinium is an effective proton relaxation agent at room temperature. This is because the electron spin flip time for gadolinium matches the inverse proton resonance at room temperature. As the gadolinium is cooled the electron spin time becomes longer and is therefore an ineffective relaxation agent below 30 K. The T_1 minima for protons relaxed by cerium occurs at ~30 K; however, at 4 K the cerium is less effective than Dy-DTPA and Ho-DTPA, therefore it is no longer of interest within this work.

The T_1 times for all of the samples are more erratic above 160 K, this is believed to be because the sample is going through the liquid-glass phase transition (which occurs at ~165 K) (53).

The experiments conducted were focused on the lanthanide chelates as they are potentially suitable for clinical studies. The toxicity of the Dy-DTPA and Ho-DTPA is assumed to be similar to Gd-DTPA because they have similar chemical properties. In clinical applications, Dy-DTPA and Ho-DTPA should be used in low concentrations and also filtered before use, if possible.

The short T_1 times in the Dy-DTPA samples suggests that the protons do not have to be in direct contact with the lanthanide to become relaxed. The mono exponential recovery curve also shows that there is a polarisation transfer between protons within the sample, probably through spin diffusion.

Other properties of the sample were also manipulated to try to optimise the relaxation rate. These properties were the pH and the WG ratio. Lowering the pH increases the relaxivity of the protons at lower temperatures and also shifted the T_1 minima to lower temperatures. This could be due to the change in the ionization state of the lanthanide-DTPA. The change in the ionisation state can be expected at pH 2 (54). The ratio of the water to glycerol in the solution does not make a large difference to the T_1 times, so long as there are approximately equal quantities of water and glycerol, the sample is optimised.

The T_1 time of protons in a lanthanide free sample, at 1.5 K and 10 T, would be short enough to reach equilibrium polarisation for a 48 hour polarisation time, and would produce an enhancement of ~700 when compared to a sample at 300 K and 3 T. The lanthanide free sample has several benefits, the primary of which is that toxicity is a much smaller issue. Another key advantage is that there is much less signal lost in the dead time of the

spectrometer. The lack of lanthanides also means that the polarisation should last longer during and after dissolution.

This low enhancement version of the brute force method would only be advantageous for laboratories that cannot afford a DNP system and for whom relatively modest polarisation enhancements would suffice. Both DNP and brute force systems can supply samples at a rate to match demand, but the level of polarisation using brute force method would be smaller than with DNP. It is likely that if this version of brute force method is employed, it would probably be run at 1.5 K or 4 K and with the largest magnet that could be purchased at a reasonable price. The temperature of 1.5 K is easily achievable with ^{4}He and a pump. Obtaining lower temperatures requires more sophisticated equipment, for example a dilution fridge, which increases the system cost significantly. This system, unlike in DNP, does not require a uniform magnetic field, which means that a cheaper magnet can be used, so long as it can produce a large field. This system does not need a microwave source which also reduces the running cost of the system compared to a DNP setup. As the sample does not contain additives, such as the free radicals used in DNP, a simpler filtration system could be used if the sample is not regarded as being clean when entering the polariser.

The polarisation still needs to be transferred to the ^{13}C from the protons. This will occur via thermal mixing while the sample is being transported between the polariser and the scanner, this is because there will be an area of low field between the instruments. This means that a field cycling capabilities are not required on the polariser. Introducing a controlled background field would ensure maximum efficiency of the thermal mixing step.

To maximise the effect of thermal mixing, the sample should undergo thermal mixing at the lowest possible temperature, as this is when the proton T_1 times are longest and therefore more like the second case of Figure 29. Allowing the thermal mixing to occur prior to dissolution also allows for the polarisation to be on the longer lived ^{13}C during transport, thus maximising the measured signal. If the sample is warmed up first, it is likely that the thermal mixing step would not work as the proton T_1 would be too short to allow for the spin temperatures of the nuclei to equilibrate before the protons lose their polarisation.

Dissolution of these samples was beyond the scope of this work, however, if dissolution was to be performed; a system similar to that used by Nelson, et al would be used. It would be expected to perform the dissolution, filtering and injection into a patient in 68 s or less

(3). It should be reminded that transport from the polariser to the dissolution unit should be done before warming the sample to allow for thermal mixing to take place.

The dissolution step used by Nelson, et al was inconsistent in the sense that the times to warm the sample ranged from 5 to 30 s. If this could be made consistent at 5 s, the dissolution time would be significantly reduced. The next step is the quality control of the sample. The lanthanide-free samples could be considered to be "clean" which mean that any filtering and quality control tests could be done prior to the sample entering the polariser. If these steps can be done prior to polarising, it decreases the time between leaving the polariser and measurement. If these improvements can be made, the dissolution to injection time should be around 30 s. For the purpose of calculation, an additional 10 s will be added to this time in the event that the quality control check is required after dissolution. This makes the total time required between dissolution to injection to be approximately 40 s. The T_1 of ^{13}C in NaAc has been measured by Comment, et al and they determined it to be of the order of 42 s at room temperature and 9.4 T (26). The value of the field is higher than what would be expected in a clinical environment; however, this T_1 time can be used to give an estimate of the final polarisation of the sample.

At the time of injection around 30-35 % of the hyperpolarised state would remain. If the sample is polarised at 1.5 K and 10 T and measured at 300 K and 3 T the enhancement after transport would be of the order of 200. Though this is a respectable enhancement, it is small compared to DNP. As this is the case, using the brute force method at temperatures above tens of millikelvin is not suitable for a clinical environment. This higher temperature brute force method could be more suited to other applications, such as chemical analysis.

3.6. *Conclusion*

In conclusion, some lanthanide-DTPA molecules can indeed decrease the time required to polarise a sample at low temperatures, this allows for hyperpolarised samples to be generated in a practical time scale. The use of hyperpolarised samples removes the need of averaging to get a high SNR which is useful in many applications of NMR. Previous work has shown that Dy-EDTA is an effective relaxation agent at low temperatures, while Cu-EDTA and Fe-EDTA are not (48). This research has shown that Dy-DTPA and Ho-DTPA are also

effective down to ~4 K (24). As the temperature is increased to 300 K, the T_1 times of protons in water containing Dy-DTPA approach 10 s, as seen in the reference (44). The T_1 for ^{13}C in a sample of 1 mM Dy-DTPA WG at 20°C and 11.7 T is around 250 s (24). Unfortunately, dysprosium is not effective at tens of millikelvin, therefore the absolute polarisation is limited to a level which cannot compete with DNP. Dysprosium can be used as a relaxation agent if moderate enhancements are acceptable, however, dysprosium should not be considered for in vivo applications.

The addition of the lanthanides is generally not necessary as the estimated polarisation time (around 48 hours) is much longer than the T_1 times of these samples at 4 K and 2 T. With such a long polarisation time, a lanthanide free sample could be polarised at 1.5 K and 10 T, as the T_1 time, assuming a cubic relation to field, would be of the order of 4 hours (20). Using a lanthanide-free sample comes with some benefits, which have been described in Section 3.5.7.

It was empirically shown in Figure 28 that the optimal conditions to achieve the maximal polarisation, after a fixed polarisation time, is when the T_1 is roughly half the length of the polarisation time, assuming that the T_1 follows a cubic relation to the parameter being varied. It is possible to vary the field and temperature, with the intention of setting T_1 to being around 24 hours, half of the polarisation time. Thermal mixing can then be used to pass the polarisation from the protons in the sample to the ^{13}C, before undergoing dissolution.

A simple polariser, which produces temperatures of 1.5 K and 10 T, could also be a good stepping stone for groups that only need a modest signal enhancement, for minimal cost. These simple polarisers could be upgraded at a later time to become more like a DNP system, if required.

Brute force polarisation, using lanthanides as a relaxant, probably does not have a place in a clinical setting, but could be useful in other applications such as chemical analysis. The brute force method might still be a valid approach to obtain very large polarisations in a clinical environment, if another relaxation agent can be found. The relaxant would have to be effective in the millikelvin regime to produce a level of polarisation similar to that of DNP.

Chapter 3. Lanthanides

Chapter 4. *Nanoparticle Relaxation Agents*

The work on the lanthanides was successful; however, it was limited to temperatures of the order of 4 K, and therefore, the level of polarisation is also limited. This chapter is aimed at trying a different additive to allow for short relaxation times, at the millikelvin temperatures, while still being ineffective at the higher temperatures. For more information of the ideal characteristics of relaxation agents see Section 3.1.1.

The initial idea was to try and put a material, with a short T_1, in close proximity to nuclei of interest in the expectation that they would interact and decrease the T_1 time of the nuclei of interest. To maximise the contact between the nuclei of interest and the fast relaxing material, it would be beneficial to use nanoparticles, as they have the largest surface area to volume ratio, thus would increase the likelihood of any interactions.

This chapter is going to be broken down into several sections. The first of which is going to be the general theories and methods that were applied to the other sections within this chapter. Following the method section, there will be several self-contained sections which are centred on the $T_{1/2}$ times of protons, ^{13}C, thermal mixing and another method of polarisation transfer. These sections will introduce additional information about techniques before displaying and discussing the results. Finally, there will be a conclusion section which will bring all of the data from this chapter together.

4.1. *General Theory and Methods*

4.1.1. *Korringa Effect*

The Korringa effect is a relaxation process in which the conduction electrons in metals interact with the metal nuclei causing them to relax (13,55,56). The energy difference in a mutual nuclei-electron flip is negligible compared to the Fermi energy of the conduction electrons. As the conduction electrons are readily excitable, they can absorb or contribute some energy to the flipping process. The process of absorbing or contributing energy is limited to the surface of the Fermi sphere with a thickness of k_bT. Assuming that the applied magnetic field is much larger than the dipole-dipole field, this process has some key

features. The most notable feature is that the T_1 relaxation time of the nuclei is inversely proportional to temperature, T, and is independent of magnetic field. At much lower fields the Korringa effect is modified, however, due to the nature of these experiments, the focus will be on the high field case.

The Korringa effect has a simple relation to the Knight shift. The Knight shift is the relative shift, K, in the NMR resonance frequency of nuclei due to polarisation of conduction electrons; this effectively increases the magnetic field, therefore, shifting the Larmor frequency. The Knight shift is measured by taking the ratio of the difference in the resonant frequency, Δf, of a metallic nuclei in both a metallic and non-metallic form. This difference is then divided by resonance frequency, f, of the nuclei, as seen in equation (25). When the metal is in a non-metallic form, the conduction electrons, and therefore the shift in the resonance frequency, is removed (57).

$$K = \frac{\Delta f}{f} \tag{25}$$

The nuclear relaxation time in the metal is due to the conduction electrons. This relaxation is based on the inelastic scattering of electrons, due to the Fermi interaction. The relaxation rate is therefore proportional to the square of the Fermi interaction, which is based on the Knight shift (58). This produces the following equation:-

$$T_1 = \frac{\hbar}{T 4\pi K_b K^2}\left(\frac{\gamma_e^{\,2}}{\gamma_n^{\,2}}\right) \tag{26}$$

Where γ_e and γ_n are the gyromagnetic ratios of the electrons and the nucleus of the metal respectively. K_b is the Boltzmann constant (59,60). An example of some samples of interest can be seen in Table 3.

Nucleus	% Natural abundance	Nuclear spin	Resonance frequency at 9.74T (MHz)	T_1 relaxation time x temperature (s K)	References
^{27}Al	100	5/2	108.1	1.8	(13)
^{63}Cu	69.1	3/2	109.9	1.27	(14)
^{65}Cu	30.1	3/2	117.7		
^{107}Ag	51.8	1/2	16.8	12.0	(56)
^{109}Ag	48.2	1/2	19.3	9.0	(56)
^{195}Pt	33.7	1/2	89.2	0.030	(14)

Table 3: Nuclear spin properties of selected metals

The aim of this chapter is to determine if the conduction electrons from the metals in Table 3 can interact with other nearby nuclei and reduce their T_1 time in the millikelvin regime.

4.1.2. *Magnetic Relaxation and Sample Considerations*

There is potential for a second relaxation mechanism to relax samples in this chapter. This mechanism could be similar to the one used in the previous chapter, it was described in Section 3.1.1. Nanoparticles are known for having different magnetic properties compared to their bulk form (15,16,61). The magnetic properties of the samples used in this chapter will be measured in Chapter 5. If this magnetic relaxation mechanism is significant, it should be exploited.

The concentrations of nanoparticles used in these samples will be very high compared to that of the lanthanides used in Chapter 3. This means that the ratio of detectable nuclei is smaller in these samples than those measured in Chapter 3 as the relaxant is replacing the nuclei of interest. There is a balance between the number of detectable nuclei and the quantity of relaxant within a sample. Without a relaxant the T_1 times are long and therefore the sample does not become polarised. However, if the sample has a large quantity of relaxant there is not enough space left for the nuclei you are trying to detect. The effect of the relaxation concentration is discussed in Section 4.3.2.1.3. and 4.3.2.2.3.

4.1.3. *Direct, Orbach and Raman Processes*

All three of the Direct, Orbach and Raman processes are ones which relate the spins in a system to the lattice via phonons. The spins usually associated with these processes are the electron spin. The mechanism of each of these processes become dominant at different temperatures and can be separated from one another by the T_1 dependence on temperature. These processes are normally studied in paramagnetic salts of iron and rare earth metals, but have been included in case they can be related to the nanoparticle system (62,63).

4.1.3.1. *Direct Process*

To relax an excited magnetisation, energy must be transferred to the lattice. This energy transfer can occur by directly producing a phonon; known as the direct process. The relaxation rate of the excited spins is proportional to the temperature, as seen in equation (27).

$$\frac{1}{T_1} = K_{Ph}\omega_0^2 T \tag{27}$$

Where K_{Ph} is the spin-lattice interaction constant and ω_0 is the transition frequency between the two energy levels (60). Since this is a resonance phenomenon, the frequency of these phonons is limited to the energy difference between the excited state and the ground state of the spin. The direct process is generally effective at the lowest temperatures.

4.1.3.2. *Orbach and Raman Process*

The Orbach and Raman processes are other ways for spins to relax while producing a phonon. Both of these processes require initial preparation of the sample to stimulate the energy transfer. In the Raman process, an initial phonon is scattered off the spin. This stimulates the de-excitation of the spin, whereby the initial phonon gains the energy lost by the spin. Phonons of any energy can be used in the Raman process. If it is assumed that the frequency of the initial phonon is Ω, then the energy of the final phonon, Ω', would be equal

to $\Omega+\omega_0$ where ω_0 is the difference in the energy levels. This is illustrated in Figure 30. As the initial phonon that stimulates the relaxation can be of any energy, the Raman process is as likely to occur as the direct process, even though it is a many particle event. The relaxation from a Raman process is proportional to T^7 or T^9 (60).
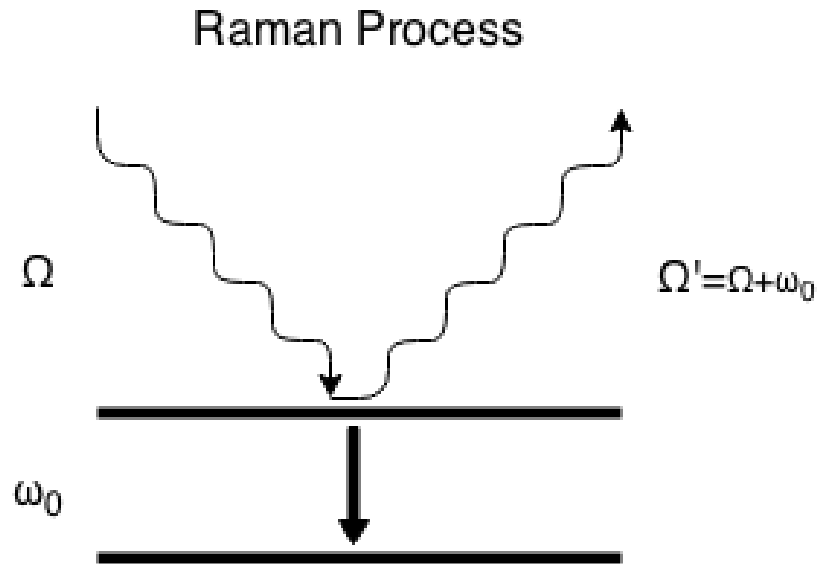
Raman Process

Figure 30: Schematic of the Raman process. An initial phonon is scattered off of an excited spin and gains the energy of spin that is equal to its change in energy level.

In the Orbach process the spin needs to be promoted to a higher energy level via thermal processes. From this higher energy state, the spin can relax by producing a phonon in a similar way to the direct process. The phonon produced from the Orbach process will have a higher energy than phonons produced from the direct process. According to the thermal activation required, the Orbach process is proportional to exp$(-\Delta/K_B T)$. Δ is the energy the spin gains from thermal excitation (60). The energy of the phonon, after the relaxation, is equal to $\Delta+\omega_0$ as seen from Figure 31. As the thermal energy is variable, the distribution of phonon frequencies is broader than the direct process.

Orbach Process

Thermal energy

$$\Omega'=\Delta +\omega_0$$

Δ

ω_0
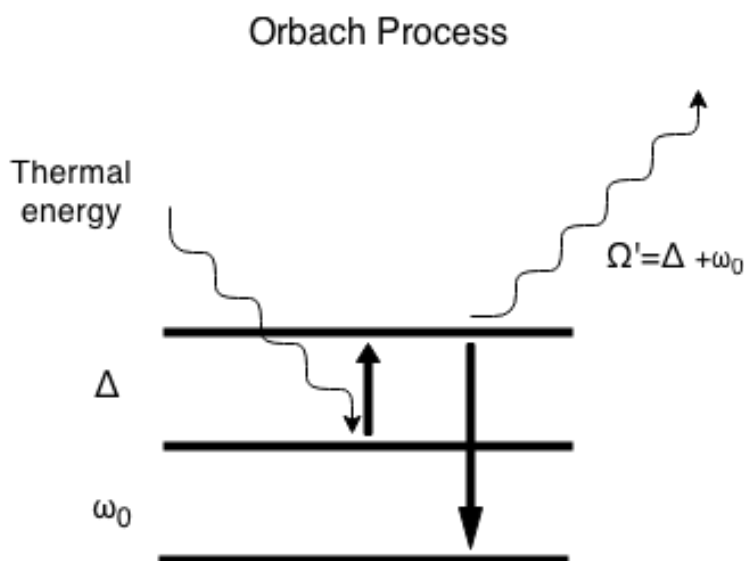
Figure 31: Schematic of the Orbach process. Thermal energy promotes the spin to a higher energy level before it relaxes to a lower energy level releasing a phonon.

All of these processes are studied at low temperatures, typically 20 K or lower and each process is dominant in a different temperature range. Generally the direct process is most effective at the lowest temperatures. The Raman process is dominant in the mid temperature range which is classified as upper helium temperatures. The Orbach process is dominant at the higher temperatures. The temperature at which each process is effective is dependent on the sample (60,64).

4.1.3.3. Phonon Bottleneck

It is generally assumed that the lattice has a large heat capacity and is therefore able to absorb any amount of spin energy without increasing in temperature. However, at liquid helium temperatures this assumption is false (65,66). The phonon bottleneck occurs when the lattice vibrations near the Electron Spin Resonance frequency (ESR) are excited and the effective phonon temperature is high. These phonons are then more likely to be re-absorbed by the spins than to be dissipated via other means. The phonon re-absorption has the effect of reducing the relaxation rate of the spins in the system. More details on this subject can be seen in the following references (65,66,67).

4.1.4. *Expected Relaxation Profile*

If the metal nanoparticles do couple with the nuclei in the solution, we expect to see relaxation due to the electrons in the metal, T_{1e}. The Korringa effect suggests that $1/T_1 \propto T$, as seen in Section 4.1.1. The now excited electrons can then relax via the phonon effects described in Section 4.1.3. Another source of relaxation was observed in Chapter 3, this was a cubic temperature dependence, T_{1M}, as seen in Figure 21. A temperature independent term has been added to represent a quantum term if it is necessary, T_{1qm}. This then means that the observed T_1 for the samples should follow the expression below:-

$$\frac{1}{T_1} = \frac{1}{T_{1e}} + \frac{1}{T_{1M}} + \frac{1}{T_{1qm}} = aT + bT^3 + c \tag{28}$$

In many cases the quantum contribution, c, is either small or zero within error. As the temperature is lowered the behaviour crosses over from being cubic to linear, depending on the relative magnitudes of a and b. Platinum, and to a lesser extent aluminium, have a very large linear contribution compared to the cubic contribution. Hence the $T_{1/2}$ closely follows a linear relationship over a large temperature range. Most other samples have a dominant T^3 contribution, as reflected in Table 5. An interesting point which should be made is that even though graphene is not a metal it does have excellent conduction properties, however, it has no linear (electronic) relaxation (68).

4.1.5. *Properties of Nanomaterials*

Nanomaterials tend to have different properties to bulk material due to scaling effects. The most well-known property of nanomaterials is that they tend to be mechanically stronger than their bulk counterparts. An example of the difference in properties between nano and bulk materials is carbon nanotubes, these are one of the strongest materials known (69). A lesser known property of nanoparticles is that they have unusual magnetic properties compared to their bulk form. An example of the unusual magnetic properties of

nanomaterials include the ferromagnetic properties of nano cupric oxide at room temperature when bulk copper oxide is not ferromagnetic (15). In the same way that paramagnetic lanthanides cause T_1 relaxation, it could be possible that the magnetic properties of these nanoparticles also cause T_1 relaxation. The magnetic properties of the nanoparticles will be discussed in detail in Chapter 5.

Nanomaterials have a tendency to aggregate, unless they are capped and suspended in a liquid. Nanoparticles that have aggregated have increased in size and therefore have a smaller surface/volume ratio. The samples used in this research will probably experience some aggregation, as they arrived as dry powders. Ideally the nanoparticles would be grown in the test solution to minimise the risk of aggregation. If further research is to take place, it would also be worth investigating the effects of capping agents, as they can help preserve the surface/volume ratio and have also been shown to affect the magnetic properties of the samples (16,70,71).

The physical properties of the samples were not tested after being sent from the supplier, therefore, the average size, size distribution and morphology of the nanoparticles is not well known. As a consequence, the sizes stated are those quoted from the supplier and these values represent the lower size limit of the particles due to the effects of aggregation.

The chemical properties of nanomaterials are also important. Metals, like copper, oxidise over time and as the reactivity of a material is dependent on its surface area, nanoparticles should be more reactive then their bulk counterpart. The nanoparticles in this chapter have a very large surface area and are not capped. This means that the samples may react with the air or the solution. In both this chapter and Chapter 5, copper and copper oxide samples are compared to determine if they can be classed as individual samples as it is possible for the copper to oxidise to copper oxide. It will also be seen in Chapter 5 that copper and copper oxide react with organic acids. This reaction may limit the possibility of using copper and copper oxide as a relaxation agent, therefore, more inert materials should be considered.

4.1.6. *Hardware*

The majority of experiments performed in this chapter were implemented on the dilution fridge, as described in Section 3.2.2. The saturation recovery pulse sequence used with the dilution fridge is explained in Section 3.3.2.2. A smaller number of experiments were run on the field cycling system, using its saturation recovery pulse sequence as explained in 3.3.2.1.1. Another pulse sequence was introduced to explore the effect of changing the field while the sample was recovering. This pulse sequence will be described in Section 4.6.1.

4.1.7. *Sample Preparation*

Many of the samples in this chapter are a mixture of nanoparticles and 50:50 water:glycerol (WG) by volume. When required, isotopes of ^{13}C and ^{31}P were added in the form of 2M [1-^{13}C] sodium acetate (NaAc) and 1M of sodium phosphate (NaPh). In other experiments, ^{13}C was added to the sample by introducing [1-^{13}C] pyruvic acid or synthesised ^{13}C potassium acetate, by reacting [1-^{13}C] Acetic acid with potassium hydroxide. The final samples were 1 part nanoparticle to 4 or 8 parts of the solution by volume, calculated by using the density of the bulk material. The samples were then placed in a sonic bath for 30 minutes to mix. The resulting mixtures were generally viscous fluids which can then be loaded into a 2 mm NMR sample tube as explained in Section 3.3.1.4.

The following chemicals were supplied by Sigma Aldrich:- NaAc, glycerol, sodium hydroxide, potassium hydroxide, [1-^{13}C] Acetic acid and [1-^{13}C] pyruvic acid.

The nanoparticles were supplied from various sources and the sizes quoted below are quoted from the source; actual sizes may be larger due to aggregation. Nanoparticles of cupric oxide (<50 nm) and platinum (<50 nm) were obtained from Sigma Aldrich (Sigma-Aldrich Company Ltd, The Old Brickyard New Road, Gillingham, Dorset, SP8 4XT, UK). Nanoparticles of copper (25 nm), graphene (11-15 nm), 14% copper in ester phosphate (5-7 nm), zinc oxide (10-30 nm), magnesium oxide (10-30 nm), aluminium oxide (20 nm), stannic oxide nanoparticles (50-70 nm), aluminium (18 nm) and silver (20-30 nm) were supplied by SkySpring Nanomaterials Inc (SkySpring Nanomaterials, 935 Westhollow Drive, Houston, TX 77082, United States). Nanoparticles of copper (40 nm) and copper oxide (9 nm) were supplied by Promethean Particles Ltd (Promethean Particles Ltd, 6 Faraday Building,

Nottingham Science Park, University Boulevard, Nottingham, NG7 2QP, UK). Micron-sized aluminium (15 µm) and copper (44 µm) metallic particles were supplied by Newmet (Newmet, Newmet House, Rue de Saint Lawrence, Waltham Abbey, EN9 1PF, Essex, UK).

Dry gold nanoparticles were supplied by L. Turyanska from the University of Nottingham. (School of Physics and Astronomy, University Park, Nottingham, NG7 2RD, UK). These nanoparticles were only measured for their magnetic measurement properties, which can be seen in Chapter 5. These gold samples are capped with citric acid.

4.1.8. *Sample list*

Below is a list of all the samples that were tested in this chapter along with control measurements on nanoparticle free 2 M NaAc WG and Pyr. It should be noted that the samples were all quench cooled (meaning that the samples were rapidly frozen from a liquid state to the solid state). This locks disorder into the solids. A sample of Pyr was also annealed to observe the difference in T_1 if the disorder of the system is allowed to be removed. These results can be seen in Section 4.3.2.2.

Sample	Solution:particle	Particle Size (nm)	Solution (Water glycerol if not otherwise stated)
Copper	4:1 & 8:1	25	2M NaAc 1M NaPh WG
Silver	4:1	20-30	2M NaAc 1M NaPh WG
Graphene	4:1	11-15	2M NaAc 1M NaPh WG
Aluminium	8:1	18	2M NaAc 1M NaPh WG
Platinum	8:1	<50	2M NaAc 1M NaPh WG
Cupric oxide	4:1	<50	2M NaAc 1M NaPh WG
Cupric oxide	8:1	9	2M NaAc 1M NaPh WG
Zinc oxide	8:1	10-30	
Stannic oxide	8:1	50-70	
Aluminium oxide	8:1	20	
Magnesium oxide	8:1	10-30	
Copper Dy-DTPA	8:1	25	2M NaAc 1M NaPh WG, 6mM Dy-DTPA
Copper	8:1	25	4M NaAc WG
Copper	8:1	25	4M NaAc WG
Copper WG	8:1	25	4M NaAc WG
Copper	8:1 &30:1	25	2M NaAc 1M NaPh WG for 8:1, WG for 30:1
Copper Ester Phosphate	7:1	5-7	
Copper Pyr	8:1	25	Pure Pyr solution
Copper Pyr	8:1	25	6:1 water:Pyr solution
Copper Pyr	8:1	25	6:1 water:Pyr solution
Copper	8:1	44000	
Aluminium	8:1	15000	

Table 4: List of NMR Samples

4.1.9. *Experimental Method*

Initially when conducting these experiments, the emphasis was on proton relaxation, the reason for this is the results from Chapter 3 showed that thermal mixing was an effective way to transfer polarisation to the ^{13}C nuclei, where it is favourable. However, as will be shown in this chapter, the $T_{1/2}$ for ^{13}C in samples containing NaAc is weakly dependent on the temperature in the millikelvin regime, consequently the $T_{1/2}$ times are short enough to

achieve high ^{13}C polarisation without thermal mixing, although thermal mixing may still be a faster method of achieving high levels of ^{13}C polarisation.

$T_{1/2}$ is used as the measure of the relaxation time because it removes the idea that the relaxation curve follows a mono exponential curve. The $T_{1/2}$ time is a measure of the time taken for the signal to reach 50% of the equilibrium value and is a method of comparing time constants between samples that do not follow simple relaxation curves. It should also be noted that if a sample does follow a mono exponential recovery, the $T_{1/2}$ time can be converted to T_1 with the following equation:-

$$T_{1/2}=T_1 * \ln(2) \tag{29}$$

Due to $T_{1/2}$ being long at the lowest temperatures, it is not always feasible to wait for the polarisation to reach its equilibrium value. In order to save time there is a hierarchy of methods which have been employed to calculating the $T_{1/2}$ value when information is limited. If the $T_{1/2}$ is short it is possible to acquire a full recovery curve. Linear interpolation is then used to find the $T_{1/2}$ value. Generally this method of ascertaining the $T_{1/2}$ value will only be used in the high temperature cases (~1 K). When the temperatures are lowered, $T_{1/2}$ lengthens, so instead of waiting for the full recovery curve, an estimate of the equilibrium signal can be calculated by scaling the equilibrium points from higher temperature measurements. This is done by using equation (5). Data is then collected until ~60 % of a calculated equilibrium value is reached and linear interpolation is used to ascertain the $T_{1/2}$ value. Finally, if the $T_{1/2}$ is extremely long, more than a day, only the first few percent of the recovery curve is measured. The collected data is scaled to a recovery curve with a known $T_{1/2}$ value, using equation (5). The collected data is then scaled in the time axis to allow for the two curves to coincide. The $T_{1/2}$ of the low temperature data is then assumed to be equal to the $T_{1/2}$ of the higher temperature curve, divided by the factor used to overlay the two recovery curves. This final method is far from ideal; however, is the only practical way of obtaining a $T_{1/2}$ estimate for a sample with a $T_{1/2}$ that is in the order of hundreds of hours.

Calculating errors for the $T_{1/2}$ time is not trivial because there are a number of factors that are hard to pin down. The main source of error is the uncertainty in the equilibrium magnetization values. The equilibrium magnetisation is hard to define with samples that don't follow a mono exponential recovery because the longer components might be missed. The equilibrium magnetisation is also affected by the temperature of the sample. The error

in equilibrium magnetization, ΔI, is typically 10% and it comes from stopping the experiment early or by the FWHM of the NMR peak changing.

The error in the temperature, *ΔT*, is also of the order of 10%. This error is associated with the difference in temperature between the thermometer and the sample itself. This is due to the thermometer only being near the sample and not in direct contact.

When the $T_{1/2}$ is estimated, by scaling the first few percent of a recovery curve to a previously measured recovery curve, an error can also be associated with how well the two curves coincide. This error is denoted as *ΔS*. If the scaling method is not used then *ΔS=0*.

$$\Delta T_{1/2} = \sqrt{\Delta I^2 + \Delta T^2 + \Delta S^2} \tag{30}$$

This typical error has been applied to all of the data in this chapter. The error bars are generally hidden under the data points, as the data is plotted on a log scale.

It has been mentioned within this section that $T_{1/2}$ will be quoted instead of T_1, as not all of the recovery curves follow a mono exponential behaviour. A mono exponential recovery has the form the form shown in equation (7). This equation can be rearranged to calculate the time of measurement, *t*, based on the signal size at a set time. To check if the recovery curve is mono exponential, the calculated measurement time and the actual measurement can be plotted against one another. If there is a linear relationship, the recovery curve follows a mono exponential; however, if the curve is not linear, the recovery is not a mono exponential. Figure 32 shows an example of samples that do and do not follow a mono exponential recovery.
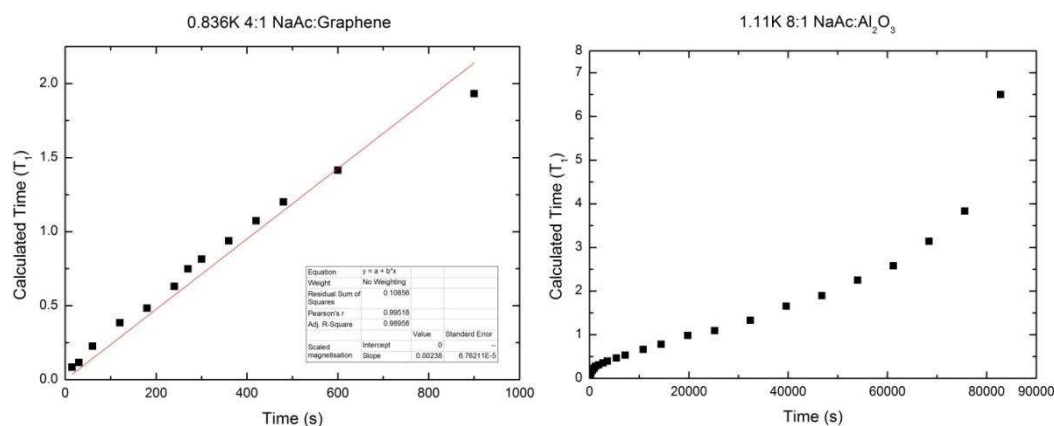
Figure 32: The graph to the left shows an example of a mono exponential recovery for a graphene doped 2M NaAc sample. The red line is a linear fit based on equation (7) mapping the calculated time vs time of measurement. The graph to the right is for an aluminium oxide doped 2M NaAc sample which demonstrates non-mono exponential growth.

4.2. *Radiation Damping*

As seen in Figure 32, not all of the relaxation curves follow a mono exponential curve. A known effect that disrupts the recovery of a sample is called radiation damping (72). This is not necessarily the only cause of non-exponential recovery.

Radiation damping is an effect that is present in all pulsed NMR experiments; however, it is often neglected because the effect of radiation damping is small in most cases. Radiation damping is an effect whereby the sample experiences feedback from the detection coil. Depending upon the type of measurements, radiation damping can be useful or a restriction (72,73,74).

4.2.1. *Theory*

Under normal circumstances the absorption of energy, by the spins, is much smaller than the energy of the RF. In cases where this is not true, the effect of radiation damping is observed. When an RF pulse flips the spins in a system, the precession of the spin induces a current in the detector coil. These currents in the coil have a magnetic field associated with them and this affects the spin system. The magnetic field produced by the feedback is in the direction which causes the spins to align towards B_0. The overall effect is that the relaxation

of the system seems faster than from relaxation processes alone. This enhanced relaxation can also broaden the FWHM of the peaks in the spectra. Radiation damping is strongest when the coil is well-tuned with a high concentration of sensitive nuclei i.e. protons. The following derivation of radiation damping was published by Bloembergen and Pound (72).

If we consider a magnetisation precessing in a coil, it is expected that a periodic voltage will be induced. It is assumed that the coil has n turns, a cross section of A, and a length of l. The filling factor of the coil is η. The angle between the magnetisation and the B_0 field is ϑ. This now allows us to calculate the induced voltage, V_s. Note that the factor of $4\pi/c$ is from using cgs units.

$$V_s = -nA\eta \frac{4\pi}{c} \frac{dM_x}{dt} = -nA\eta\omega_0 \frac{4\pi}{c} M_0 \sin(\theta) \cos(\omega_0 t) \qquad (31)$$

As the sample is relaxing in the coil, the value of ϑ is decreasing. Now, by considering the torque exerted on the magnetisation, we can see how the magnetisation aligns back to B_0. First the induction field produced from the coil.

$$H_x = 4\pi V_s \frac{n}{clR} = 4\pi\eta Q M_0 \sin\theta \cos\omega_0 t$$

Where Q is the quality factor of the coil and is given by:-

$$Q = \frac{\omega L}{R} = \frac{\omega 4\pi n^2 A}{Rlc^2}$$

The torque produced from this induced field gives rise to the equation of motion of the magnetisation.

$$\frac{dM_z}{dt} = -\gamma M_y H_x$$

It is also possible to consider relaxation as the change of θ with respect to time, which gives the equation:-

$$\frac{d\theta}{dt} = 2\pi\gamma\eta Q M_0 \sin\theta \qquad (32)$$

In the special case that $\vartheta=\pi/2$ at $t=0$ the differential equation (32) can be solved to show

$$\tan(\theta/2) = \exp(-2\pi\gamma\eta Q M_0 t) \qquad (33)$$

The amplitude of the induced signal decreases proportionally to *sech ($2\pi\gamma\eta QM_0t$).*

A simple test to determine if radiation damping has a large effect on a sample is to detune the receiver coil. This should mean that the voltage decreases by a factor of the order of *Q,* and the width of the peak will become narrower. Another effect, which can be observed in high resolution spectrometers, is the relative intensities of the peaks in a multiplet do not follow a binomial distribution if radiation damping is present. The spectrometers used in this research cannot produce high resolution spectra, therefore, we can only test the radiation damping by checking the broadening effect on the line shape and by moving the coil off resonance.

Finally, it should be noted that some pulse sequences requires times where the nuclei have free precession, but if radiation damping is present it can have unusual influences on the signal received. This is because the feedback from the coil means that the nuclei is no longer in a strictly free precession (72).

4.2.2. *Results and Discussion*

Here we show the profound effect of radiation damping on the NMR spectra and the relaxation curve. As noted above, these effects can be minimised if the receiver coil is off resonance to the Larmor frequency of the nuclei.

Figure 33 shows the difference in the NMR spectra when the coil is on and off resonance to the protons in a sample of 20:1 WG 2M NaAc:CuO at 20 mK. The splitting of the peak on the 104.85 MHz spectra is due to the radiation damping. When the magnetization of the sample is small or the coupling to the coil is weak, for example, when the coil is off resonance, the effect of radiation damping is negligible, as seen in the 84.77 MHz (red) and 127.76 MHz (blue) spectra.
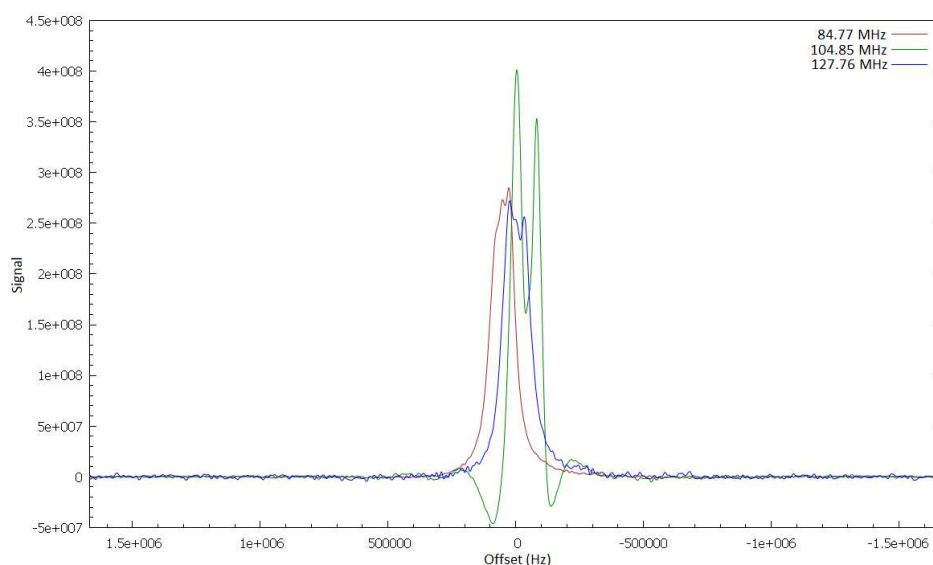
Figure 33: The effect of radiation damping on the spectra at 20 mK.

An example of differences in the recovery rates of the sample, when using the same three frequencies as used in Figure 33, can be seen in Figure 34. The recovery curves have been normalised to one another and it can be seen that at 2.46 T, the coil resonance to the protons, the equilibrium polarisation seems much smaller than in the other two cases. If the effect of radiation damping was not check for, users of the system would probably assume that the $T_{1/2}$ of the sample is much shorter than it actually is. This emphasizes the importance of measuring $T_{1/2}$ away from the coil resonance frequency, in cases where the samples has a large magnetisation.
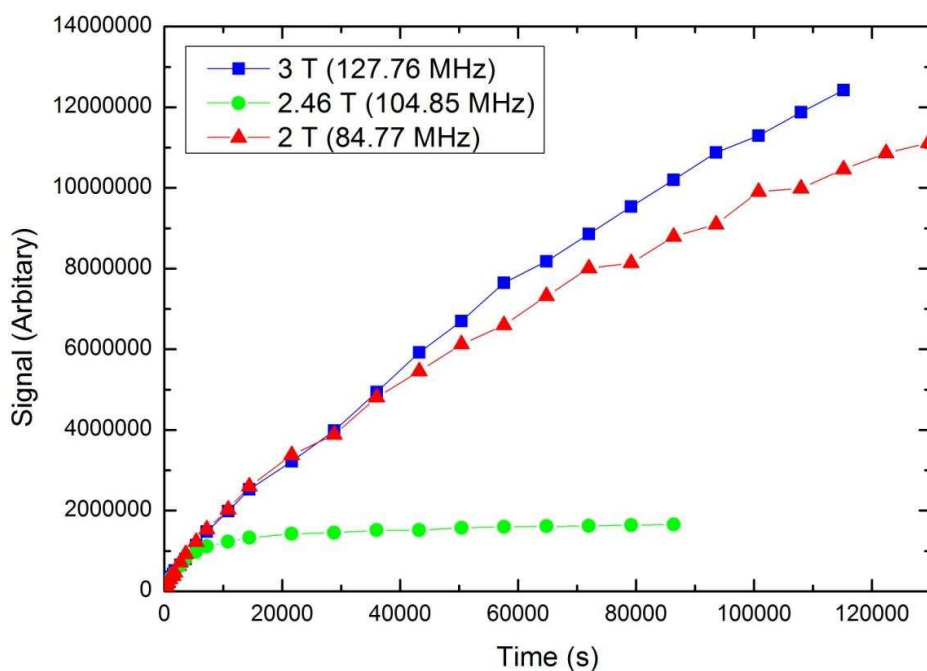
Figure 34: Proton T_1 recovery curves at various frequencies showing the depression in the signal on resonance.

Another technique has been used to measure T_1 at the resonance frequency of the coil, namely spin noise. Spin noise involves measuring the noise produced in the coil without applying any RF pulses to the system. Averaging thousands of scans of noise, removes actual noise, to retain the interactions between the nuclei and the coil. This process of acquiring thousands of scans takes around 15 minutes. If a sample is saturated, it is possible to measure a $T_{1/2}$ time, in real time, by measuring the spin noise. However, as the acquisition time is so long, it is hard to obtain accurate $T_{1/2}$ times. This is because each point in the recovery curve is the average magnetisation over the 15 minute data acquisition. It is possible to get an idea for the length of $T_{1/2}$, if the $T_{1/2}$ is in the order of one hour or longer.

The recovery curve of the 20:1 WG 2M NaAc:CuO sample at 20 mK, using spin noise, is shown in Figure 35. It can be seen that the $T_{1/2}$ of the sample at 2.46 T (104.85 MHz) is between the $T_{1/2}$ times measured using a pulsed method at 2 T and 3 T. As spin noise is measurable in the dilution fridge, it verifies that radiation damping is observed (74,75).
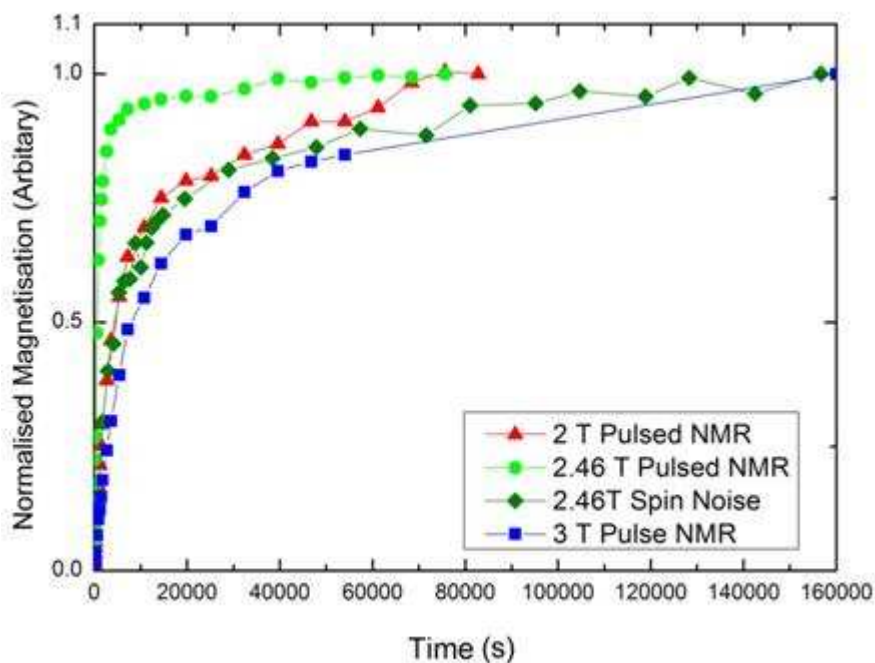
Figure 35: Proton $T_{1/2}$ measured using spin noise measurements on a 20:1 WG 2 M NaAC:CuO sample at 20 mK

4.2.3. *Discussion and Conclusion*

The observation of a distorted NMR spectrum in the dilution fridge system, along with the apparent shortening of the $T_{1/2}$ time of the sample, when on the coil resonance, proves that radiation damping will affect our measurements. As a result, the magnetic field will be taken off resonance to the coil, to minimise the effect of radiation damping at the lower temperatures, as this is where the effect is most apparent.

4.3. *Proton T_1 Enhancement with Nanoparticle additives*

As mentioned in Section 2.7. producing a sample with a short proton $T_{1/2}$ is desirable. Even though the polarisation must ultimately be on ^{13}C for the intended application, the proton $T_{1/2}$ can be 30-fold shorter than that of the ^{13}C. Thus, polarising protons, followed by thermal mixing, to transfer the proton polarisation to the ^{13}C, can be an effective way of producing the ^{13}C polarisation.

4.3.1. *Methods*

The T_1 and $T_{1/2}$ times in this section were obtained using the same methods as in Chapter 3, as described in Section 3.3.2.1.

4.3.2. *Results*

4.3.2.1. Proton Relaxation at Ultra Low Temperatures

This section has been divided further into six parts, as follows:-

1. Metallic Nanoparticles
2. Non-Metallic Nanoparticles
3. Copper and Copper Oxide Measurements
4. Copper Nanoparticles in Various Solvents
5. Copper in Pyruvic Acid
6. Polarisation Achieved Over Various Temperatures and Fields

4.3.2.1.1. Metallic Nanoparticles

Figure 37 shows the proton relaxation rates, *1/$T_{1/2}$*, against temperature for 2 M NaAc solutions containing various metallic nanoparticles. These experiments were done at various temperatures ranging from 10 mK to 2 K. At the higher temperatures, where the sample magnetisation is small, a field of 2.45 T was used, this corresponds to the probe's maximum sensitivity to protons. However, at lower temperatures, where the sample magnetisation is larger, radiation damping becomes apparent, therefore, the experiments were carried out at 3 T, intentionally misaligning the proton's Larmor frequency from the probes tuning frequency.

Figure 37 shows the same data as Figure 36 plotted as 1/$T_{1/2}$, the rate of proton polarization build-up. This data is fitted to equation (28) with the corresponding fitting parameters given in Table 5. It can be seen from Figure 37 that the copper and platinum are the most effective relaxation agents at the lowest temperatures (10 mK to 800 mK), while

above that range graphene becomes more effective than the platinum. Throughout the range 10 mK to ~ 500 mK, copper nanoparticles relaxes protons ~450 times faster than the undoped 2 M NaAc WG, whereas Pt nanoparticles exhibit ~100-fold effects. Meanwhile, silver, aluminium and graphene nanoparticles each exhibit a 10-fold enhancement of the proton polarisation rates below 500 mK.
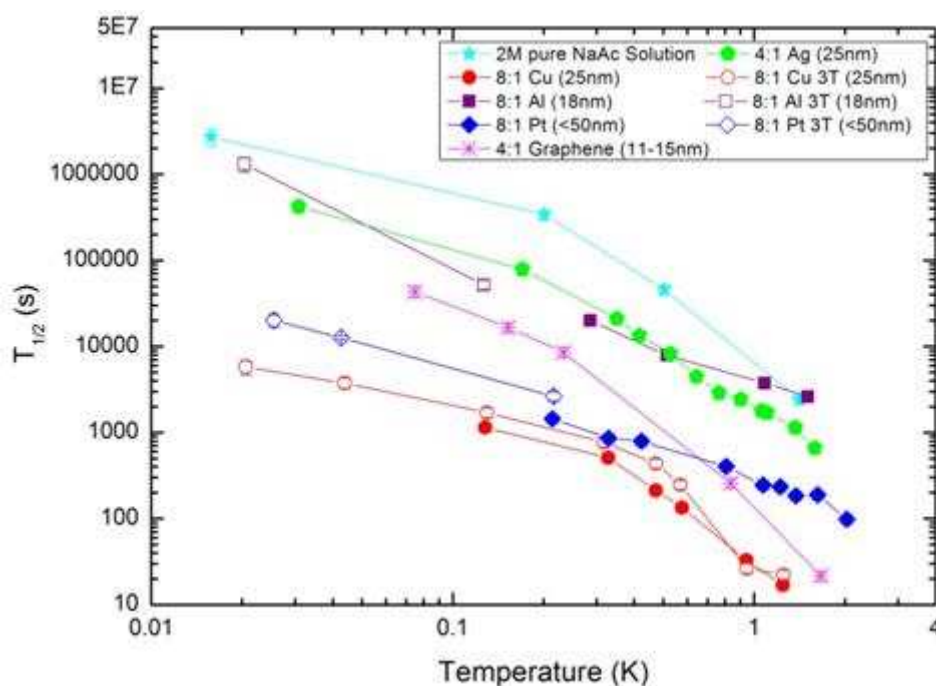
Figure 36: Proton $T_{1/2}$ times of frozen 2 M NaAc W:G samples with various metallic nanoparticles as a function of temperature. The external field is 2.45 T unless otherwise specified.
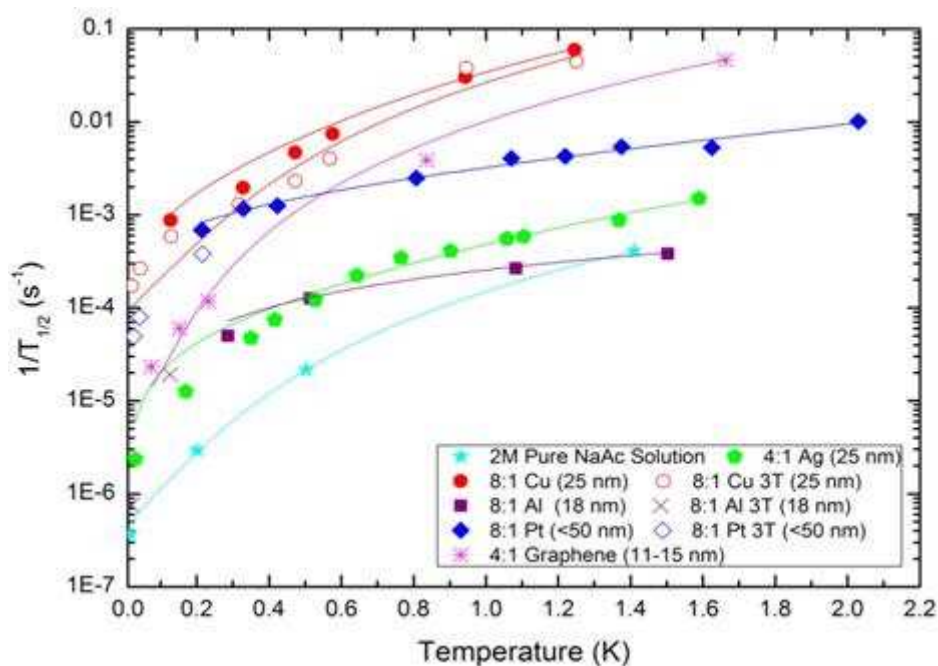
Figure 37: Rate of proton polarisation expressed as 1/$T_{1/2}$ for frozen 2M NaAc WG samples containing metallic nanoparticles at millikelvin temperatures. Curves are fitted following equation (28).

Metal	Intercept (quantum component)	Linear (electronic component)	Cubic component
2 M NaAc Solution	0.4×10^{-6}	6×10^{-6}	0.00014
Copper (3 T)	80×10^{-6}	0.0010	0.0254
Copper (2.45 T)	0	0.0072	0.0269
Platinum (3 T)	N/A	N/A	N/A
Platinum (2.45 T)	0.000320	0.0024	0.0006
Graphene (2.45 T)	10×10^{-6}	0	0.0110
Aluminium (3 T)	N/A	N/A	N/A
Aluminium (2.45 T)	0	0.0002	10×10^{-6}
Silver (2.45 T)	0	0.0002	0.0003

Table 5: Fitting parameters for profiles of 1/$T_{1/2}$ vs temperature, including results for 2M NaAc WG and as composed with noted metallic nanoparticles

4.3.2.1.2. Non-Metallic Nanoparticles

In order to further understand the relaxation mechanisms of the nanoparticle samples, non-metallic nanoparticles were investigated to provide a comparison with metallic

examples. Since some of the nominally pure metals may have become oxidized on exposure to the atmosphere, measuring the metal oxides also gives an indication to the level of oxidisation of the 'pure' metal sample.

Figure 38 shows the $T_{1/2}$ times of a series of metal oxide samples in a 2M NaAc WG solution over a range of temperatures covering ~20 mK to ~1.5 K. The oxide samples are generally non-conducting and should not have a free electron contribution to impact on the proton spin relaxation. Therefore, the overall relaxation rate should be smaller than the metallic counterparts. At temperatures above ~500 mK most of the oxide samples have $T_{1/2}$ values similar to that of the undoped NaAc sample. This suggests that the metal oxides have a negligible enhancement of the proton relaxation rate. As the zinc oxide, tin oxide, aluminium oxide and magnesium oxide samples were not effective, the number of measurements were not extended to lower temperatures, therefore, making it impossible to fit equation (28), however, the copper oxide samples measured at 2.45 T have been fitted with the fitting parameters shown in Table 6.

Copper oxide was the only effective metal oxide relaxation agent, it shows similar levels of relaxation enhancement, over the 20 mK to 2 K temperature range, as the pure copper nanoparticles. The unusually fast relaxation times associated with the copper oxide samples indicates that there is either a different relaxation mechanism in effect or that the copper nanoparticles are the same as the copper oxide particles, i.e. they have become oxidised. Either way, if the copper oxide relaxation follows a different mechanism than the metallic nanoparticles, it is probably related to the magnetic properties of the copper oxide nanoparticles. Further discussion and details on these properties can be found in Chapter 5.
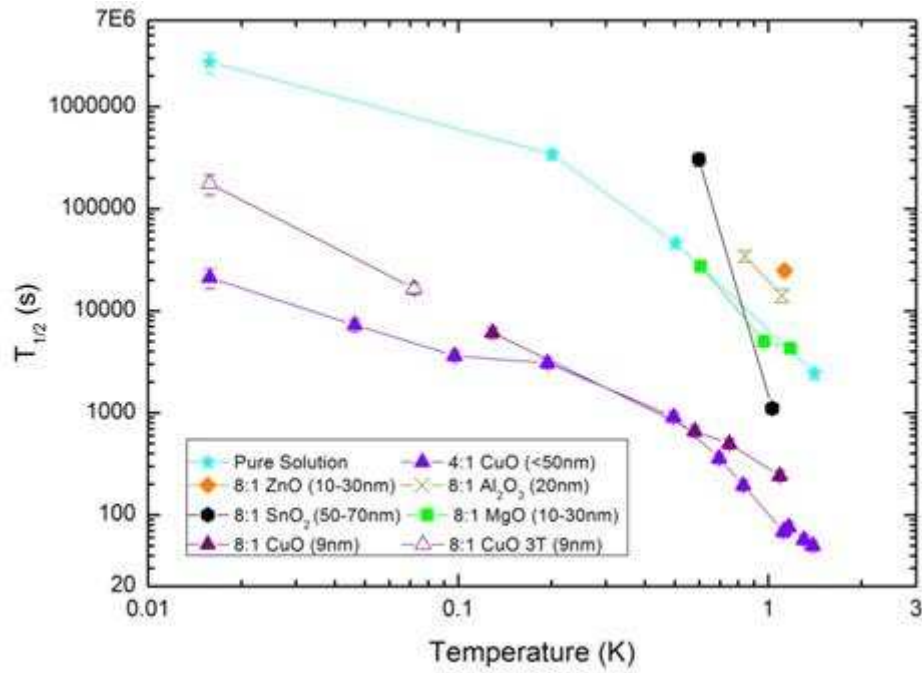
Figure 38: Proton $T_{1/2}$ of metal oxide nanoparticles as a function of temperature
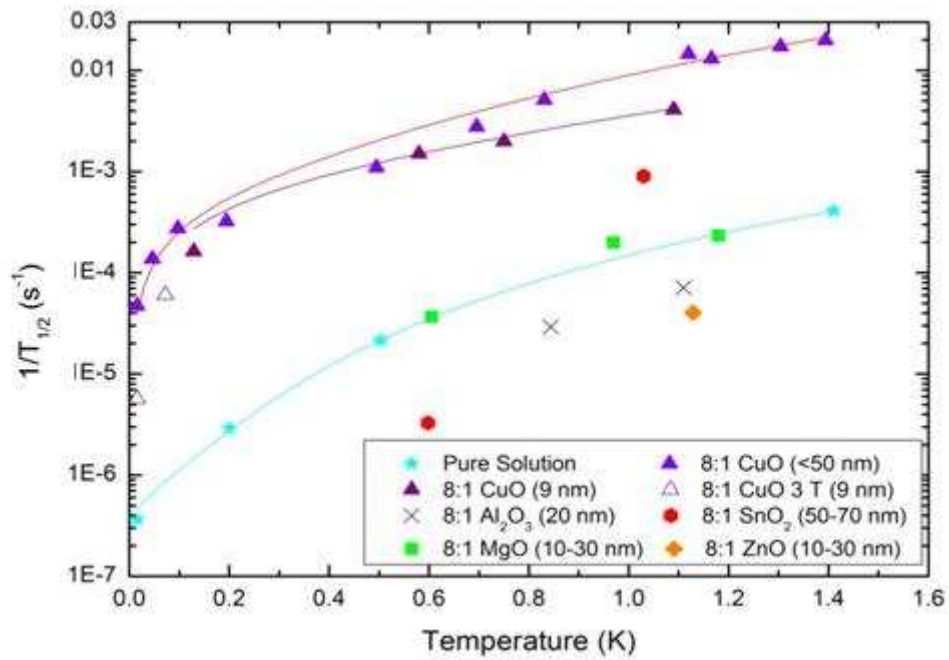
Figure 39: Proton $1/T_{1/2}$ for non-metallic nanoparticles at millikelvin temperatures

Sample	Intercept	Linear (electronic	Cubic

	(quantum component)	component)	component
2 M NaAc Solution	0.4×10^{-6}	6×10^{-6}	0.00014
Copper Oxide (9 nm)	0	0.0021	0.0015
Copper Oxide (<50 nm)	0	0.0025	0.0065

Table 6: Fitting parameters for non-metallic nanoparticles

4.3.2.1.3. Copper and Copper Oxide Measurements

As both copper and copper oxide showed large enhancements to the relaxation rate, further studies were conducted on these samples to attempt to optimise their enhancement. Thus, I measured the $T_{1/2}$ vs temperature for copper and copper oxide samples at different sizes and dilutions. Figure 40 shows results for a variety of samples, including particles from 9 to ~50 nm and dilutions from 8:1 to 30:1.

The results, as displayed in Figure 40, show that the copper samples have a shorter $T_{1/2}$ than the copper oxide samples. Among the copper samples, the relaxation rate of the protons as a function of temperature, for 40 nm copper is different to the 25 nm copper samples. The relaxation of the protons in the 40 nm copper seems more similar to the copper oxide samples, which might suggest that the 40 nm copper has oxidised. In the copper samples, the $T_{1/2}$ between the 25 and 40 nm particles differ by an order of magnitude for temperatures > 100 mK, which is a dramatic effect, but the origin of the difference is not clear and may depend on the purity, oxidation state and the morphology of the particles.

The copper oxides are less effective relaxants than the copper nanoparticles. The copper oxide samples seem to follows a power law of around 1.5 over the full temperature range tested in Figure 41, however, can still be fitted to equation (28). The higher dilution of 40 nm 30:1 copper oxide sample, compared to 50 nm 8:1 copper oxide sample, clearly shows the impact of the greater nanoparticle dilution, rendering them less effective as relaxation agents. In the 30:1 case, the protons are now, on average, in weaker contact with the copper oxide, hence the lessened relaxation enhancement. As with the copper samples, other parameters could be coming into effect, including particle size distributions, impurity levels and morphologies.
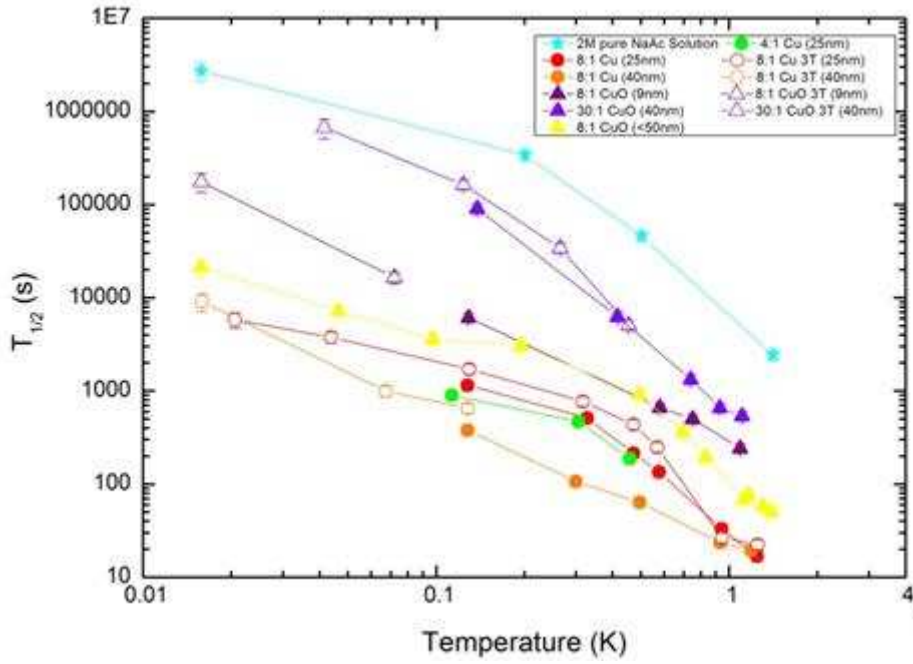
Figure 40: Proton $T_{1/2}$ of copper and copper oxide nanoparticle samples as a function of temperature
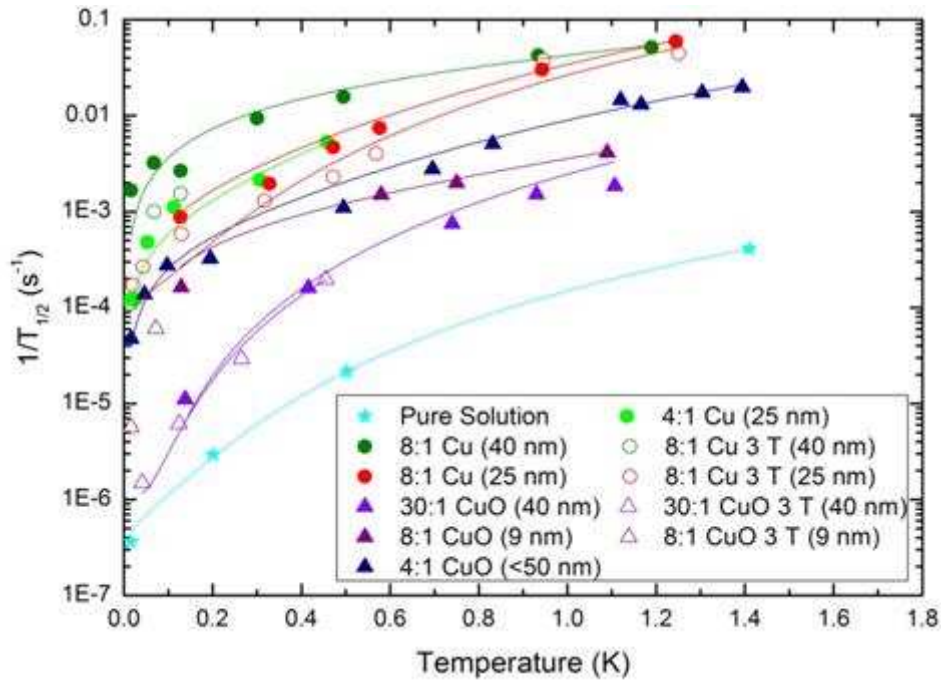
Figure 41: Proton $1/T_{1/2}$ for copper and copper oxide nanoparticles at millikelvin temperatures

Sample	Intercept (quantum component)	Linear (electronic component)	Cubic component
2 M NaAc Solution	0.4×10^{-6}	6×10^{-6}	0.00014

30:1 Copper Oxide (40 nm)	0	0.0025	0
30:1 Copper Oxide 3 T (40 nm)	1×10^{-6}	0	0.0021
8:1 Copper Oxide (9 nm)	0	0.0021	0.0015
4:1 Copper Oxide (<50 nm)	0	0.0028	0.0065
8:1 Copper (25 nm)	0	0.0072	0.0269
8:1 Copper 3 T (25 nm)	80×10^{-6}	0.0010	0.0254
8:1 Copper (40 nm)	0	0.0363	0.0063
4:1 Copper (25 nm)	30×10^{-6}	0.0052	0.0295
8:1 Copper Oxide 3 T (9 nm)	N/A	N/A	N/A
8:1 Copper 3 T (40 nm)	N/A	N/A	N/A

Table 7: Fitting parameters for copper and copper oxide samples

4.3.2.1.4. Copper Nanoparticles in Various Solvents

An important benefit of the brute force method is that it is a general method of achieving a hyperpolarised state, meaning it polarises all nuclei with a spin in a sample. To become a truly general method, it would be useful to have one relaxation agent that can decrease the $T_{1/2}$ times of all of the nuclei in a sample down to a practical time scale, when polarising in the millikelvin regime. As mentioned in Chapter 3, a polarisation time of 48 hours would be acceptable. The effectiveness of these nanoparticle relaxation agents will also be tested on other solvents in this section. This will give an idea as to other fields of research where the brute force method could be applied.

To avoid time consuming and costly measurements of $T_{1/2}$ times for each undoped solvent, only two undoped solvents, 2M NaAc WG and Pyr, will be used as reference points. It is then assumed that other undoped solvents would have similar $T_{1/2}$ times. As copper was the most effective relaxation agent for the 2M NaAc WG samples, it is selected to be the relaxation agent in these experiments. Figure 42 displays the results of the proton $T_{1/2}$ vs temperature of various solvents. The solvents include 2M NaPyr WG, 6M Dy-DTPA WG, 4M KAc WG, 4M NaAc WG, an ester phosphate and neat Pyr

Equation (28) was fitted to the data in Figure 43 and the values for the parameters can be found in Table 8. The fits suggest that the Pyr:copper and the ester phosphate:copper samples do not experience any electronic or quantum contributions, this could be due to a reaction between the solvents and the copper. The other samples all exhibit either an 'electronic' (i.e. linear) or quantum (i.e. intercept) contributions, which allows for shorter $T_{1/2}$ values at the lowest temperatures.

The first point to be made is that above 300 mK, the $T_{1/2}$ of the protons in the undoped NaAc and Pyr are very similar which helps justify the assumptions that all solvents, in the absence of relaxants, have similar $T_{1/2}$ times. This argument cannot be extended with certainty below 300 mK due to lacking pyruvate data, but the assumption seems reasonable given the close overlap of the 2 M NaAc WG and Pyr between 300 mK to 2 K.

Secondly, the Pyr:copper sample has a $T_{1/2}$ longer than the undoped NaAc sample at 80 mK, suggesting that copper is not effective on all solvents and is likely due to a chemical reaction, more details about the chemistry can be found in Section 5.10. The ester phosphate:copper also has a similarly long $T_{1/2}$ at 100 mK. The NaPyr:copper and all of the acetate:copper solutions have a much more reasonable $T_{1/2}$ times below 300 mK, with a 100 fold proton relaxation enhancement over the range of 20 mK to 2 K.
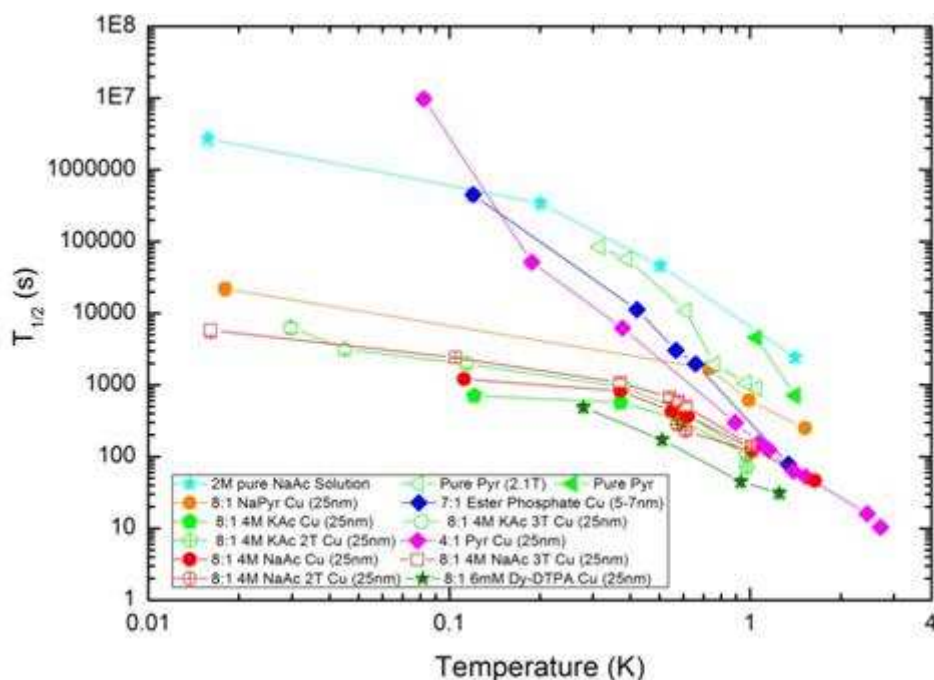
Figure 42: Proton $T_{1/2}$ for copper in various solutions as a function of temperature

~ 96 ~
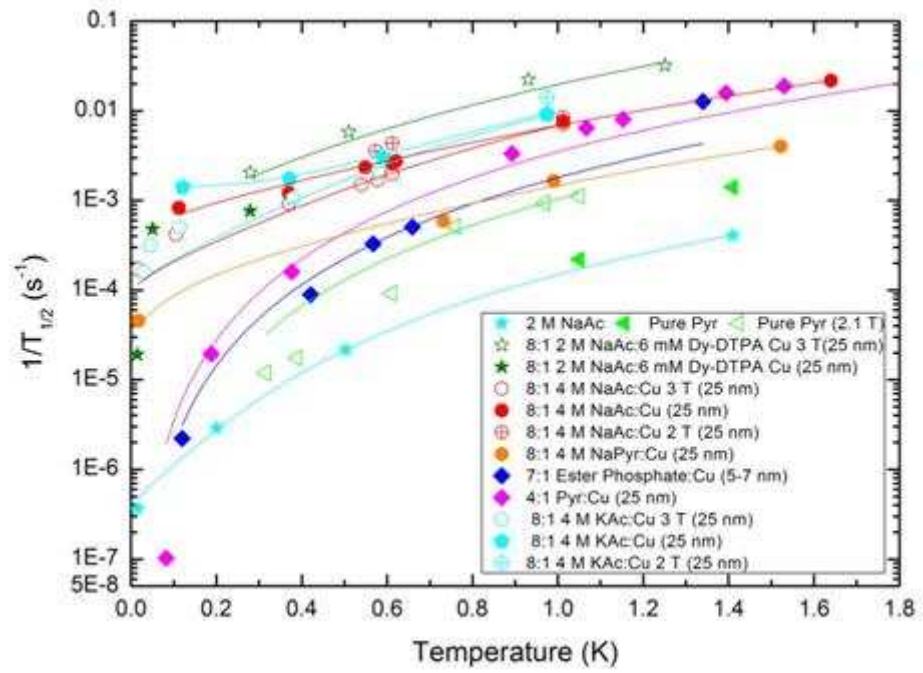
Figure 43: Proton 1/$T_{1/2}$ plot of copper in various solutions

Sample	Intercept (quantum component)	Linear (electronic component)	Cubic component
2 M NaAc Solution	0.4×10^{-6}	6×10^{-6}	0.00014
Pure Pyr 2.1 T	0	0	0.0010
8:1 2 M NaAc:6 mM Dy-DTPA Cu 3 T (25 nm)	0	0.0053	0.0014
8:1 4 M NaAc:Cu 3 T (25 nm)	0.0001	0.0010	0.0057
8:1 4 M NaAc:Cu (25 nm)	0.0004	0.0026	0.0039
8:1 4 M NaPyr:Cu (25 nm)	30×10^{-6}	0.0006	0.0009
7:1 Ester Phosphate:Cu (5-7 nm)	0	0	0.0018
4:1 Pyr:Cu (25 nm)	0	0	0.0011
8:1 4 M KAc:Cu 3 T (25 nm)	0.0001	0.0011	0.0083
8:1 4 M KAc:Cu (25 nm)	0.0014	0	0.0087
8:1 4 M KAc:Cu 2 T (25 nm)	N/A	N/A	N/A
Pure Pyr	N/A	N/A	N/A
8:1 2 M NaAc:6 mM Dy-DTPA Cu (25 nm)	N/A	N/A	N/A
8:1 4 M NaAc:Cu 2 T (25 nm)	N/A	N/A	N/A

Table 8: Fitting parameters for copper in various solutions

4.3.2.1.5. Copper Nanoparticles in Pyruvic Acid

Recent research has highlighted pyruvic acid as a useful metabolite for cancer detection in humans (3). With this in mind, it would be useful to be able polarise pyruvic acid in a timely manner, using the brute force method. However, the results from Figure 42, in which the neat Pyr were admixed with nanoparticles, were not promising. Therefore, by diluting the Pyr with water it was thought that the water could act as a pathway to pass polarisation to the ^{13}C through thermal mixing. This idea was based on the results from Figure 42, the samples containing WG relax much faster than the other samples. Figure 44 shows that adding water to the Pyr is not an effective method of gaining proton polarisation, i.e. the $T_{1/2}$ of protons in the Pyr:copper samples and the Pyr:water:copper samples are similar. Instead, results were much better when sodium pyruvate is diluted in water as a solvent instead of neat pyruvic acid. This improvement is probably because the sodium pyruvate is not reacting with the copper.
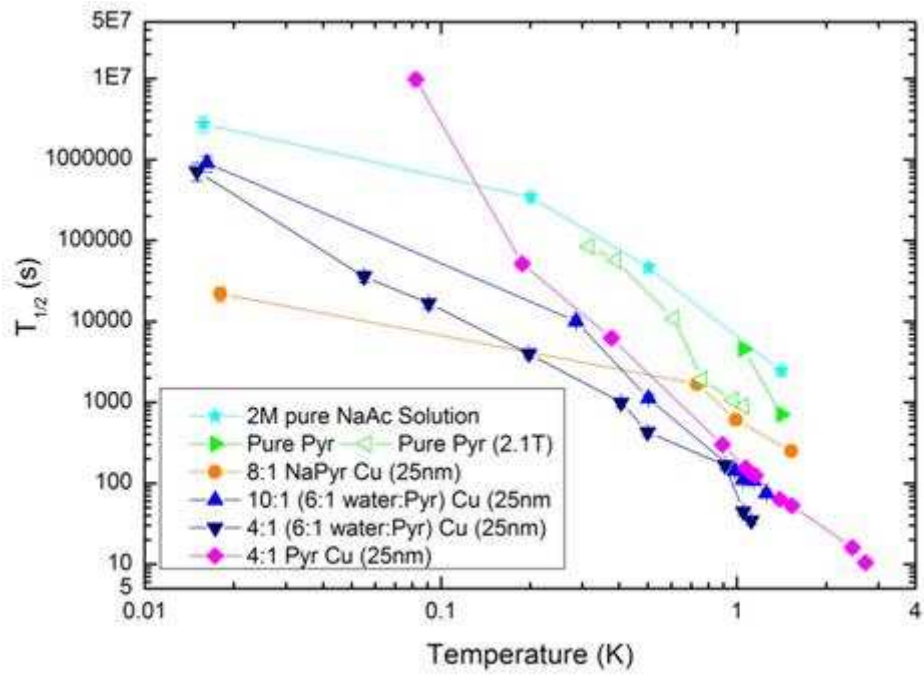
Figure 44: Proton $T_{1/2}$ vs temperature Pyr samples
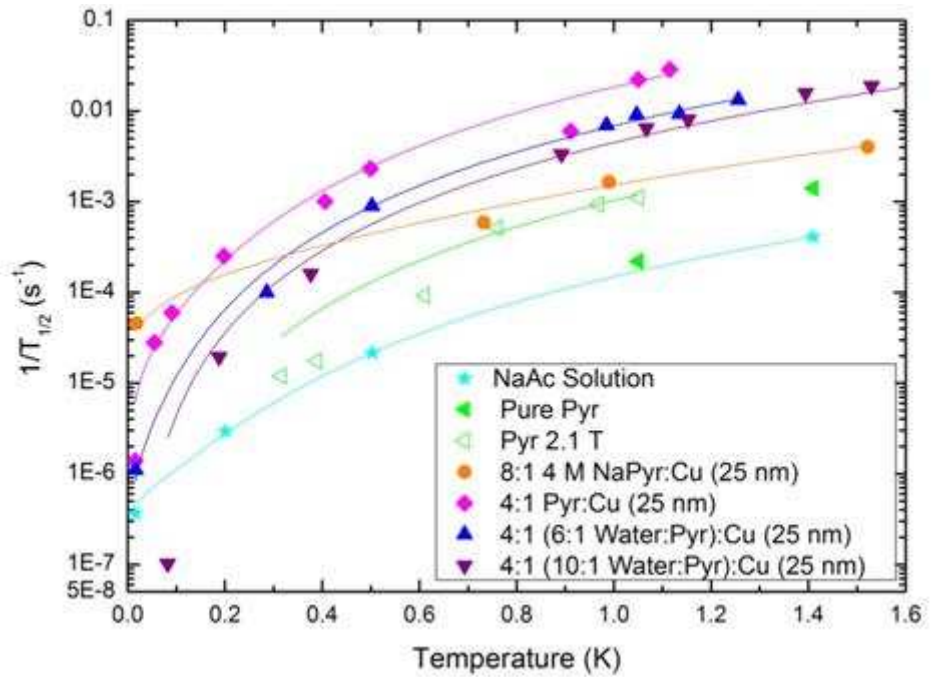
Figure 45: Proton $1/T_{1/2}$ for copper in various Pyr samples

~ 99 ~

Sample	Intercept (quantum component)	Linear (electronic component)	Cubic component
2 M NaAc Solution	0.4×10^{-6}	6×10^{-6}	0.00014
Pure Pyr 2.1 T	0	0	0.0010
8:1 4 M NaPyr:Cu (25 nm)	30×10^{-6}	0.0006	0.0009
4:1 Pyr:Cu (25 nm)	0	0	0.0011
4:1 (6:1 Water:Pyr):Cu (25 nm)	0	50×10^{-6}	0.0068
4:1 (10:1 Water:Pyr):Cu (25 nm)	0	0	0.0045
Pure Pyr	N/A	N/A	N/A

Table 9: Fitting parameters for copper in various Pyr samples

Table 9 shows that the pure Pyr and the Pyr:water samples seem to be dominated by the cubic contribution through the entire temperature range. The addition of water to the Pyr introduces an offset that uniformly lowers the $T_{1/2}$ profile. NaPyr, dissolved in water, is a better solvent than neat Pyr. For example, as at 20 mK the $T_{1/2}$ time of the protons is of the same order as the WG:copper samples from earlier experiments.

The $T_{1/2}$ times measured in the Pyr samples may be larger than the actual $T_{1/2}$ time. This is due to the lineshape of the spectra broadening as the sample was cooled. This broadening effect is not taken into account when calculating the equilibrium point, therefore the expected equilibrium is an overestimate.

It should be noted that the lineshape of the Pyr:copper samples gets broader as the temperature decreases. This is probably due to the increased magnetism of the nanoparticles, which, in turn, increases the proton linewidth via a larger variation in the local field, B_{loc}, experienced by the protons. This hypothesis was investigated and supported in Chapter 5. Figure 100 shows the extent of the magnetisation of a Pyr:copper sample compared to water:copper sample. The magnetisation enhancement is in the order of 1000.
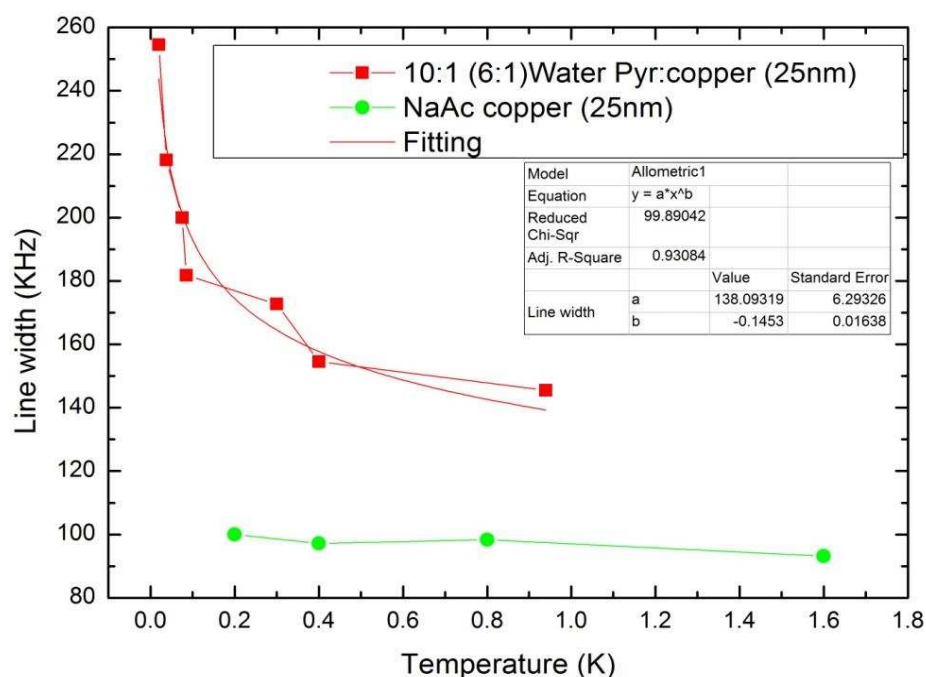
Figure 46: Line width of an Pyr:copper sample and a NaAc:copper sample as a function of temperature

Figure 46 demonstrates how the line width of the Pyr:copper samples increase as the temperature decreases. Figure 47 shows the lineshape broadening of a different Pyr:copper sample at 20 mK and 1.1 K.
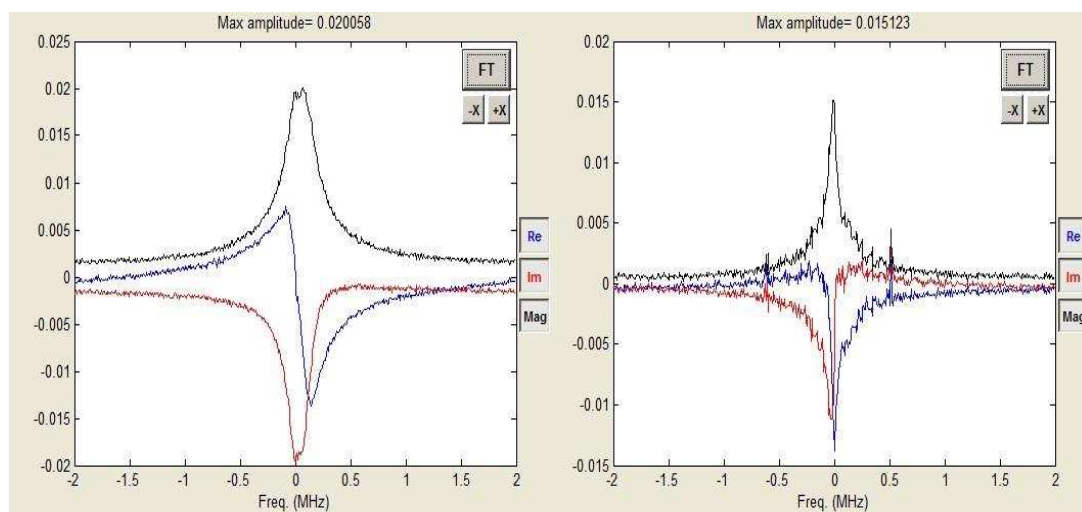
Figure 47: Spectra of the effect of line broadening in Pyr copper samples. On the left is at 20 mK while on the right is at 1.1 K

~ 101 ~

4.3.2.1.6. Polarisation Levels Achievable for Various Temperatures and Fields

The $T_{1/2}$ of a 8:1 4M NaAc WG:copper sample was measured over a range of fields and temperatures, in order to determine favourable conditions to achieve high proton polarisation in a fixed amount of time. Figure 48 shows that at the $T_{1/2}$ times increase roughly in proportion to the absolute achievable polarisation. If the absolute achievable equilibrium polarisation is between 1-10 %, the $T_{1/2}$ is dependence is less than linear. The $T_{1/2}$ time is also more dependent on B_0 than temperature. The stronger B_0 dependence can be seen when comparing the 2 T points with the 3.2 T points on Figure 48. The 2 T points have a shorter $T_{1/2}$ value than the 3.2 T, at the equivalent absolute equilibrium polarisation. This suggests that the polarisation conditions should be set such that the $B/T \sim 100$, with a bias towards lower temperatures and fields. This can be seen more clearly in Figure 49. Higher polarisation can be achieved with a larger B/T ratio, but at the expense of a disproportionate amount of time.
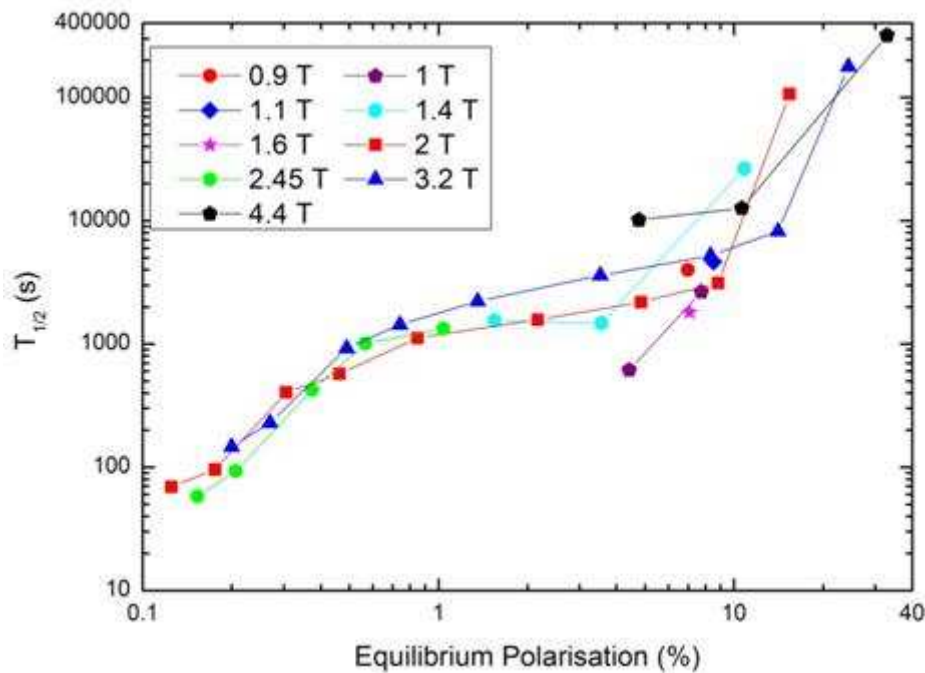
Figure 48: The proton $T_{1/2}$ time is shown with respect to the calculated equilibrium polarisation, proportional to B/T. To achieve the maximal amount of polarisation per unit time, the B/T values corresponding to a maximal polarisation of around 10 % are appropriate.
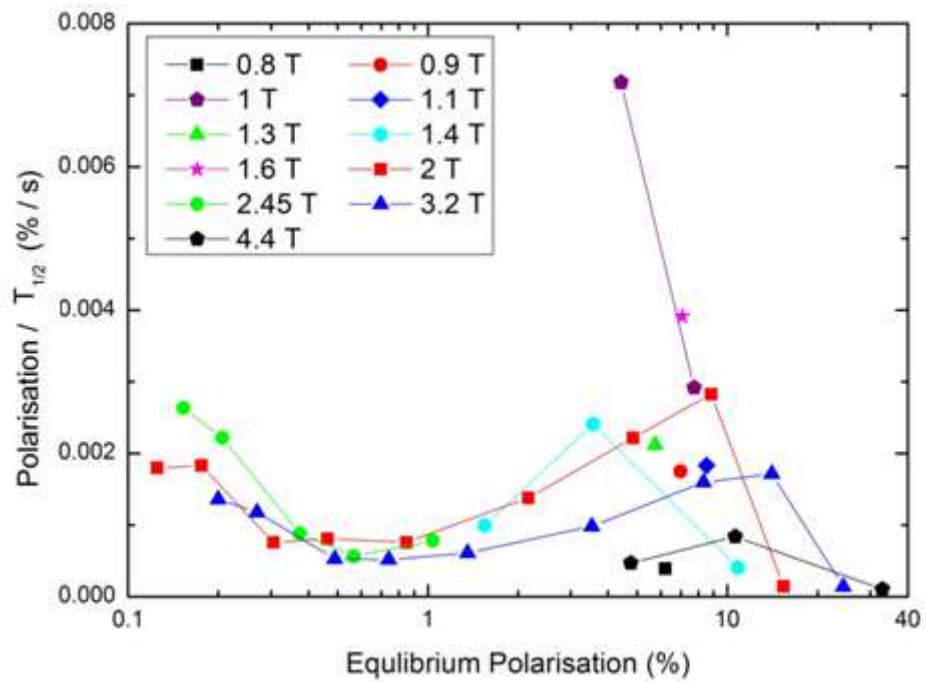
Figure 49: This graph shows the build-up of polarisation per unit time against the equilibrium polarisation. At 0.1 % equilibrium polarisation the build-up time is short as is the build-up time with an equilibrium polarisation between 5-10 %.

Figure 50 shows the B_0 field dependence of $T_{1/2}$ for the 8:1 4M NaAc WG:copper sample at various temperatures. A simple power law has been fitted to the data to produce Figure 50. However, it only seems to be an accurate representation at the higher temperatures.

~ 103 ~
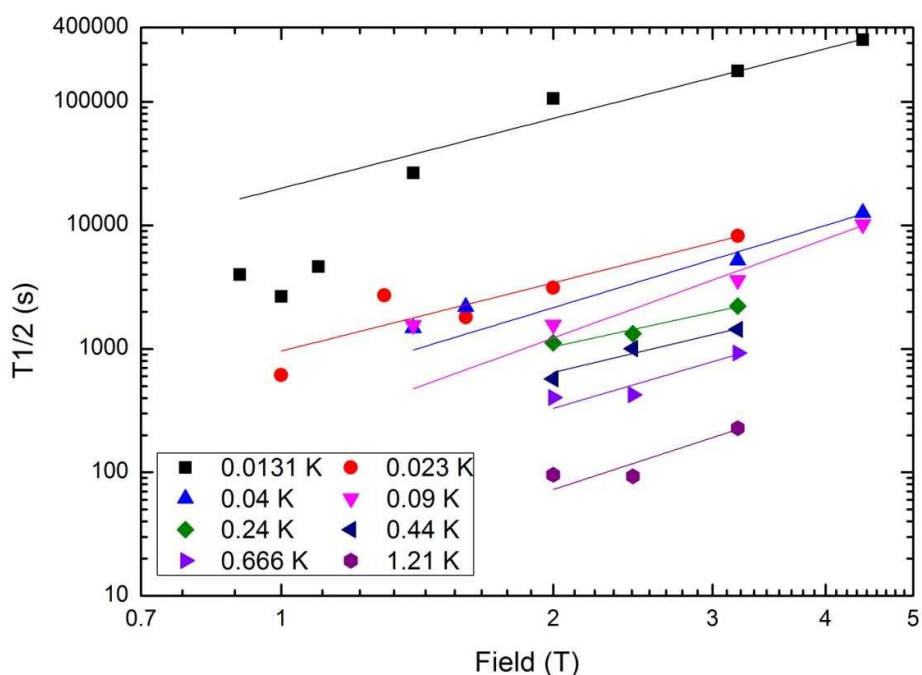
Figure 50: The Proton $T_{1/2}$ as a function of field at different temperatures

Temperature (K)	Coefficient	Power
0.0131	20000	1.88
0.023	959	1.84
0.04	465	2.21
0.09	194	2.66
0.24	345	1.59
0.44	1190	1.74
0.666	74	2.14
1.21	13	2.39

Table 10: Fitting parameters used in fitting data sets of Figure 50

4.3.2.2. High Temperature Relaxation

The T_1 values at the higher temperatures (4 to 300 K) provide a sense of whether the polarisation of the sample would survive the dissolution process. At higher temperatures, the T_1 values can easily be obtained using a standard saturation recovery experiment in the field cycling magnet apparatus used in Chapter 3. A schematic of the saturation recovery experiment can be found in Figure 12. In the higher temperature regime it is beneficial to

have long T_1 values as it will allow for polarisation to be maintained during the dissolution process. This section will be subdivided into five sections:-

1. Metallic Nanoparticles
2. Metallic Oxide Nanoparticles
3. Particle Size
4. Nanoparticle Dilution
5. Annealed Pyr Samples

4.3.2.2.1. Metallic Nanoparticles

Figure 51 contains T_1 data for the metallic nanoparticles at a higher temperature range, with a polarisation field of 2 T. This field is similar to the fields used for the studies at millikelvin in the dilution fridge. It also matches the field used by Hirsch, et al to hold samples for dissolution after ejecting it in the frozen state from a brute force polariser (76). Thus, understanding relaxation at 2 T is relevant.

The proton T_1 values induced by platinum, aluminium, silver and graphene reach their T_1 minima near 50 K, whereby the T_1 times become very short and therefore should be avoided, i.e. pass through it quickly. The proton T_1 from samples doped with platinum, aluminium and graphene follows the linear dependence of the electronic contribution below 40 K. Above that, other mechanisms start to dominate, such as solvent vibrations.

The copper sample, on the other hand, has a relatively small effect on the relaxation rate at these higher temperatures and is comparable to pure NaAc sample. The proton T_1 for the copper sample stays above 10 s, until ~250 K, where the T_1 rapidly drops. During dissolution this would not be an issue, as the copper relaxant is readily filterable. This suggests that the copper nanoparticles have great promise as relaxation agent. This is in addition to the already excellent results from copper nanoparticles in the millikelvin regime shown in Figure 37.
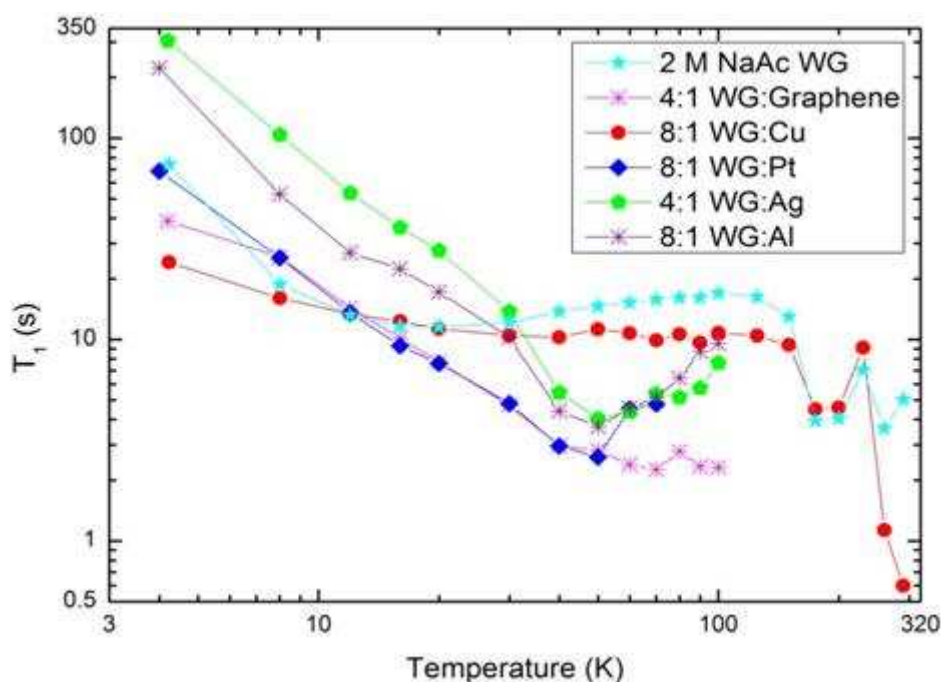
Figure 51: Proton $T_{1/2}$ for metallic/metallic like nuclei at the high temperatures

Finally, there may be options to tune the copper nanoparticles to further enhance their proton relaxation. These options include changing the particle size, shape and adding capping agents. The present attempt at optimising the particle size of copper and copper oxide in the millikelvin regime, as seen in Figure 40, was somewhat inconclusive. This is mainly due to the experiments being very time consuming at millikelvin temperatures. At the higher temperatures the experimental times become shorter, allowing for faster data acquisition. This allows for a more conclusive evaluation than was practical from the first study.

4.3.2.2.2. Particle Size

The relationship between the size of the particle and T_1 is still unknown as the variation in the particle size, presented in Figure 40, only covered a small range. To cover a larger particle size range, micron-sized copper and aluminium were tested in the higher temperature range. These larger particles are expected to be less effective than their nanoparticle counterpart because the larger particles have a smaller surface/volume ratio. This means that the average contact, by weight, between the metal and the target nuclei is weaker overall because the average distance between the target nuclei and the

nanoparticles is larger. It is also noted that larger particles do not appear to show the same magnetic behaviour as the nanoparticles and this could also affect how the particles interact with the solution. The dependence of the magnetic properties with respect to the particle size is discussed in detail in Section 5.5.2.
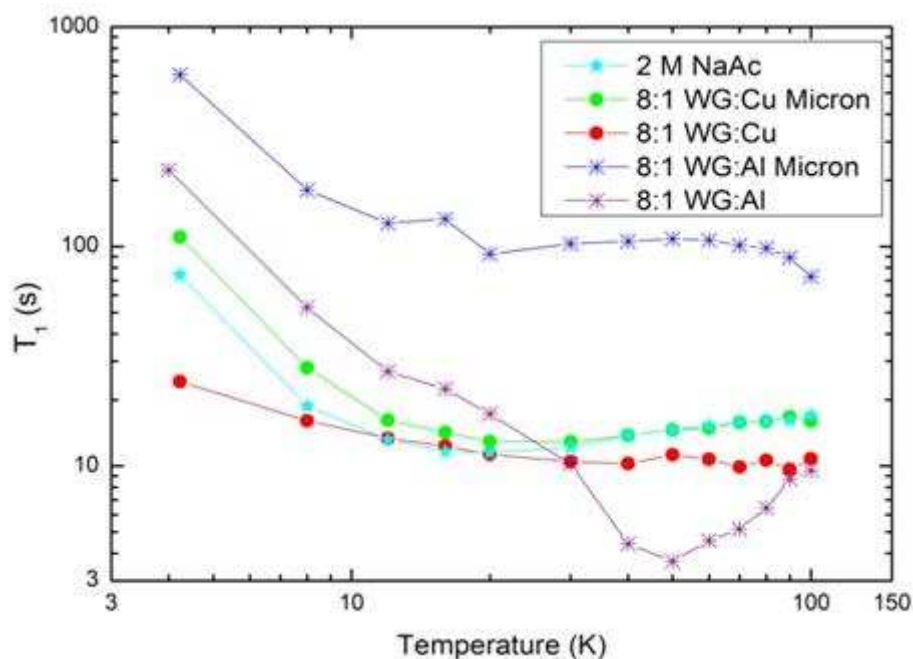
Figure 52: Proton relaxation at temperatures between 4-100 K. Two sizes of copper and aluminium are used as relaxants.

As expected, the micron-sized copper is an ineffective relaxant, this can be deduced as the relaxation curve follows that of the undoped sample, as seen in Figure 52. Below 30 K the nano aluminium inhibits the T_1 relaxation rate of the protons in the solution, while between 30-100 K, the T_1 time is shorter than the 2M NaAc WG solution. The micron-sized aluminium sample does not behave like the undoped sample, which was the expectation, but actually it increases the T_1 of the protons in the sample. The increased T_1 time could, however, be useful in maintaining the polarisation of the sample to the higher temperature range, provided that the sample can become polarised to begin with.

4.3.2.2.3. Nanoparticles Dilution

The nanoparticle dilution is important in sample optimisation. The less nanoparticles added to the sample the more nuclei of interest will be in your sample, therefore, increasing

the absolute signal, if the sample at its equilibrium. However, with fewer nanoparticles added to the sample, the T_1 time of the sample will be longer. Thus, there is a trade-off for having many nanoparticles in the sample: a reduced T_1 time at the expense of diluting the source of the signal.

It is expected that increasing the dilution of the copper increases the T_1 time of the protons. This is simply due to a weaker contact between the copper and the protons. This logic seems to hold true, except for the 50:1 sample, which has a longer than expected T_1 at all temperatures. The explanation for long T_1 of the 50:1 sample is that the sample is not homogenously mixed, therefore, the sample was not at the expected solvent:nanoparticle ratio. It would seem that a sample with a ratio of around 10:1 WG:copper is the best selection from the range tested in Figure 53. This is determined because the T_1 time of the 8:1 sample is similar to the 2:1 sample but with a factor of 4 more protons available to become polarised.
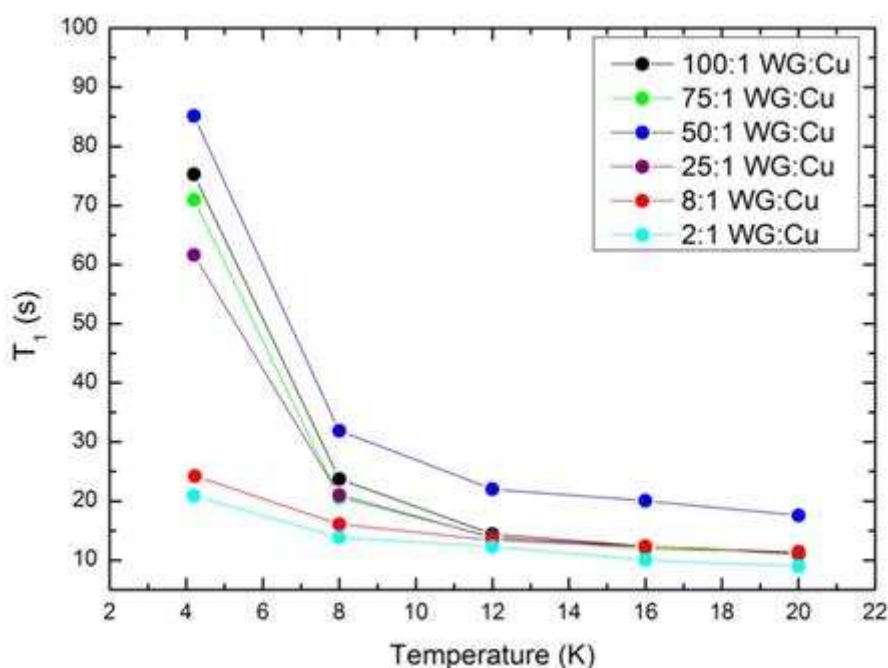
Figure 53: Proton T_1 as a function of copper dilutions at high temperatures

It would be useful to also test how the concentration of the aluminium nanoparticles affects the T_1 times. Samples which contain aluminium have a longer T_1 time, at a given temperature, than the undoped 2 M NaAc WG solution. It would be expected that as the aluminium is diluted the T_1 times become more similar to the undoped sample. Figure 54

shows the proton T_1 does indeed become more like the undoped sample as the aluminium nanoparticles are being diluted.
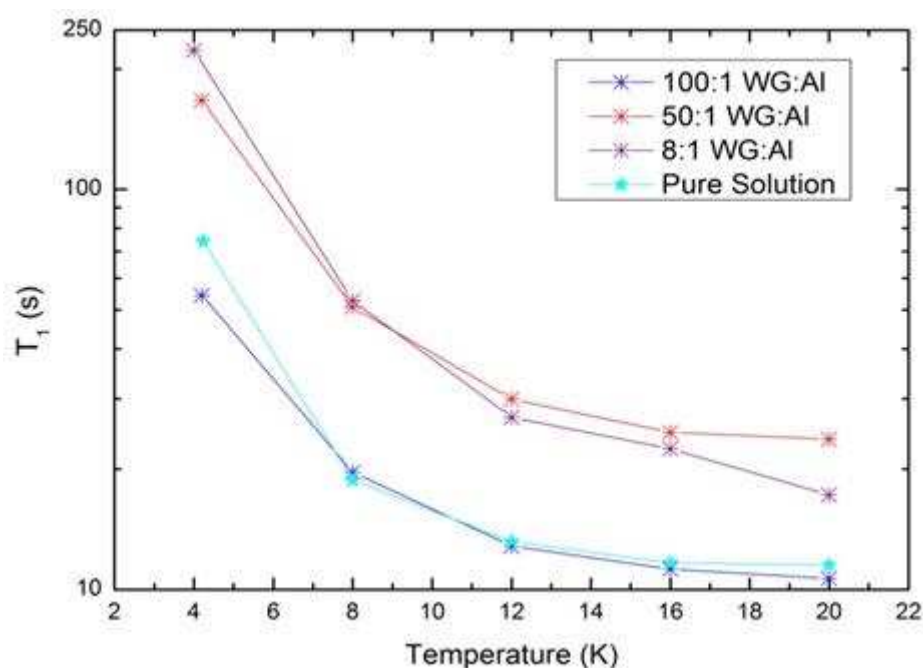
Figure 54: Proton T_1 as a function of aluminium dilution at high temperatures

4.3.2.2.4. Metallic Oxide Nanoparticles

With the exception of the copper oxide, all the other metallic oxides in Figure 55 follow a similar T_1 curve to the undoped sample. The zinc oxide and magnesium oxide samples have a proton T_1 of a factor of two longer than the undoped sample.

As the 2 M NaAc WG:copper oxide sample was effective in the millikelvin temperature regime, the proton T_1 of the copper oxide sample has also been measured at the higher temperatures. This was to gauge if the copper oxide would be a better relaxation agent than the pure copper over the full temperature range. The copper oxide has a shorter T_1 than copper between 4-100 K and would therefore lose more polarisation than copper during dissolution. These higher temperature measurements also provide evidence that the copper used in this chapter has not been oxidised.
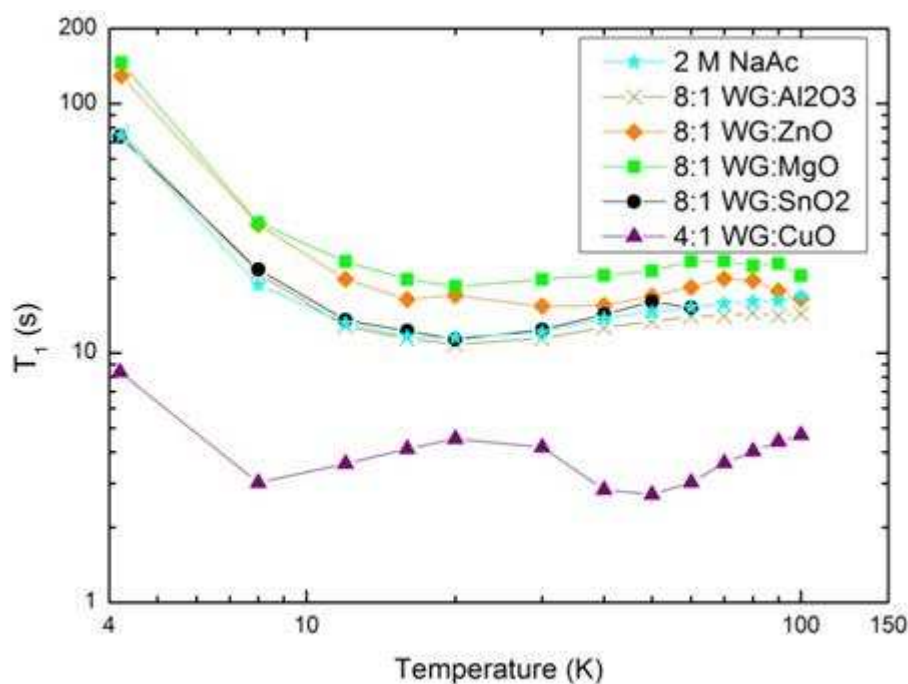
Figure 55: Proton T_1 at high temperatures with metal oxides additives

4.3.2.2.5. Annealed Pyr Samples

The sample preparation is another important consideration when studying low temperature NMR, as the samples change phases during cooling. In all of the experiments thus far, the samples were quench cooled meaning they were cooled very rapidly, therefore, locking any disorder into the sample. The disorder in the sample means it has an amorphous property. Heating the sample to near the phase transition temperature allows for this disorder to be removed and is known as annealing.

Annealing a sample can increase the T_1 times of samples as the sample becomes more crystalline. Annealing the sample could be another parameter that can be used to tune the T_1 values of the sample for the use in different applications.

With the WG samples, the final product will be disordered as the mixture is glassy. Other solvents can form crystals, for example, Pyr (53). The focus so far has been to shorten the T_1 of the sample, so that the sample can be produced on site. Quench cooling has allowed for these shorter T_1 times. If a sample with a long T_1, at more moderate temperatures (4-77 K),

could be produced, it opens up the possibility of transporting polarised samples from a central location to the sites where it can be used.

The proton $T_{1/2}$ time for pure degassed Pyr was measured in the field cycling magnet at 0.5 T. It should be noted that the $T_{1/2}$ time is used rather than T_1; this is because the semi-annealed sample shows bi-exponential behaviour, while the non-annealed sample is mono-exponential and using the $T_{1/2}$ time is a convenient way to compare the samples.

Figure 56 shows that annealing the Pyr sample for several hours at 250 K, increases the $T_{1/2}$ time by a factor of 10, which demonstrates the potential impact of annealing a sample compared to quench cooling the sample. It is not known if the sample was fully or partially annealed upon measurement as the transition temperature of the sample is not well known.
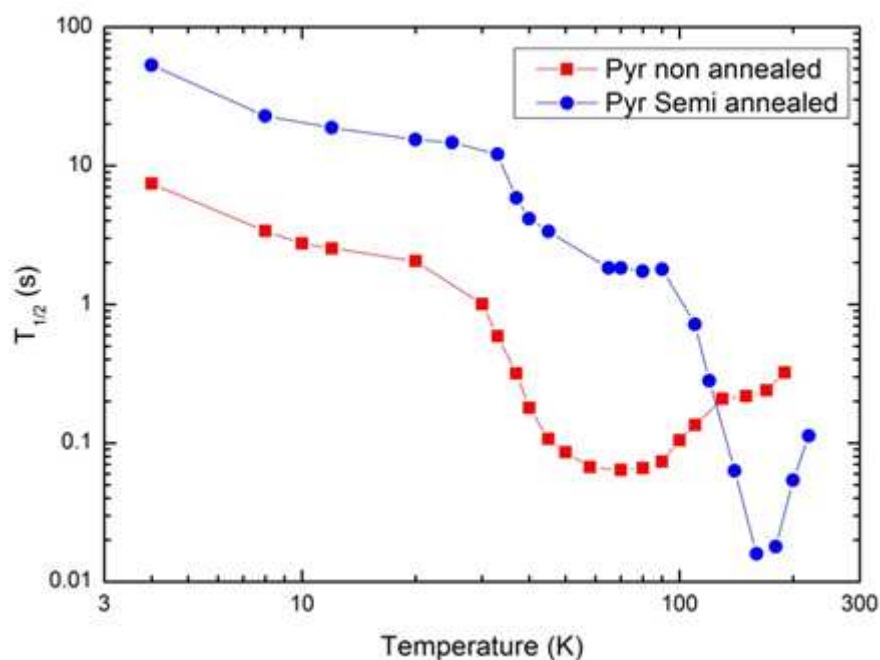
Figure 56: Proton T_1 dependence as the Pyr sample is annealed

4.3.3. *Discussion*

4.3.3.1. Addition of Nanoparticles

The addition of metallic nanoparticles to solutions does enhance the relaxation rate of nuclei in a sample at temperatures ranging from 20 mK to 2 K. Copper oxide nanoparticles

have also been shown to be an effective relaxation agent, while other metal oxide nanoparticles are ineffective. The majority of samples seem to three relaxation components; these are a quantum contribution that is uniform with temperature, an electronic contribution that has a linear dependence with temperature and a cubic contribution of unknown origins. These different temperature dependences are accounted for in equation (28). With this model, it is assumed that the electron contribution will only take effect if the nanoparticles have conduction electrons. However, the copper oxide, which does not have conduction electrons, is only well fitted when including an electronic component. Therefore, copper oxide must provide another relaxation mechanism, with a linear dependence on temperature. It cannot be ruled out that the other nanoparticles, including metallic nanoparticles, may also share this alternative relaxation mechanism. It is known that nanoparticles can have very unusual magnetic properties and this may be the cause of the relaxation enhancement (15,16). This will be further studied in Chapter 5, which is solely dedicated to the magnetic properties of the nanoparticles.

In some cases the addition of nanoparticles actually lengthened the T_1 of the protons. The cause for the lengthened T_1 is unknown, but it could be useful for maintaining polarisation, if the samples are transported over longer distances. For example, the micron-sized aluminium nanoparticles, characterised in Figure 52, caused the proton T_1 time to be around 10 times longer than the undoped 2 M NaAc WG solution. Similarly, but to a lesser extent, Figure 55 shows that magnesium oxide and zinc oxide increased the T_1 of protons by a factor of 2.

4.3.3.2. Temperature and Field Dependence

Generally, samples which contain nanoparticles exhibit the same temperature vs T_1 profile as the equivalent undoped sample, between 10 mK and 1 K. The exceptions are platinum, copper oxide and, to a lesser extent, aluminium, each of which has a more linear temperature dependence over this range. Many samples show a T_1 minima near 50 K, but with different values for the minimum T_1.

As most of the samples reach a T_1 minimum at around 50 K, during dissolution this temperature should be passed through quickly to minimise the loss of polarisation. It is

important to remember that the polarisation of the sample, as it is measured in the scanner, is the most important value, not the maximum polarisation of a sample while it is still trapped in the polariser.

The 2 M NaAc WG:copper is the best relaxation switch, as it has a short proton $T_{1/2}$ at 10 mK and follows the T_1 curve that of an undoped sample between 4-300 K. This means that a NaAc:copper sample can be polarised in a practical timescale in the millikelvin temperature range and the polarisation can be maintained during dissolution and transport to the scanner.

Choosing the most effective polarisation conditions is the next focus. Figure 48 shows how the proton $T_{1/2}$ time changes as a function of polarisation. The remarkable point is that the $T_{1/2}$ has very similar temperature and field dependences below 2 K and fields between 0.9-4.4 T. From Figure 49 it can be seen that the protons polarise fastest when $B/T \sim 100$, this equated to an achievable polarisation of around 10 %. From the combinations of fields and temperatures measured, there is a slight benefit of using lower temperatures and fields when producing polarising conditions with a $B/T \sim 100$.

4.3.3.3. Solvents

The T_1 of a nucleus is not only dependant on the physical conditions of the experiment, the field and temperature; it also depends on the chemical environment. If the nucleus is in a different molecule, the chemical environment will change and therefore the T_1 can vary. The experiments in this work revolve around small organic molecules, the main three being NaAc, NaPyr and Pyr, whose molecules are similar in size, but have different chemical properties.

[1-^{13}C] Sodium acetate   [1-^{13}C] Pyruvic acid   [1-^{13}C] Sodium pyruvate
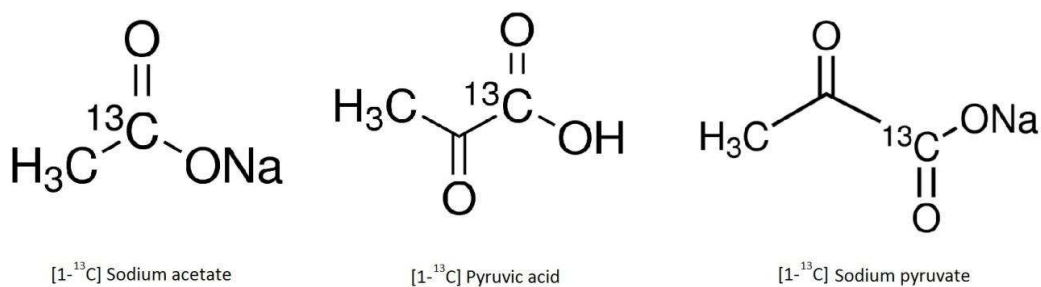
Figure 57: Chemical structure of NaAc, NaPyr and Pyr

The copper nanoparticles, when mixed with the Pyr and NaPyr, had longer proton $T_{1/2}$'s than the NaAc, as seen in Figure 42. As the $T_{1/2}$ times are longer in these samples, it may be beneficial to use other nanoparticles when considering these solvents. The longer $T_{1/2}$ is believed to be due to a chemical reaction between the copper and Pyr. An alternative relaxation agent for these solvents would be platinum, as that was effective at relaxing protons in NaAc, as seen in Figure 36 and should be inert.

4.3.3.4. Particle Dilution

As the nanoparticles become more diluted it would be expected that the T_1 enhancement will diminish, as the average distance between the nanoparticle and the target nuclei increases. The average distance, d, between nanoparticle and target nuclei follows a simple relationship with the number density, n, of the nanoparticles based on geometric arguments.

$$d \propto n^3 \tag{34}$$

From Figure 53 it can be seen that as the copper nanoparticles are diluted the relaxation enhancement also decreases. The 50:1 NaAc:Cu is an exception and it is believed to be due to an anomaly with the homogeneity of sample. In Figure 53 the T_1 times are inversely proportional to d within error. This would suggest that the copper has a short range interaction and that the dilution of the nanoparticles is of importance.

4.3.3.5. Particle Size

For nanoscale particles, particular particle sizes, ranging from ~10-100 nm, are often not well determined as the particles tend to aggregate. Furthermore, no size measurements have been conducted to independently confirm the size and morphology of the nanoparticles under review in this research. As mentioned in Section 4.1.5. nanoparticle sizes quoted here are provided by the manufacturer. As many manufacturers give a wide size distribution, I have chosen to investigate the impact of particle size in a more well-defined comparison i.e. between particles on the nano and micron-size scales.

Figure 52 showed data revealing that the larger particles are less effective relaxation agents than smaller particles. This may be due to the fact that larger particles will yield regions of the sample which are in poor contact with the relaxant. As the particle size increases, their spacing also increases. The dilution experiments in Section 4.3.2.2.3. suggest the nanoparticles only have a short range interaction. Thus, it is reasonable to assume a model where the protons in the large inter-particle spaces will experience little to no relaxation enhancement. Figure 58 schematically shows the effect of increasing the particle size while maintaining the same relaxant:solvent mass ratio. In the case of micron aluminium, it is expected that the larger particles would mean that the T_1 of the sample becomes more like an undoped sample. This is not observed, but instead the T_1 times increase, the reason for why this is the case is not known.
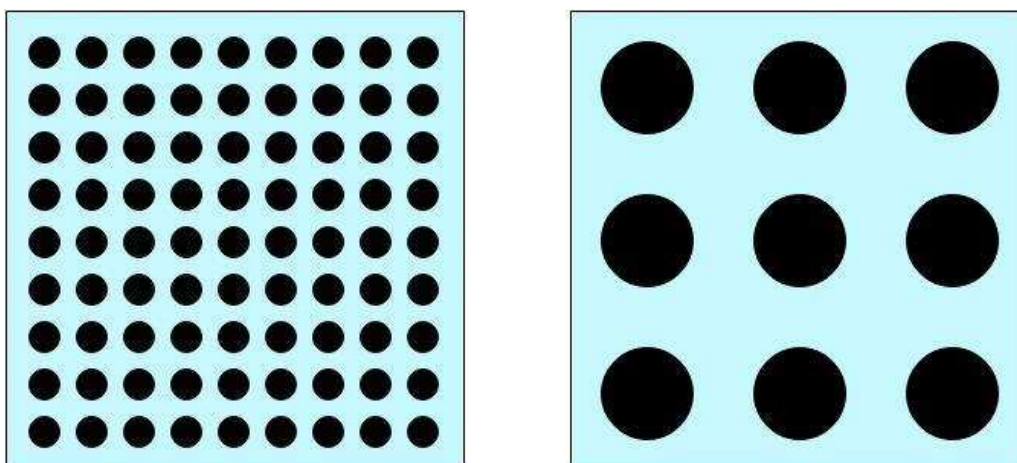
Figure 58: Diagram showing the decrease in average distance between particles against particle size. This assumes the two samples have the equivalent mass percentage of nanoparticles.

4.3.3.6. Annealing the Sample

An area of sample preparation, which is easy to overlook, is the cooling of the sample. Rapid cooling of the sample, known as quench cooling, allows disorder to be frozen into the sample, therefore, the structure of the final sample is different from that of an annealed sample. The annealed sample is made by leaving the sample near its melting point, so there is enough molecular motion available for the system to become re-organised into its positional minimum potential energy. Figure 56 shows the effect on the T_1 times of protons

in an annealed and non-annealed Pyr sample. Annealing the sample increases the proton T_1 time at the lower temperatures. This could be useful if samples were to be transported from a central location to the site where they would be used. However, in the case that the samples were polarised on site, having a non-annealed sample is preferable, as the T_1 is shorter. The sample preparation should be carefully considered and depends on where the samples will be polarised.

4.4. *Carbon T_1 with Nanoparticle Additives*

This research is primarily aimed at achieving high levels of ^{13}C polarisation for, but not limited to, in vivo applications. The drawback of the brute force method is that the T_1 times become very long; therefore, the polarisation time becomes impractical. The key advantage of the brute force method is that it is easy to increase production.

In the previous chapter it was shown that thermal mixing is an effective way of transferring polarisation between protons and other nuclei in the system. To see the benefit of the thermal mixing it is necessary to determine the T_1 of ^{13}C without thermal mixing. The measured temperature dependence of the ^{13}C $T_{1/2}$ was surprisingly weak in the millikelvin regime. This discovery implies that it is important to polarise at the lowest possible temperature because the equilibrium magnetisation has a stronger dependence on temperature than the $T_{1/2}$ time. There is a technological limit to the lowest achievable temperature in a dilution fridge of around 2 mK, but this is still a factor of ~7 colder than the fridge used for these experiments and could therefore increase the final ^{13}C polarisation yielded.

4.4.1. *Methods*

The T_1 and $T_{1/2}$ times in this section will be using the same methods used in Chapter 3 and are described in Section 3.3.2.1. As this section is focused on ^{13}C, the B_0 for these experiments will be 9.74 T, to account for the difference in γ between protons and ^{13}C, as the probe is resonant at a fixed frequency (104.5 MHz). It should also be noted that the

effects of radiation damping is quite weak when considering ^{13}C as it is much less sensitive than protons and has a much smaller number density.

4.4.2. *Results*

Figure 59 shows the recovery curve of the ^{13}C in 8:1 2 M NaAc 1 M NaPh WG:copper, which has been normalised to an expected infinity value for each temperature. The B_0 for these experiments is 9.74 T. The interesting point which can be made is that the normalised 391 mK, 121 mK and 19 mK recovery curves roughly overlap one another, meaning that they must have very similar $T_{1/2}$ times; however, the maximum polarisation of the sample at 391 mK and 19 mK differs by a factor of 20. This would mean at 20 mK the relaxation is dominated by a quantum component, as described in equation (28). It would also imply that decreasing the temperature would yield a higher ^{13}C polarisation with the same polarisation time.
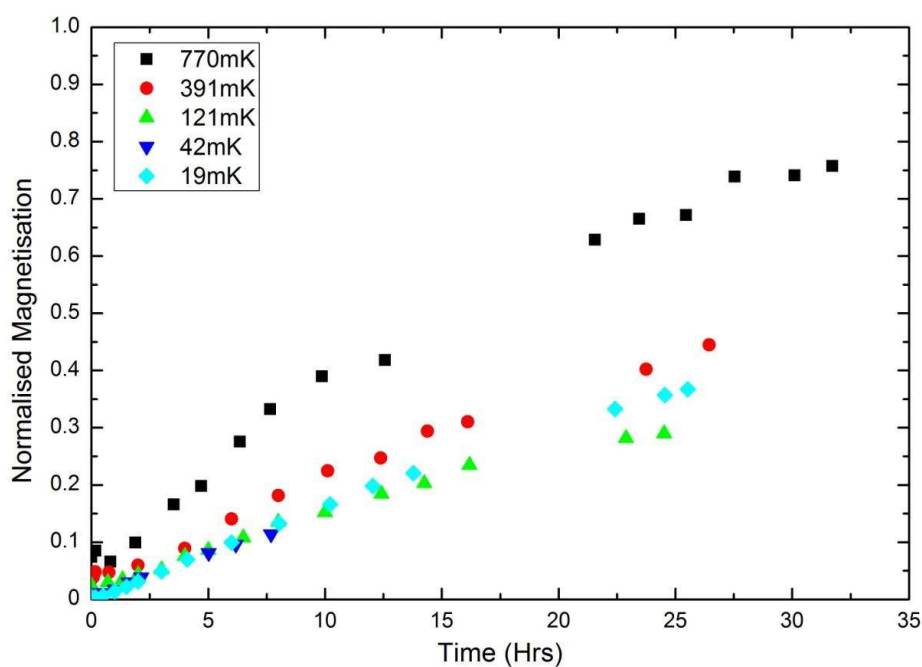
Figure 59: [13]C recovery curves for 8:1 WG:copper (2M sodium acetate 1M sodium phosphate) at various temperatures

Figure 60 shows the [13]C $T_{1/2}$ times for the various samples which use different nanoparticles and solvents. The temperature dependence of $T_{1/2}$ was only measured on two samples in detail; these samples were 4:1 and 8:1 2 M NaAc WG:copper. The $T_{1/2}$

dependence on temperature for these samples is very weak; over the measured temperature range a power law of ~-0.5 can be fitted. It can be seen that all of the samples that contain copper have a similar $T_{1/2}$ at around 20 mK, which indicates that either the nanoparticle size is of little importance or the size of the nanoparticles are similar to one another due to aggregation.

Finally, samples containing copper oxide, platinum and silver were assessed. The platinum and silver would seem to be ineffective ^{13}C relaxation agents when compared with the 4:1 2 M NaAc WG:copper sample. There is a possibility that the copper oxide sample has a shorter $T_{1/2}$ than the copper samples at 20 mK, though the error bars in the $T_{1/2}$ times do overlap.
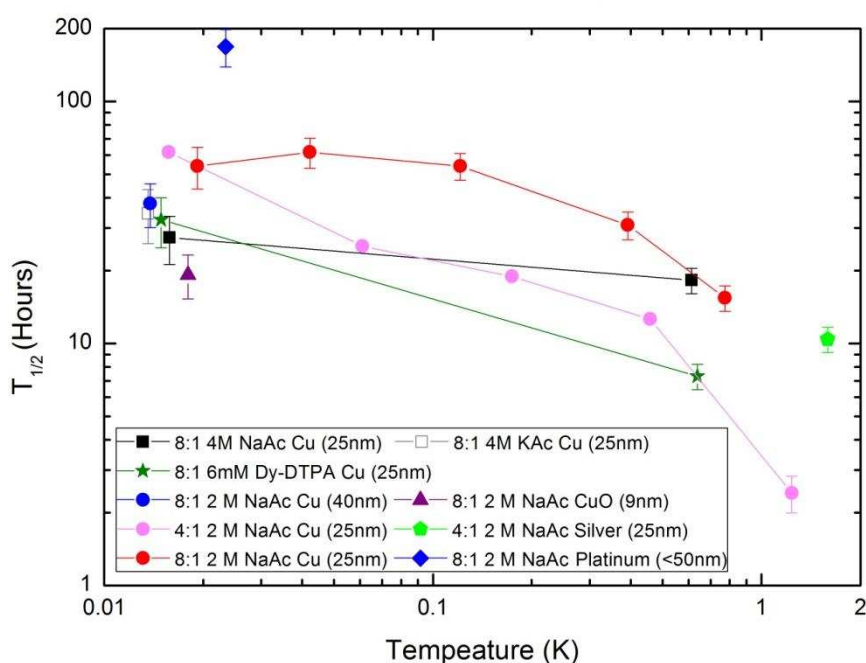
Figure 60: [13]C $T_{1/2}$ data for other metal nuclei.
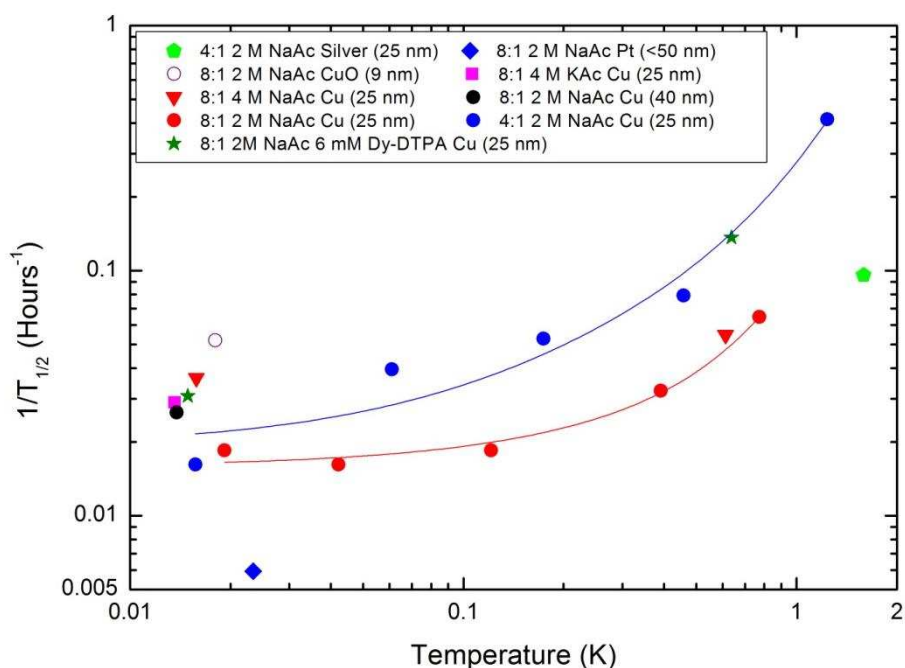
Figure 61: $1/T_{1/2}$ for ^{13}C of various samples

Sample	Intercept (quantum component)	Linear (electronic component)	Cubic component
8:1 2 M NaAc Cu (25 nm)	0.0159	0.0327	0.0509
4:1 2 M NaAc Cu (25 nm)	0.0193	0.148	0.11

Table 11: Fitting parameters used for ^{13}C $1/T_{1/2}$

The quantum components in the 4:1 and 8:1 2 M NaAc WG:copper are much greater than the quantum components measured on any of the proton T_1 times and is the source of the weak temperature dependence at the low temperatures.

4.4.3. *Discussion*

The temperature dependence of the 13C in the 8:1 2M NaAc WG:copper sample is interesting; below 300 mK, the relationship between T1/2 and temperature is less than linear and seems to be heading towards a constant value, as seen by a significantly large quantum contribution in Table 11. If the T1/2 value is constant below a temperature limit,

then reducing the temperature increases the equilibrium polarisation without increasing the polarisation time.

As an example, if the $T_{1/2}$ reaches a fixed value at 20 mK, it is in the interest of the user to polarise the sample at the lowest possible temperature, let's say 5 mK. The absolute polarisation would then increases by a factor of 3.7, while the time to reach equilibrium is the same. It should be noted that the polarisation enhancement is not 4 because the sample is not in the high temperature limit; therefore, the polarisation follows the tanh curve expressed in equation (5). To clarify, this theoretical $T_{1/2}$ recovery experiment does not use thermal mixing or other techniques to pass the polarisation to the carbon, therefore, this $T_{1/2}$ time could be reduced further with the addition of these techniques.

If this weak temperature dependence continues down to 2 mK, the lower limit of a dilution fridge, it could be possible to get an absolute polarisation of ~40% in 37-40 hours. This is slow compared to DNP, but due to the scalability of production, the effective polarisation time for each sample could be reduced to tens of minutes. Again, this calculation does not include any decrease of the effective $T_{1/2}$ via thermal mixing.

A possible explanation for the weak dependence temperature dependence of $T_{1/2}$ is the similarity of the gyromagnetic ratios between copper and ^{13}C. If the copper undergoes a flip flop interaction with the carbon, the carbon can become polarised very quickly, as the copper is able to relax quickly due to the Korringa effect. Aluminium has a gyromagnetic ratio which is even more similar to ^{13}C than copper; therefore, one might also expect a flip flop interaction between aluminium and carbon. If were the case, the $T_{1/2}$-temperature dependence should be similar to the copper sample.

After measuring the ^{13}C $T_{1/2}$ of a 8:1 2 M NaAc WG:aluminium sample for two days at 15 mK there was no significant recovery of magnetisation. Extrapolating the data, with a calculated infinity from a higher temperature, the $T_{1/2}$ of the ^{13}C was estimated to be greater than a year, therefore, demonstrating that having a similar gyromagnetic ratio to the target nuclei does not necessarily enhance the relaxation and that another relaxation mechanism is involved.

4.5. *Effects of Thermal Mixing*

Thermal mixing has been shown to be effective at transferring polarisation from protons to ^{13}C by Gadian, et al (20). It was also shown to be somewhat effective in Chapter 3; however, it would be useful to test the effectiveness of thermal mixing in the nanoparticle samples.

4.5.1. *Method*

Thermal mixing will be conducted in both the dilution fridge system and the fast field cycling system. Details of the pulse sequences for the fast field cycling machine can be found in Section 3.3.2.1.2. Thermal mixing in the dilution fridge will occur in a similar manner to that of the field cycling machine, with the exception that a measurement of the polarisation of each nucleus will be made prior to a saturation pulse. Also both the ^{13}C and the ^{31}P will be measured in the same experiment, as the experiment is very time consuming. It should be noted that even though the dilution fridge has a much more limited ramp rate compared to the fast field cycling system, it is still possible to perform thermal mixing, as the time spent ramping the field is small compared to the proton $T_{1/2}$ of the sample at the low temperatures.

4.5.2. *Ultra-Low Temperature Thermal Mixing*

In Chapter 3, thermal mixing at 4 K was demonstrated on lanthanide samples as a method of transferring polarisation from protons to carbon. As a proof of concept, a thermal mixing experiment was conducted at ~16 mK with a 4:1 2 M NaAc 1 M NaPh WG:Copper sample. The sample was allowed to polarise at 14 T for 24 hours. It should be noted that the sample was already in a partly polarised state before the 24 hour polarisation period. The initial NMR signal for ^{1}H, ^{13}C and ^{31}P were measured before a saturation pulse train was applied to destroy the polarisation of ^{13}C and ^{31}P. A measurement for any remnant polarisation of ^{13}C and ^{31}P was then made. The field was then reduced to allow for the thermal mixing step to occur. The field was swept from $+B_0$ to $-B_0$ at a rate of 0.3 T/min and

the NMR signal values were re-measured for each nucleus. The results can be seen in Figure 62.
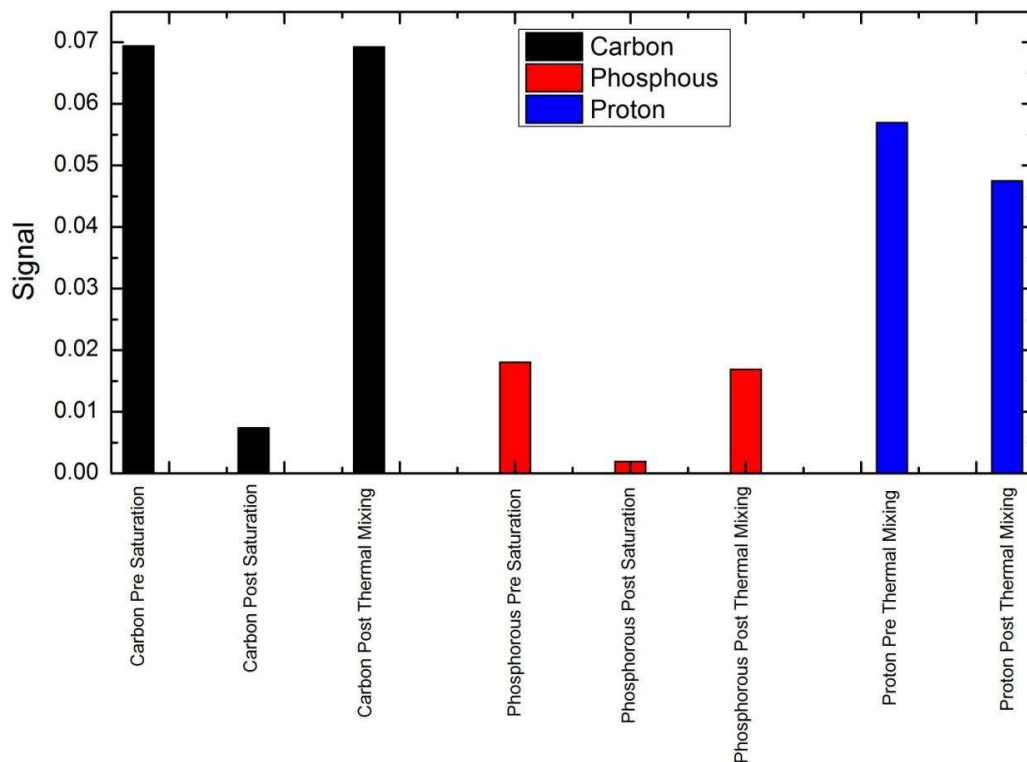
Figure 62: Graph showing the recovery of signal after thermal mixing at ~16 mK

As noted earlier, the hardware is not designed to do fast field cycling, so is not optimised for thermal mixing, yet almost the entire ^{13}C and ^{31}P signal has been recovered during the thermal mixing process. A small loss of proton polarisation is expected as the spin temperatures have to equilibrate; however, the observed loss in proton polarisation is much larger than would be expected from the spin temperatures reaching equilibrium. As mentioned in Section 3.5.6. the T_1 values of all of the nuclei become short, particularly protons, at the low fields used during thermal mixing, this allows for the polarisation of all of the nuclei in the sample to rapidly decay even though the field ramping only takes a fraction of the proton T_1 time.

There is much less control of the thermal mixing in the dilution fridge, therefore, conducting an in depth study is impractical. These experiments should instead be thought as a proof of concept.

Figure 63 shows the proton $T_{1/2}$ as a function of field at 23 mK. It can be seen that the $T_{1/2}$ of protons is in the order of 10 minutes at 1T. Combining this with the maximum ramping rate of the system, 0.3 T/min, the protons will be expected to lose at least 20% of their polarisation from relaxation processes during the field cycling process, assuming the $T_{1/2}$ is fixed at 10 minutes. This just highlights the inefficiency of the low temperature thermal mixing. In practice, at the lower fields required for thermal mixing, the $T_{1/2}$ will be shorter than 10 minutes and a larger proportion of the proton polarisation is lost.
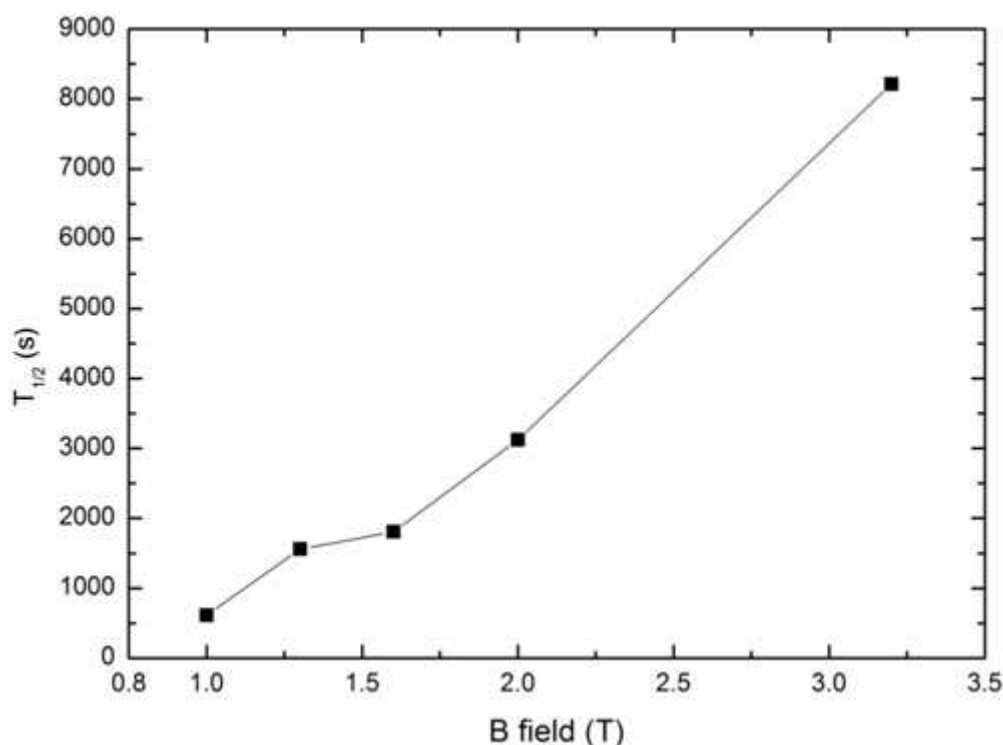
Figure 63: Proton Field dependence at 23 mK

The slow field cycling rates can be avoided if the sample is physically removed from the polariser. The field experienced by the sample can be dropped to tens of gauss, in the order of seconds, rather than minutes, if the sample was to be removed. The mixing time of the sample could also be optimised more easily. The required mixing time is not known; however, if it is of the order of milliseconds, like in the 4 K data of Figure 64, maintaining the low field for a long time destroys the proton signal as well as the ^{13}C and ^{31}P signal, as the spin systems are connected.

4.5.3. *Low Temperature Thermal Mixing – Pyr*

Thermal mixing experiments were performed in the field cycling system on a pure pyruvic acid sample in an attempt to optimise the thermal mixing process. The time spent at the mixing field and the strength of the field was varied to find the conditions under which the thermal mixing process was most efficient. The point of maximum efficiency was considered to be when the carbon signal was maximised.

The method proceeds as follows: The pyruvic acid was allowed to polarise for 40 s at 4 K and 2 T before saturating the carbon signal and performing the thermal mixing step. In each run, the thermal mixing step was altered by changing the mixing time or the mixing field. The magnetic field was then increased to the carbon resonance field and a ^{13}C signal was measured. The results of these measurements can be seen in Figure 64.
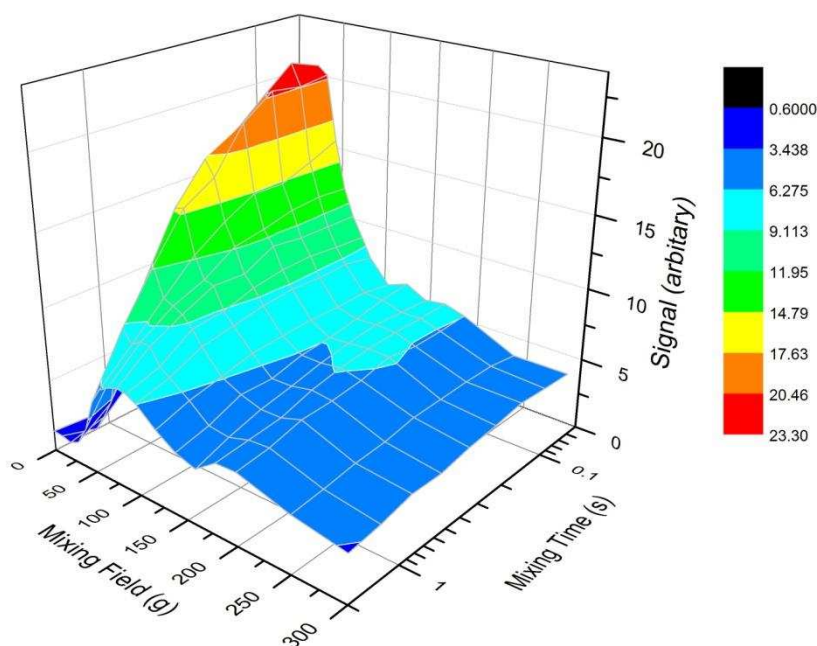
Figure 64: 2D representation of carbon signal of Pyr after thermal mixing at different mixing fields and mixing times

Figure 64 shows that the thermal mixing step is most efficient for ^{13}C in Pyr at 4 K when the mixing time is 50-100 ms and the mixing field is 0.005 T. In a practical system the likely temperature for a sample to be removed from the polariser will be 4-10 K. As the T_1 time is

going to be short at the low fields, it is crucial to minimise the time that the sample spends in these low field.

4.5.4. *Discussion*

The thermal mixing step has been shown to work in the millikelvin temperature region, though there is some unavoidable inefficiency. The inefficiency is because the T_1 of the nuclei at the low fields is more comparable to the field cycling speed than first anticipated. The thermal mixing process can be made more efficient if the field change only takes a few tenths of a second rather than several minutes. This could be achieved if the sample is physically removed from the field, either mechanically or pneumatically, rather than changing the current inside the superconducting magnet. As the sample will be exposed to low fields as it is being transported between the polariser and the scanner, there will be no need to change the B_0 field.

Optimising the thermal mixing process is important, as it allows for the maximal amount of polarisation to remain for measurement. The thermal mixing optimisation experiments were conducted on neat Pyr, this is because S. Nelson, et al has shown the success of Pyr samples in human trials (3). Figure 64 shows that the mixing time has to be very short, otherwise the benefit of thermal mixing is lost. This is an issue, as the transport time from the polariser to the scanner is likely to take several seconds, making the process less efficient than desired. To overcome this issue, the user could transport the sample in a magnetic field until it is close enough to the scanner that it can be inserted quickly, therefore, minimising the exposure to low fields.

4.6. *Relaxation Induced by Changing the Applied External Field (Ramping Effect)*

An apparent relaxation enhancement was observed in experiments when the external field was ramped between two values in the nanoparticle samples. It was noticed that the ^{13}C NMR signal appeared to recover at a greater rate than if the field were static. In other words, by changing the applied B_0 field, an increase in relaxation rate was induced.

In general, spin-lattice relaxation is caused by changes in the local magnetic field with time varying components near the Larmor frequency (see Section 2.6.1.). If the B_0 field were varied, then this may cause spins to flip in the domains of the nanoparticles. This could then induce extra relaxation in a sample. Another possibility explanation for this effect is that there is cross relaxation between nuclei in the sample.

4.6.1. *Probing the Field Ramping Effect*

The focus of this section is to try to determine the level of contribution of the ΔB_0 term to the T_1 relaxation. To enhance the ΔB_0 term, it is preferential to have large sweeps in field. The rate at which the B_0 field can be ramped is limited by the system; the superconducting magnet in the dilution system has a large inductance, therefore, changing the field at a rate greater than 0.3 T min^{-1} is not feasible. Another limiting factor of ramping the field is from heating caused by eddy currents which could also disrupt the results.

During the ramping sequence, the B_0 field will be changed by 1.7 T and returned to the resonance field of the target nuclei. The ramping sequence takes a long time (15 min) even when conducted at 0.3 T min^{-1}. For protons, even at low temperature, a significant amount of relaxation back to equilibrium will occur in this ramping time; this means it is hard to observe an enhanced relaxation rate. However, ^{13}C has a longer T_1 which is more suitable for these experiments.

In order to perform the ramping experiment, a sequence similar to the one shown in Figure 65 was employed. The ramping rates used were 0.1 T min^{-1}, 0.15 T min^{-1}, 0.2 T min^{-1} and 0.3 T min^{-1}. The ramping rates were varied among these values during experiments. In later experiments various nuclei (^{1}H, ^{23}Na etc.) were saturated in addition to the target nuclei before running the pulse sequence to try and narrow down the cause of relaxation.
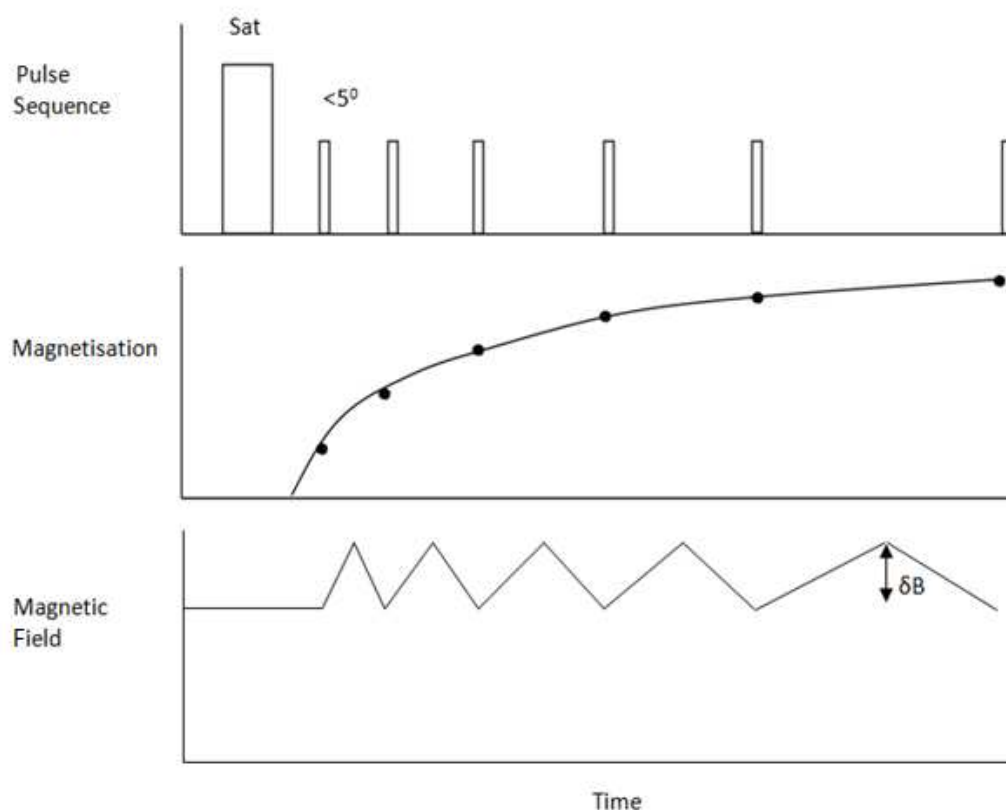
Figure 65: Schematic diagram of a pulse sequence for ramping experiments

4.6.1.1. T_1 Relaxation Curve (S Curve)

A simple experiment has also been devised to determine if the T_1 relaxation rate has increased due to a period of field ramping, this is done by comparing the gradients of the magnetisation measured between periods of a static B_0 and ramping the B_0 field. Once the T_1 of a nucleus is known, it is possible to set up experiments which are short enough to be in the near linear section of the T_1 recovery curve ($t < 0.1*T_1$), but set so a large section of the linear recovery is measured. This simpler experiment starts by saturating the ^{13}C nuclei and any other nuclei of interest. A measurement is then made and is represented as point one on Figure 66. The static field relaxation rate is assessed by measuring the signal after a delay (an hour in this case) this is point two on Figure 66. B_0 is now ramped to a new field and back before a third point is taken. The fourth and final point is measured after another time delay with a static field; this time delay was also an hour. The gradients between the first two points and the last two points should be nearly equal, as B_0 was held at a static field. To

confirm if there is an enhanced relaxation, the gradient between the second and third point is compared to the gradients in the static field. In the example used in Figure 66, ramping the field clearly induces an increased rate of relaxation.
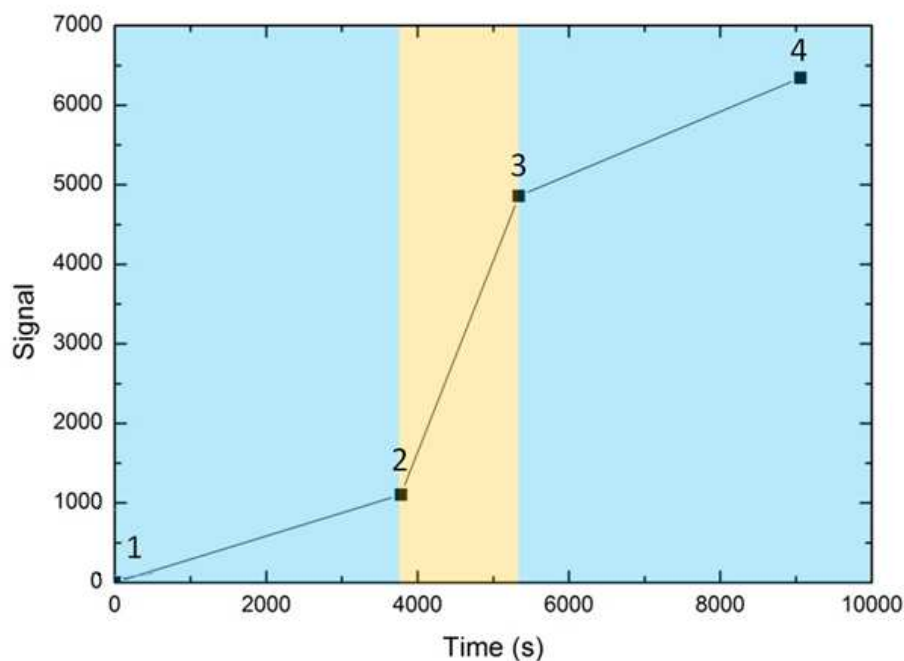
Figure 66: Example of an S curve on ^{13}C in NaAc 8:1 Cu. Blue sections are times when the magnetic field is static and the yellow section is when the B$_0$ field was ramped.

4.6.2. *Results*

The initial experiments were performed to determine if the field ramp rate or direction of field change had any significant effect on the relaxation rate. These experiments allowed a 8:1 4 M NaAc WG:copper sample to become polarised before saturating the ^{13}C and running a field ramping experiment, as seen schematically in Figure 65. The initial growth of magnetisation recovery curve is assumed to be linear, therefore, comparing the gradients of the relaxation curves in a static field and changing field, an estimate of the $T_{1/2}$ of the sample can be made. The results from the initial ramping experiment can be seen in Figure 67. The ramped experiment was offset in time, so that the first point matched the $T_{1/2}$ recovery curve of a standard saturation recovery experiment of the same sample. It can be seen that regardless of the ramping rate or direction, applying the 1.7 T ramping sequence enhances the relaxation rate by a factor of ~2.
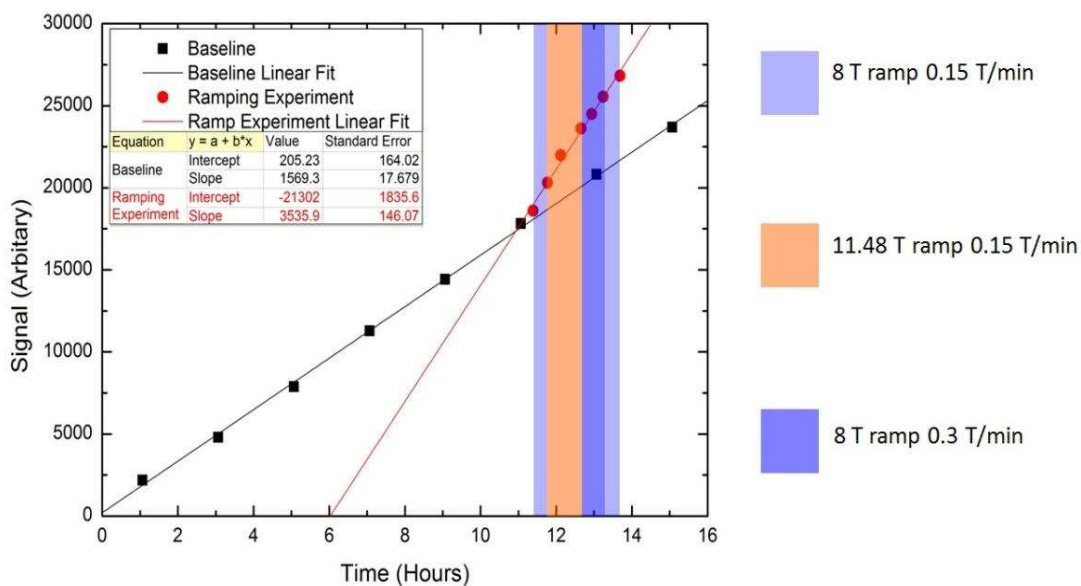
Figure 67: 8:1 4M NaAc WG:copper ramping rate tests compared to normal $T_{1/2}$ relaxation

Figure 68 shows the results of a similar experiment whereby a 8:1 4M NaAc WG:copper sample has no stored polarisation, except in copper, as it has a short T_1 time (see Table 3). The starting state was produced by allowing the sample to relax in the earth's magnetic field before ramping up to the ^{13}C resonance field.
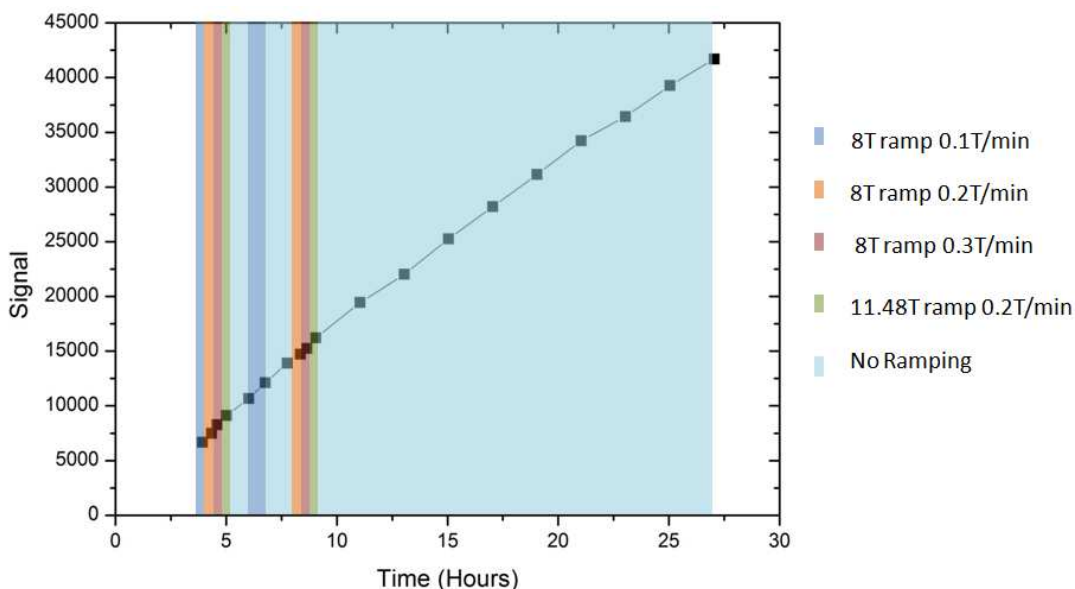
Figure 68: Magnetisation build-up of a 8:1 4M NaAc WG:copper sample with no stored polarisation

In Figure 68 the ramping effect can no longer be observed, which would suggest that polarisation is being passed from one nucleus to another. Nuclei which could be transferring

polarisation to the ^{13}C are likely to be nuclei with a similar gyromagnetic ratio to ^{13}C. In this sample it would be sodium or copper. As copper is known to have a short T_1 time at the low temperatures, it is likely that polarisation is being passed from the sodium to the ^{13}C. To confirm the hypothesis that the polarisation is being transferred from one nucleus to the ^{13}C, it is possible to determine whether the ramping effect disappears after several ramping sequences because the two spin systems should come into equilibrium with one another.

In Figure 69 the 8:1 4 M NaAc:copper sample was allowed to polarise before the ^{13}C was saturated. The B_0 field was then ramped several times to allow the nuclei in the sample to become equally polarised. The polarisation was then allowed to grow for 15 hours before ramping the field again. The ramping effect was no longer observed; in fact, the final point in the graph is equal to the penultimate which would suggest that the ^{13}C is more polarised that the sodium and the cross polarisation could be occurring in reverse.
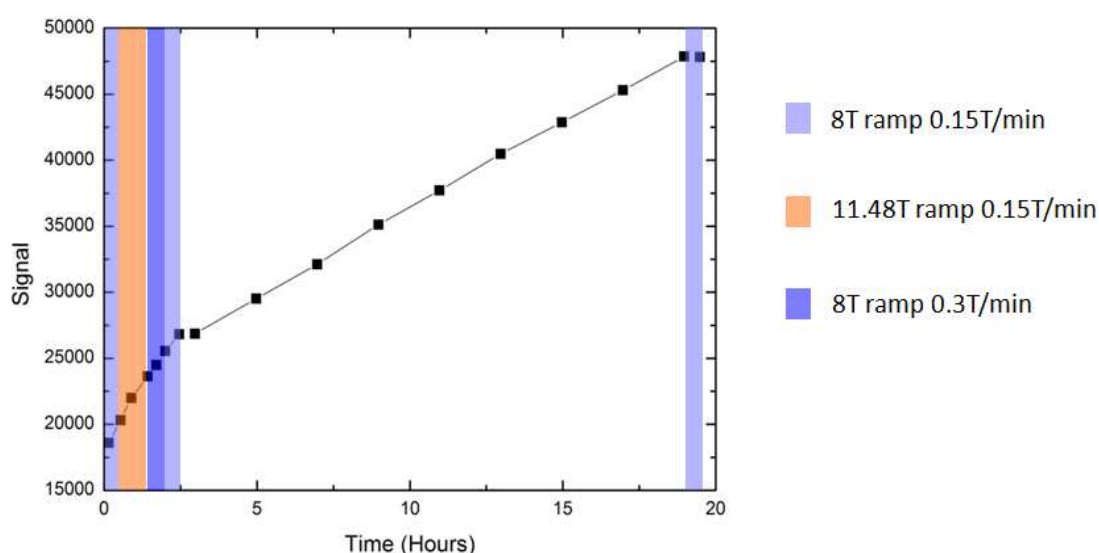
Figure 69: Recovery curve of 8:1 4 M NaAc:copper over a long period of ramping

The results from Figure 68 and Figure 69 would confirm that polarisation is probably being transferred between ^{13}C and sodium. However, there are two methods of explicitly determining if this is the case. The first is to replace the sodium in the sample with another nucleus that has a gyromagnetic ratio which does not match the ^{13}C's gyromagnetic ratio, but is chemically similar to sodium. The second is to saturate the sodium as well as the ^{13}C before undergoing the B_0 ramping sequence.

A sample of 8:1 2 M KAc WG:copper was measured to test the effect of a sodium free sample. Figure 70 clearly shows that for the first 17 hours the magnetisation grows at a constant rate, regardless of the field oscillations. After 17 hours and 20 hours the sample was ramped and there was a disturbance in the growth of the ^{13}C magnetisation. The reasoning behind the loss of magnetisation is not understood. If polarisation was being transferred between nuclei in the system, it would have been expected that an enhanced relaxation rate would have been measured in the first 5 hours of the experiment as the sample was polarised before beginning the experiment.
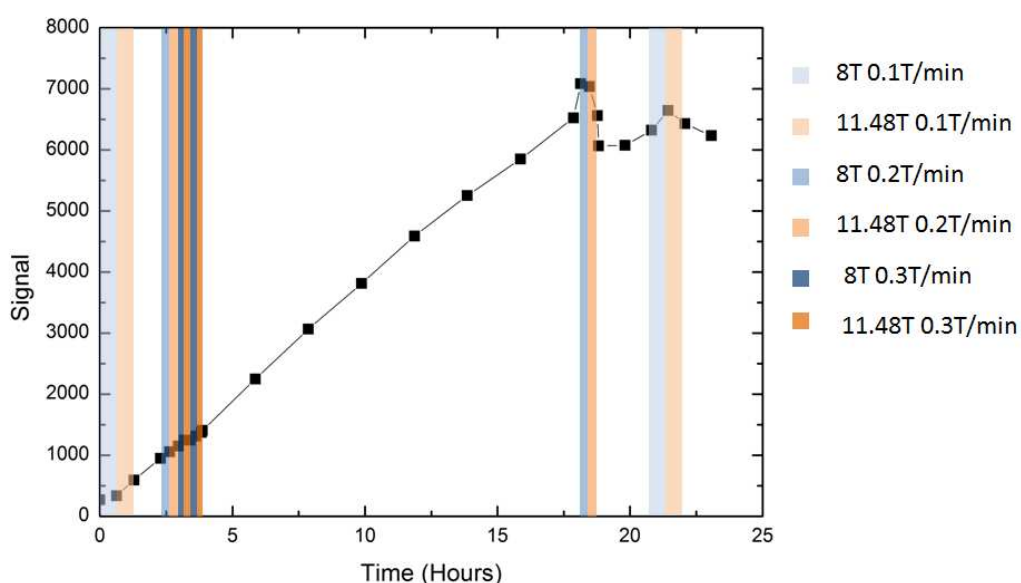
Figure 70: 2 M KAc:copper ramping experiment

Finally, for completeness, another 8:1 4 M NaAc:copper sample was measured. The experimental preparation was changed to make the experiment shorter. Instead of running a full ramping experiment, the S-curve routine was used, as detailed in Section 4.6.1.1. The experiment was run twice, once with the sodium being saturated and once without sodium saturation.
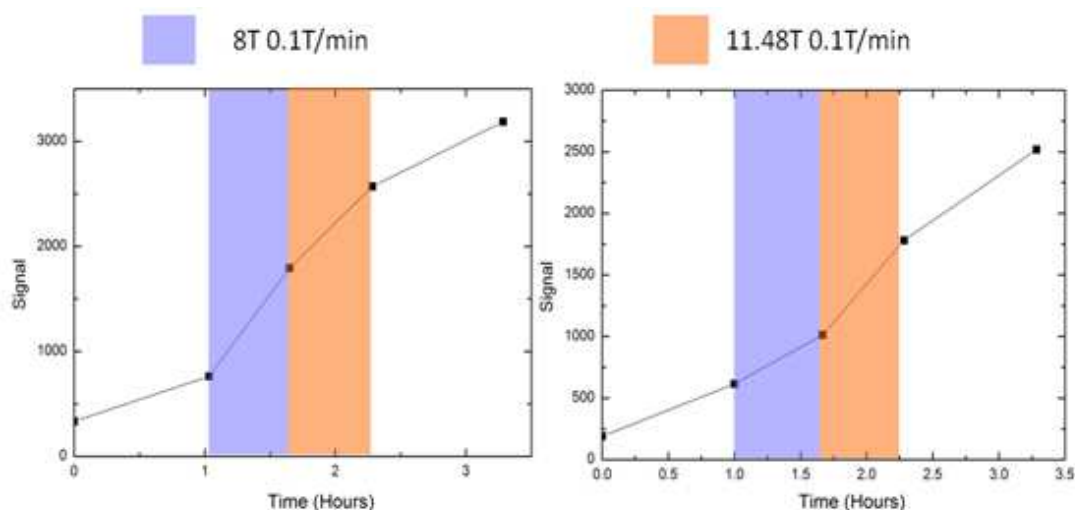
Figure 71: These graphs show the magnetisation recovery with ramping. The graph to the left shows the recovery when the sodium nuclei have not been saturated. The graph on the right saturated the sodium signal before the recovery.

Figure 71 shows that when the sodium was polarised, the field ramping does increase the carbon recovery rate by a factor of 2. However, if the sodium was saturated prior to the ^{13}C, the ramping effect is smaller, closer to 1.5. It was expected that there would be no enhancement, however, due to an imperfect saturation protocol, the sodium could have recovered some polarisation from the ^{13}C when ramping to the ^{13}C field for saturation. As both the sodium and ^{13}C were polarised before saturation, it allows the polarisation to be redistributed while changing the resonant field to saturate the other nuclei. A schematic of this redistribution can be seen in Figure 72.
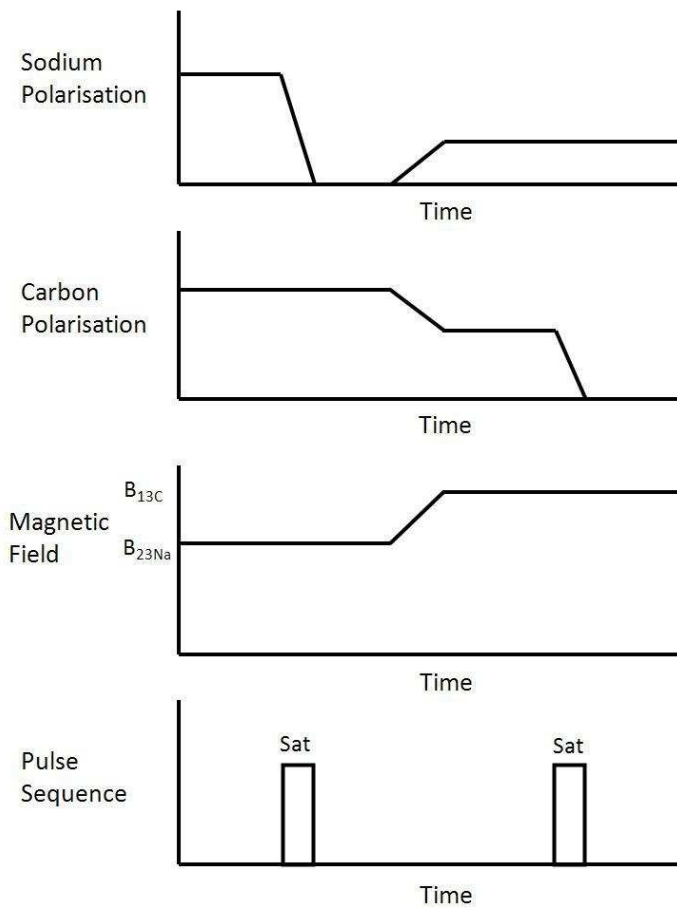
Figure 72: Schematic of the saturation sequence demonstrating how the sodium could have recovered polarisation during field switch to saturate carbon

Another pair of similar molecules were also investigated to determine if the ramping effect occurs. These tested molecules were a pure Pyr sample and 8:1 NaPyr:copper sample. The results of these experiments can be seen in Figure 73.
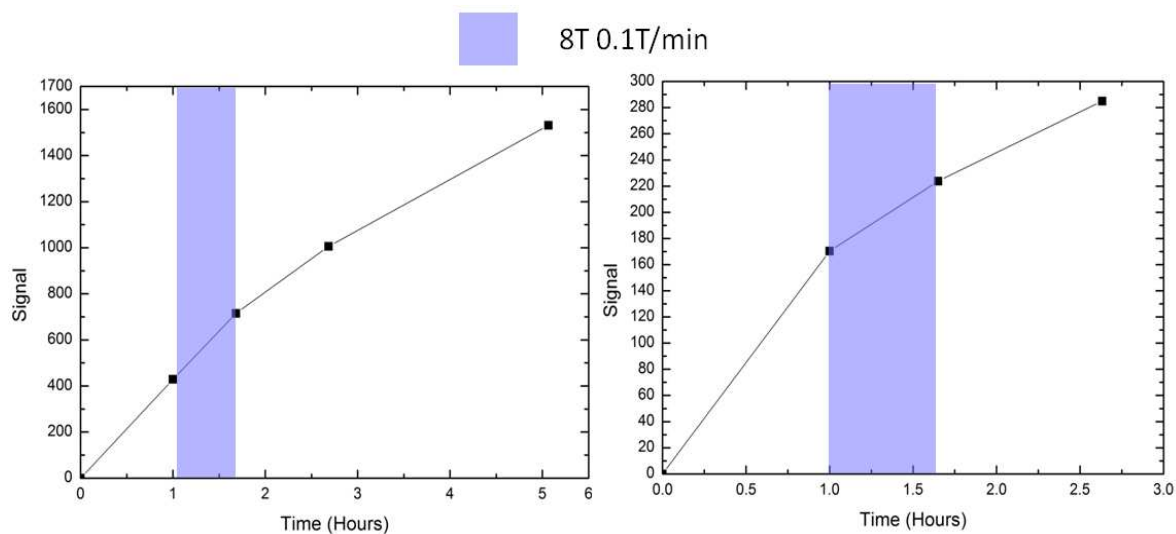
Figure 73: These graphs show the magnetisation recovery for NaPyr and Pyr. The graph to the left shows the recovery of the magnetisation of the NaPyr. The graph to the right shows the recovery for Pyr.

The first point to make is that the measurement time is long compared to the $T_{1/2}$ values of the ^{13}C. This has been determined by the fact that the magnetisation of the sample is not growing linearly while in a static field. The $T_{1/2}$ of the ^{13}C has not been measured in static conditions for these samples, therefore, the $T_{1/2}$ times are unknown. The second point that should be made is that the ramping effect does not seem to be effective in these samples. This could be due to the ^{13}C $T_{1/2}$ already being relatively short compared to the measurement time or because the effect is limited to certain molecules.

4.6.3. *Discussion*

There are two hypothesis as to how ramping the field caused relaxation enhancement. The first is that by changing the B_0 field the domains, and therefore the magnetisation of the nanoparticles in the sample, will also change via a spin flip. These spin flips could potentially induce relaxation in the surrounding nuclei, in a similar way to the electron spin flip of the lanthanide relaxants described in Chapter 3. If this is the relaxation mechanism, the relaxation of the nuclei would not depend upon the polarisation levels of other nuclei in the sample. The results in this section do depend upon the polarisation of the nuclei in the sample, therefore, the idea that the domains within the nanoparticles flip orientation is not the cause of the relaxation.

The second hypothesis for the relaxation enhancement is an effect which could be envisaged to be similar to that of thermal mixing. In thermal mixing, the field is reduced so that the resonance peaks of all the nuclei in the sample overlap. This then allows for the nuclei to interact with one another. In this case, the ^{13}C and sodium have a similar gyromagnetic ratio to the target nuclei, therefore, the resonance peaks would overlap at a much higher field than in traditional thermal mixing experiments. It has been demonstrated that sodium polarisation is required to enhance the carbon relaxation; therefore, the sodium is acting like a thermal bath for the carbon.

If the ramping effect is truly analogous to thermal mixing, the specific heats of the nuclei should be considered. The spin temperature equilibrium of the sample is normally weighted toward that of the nuclei with the largest thermal reservoir; this is effectively the thermal bath of the system. In this sample, the equilibrium point should be at the midpoint between the sodium and carbon spin temperature; this is because the number of sodium nuclei in the sample and the sodium's specific heat is almost the same as the carbon, see equation (19).

Ramping the B_0 field is a way of transferring polarisation to the carbon in NaAc; however, it is ineffective on the NaPyr sample. This does limit the effectiveness of the technique. As the polarisation has to be transferred from sodium, the sodium $T_{1/2}$ is an important parameter to be aware of. If the sodium has a short $T_{1/2}$, then the ramping effect would have become apparent in the first a few hours of measurement within Figure 68. Since this was not observed and the ramping effect tended to vanish after several hours, we can imply that sodium has a $T_{1/2}$ that is similar or longer than ^{13}C. The usefulness of the field ramping technique is not to reduce the effective T_1 of ^{13}C; but to store polarisation which can then be passed to the ^{13}C after a measurement. A major drawback of hyperpolarised samples is that they can only be used once. If the sodium is also polarised, it could be possible to use the ramping sequence to revitalise the ^{13}C, therefore, make signal average possible with hyperpolarised samples.

4.7. *Overview*

The current knowledge, from all of the experiments conducted in this chapter, would suggest that the sample used in the brute force method should consist of a relatively high

concentration (10:1) of the smallest sized copper nanoparticles diluted in a NaAc WG solution. The exact polarisation conditions required to maximise the signal enhancement should be considered after an acceptable polarisation time has been set. The polarisation time will probably be similar to that calculated in Section 3.4.5. (48 hours). In this time a 2 M NaAc WG:copper sample, at 19 mK and 9.74 T, could achieve a carbon polarisation of 6.5 % without any thermal mixing. The proton polarisation in 48 hours would be its equilibrium value of 50 %, though it would reach this level of polarisation after approximately 35 hours. If thermal mixing was used and was efficient the carbon polarisation could become as high as 13 % in 48 hours, if the thermal mixing procedure was perfect.

Measurements on Pyr:copper samples are much less useful, as the signal undergoes line broadening. This line broadening is due to a reaction between the copper and the Pyr and is discussed in more detail in Chapter 5. As other groups have shown interest in polarising Pyr and other similar metabolites, it would be useful to develop nanoparticles that would make suitable relaxation agents for these metabolites (3,77,78,79). Platinum has been shown to be an effective relaxation agent for protons in NaAc. As platinum is an inert material it should not chemically react with the metabolites and therefore might prove promising as an effective relaxation agent for the other metabolites.

Achieving a carbon polarisation of greater than 20% within 48 hours should be possible, if the temperature of the polariser is decreased to the lower limits of a dilution fridge, assuming the carbon $T_{1/2}$ remains constant. Thermal mixing could also be used to potentially speed up the polarisation process.

The polarised sample, when ready, can then be transported, pneumatically or otherwise, from the polariser to a collection box near the scanner. During transport the solid sample will pass through a low field region to allow for thermal mixing. Thermal mixing should be implemented as soon as possible, so that the proton polarisation is transferred to the longer lived carbon nuclei, therefore, maintain the maximal polarisation for measurement. Finally, the sample will go through a dissolution step where warming, filtering and quality control processes can occur before measurement. This procedure should allow for the highest possible signal to be measured.
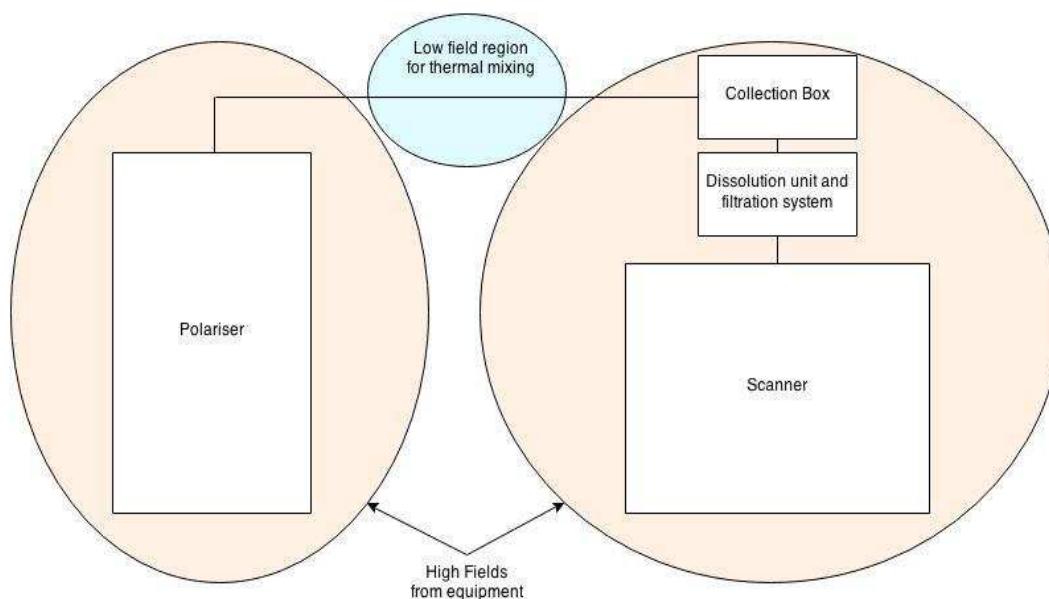
Figure 74: Schematic of polariser and scanner setup

As mentioned in Section 3.5.7. S. Nelson, et al have made a dissolution set up that can prepare a sample in around 68 s (3). By changing the ordering of the processes used, the dilution step could be much more efficient. Using a protocol similar to that described in Section 3.5.7. it is expected that around 40-50 % of the achieved polarisation would remain for measurement.

Finally, ejecting solid samples allows for the opportunity to transport the samples from a central location to a site where they can be used. In this scenario having a short T_1 time would be an issue. If transport and storage of a sample were to be used, it would be beneficial to have long T_1 times. This can be achieved by annealing the samples and adding materials like micron aluminium. A proof of concept experiment by J. Kempf and M. Hirsch, showed that it was possible to transport an annealed Pyr sample, with an expected $T_1(^{13}C) >$ 2 hours, for 8 minutes before measurement. It was estimated that with a transport time of 1 hour the loss of polarisation would be ~40% (76). The only concern with having samples with a long T_1 time is that the rate of production is slow; therefore, many polarisers would have to run simultaneously to produce enough samples to accommodate the demand.

4.8. *Conclusion*

Though this research is not complete, it covers a wide range of parameters, which paves the way for the transformation from concept into a commercial product. The use of metal nanoparticles as relaxation agents has been proven to be effective, as well as a metal oxide nanoparticle, copper oxide. Further research is required to understand the fundamental physics of the relaxation mechanism, so that more effective relaxation agents can be developed. The future of this research would be to build up an understanding of the size dependence of particles, with independent measurements of the sizes and morphology, test a wider range of metallic nanoparticles, characterise both thermal mixing and field ramping cross polarisation methods and finally, develop a dissolution system that can be used in conjunction with a dilution fridge capable of solid sample ejection. Work on a solid sample ejection system has been started by J. Kempf and M. Hirsch (76).

The level of carbon polarisation produced from the brute force method in 48 hours is around half of that produced by DNP (41). However, there are other advantages to the brute force method that could make it more versatile than DNP. These advantages include:

- The brute force approach is theoretically a broadband polarisation method, meaning all nuclei can be polarised in this system. Hyperpolarising multiple nuclei in a single sample could lead to new pulse sequences being developed.

- Scaling the production of samples in the brute force method could be easier than scaling production in DNP. This is because production of samples, using the brute force method, is limited by the physical volume of the polariser, while DNP is also limited by the microwave access to the sample.

Chapter 5. Nanomagnetism

In Chapter 4 the nanoparticles showed promise that they could be effective relaxation agents in the millikelvin regime, although the Korringa effect might not be the cause of the relaxation. In order to understand how the nanoparticles cause spin-lattice relaxation, it is important to know more about the magnetic properties of nanoparticles.

5.1. *Introduction*

The interest in the magnetic properties of nanoparticles began several decades ago with various applications in mind, from magnetic memory to clinical diagnostics (61,80,81,82). There is an interest in understanding the fundamental physics of these nanoparticles as technologies, such as magnetic data storage, are limited by the effects of the magnetic properties of small nanoparticles.

In an ideal data storage device, the size of the bits used to record data would be as small as possible, this allows for the maximum data storage in the smallest physical space. The problem with using physically small bits is that the data stored is more susceptible to corruption due to thermal fluctuations of the bits. In this data storage example, the objective is to store the most information in the smallest space, while being acceptably immune to corruption. The size at which a bit is too easily corrupted is known as the superparamagnetic limit.

Another area of research that has increased in popularity, is using nanoparticles in clinical applications for diagnostics or even to fight cancer (82,83). The idea is that a nanoparticle can be functionalised by adding a chemical coating, a capping agent, which will make the nanoparticle more likely to bond to target cells. Once the nanoparticle reaches the target cell, various objectives can be achieved, for example, killing the target cells. This can be achieved by applying radio waves to gold nanoparticles to generate heat. The heat then dissipates into the local environment, i.e. the target cells, killing them. The potential for

nanoparticles can be seen in the wide range of research and nanoparticles are freely available from companies such as Innova.

The first example, with the hard drive, demonstrates that the nanoparticles may not act in an intuitive way. Other research within the literature has shown that various nanoparticles can be very magnetic, unlike their bulk counterparts. This is generally attributed to the fact that the electrons in the nanoparticles are quantum confined (15,16,61,80).

Research into the magnetic properties of gold nanoparticles has been the focus of many groups. Even within one material, gold in this case, the measured magnetisation per atom has a large range from 0.002-0.3µB, depending on parameters such as size and capping agent (16). Not only does the level of magnetisation vary, but the type of magnetism can also change. Nano thiol-capped gold has been recorded to be a giant paramagnet, superparamagnetic and even a permanent magnet (16). Even though there are many reports on the elevated magnetisation, the mechanism of the magnetisation is still poorly understood.

In this research, an understanding of how the nanomagnetism arises is less important than knowing which properties enhance the relaxation rate. A wide range of materials will be measured in this chapter, the focus being to correlate the magnetic properties of the nanoparticles with those that are effective relaxation agents. However, this data may also be useful for those with a greater understanding of the mechanisms behind nanomagnetism.

5.2. *General Theory*

This section will start by giving a background of the various types of magnetic ordering found in materials. There will also be a brief overview of how nanomagnetism differs from bulk magnetism. This should give some insight as to why samples that seem similar can have a wide range of magnetic properties and why analysis of these samples are not necessarily simple.

5.2.1. *Types of Magnetisation in bulk materials*

There are several types of magnetism that materials can exhibit; examples include paramagnetism, diamagnetism, ferromagnetism and antiferromagnetism. An object is regarded as magnetic when its electronic moments align with one another and produce a net magnetisation.

5.2.1.1. Diamagnetism

A Diamagnetic object is one that produces a magnetisation which opposes an external magnetic field (84). Metals are generally diamagnetic due to the circulating electron currents. An example of a bulk material that is diamagnetic would be bismuth. Diamagnetic objects have a magnetic susceptibility, χ, of less than zero (χ=-1 is a perfect diamagnetic). It should be noted that superconductors, which could be considered purely diamagnetic, are more complicated than just being pure diamagnets. They also express the Meissner effect, which will not be discussed in this research (85,86).

5.2.1.2. Paramagnetism

Paramagnetic materials are only magnetic in the presence of an external magnetic field as their electron moments align to the applied external field (84). Examples of paramagnetic materials are the lanthanides used in Chapter 3. Paramagnetic materials have a positive magnetic susceptibility, χ, which is inversely dependant on temperature. The level of magnetism in these samples is proportional to the external field, B, and inversely proportional to the temperature, T. A schematic of the magnetisation during a field cooling experiment can be seen in Figure 75.

$$M \; \alpha \; \frac{B}{T} \qquad\qquad (35)$$
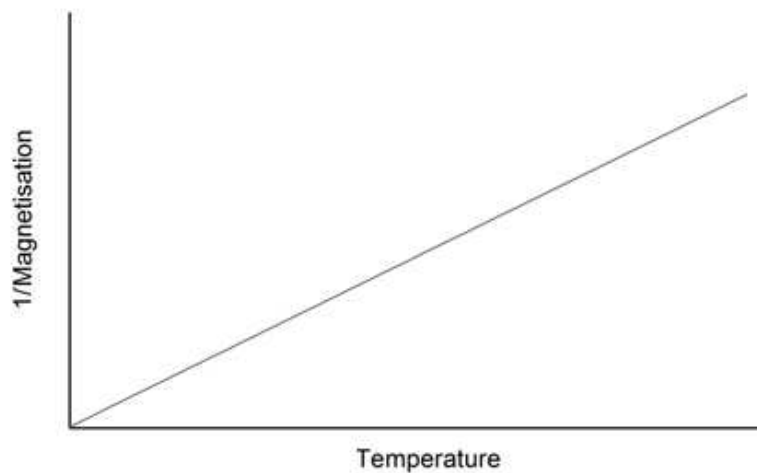
Figure 75: Schematic of a paramagnetic sample during field cooling

5.2.1.3. Ferromagnetism

Ferromagnetism is the most familiar type of magnetism and is responsible for permanent magnets. There are only three elements which are ferromagnetic in their bulk form at room temperature; these are iron, nickel and cobalt. Ferromagnetism can only occur in materials with unpaired electrons. When a ferromagnetic material is cooled below its Curie temperature, it becomes permanently magnetised (84). The permanently magnetised state is achieved by applying a magnetic field to the ferromagnet while the material is below the Curie temperature. The external magnetic field can now be removed and a proportion of the electrons will stay aligned to one another resulting in a net magnetisation.

The ferromagnet remains magnetised due to it being energetically more favourable for the magnetic moments to stay aligned to one another as the exchange interaction is stronger than the magnetic dipole-dipole interaction. Once the ferromagnet has been magnetised in one direction, it can resist the effect of being magnetised in a new direction, if that field is weak. This causes a hysteresis effect, a schematic of the hysteresis can be seen in Figure 76.
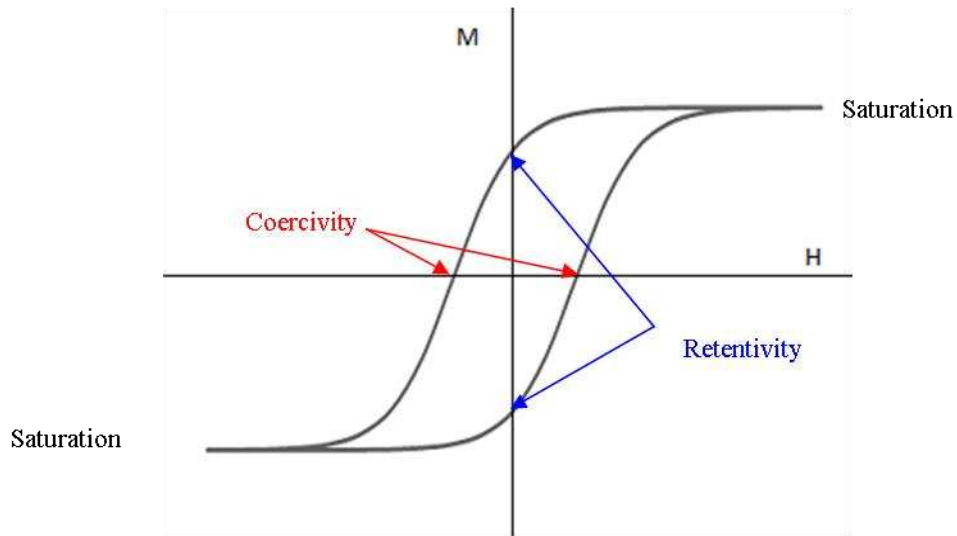
Figure 76: Hysteresis loop for ferromagnetic material

Figure 76 shows the features of a hysteresis loop that tell us the important properties of the ferromagnetic material. These are the saturation points, the coercivity and the retentivity. The saturation point is the point at which increasing the magnitude of the external field does not increase the magnetization of the sample. The coercivity is a measure of how well the ferromagnet can resist being magnetised in a new direction from an external magnetic field. The retentivity is the magnetization of a sample after the external magnetic field has been removed.

Ferromagnets consist of several magnetic domains. Within each domain the electron spins align in a single direction, via the exchange interaction, however, these domains do not necessarily line up with one another, as over long ranges the magnetic dipole-dipole interaction dominates over the exchange interaction. Between each domain is a domain wall, which is a thin section of material, a few atoms thick, that allows for the direction of the magnetisation to transition smoothly between two neighbouring domains. There are two types of domain wall. The first is known as a Bloch wall, this is where the magnetic moments rotate outside the plane of the domain wall. The second type is known as a Néel wall, this is where the magnetic moments rotate in the plane of the domain wall.
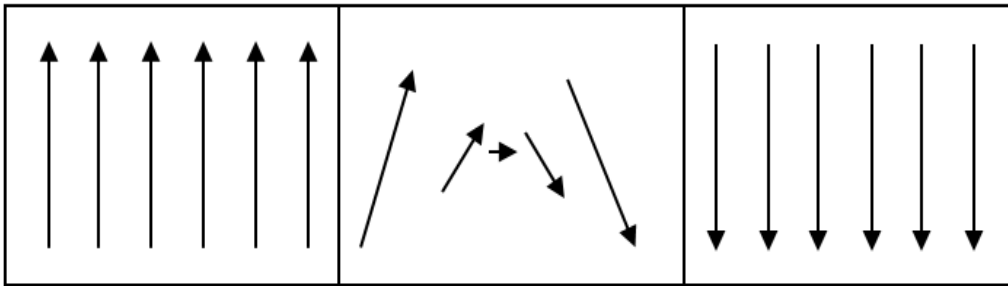
Figure 77: This is a Bloch wall showing the rotation of the magnetic moments over the domain wall. A Néel wall would rotate the magnetic moments into or out of the page

The net magnetisation of ferromagnetic material is the sum of magnetisation of the domains. When an external magnetic field is applied, the domain walls can move. Removing the external field means that the domain walls move back towards equilibrium but can become pinned on defects within the ferromagnetic material, therefore having a magnetisation greater than zero. Heating a ferromagnetic material, which is magnetised, above the Curie temperature makes the material paramagnetic and the permanent magnetisation is lost, as seen in Figure 78.
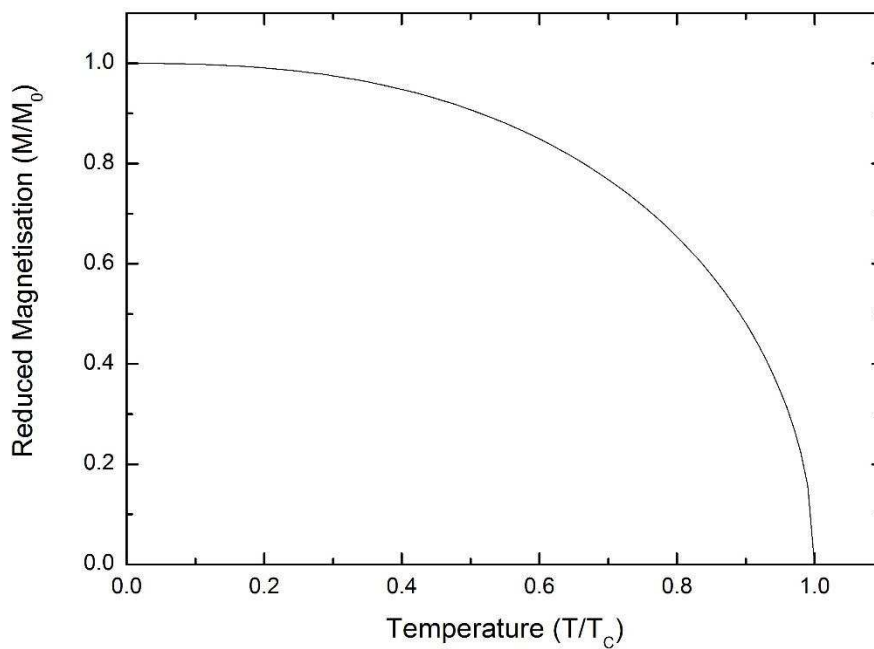
Figure 78: Schematic of a ferromagnet below its Curie temperature

5.2.1.4. Antiferromagnetism

Antiferromagnetic materials, similar to ferromagnetic materials, have a critical temperature whereby their properties change. If an antiferromagnetic material is cooled below a transition temperature, called the Néel temperature, the object becomes less magnetic. This is due to the magnetic moment in one sub lattice align antiparallel to the spins in the other sub lattice, meaning that magnetisations cancel with each other (84). As the spins are trying to oppose each other in the antiferromagnetic state, there are cases where a material can have multiple ground states. This is known as frustration, a more detailed explanation of frustration is found in Section 5.2.3.2. The magnetisation will only become zero if the temperature of the antiferromagnetic material is zero. Generally above the Néel temperature, antiferromagnetic materials are paramagnetic. A schematic of the magnetisation of an antiferromagnet can be seen in Figure 79.
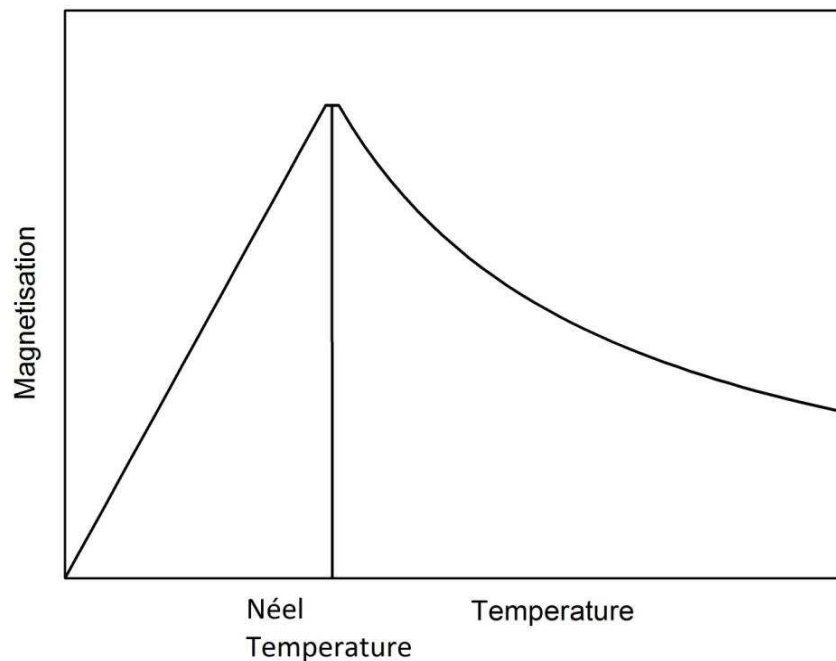
Figure 79: Schematic of the magnetisation of an antiferromagnetic material during field cooling

5.2.1.5. Ferrimagnetism

Ferrimagnetic materials share a common property with antiferromagnetic materials, as the temperature decreases the net magnetisation also decrease. In ferrimagnetic materials the magnetisation can even reverse direction. The decrease in magnetisation is due to spins in two sub lattices opposing one another. Unlike antiferromagnetism, the magnetisation of the spins in each sub lattice differ from one another. This is normally due to there being multiple ions of the same element, or two elements of different magnetisations, coexisting in the same material (84). Ferrimagnetic materials can be thought of as a combination of ferromagnetic materials and antiferromagnetic materials, though they only have a Curie temperature. Above the Curie temperature, the ferrimagnetic material generally behaves like a paramagnet; although, as it is cooled and crosses the Curie temperature it becomes ferromagnetic. As the ferrimagnet is cooled further, the sub lattices begin to oppose one another; however, a net magnetisation can generally be observed. In some materials further cooling can allow for the direction of the magnetisation to switch, as one sub lattice dominates over the other. The temperature at which the magnetisation from the sub lattices are equal and opposite is known as the magnetisation compensation point (87). A schematic of a ferrimagnetic material can be seen in Figure 80.
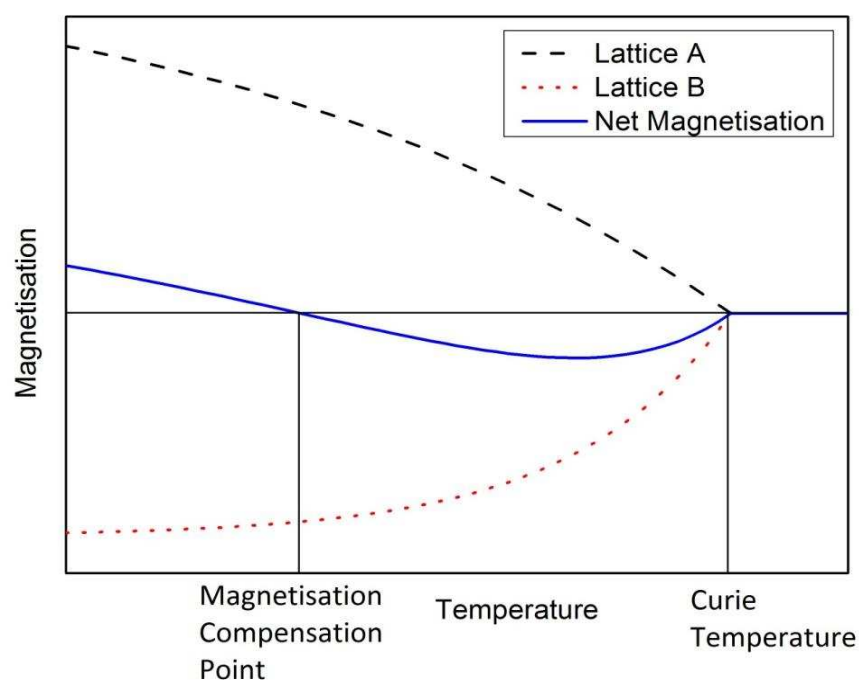
Figure 80: Schematic of a ferrimagnetic material

5.2.2. *Theories of Nanomagnetisation*

Before reading this section it should be noted that within the literature the magnetic properties of nanoparticles, mainly gold, are well documented. However, the phenomenon as to why seemingly similar nanoparticles can behave so differently is not well understood (88,89). The general theories behind the causes of the enhanced magnetism come from the idea that the electrons in a material become confined and there is a breaking of symmetry within the sample (70).

The small size of these nanoparticles means that the electrons are confined to a space which is similar to that of characteristic lengths of, for example, magnetic domains. The small size of the particles also means that symmetry is likely to be broken and that sites can have a reduced coordination number, leading to frustration in the system. Finally, in nano-sized particles, a high proportion of the particle is on the surface, therefore amplifying surface effects. This means that interactions between two interfaces will be magnified. It should also be noted that reducing the size of a bulk material does not necessarily make it more magnetic (88).

5.2.2.1. Quantum Confinement of Electrons

The electronic band structure of a material is dependent on its size. For a conducting solid, the electrons in that solid can be treated like free electrons or a Fermi gas. These electrons are trapped in an infinite potential well, the size of which is governed by the size of solid material. This limits the number of available electron states, measured by the density of states, $D(E_F)$. A solid can be treated as a two dimensional object if one of its dimensions is extremely small compared to the other two dimensions, thus changing the $D(E_F)$ of the electrons.

By solving the time-independent Schrödinger equation, it is possible to obtain the energy of the allowed states within an infinite potential well. The size of the potential well is defined by the nanoparticle size. Knowing the energy of each allowed state means that the $D(E_F)$ of the system can be calculated.

$$D(E) = \frac{dN}{dE} \qquad (36)$$

Where N is the allowed states and E is the allowed energy. The quantum confinement occurs when the length of one side of the potential well is in the same order as the Fermi wavelength of the electrons. A full derivation of the density of states can be found in reference (70).

The density of states is useful for calculating various physical properties of a sample, such as, the Pauli susceptibility and the conduction electron contribution to specific heat. The Pauli susceptibility, χ_P, is a measure of the response of free electrons in an applied magnetic field and is given by:-

$$\chi_P = \mu_0 \mu_B^2 D(E_F) \qquad (37)$$

Where μ_0 is the magnetic susceptibility, μ_B is the Bohr magneton and $D(E_F)$ is the density of state of the electron at the Fermi energy. As the density of states depends upon the dimensionality of the object, so does the Pauli susceptibility. As the electrons response to the magnetic field is related to the Pauli susceptibility and therefore the density of states,

it can be concluded that the electrons response also depends on the dimensionality of the object the electron is bound within.

5.2.2.2. Surface Atoms and Reduced Coordination Number

Atoms in the centre of a structure will have more neighbouring atoms than those on the surface. The geometry of the structure can determine the number of neighbours an atom has. For example, an atom in a concave surface would be expected to have a larger coordination number than an atom on a convex surface, this is because there are more neighbouring atoms. The coordination number of an atom changes the electronic structure of an atom. The smaller the coordination number is, the narrower the density of states curve becomes (70).

If there are two different elements in a sample, then the density of states near each element is dependent on the neighbouring atoms. For example, if there is a system of copper atoms and oxygen atoms and all of the copper atoms have the same coordination number, the density of states can still vary, depending upon whether each copper atom is next to other copper atoms or oxygen atoms. This means that the neighbourhood in which the atom is found also changes the density of state of the electrons. Expanding upon this idea, it could be expected that impurities in a sample could have a large effect on the final density of state of the electrons. This in turn effects the magnetisation of the nanoparticles.

5.2.3. *Types of Magnetism in Nanoparticles*

Now that the magnetism of bulk materials has been described, along with why the magnetism in nanoparticles can differ, the following subsections are focused on types of magnetisation that are found in nanoparticles.

5.2.3.1. Superparamagnetism

Superparamagnetism is a special case of ferromagnetic materials. Consider having a ferromagnetic material which is only several nanometers across (61). At this scale there is only one domain in each nanoparticle, unlike in its bulk form where there are multiple

domains. The single domain particles exist because the energy required to create a domain wall is larger than the energy saved from the demagnetisation between the new domains. The critical radius, r_c, for a single domain particle can be calculated based on the exchange constant, A, the uniaxial anisotropic constant, K_u, the magnetic permeability, μ_0, and the saturation magnetisation, M_s, as seen in equation (38).

$$r_c \approx \frac{(AK_u)^{1/2}}{\mu_0 M_s^2} \tag{38}$$

These nanoparticles usually have two states; these are when the magnetisation is aligned parallel or antiparallel to the nanoparticles easy axis. The easy axis is the preferred direction of magnetisation in the material and is due to anisotropies within the material. Thermal fluctuations can flip the magnetisation between being parallel and antiparallel to the easy axis. Considering the anisotropic energy density of the nanoparticle, which is based on the angle of the magnetisation with respect to the easy axis, θ, the anisotropy energy density, K, and the volume, V, the energy density can be found.

$$E = KV \sin^2\theta \tag{39}$$

The energy barrier between the two states is KV. A flipping rate can be determined by considering the size of this energy barrier and the available thermal energy. The average time between these flips is called the Néel relaxation time, τ_N, and is caused by thermal fluctuations. The difference between paramagnetism and superparamagnetism is that instead of a single electron flip, the magnetisation of the whole nanoparticle flips. The Néel relaxation time can be calculated by using equation (40).

$$\tau_N = \tau_0 exp\left(\frac{KV}{K_B T}\right) \tag{40}$$

τ_0 is the attempt time. If $K_B T \gg KV$, where K_B is the Boltzmann's constant, the system will behave like a paramagnet as the domains are constantly flipping direction. Since the magnetisation of the sample flips between two states, the measured magnetisation also depends upon the measurement time, τ_m. This introduces the concept of the blocking temperature. The blocking temperature is the temperature at which the Néel flipping time is equal to the measurement time of the device.

$$T_B = \frac{KV}{k_B ln\left(\frac{\tau_m}{\tau_0}\right)} \tag{41}$$

When the temperature of the nanoparticles is below this blocking temperature, the magnetic moments do not have time to flip, therefore, a net magnetisation can be measured. If the temperature is above the blocking temperature, the magnetisation of the particles flip during measurement and the measured magnetisation approaches zero. This blocking temperature is only valid for particles that do not interact with one another (61).

5.2.3.2. Superspin Glass

A spin glass is a system in which there is randomness and frustration (61,90). A frustration is when a spin has multiple ground states. If an antiferromagnetic material is arranged in a square lattice, it is possible, after assuming the first spins orientation, to calculate the orientations of the other spins to find the minimum energy I.e. opposite corners will align. However, if the antiferromagnetic material is arranged in a triangular lattice and the orientation of the first spin is known, it is impossible to determine a single minimum energy state.
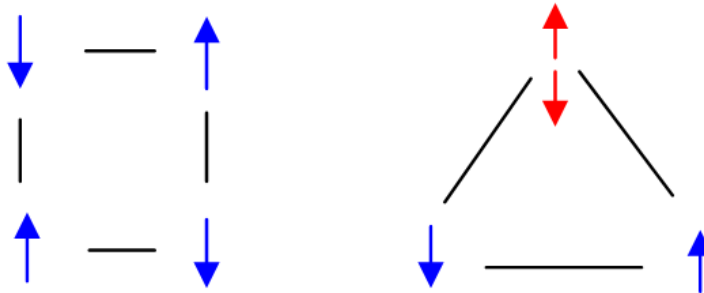
Figure 81: Demonstration of frustration in a system. The red arrow can be in either state and the energy of the system would be the same.

To imagine a spin glass we shall begin by considering a non-magnetic material that is slightly doped with magnetic moments. These magnetic moments are randomly distributed through the system. The magnetic moments should have a small population compared to the non-magnetic material. Such a doped system would show a phase transition which is not fully ordered or disordered below a freezing temperature, T_f. This magnetic system has

interactions characterized by a random, yet cooperative, freezing of spins. Below the freezing temperature a metastable frozen state occurs without there being long range ordering, this is known as a spin glass. Within this spin glass there will be spins that are locally correlated to one another and form small clusters. At temperatures above the freezing temperature the magnetic behaviour is dominated by thermal fluctuations, i.e. the magnetic moments will be practically independent of each other (61).

If each spin in the spin glass were replaced by a superspin, i.e. a nanoparticle, then the system is a superspin glass, where groups of nanoparticles can interact with each other; however, there is still no overall long range ordering.

One of the most recognisable features of a spin glass is a non-linear susceptibility at low external fields, H, (61).

$$M = \chi_1 H + \chi_3 H^3 + \chi_5 H^5 + \dots \tag{42}$$

Where χ_1 is the linear susceptibility and χ_3, χ_5 are the non-linear susceptibilities. At the glass transition temperature T_g (=freezing temperature T_f when time $\rightarrow \infty$, i.e. in thermal equilibrium) χ_1 is non-divergent, while the higher order terms do diverge.

$$\chi_3 = \chi_3^0 (T / T_g - 1)^{-\gamma} \tag{43}$$

$$\chi_5 = \chi_5^0 (T / T_g - 1)^{-(-2\gamma + \beta)} \tag{44}$$

Where γ and β are critical exponents. Another set of other important characteristics of spin glasses are ageing, memory and rejuvenation. The data taken in this chapter does not consider these three effects, however, details of these phenomena can be found in the following references (91,92,93).

5.2.3.3. Superferromagnetism

A superferromagnetic material can be considered to be a spin glass with a higher proportion of magnetic moments. As the spacing between single domain ferromagnetic particles in a superspin glass decreases, the sample enters the regime of being a

superferromagnet. In the superferromagnetic regime, the interactions between the particles becomes stronger and produce ferromagnetic domains within the sample. These domains consist of ferromagnetic nanoparticle. The number of observed superferromagnetic systems seems to be quite limited. An example of superferromagnetism can be found in work by S. Bedanta, et al, where $Co_{80}Fe_{20}$ was layered between Al_2O_3. By changing the thickness of the $Co_{80}Fe_{20}$ layer, superparamagnetic, superspin glass and superferromagnetism ordering was observed (94).

5.2.3.4. Anisotropy

The effects of superparamagnetism has a strong relation to the anisotropy of the particles, as such, knowing the sources of the anisotropy is important. There are several types of anisotropy which include magnetocrystalline anisotropy, shape anisotropy, and strain anisotropy.

Magnetocrystalline anisotropy is related to the directionality of a crystal structure. In the simplest structures, like hexagonal and cubic crystal structures, they are uniaxially anisotropy. This means that there is one preferred direction which is known as the easy axis. The energy associated with a uniaxial symmetry is given by:-

$$E_a^{uni} = K_1 V sin^2\theta + K_2 V sin^4\theta + \cdots \tag{45}$$

Where K_1 are anisotropy constants, V is the particle volume and θ is the angle between the easy axis and the magnetization. For single domain particles, K_2 and higher are often neglected, this allows for the simplification of equation (45) to equation (39).

Shape anisotropy is concerned with the geometry of the nanoparticles. In spherical particles, there is no shape anisotropy, therefore, the sphere is uniformly magnetised. Many nanoparticles are not spheres due to aggregation. This gives the particles an anisotropic property, whereby the magnetisation prefers to align with the longest dimension of the particle.

When nanoparticles are produced, it is possible that internal strains can be locked into the nanoparticles. Strain in a particle can cause magnetisation anisotropy through the

magnetostrictive effect. This kind of anisotropy is often described by a magnetostatic energy term:-

$$E_a^{strain} = -\frac{3}{2}\lambda_s \sigma S cos^2 \theta' \qquad (46)$$

Where λ_s is the saturation magnetostriction, σ is the strain value by surface unit, S is the particle surface and θ' the angle between magnetization and the strain tensor axis. (61)

5.3. *Experimental Setup*

5.3.1. *Superconducting Quantum Interference Device Magnetometer*

The Superconducting Quantum Interference Device (SQUID) uses Josephson junctions (JJ) to measure the magnetic properties of the sample. The SQUID being used is a DC SQUID, which consists of a pair of JJs in a superconducting loop with an applied current, I_A. When an external field is applied, a second current in generated in the loop, which is known as the screening current, I_s, to cancel out the applied external flux. In the absence of an external flux the current applied should be split equally between the two JJ. However, with the external field, the induced screening current changes the balance of current between the two JJ. By increasing the applied current, it is possible to reach the critical current for one of the two JJ, therefore, making it possible to measure a voltage across the JJs.

Now consider that the flux trapped in the JJ loop is increased by half a magnetic flux quantum, $\Phi/2$. The system wants to have an integer number of flux quanta contained within the superconducting loop, therefore, the screening current switches direction to allow for the change in flux. For each half integer flux quanta the external flux increases by, the screening current will change direction, thus, switching which JJ is resistive. As the screening current is produced to oppose the external field, the value of the external field can now be calculated. The screening current can be calculated if the resistance of the JJ, applied current and the measured voltage is known. The voltage-current characteristics of the SQUID mean there is hysteresis, but by adding a shunt resistor to the loop the hysteresis effect is removed (95,96).
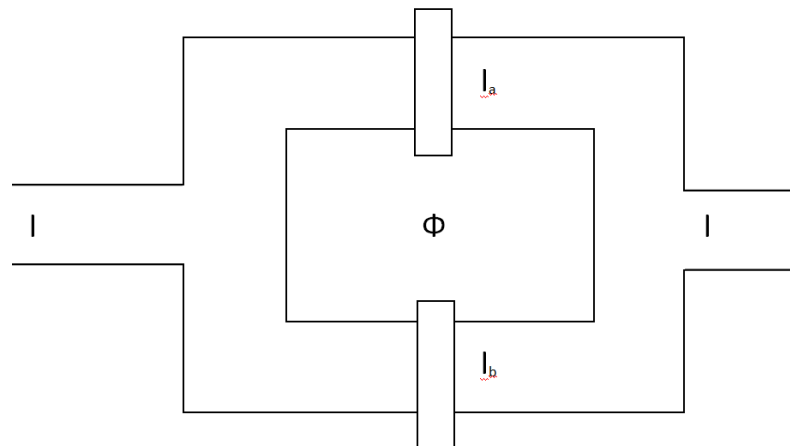
Figure 82: Josephson junctions in a DC SQUID

Figure 82 shows current I_a and I_b through each JJ. It is known that $I=I_a+I_b$ and that the difference between I_a and I_b is the screening current, produced by Φ. The screening current is dependent on the induction of the coil, L, and the flux in the coil, Φ. If this is applies with ohms law, it is possible to derive.

$$\Delta V = \frac{\Delta \Phi R}{L} \qquad (47)$$

When making a magnetic measurement on a sample, it is first loaded into the SQUID magnetometer. A fixed temperature and external magnetic field can be set. The sample is then moved through a pickup coil to find the largest absolute voltage; this is generally when the sample is in the centre of the coil. The pickup coil is around 4 cm long and is linked to a surface coil. The surface coil is physically close to the superconducting loop which contains the JJ's. Moving the sample within the pickup coil induces a current which then goes to the surface coil. The surface coil will produce a magnetic field near the JJ's, where a voltage across the JJ's can be measured. The voltage can then be used to calculate the magnetisation of the sample. It should be noted that the pickup coil is wound in such a way that when the sample passes through the centre of the coil, the induced current is in the opposite direction to when the sample is at the edge of the pickup coil. This is to calibrate the SQUID magnetometer and to ensure that the sample is centred in the pickup coil to achieve the maximum sensitivity of the SQUID. If the centring of the sample is lost during a

measurement, the measured magnetisations are incorrect. A schematic of the magnetometer can be seen in Figure 83.
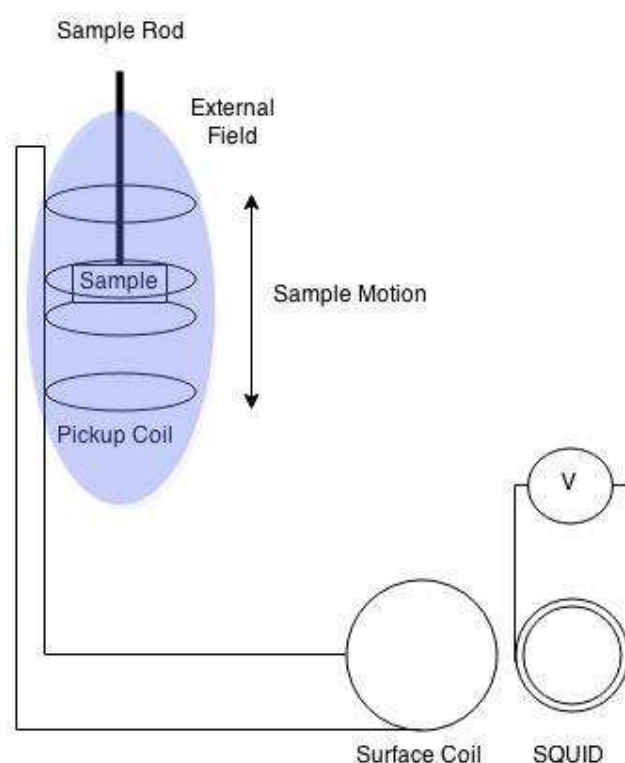
Figure 83: Schematic of SQUID magnetometer

5.4. *Method*

The fundamental concepts behind how the SQUID operates and measures the magnetisation of a sample have been described above. To find the magnetic ordering of a sample, the magnetisation of the sample has to be measured at a variety of fields and temperatures. The magnetometer used in this research is a Quantum Design XPMS, which runs the following procedure:-

1. Load a sample into the magnetometer at room temperature and with no external field.

2. Apply an external field to the sample and run calibration checks i.e. centre the sample in the pickup coil.

3. Cool and measure the sample in a fixed external field, 1 T in this case. This is known as field cooling the sample.

4. At the minimum sample temperature, 2 K, a hysteresis loop is performed. This is done by measuring the magnetisation as a function of field. The external field is swept from 1 T to − 1 T and finally back to 1 T.

5. The sample can then be warmed to a new temperature for more hysteresis loops. If this is done the sample should be cooled down to the minimum temperature before proceeding with the final step.

6. At the minimum temperature, the external magnetic field is removed and the magnetisation of the sample is measured while the sample is brought back to room temperature.

In the field cooling sections of the experiments, an external field of 10000 Oe (1 T) was applied while the temperature was lowered from 300 K to 2 K. A hysteresis loop was then conducted at 2 K between ±1 T. In some cases the temperature was then raised to 4 K and 10 K to conduct more hysteresis loops before the temperature was dropped back down to 2 K. The external field was then removed and the sample was warmed from 2 K to 300 K.

The field cooling step is used to determine whether the sample is paramagnetic or diamagnetic and also the level of magnetisation experienced by the sample. The hysteresis loops can be used to determine if the sample is ferromagnetic and also the Curie temperature of the sample, if a hysteresis loop is performed either side of the Curie temperature. The zero field warming is used to measure the retentivity of ferromagnetic samples, as well as the Curie temperature.

5.4.1. *Sample Preparation and Calibration*

Dry and liquid samples were secured in a resealable container, which fits onto the end of the loading rod of the susceptometer. The susceptometer measures all of the material within the coil; therefore, the containers were measured without a sample so that the container magnetisation, M_c, can be subtracted from the measured magnetisation, M_m, leaving the sample's magnetisation, M_s.

$$M_m = M_c + M_s \qquad (48)$$

The magnetisation subtraction is not perfect as the alignment of the container, with and without a sample, is slightly different because the susceptometer is searching for the highest absolute magnetisation. The experimental error of the susceptometer is of the order of 10^{-5} emu. The error was calculated by considering the variation of the magnetisation to a fitted curve. The error checking procedure was conducted on an empty sample holder during a field cooled measurement.

The magnetisation of the sample is converted to Bohr magnetons per atom. In cases where the nanoparticles have been mixed with a solvent, only the nanoparticle mass is used. This is because the in some samples the solvents reacted with the nanoparticles. If a reaction occurs, it is hard to determine how much of the solvent has reacted. However, as the nanoparticles are generally the limiting factor in these reactions, due to their smaller number, we can still assume the magnetisation is dominated by the nanoparticles and their products and not the solvent. It should also be noted that the solvents were generally weakly diamagnetic and therefore would only produce a small contribution.

5.4.2. *Sample List*

This chapter reports on four sets of experiments. The first set was focussed on the magnetisation of each of the nanoparticles in their dry form, along with some control samples for reference points. The second set of experiments were conducted on samples analogous to those measured in Chapter 4. The focus was to correlate the NMR relaxation rates with the sample's magnetisation. The third set of experiments were designed to test the change in magnetisation of copper and copper oxide samples in various dilutions of water, Pyr and a mixture of water and Pyr. The final set of experiments were to test a wider variety of solvents on copper and copper oxide nanoparticles. This was too try and determine the cause of the enhanced magnetisations measured in other experiments.

Samples	Size (nm)	Samples	Size (nm)
Pure WG	-	Pure Pyr	-
Aluminium Oxide	20	Copper Oxide	<50
Aluminium	18	4:1 WG:Copper Oxide	<50
Aluminium	15000	8:1 WG:Copper Oxide	<50
4:1 WG:Aluminim	18	8:1 Pyr:Copper Oxide	<50
8:1 WG:Aluminium	18	Graphene	42309
8:1 Pyr:Aluminium	18	Magnesium Oxide	10-30
Copper	25	Platinum	<50
Copper	44000	Stannic Oxide	50-70
8:1 WG:Copper	25	Silver	20-30
8:1 Pyr:Copper	25	8:1 WG:Silver	20-30
50:1 Pyr:Copper	25	Zinc Oxide	10-30

Table 12: List of samples that can be compared with NMR data.

Sample	Size	Sample	Size
Copper	25	64:1 Pyr:Copper	25
8:1 Pyr:Copper	25	128:1 Pry:Copper	25
8:1 Water:Copper	25	128:1 Water:Copper	25
6:2:1 Water:Pyr:Copper	25	64:64:1 Water:Pry:Copper (mixture)	25
4:4:1 Water:Pyr:Copper	25	64:64:1 Water:Pry:Copper (green layer)	25
2:6:1 Water:Pyr:Copper	25	64:64:1 Water:Pry:Copper (purple layer)	25
16:1 Pyr:Copper	25	8:1 Acetic Acid:Copper	25
8:8:1 Water:Pyr:Copper	25	8:1 Buffered Pyr:Copper	25
32:1 Pry:Copper	25	64:64:1 Water:Pry:Copper oxide DAY 1	<50
32:1 Water:Copper	25	64:64:1 Water:Pry:Copper oxide DAY 2	<50
16:16:1 Water:Pyr:Copper	25	64:64:1 Water:Pry:Copper oxide DAY 3	<50
32:1 Pry:Copper oxide	<50	128:1 Acetic acid:Copper oxide	<50
32:1 Water:Copper oxide	<50	128:1 Oxalic acid:Copper oxide	<50
16:16:1 Water:Pyr:Copper oxide	<50	128:1 Acetone:Copper oxide	<50
Copper Sulphate Solution		Gold	6, 12, 30

Table 13: List of sample measured to explore the magnetic properties of nanoparticles.

5.5. *Control Samples and Dry samples*

We first conducted some experiments on control sample to get an idea of how best to run these experiments. From the literature it is calculated that iron should have a saturation magnetisation, in its bulk form, of 2.18 μB/atom and nickel has a saturation magnetisation of 0.57 μB/atom (97). Copper-nickel alloys are another material which are known to have ferromagnetic behaviour and would make for a useful test run (98).

5.5.1. *Control Samples*

5.5.1.1. *Copper-Nickel*

A previously studied copper-nickel slug was used and it has a known Curie temperature of 108 K. The slug was filed down to make a powder, so that it could be loaded into the SQUID. Hysteresis loops were set up at 2 K, 100 K and 120 K to try and measure the ferromagnetic transition. Unfortunately, the Curie temperature of the sample seems to be at a higher temperature than 120 K, as the sample still displays ferromagnetic properties at 120 K, as seen in Figure 84.
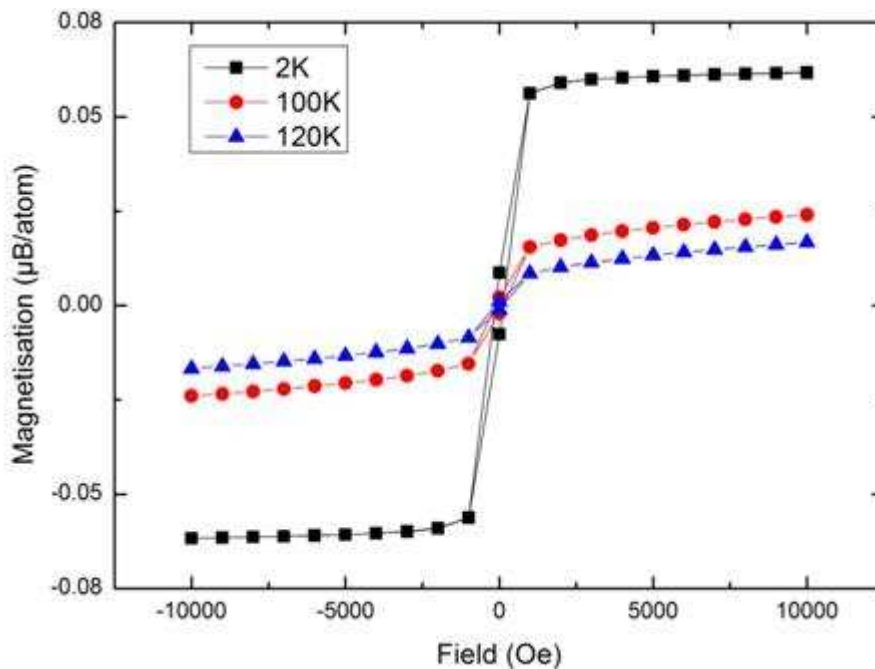
Figure 84: Copper-nickel hysteresis loops at various temperatures

From the zero field warming experiment, seen in Figure 85, the Curie temperature transition seems to be around 140 K. This means that the copper-nickel's Curie temperature in the powdered form is higher than a solid slug which shows the Curie temperature also has a size dependence. The copper-nickel sample has a saturation magnetisation which is just over 10% of pure nickel, at 0.06 μB/atom.
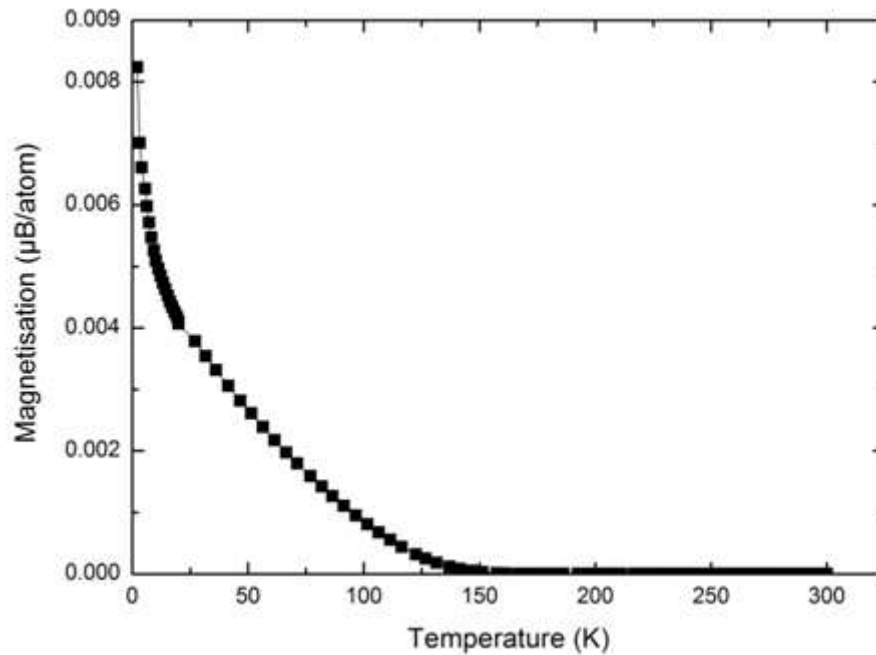
Figure 85: Zero field warming of copper-nickel sample

5.5.1.2. Water

Figure 86 shows that the water is weakly diamagnetic because it has a small negative gradient. The measured magnetisation of the water sample is of the order of 10^{-5} μB/atom which is near the limit of the sensitivity of the susceptometer. Water is one of the most weakly interacting materials measured in this research.
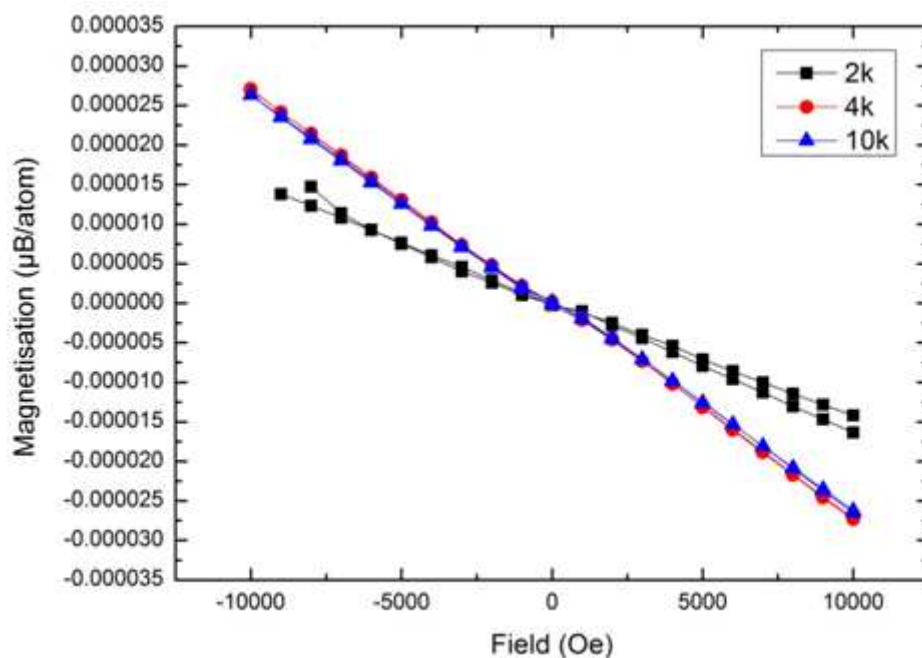
Figure 86: Hysteresis loop of water

5.5.1.3. Pure Pyruvic Acid

Figure 87 shows the hysteresis loop for Pyr and it can be seen that its magnetic ordering of the sample changes as a function of temperature. At 10 K the sample is clearly diamagnetic, however, as the sample is being cooled further, a more ferromagnetic or superparamagnetic component seems to be apparent. This is probably a nanoparticle contamination from another experiment. It should also be noted that the level of magnetisation measured in Figure 87, is close to the experimental limit of the susceptometer, meaning that the validity of the interpretation is limited.
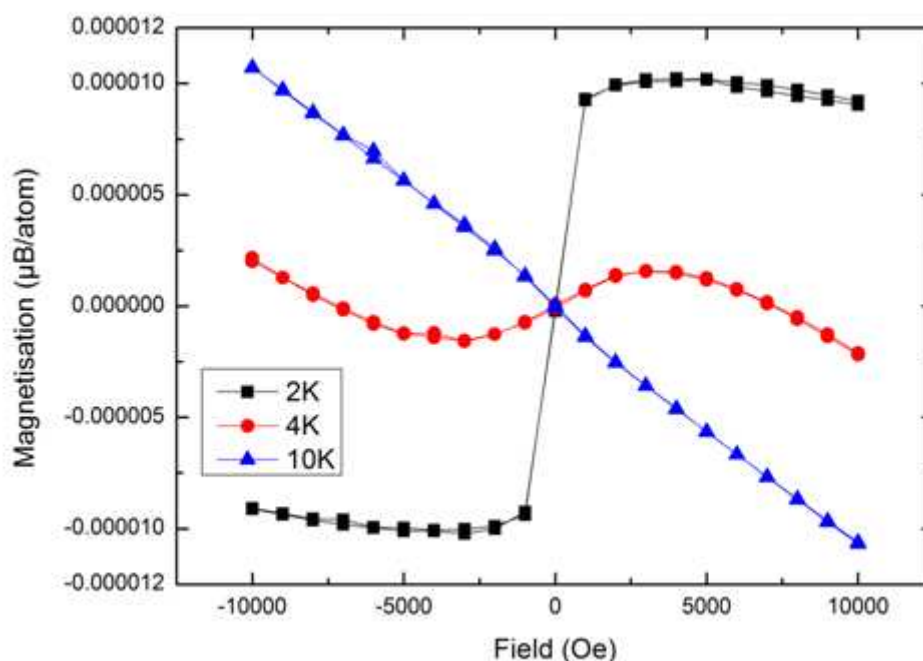
Figure 87: Hysteresis loop for pure pyruvic acid

5.5.2. *Dry Samples*

The above experiments have given a range of magnetisations that could be expected in the following experiments, it also shows that analysis of this data may not be straightforward. The dry sample data set is focused on checking the purity of the samples. For example, determining if the copper and copper oxide samples are independent of one another. Some micron-sized powders were also measured to show the effect of particle size on the magnetisation. The particles have been separated into groups that demonstrate strong and weak magnetic interactions at the 2 K.

5.5.2.1. *Strongly Magnetic Particles*

Figure 88 shows the hysteresis loop of various dry nanoparticles at 2 K. It can be seen that all of the particles, except copper oxide and magnesium oxide, show paramagnetic behaviour, as their magnetisations are linearly dependent on the external applied field. The magnesium oxide shows superparamagnetic properties, as it does not have an opening in

the hysteresis loop, but does have a saturation magnetisation. The copper oxide shows
ferromagnetic ordering as the hysteresis loop has an opening.
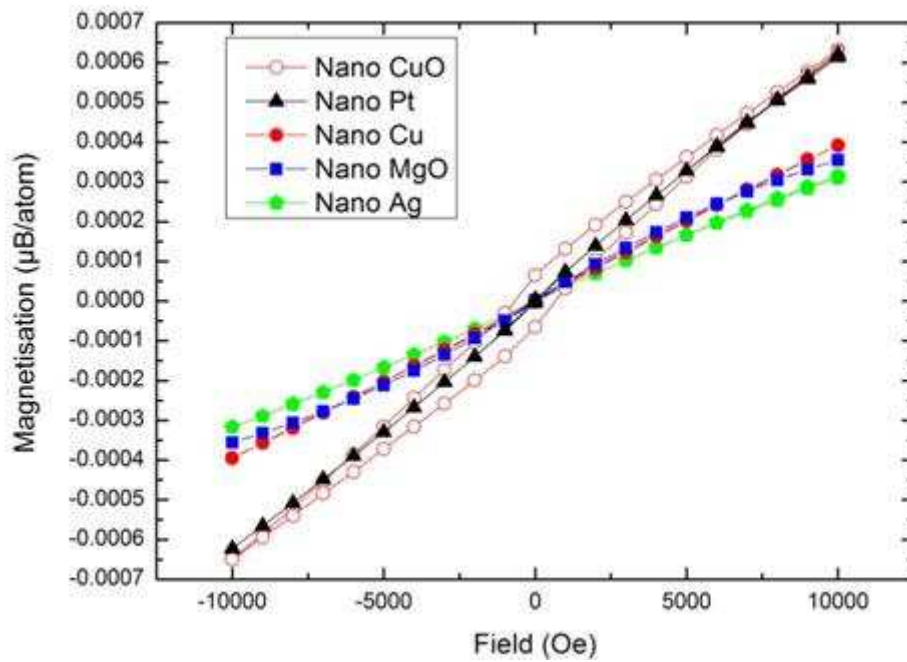
Figure 88: Hysteresis loop of the strongly magnetic particles at 2 K

Figure 89 shows that the copper oxide has a permanent magnetisation, as expected of a
ferromagnet. The Curie temperature of the copper nanoparticles is above 300 K, which
agrees with the literature (15).
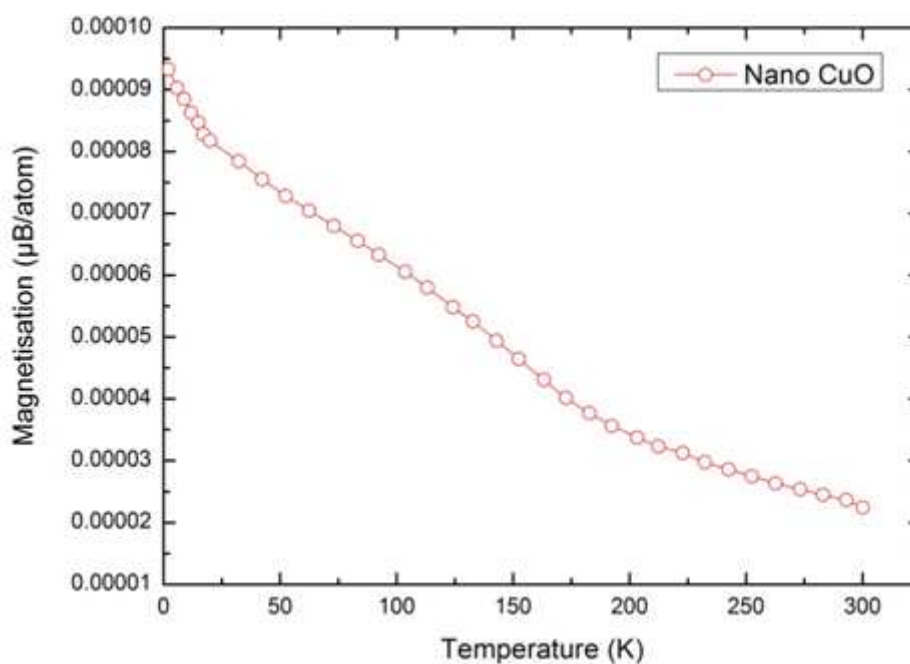
Figure 89: Zero field warming of copper oxide nanoparticles

Three samples of gold in different sizes (6 nm, 12 nm and 30 nm) had large magnetisations measured at the low temperatures. These samples have been separated from the other nanoparticles in this chapter because they have been capped with citric acid. Figure 90 shows that all three samples are diamagnetic, and interestingly, not in size order. In the literature the gold nanoparticles are normally capped with thiol groups rather than citric acid, therefore, comparing these samples to those in the literature is not possible (16,89).
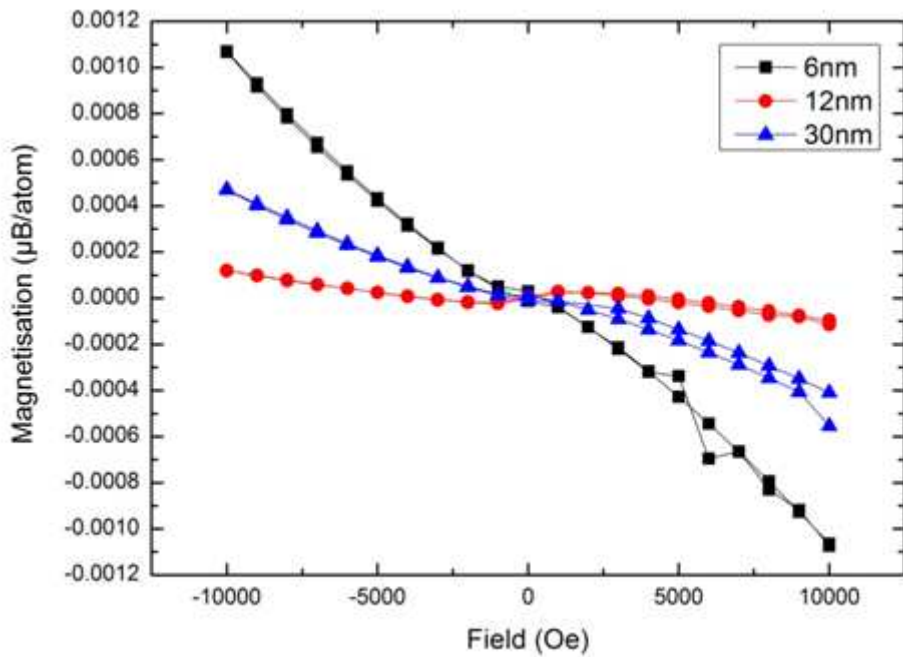
Figure 90: Hysteresis loop for nano gold samples at 2 K

These gold samples show a change in their magnetic ordering at around 50 K, as seen in Figure 91. The cause of the change in magnetic ordering could be due to impurities gained from drying out the gold samples.
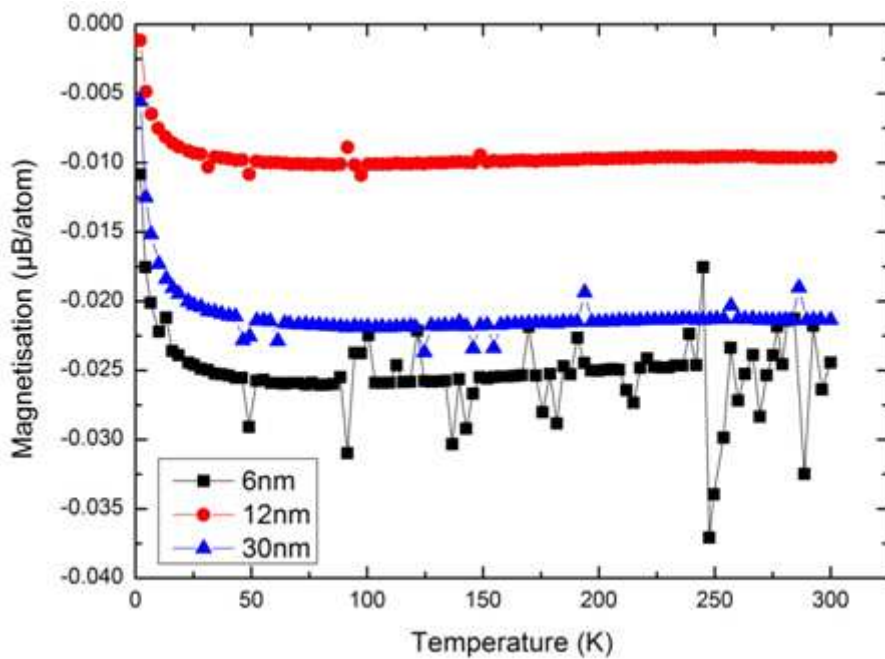
Figure 91: Field cooling of gold nanoparticle samples.

~ 166 ~

5.5.2.2. Weakly Magnetic Particles

Figure 92 shows the weakly magnetic particles at 2 K. The magnetic ordering of the samples in Figure 92 is much more diverse than those seen in Figure 88. The graphene and the micron-sized copper both show ferromagnetic properties, as they display an opening in the hysteresis loop and are tending towards a saturation magnetisation. The fact that graphene is ferromagnetic might be due to the layering of graphene (99). The micron-sized Aluminium shows paramagnetic ordering. The aluminium oxide and the tin oxide show super paramagnetic ordering. The tin's superparamagnetic ordering can be seen more clearly in Figure 93. Finally, both the nano-sized aluminium and the zinc oxide show diamagnetic behaviour.
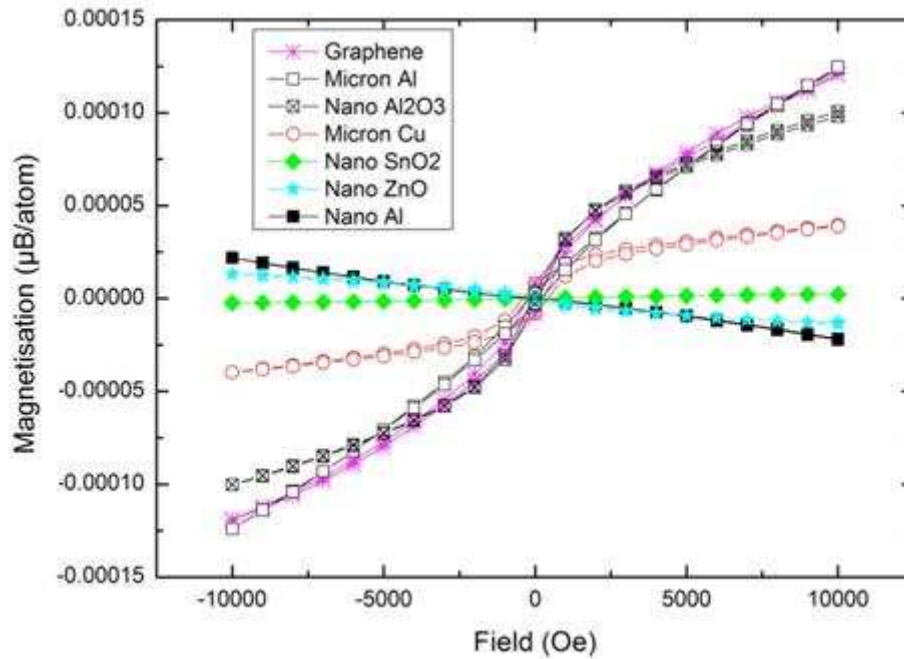
Figure 92: Hysteresis loop for weakly magnetic particles at 2 K
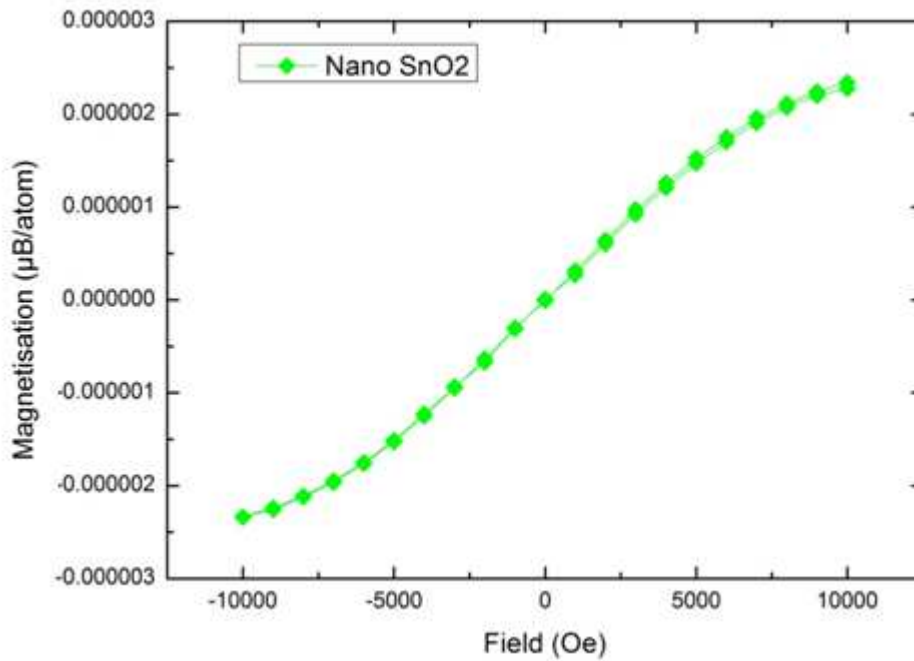
Figure 93: Hysteresis loop of tin oxide at 2 K

As both the graphene and the micron-sized copper show ferromagnetic behaviour, it is possible to find the Curie temperature by viewing the zero field warming of these samples. From Figure 94 it can be seen that the graphene has a Curie temperature of around 250 K, while the micron-sized copper's Curie temperature is much lower at around 100-150 K.
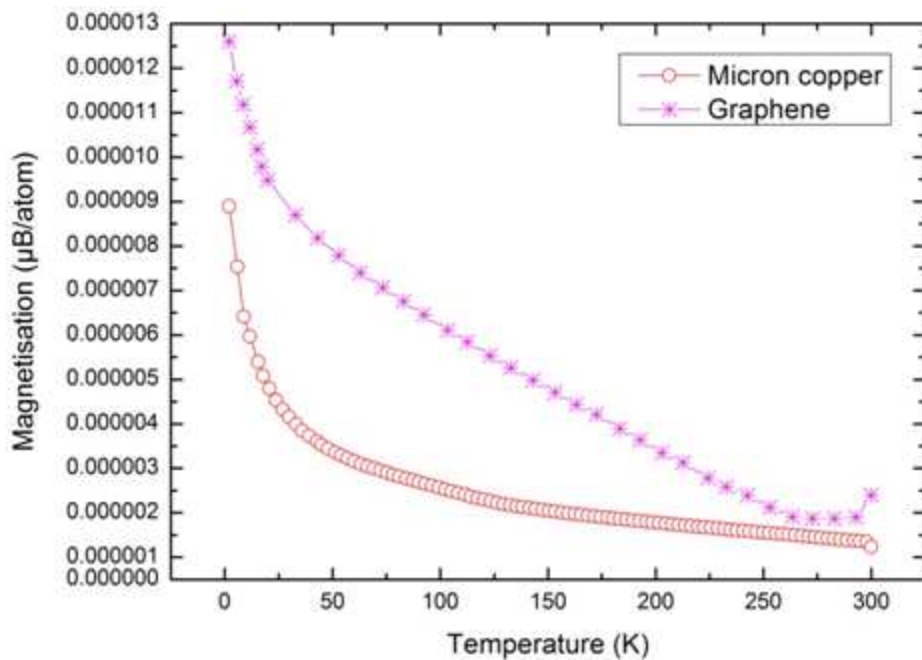
Figure 94: Zero field cooling of graphene and micron copper

~ 168 ~

5.5.2.3. Samples from SSnano

It was noticed during the field cooling experiments that samples from SSnano had diamagnetic properties above 50 K, and tended to show paramagnetic ordering below this temperature, as seen in Figure 95. This would raise suspicions that samples from SSnano have been contaminated.
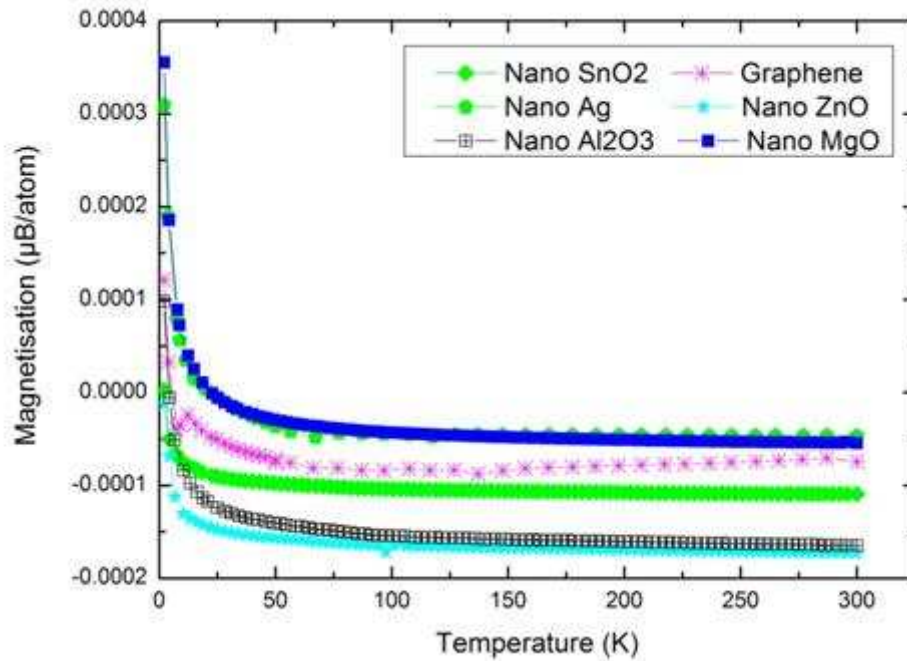
Figure 95: Field cooled experiment with the nanoparticles supplied by SSnano

5.5.3. Discussion

The first thing to note is the level of magnetisation of these dry samples are far lower than that of the tested copper-nickel and of the values obtained from the literature for iron and nickel (97).

Another important piece of information collected from this research is that the micron-sized copper, nano-sized copper and nano-sized copper oxide show different magnetic ordering and levels of magnetisation to one another. This is important for several reasons, the first is that it proves that the copper and copper oxide samples are independent to one another, therefore, the copper sample has not been fully oxidised into copper oxide. The

second reason is that this research demonstrates that the size of the particles is an important factor when considering the magnetic state of a sample. This means that changing the size of the particle affects both the level of contact between the particles and the potential solvent, but also the potential strength of the interaction itself.

The conclusions made with the copper and copper oxide samples are also seen in the micron-sized aluminium, nano-sized aluminium and nano-sized aluminium oxide samples. It should, however, be noted that bulk aluminium is a superconductor below 1.2 K and 0.01 T. These conditions could be experienced during transportation of the sample, if the temperature of the sample is very low during transport (100,101).

The metal oxides, silver and graphene, supplied by Skyspring, are all diamagnetic at high temperatures and become paramagnetic at around 25 K. This behaviour is suspicious, it suggests that either the background subtraction was not correct or the samples all have very similar magnetic properties, which seems unlikely. A conjecture which seems more plausible is that these samples contain multiple magnetic components, maybe from impurities, and these extra magnetic components are common to all of the samples. The nano copper, which was supplied by Skyspring, already displays a paramagnetic ordering, therefore, any contamination in the sample could already be masked by the paramagnetism of the copper.

5.6. *Magnetisation of Samples used in NMR Experiments*

The samples used in this section are identical to samples used in the NMR experiments in Chapter 4. This allows for cross referencing of data and to draw some conclusions between the NMR data and the magnetisation data.

5.6.1. *8:1 WG:Copper*

The WG:copper sample is paramagnetic, as seen in Figure 96. The level of magnetisation is similar to the dry copper sample, seen in Figure 88. The level of magnetisation in the WG:copper sample is slightly smaller than the dry copper sample; this suggests that the WG does not react with the copper and that the WG is adding a diamagnetic offset. It should be

reminded that only the mass of the nanoparticles are being considered in all of the samples that contain a solvent.
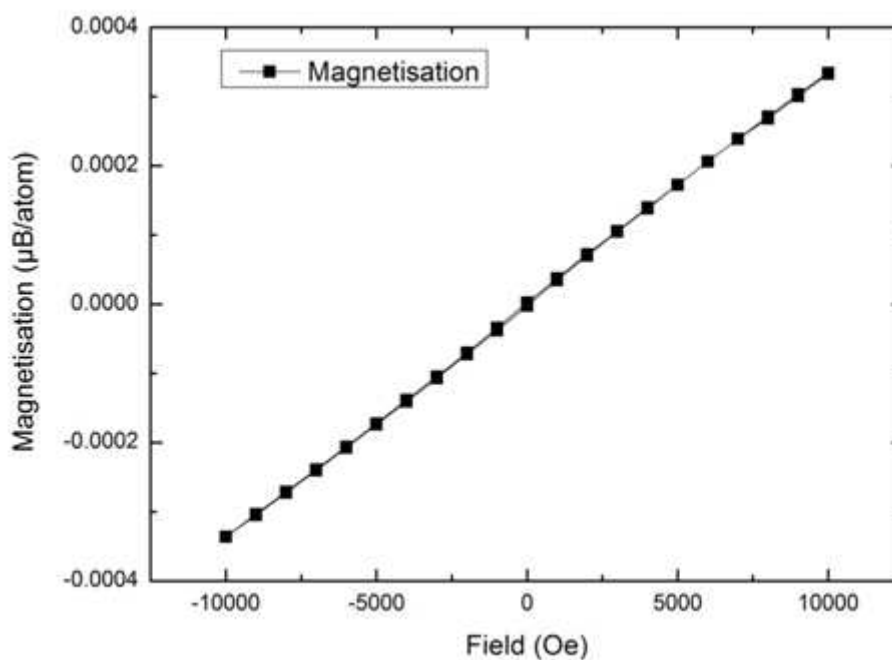
Figure 96: Hysteresis loop of 8:1 WG:copper at 2 K

5.6.2. *8:1 WG:Aluminium*

Figure 97 shows that this sample is more diamagnetic than the dry aluminium sample, suggesting that the WG is more diamagnetic than the aluminium nanoparticles. The idea that the WG is diamagnetic would agree with the results from Figure 96. To determine if WG is diamagnetic, a pure WG sample should be measured.
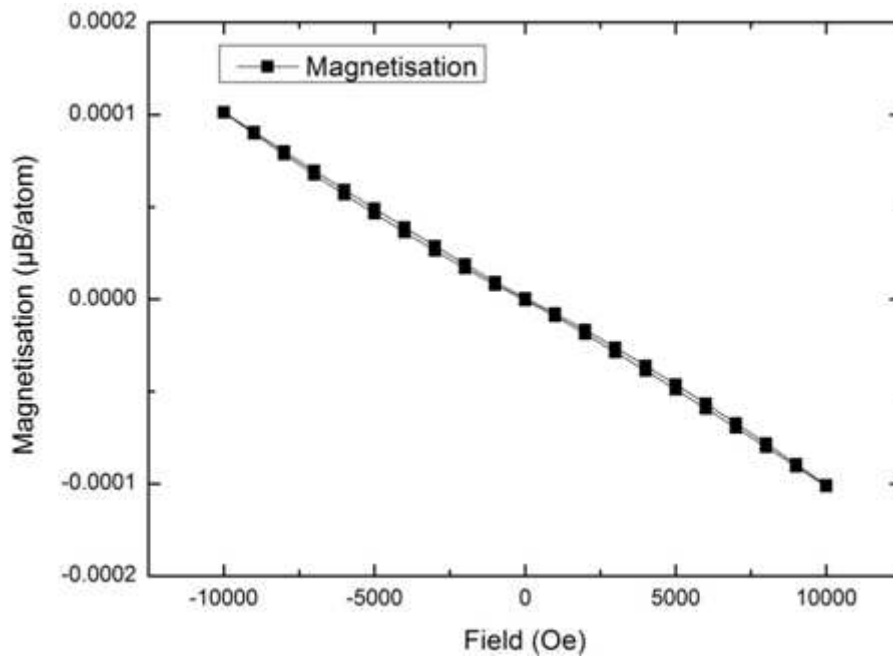
Figure 97: Hysteresis loop of 8:1 WG:aluminium at 2 K

5.6.3. *8:1 WG:Silver*

Figure 98 shows a very complicated hysteresis loop. It would appear that the sample comprises of a ferromagnetic and a diamagnetic component. The ferromagnetic component is suspected as there is an opening in the hysteresis loop, the diamagnetic component is suspected because the magnetisation gradient is negative at the high fields. The ferromagnetic component could be from an impurity in the sample or from an interaction between silver and WG. At a field of 2000 Oe the diamagnetic component is becoming dominant, this would suggest that the saturation magnetisation of the ferromagnetic component in the sample is quite small. It should be noted that there were no clear indications of an interaction between the WG and the silver, unlike Pyr and copper, which showed a colour change (see Figure 120) so it is more likely that an impurity has entered the sample.
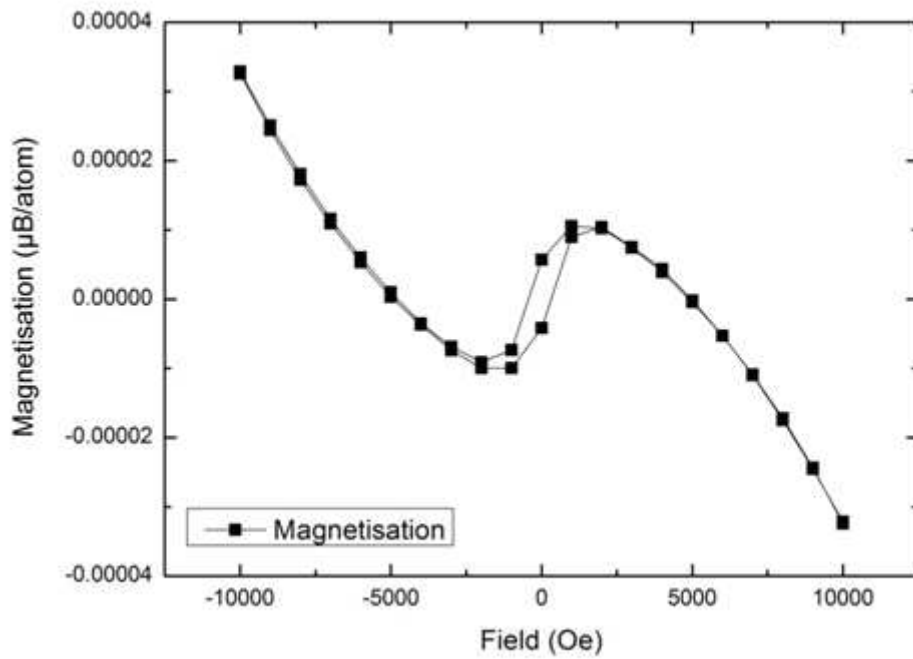
Figure 98: Hysteresis loop of 8:1 WG:silver at 2 K

In the zero field sweep, Figure 99, there seem to be two transition temperatures. These are at 20 K and 132 K. Exploring the magnetisation around these temperatures may give a clearer idea of the processes which produced the unusual hysteresis loop in Figure 98.
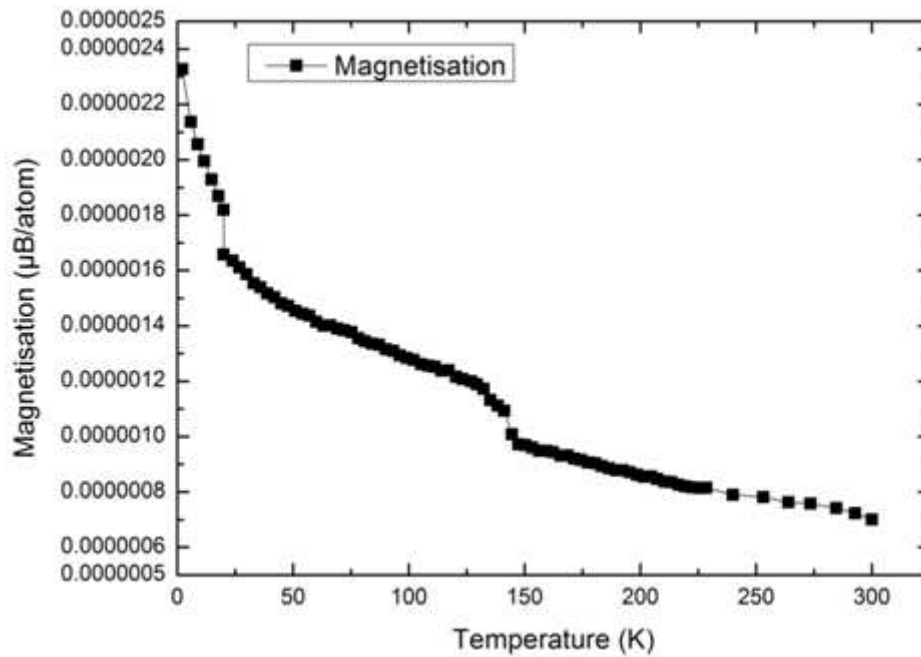
Figure 99: Zero field warming of 8:1 WG:silver

5.6.4. *Discussion*

The 8:1 WG:copper sample measured in this section has a very similar set of magnetic properties as the dry copper sample. This is expected, as the copper is very magnetic while the water is weakly diamagnetic and does not seem to be reacting with the sample, unlike other solvent. Samples which do show an interaction will be discussed in 5.8.

The 8:1 WG:aluminium sample also showed an increase in diamagnetism. Both the dry aluminium and pure water samples showed signs of diamagnetism, as shown in Figure 92 and Figure 86 respectively. If two sources of magnetisation are seen within a sample, it would be expected that the measured magnetisation would be a scaled summation of the two sources because only the metal mass within the sample is being considered. This result would suggest that the glycerol is diamagnetic. The glycerol is known to be slightly diamagnetic at room temperature, but its magnetic properties are not known at 2 K, the temperature at which these samples were measured (102).

The 8:1 WG:silver had the strangest results. First, consider the data in Figure 98. The sample shows a combination of both ferromagnetic and diamagnetic components. At the low fields, the ferromagnetic component is dominant, while at the higher fields the diamagnetic component is dominant. This is unusual as normally only one type of magnetic ordering is observed in a hysteresis loop. A possible explanation for this is that the sample consists of small quantity of a ferromagnetic component and a larger quantity of a weaker diamagnetic component. The ferromagnetic component must be limited in quantity so that the low saturation magnetisation can be dominate by the diamagnetic component at the higher fields. The likely cause of the ferromagnetic component is that there is an impurity in the sample as dry silver and pure water are both diamagnetic. It is also seen in the WG:copper and WG:aluminium samples that the WG makes the samples more diamagnetic than their dry metal counterpart. Other evidence for impurities can be found in Figure 99, as two transition temperatures can be observed at around 20 K and 130 K. If there was an interaction between the WG and silver, it would be expected to only see one transition temperature for that component, however, there is two transitions. These features do not appear in the dry silver sample (Figure 88) so might be from cross contamination caused by reusing the resealable SQUID container.

5.7. *Copper, Copper Oxide, Water, Pyr Samples*

In Chapter 4, a set of Pyr:copper samples displayed broad NMR lineshapes as the samples were cooled, this suggests that the samples are becoming very magnetic at the low temperatures. Upon measuring a Pyr:copper sample and finding a very large magnetisation, it was decided to investigate this phenomenon further. This section is dedicated to trying to understand the cause of the high levels of magnetism experienced by copper and copper oxide suspended in pyruvic acid and water. It should be noted that in this section Pyr will be abbreviated to P and water will be abbreviated to W.

5.7.1. *Pyr Dilution*

5.7.1.1. *8:1 Solution:Copper*

In Figure 100 the hysteresis loop of various 8:1 solution:copper samples are shown, all of these samples, except the 8:0:1 P:W:Cu, are paramagnetic. The maximum magnetisation of these samples depends upon the amount of Pyr in the sample. A larger ratio of Pyr produces more magnetic samples. The 8:0:1 P:W:Cu sample has a superparamagnetic hysteresis loop, however, the saturation magnetisation has not been reached. It should be noted that the measurements of the 8:0:1 P:W:Cu sample stopped at 4 K because the SQUID was overloaded.
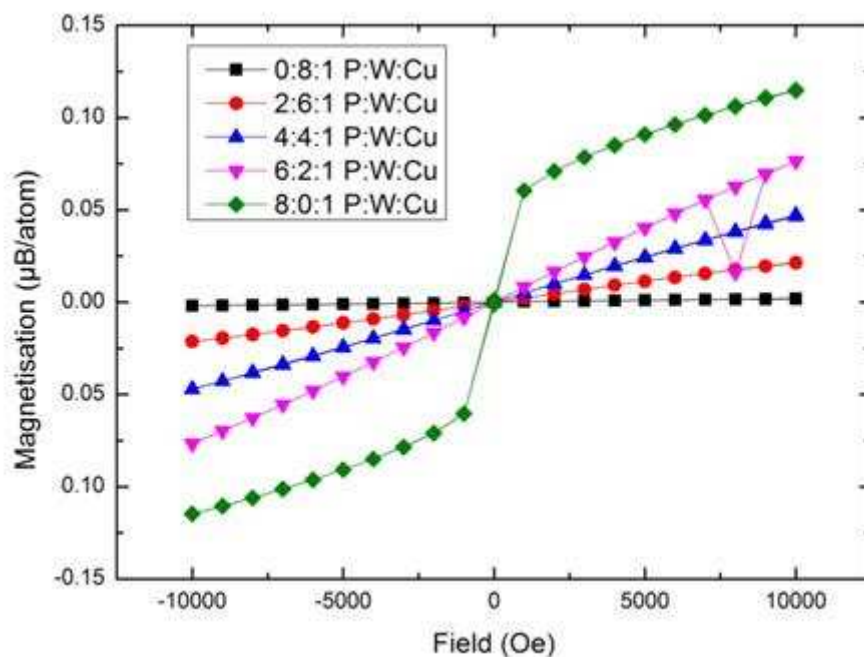
Figure 100: Hysteresis loops of 8:1 solvent:copper at 4 K

5.7.1.2. 16:1 Pyr:Copper

In this sample, the transition from paramagnetism to superparamagnetism can be seen. At 10 K it is clear that the magnetisation is linear dependent on field, demonstrating that the sample is paramagnetic. At 2 K the sample demonstrates a superparamagnetic hysteresis curve, as it features a saturation magnetisation and no opening in the hysteresis loop.
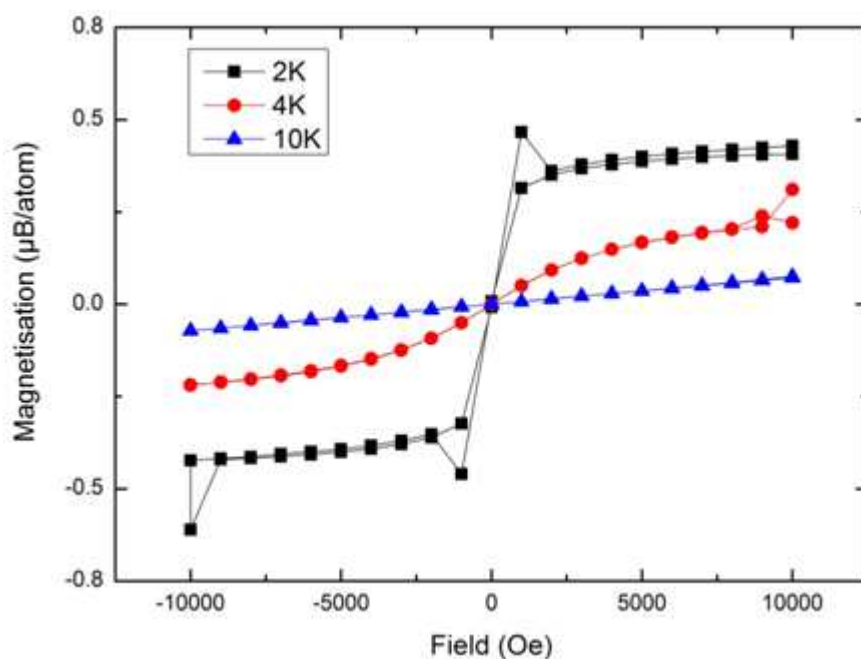
Figure 101: Hysteresis loops for 16:1 Pyr:copper at 2 K

5.7.1.3. 32:1 Solution:Copper

Figure 102 shows that the sample containing pure Pyr is superparamagnetic, while the other two samples both show a paramagnetic response. The 16:16:1 P:W:Cu shows a fork in the hysteresis curve, which would suggest that the sample has moved within the SQUID. The misalignment of the sample changes the measured magnetisation because the calibration has been lost. The measurement of the 16:16:1 P:W:Cu sample should be repeated, though it is expected that the measured magnetisation at 2 K and 10000 Oe will be 0.2 μB/atom.
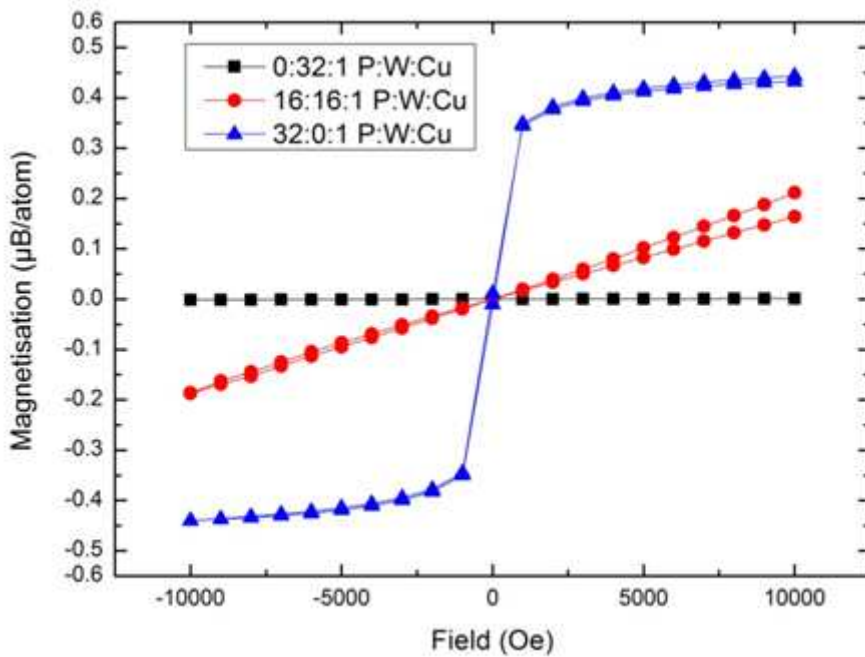
Figure 102: Hysteresis loop of 32:1 solvent:copper samples at 2 K

Figure 103 is an example of how the magnetism of the sample is strongly related to temperature. The SQUID is limited to T ≥ 2 K, but it would seem clear that the magnetism would keep growing at lower temperatures.
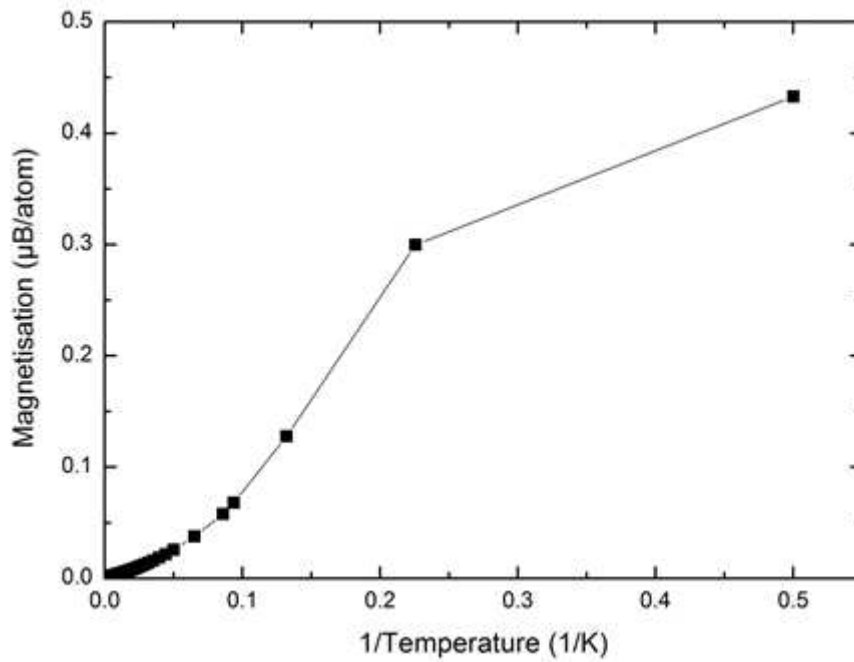
Figure 103: Field cooling of 32:1 Pyr:copper

~ 178 ~

5.7.1.4. 64:1 Pyr:Copper

Figure 104 shows the transformation from a paramagnetic response to a superparamagnetic response as the temperature decreases to 2 K. This is similar to the 16:1 Pyr:Copper sample in Figure 101, though the transition in the 64:1 Pyr:copper is much clearer.
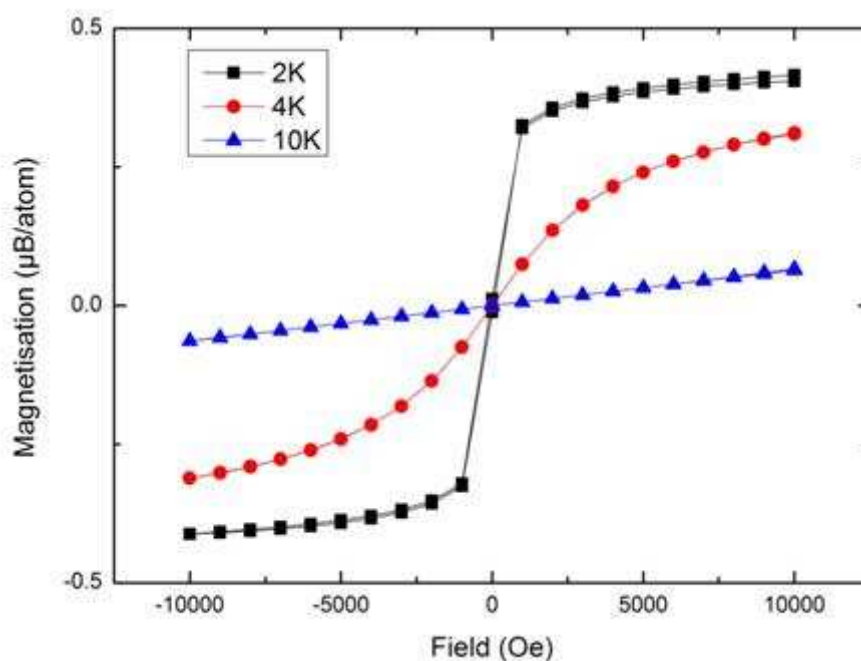
Figure 104: Magnetisation transition of 64:1 Pyr:copper as a function of temperature

5.7.1.5. 128:1 Solution:Copper

Figure 105 is more complicated than the previous figures, due to reactions between the copper and Pyr. For example, the 64:64:1 P:W:Cu sample seems to undergo a non-homogeneous reaction whereby two layers of material are produced, a green layer and a purple layer. There are more details about the colours of the samples in Section 5.9.

A Pure 128:0:1 P:W:Cu shows superparamagnetic ordering like the other pure Pyr:copper samples. The 64:64:1 P:W:Cu sample was measured several times taking each layer of the sample and a mixture of the two layers. These measurements were made to try

to capture the effect of each reaction pathway. The mixed layer sample was run only several hours after the sample was made, the green and purple layers were run 24 and 48 hours later respectively.

Another noteworthy point is that the individual layers of the 64:64:1 P:W:Cu sample have a larger magnetisation than the 128:0:1 P:W:Cu sample. The 128:0:1 P:W:Cu sample was run only hours after being produced, while the individual layers of the 64:64:1 P:W:Cu sample were measured between 24 and 48 hours after production. The fact that the 64:64:1 P:W:Cu sample is more magnetic that the 128:0:1 P:W:Cu sample is unusual, this is because in every other set of experiments so far, the samples with the higher ratios of Pyr to water have the largest magnetisations. This implies that the chemical reaction between Pyr and copper takes longer than several hours to reach completion. Magnetic measurements of a copper oxide sample show that the reaction time between Pyr, water and copper oxide is in the order of 24 hours, which supports the above claim. These copper oxide results can be seen in section 5.7.1.7.
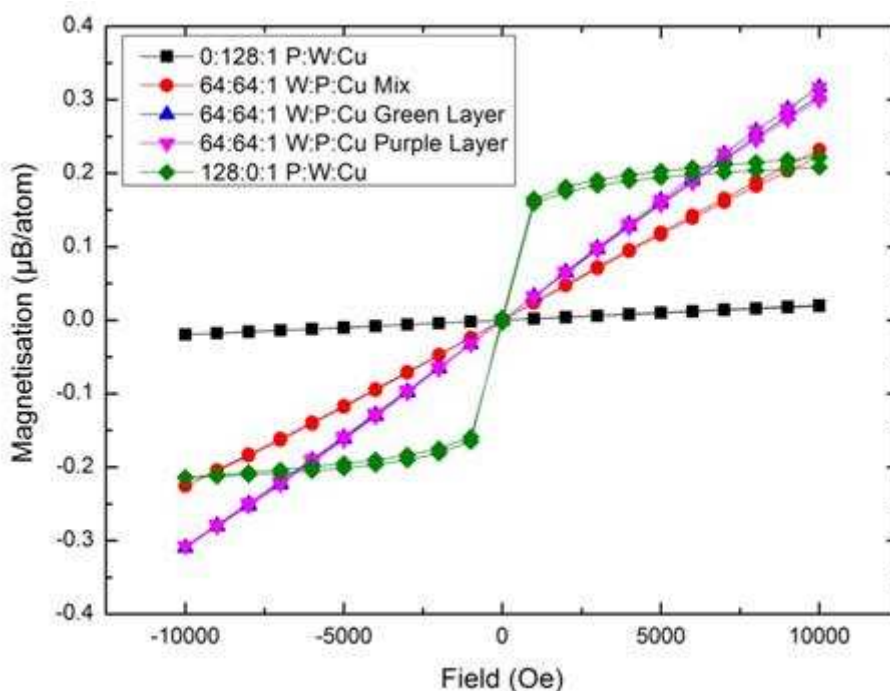
Figure 105: Hysteresis loops for 128:1 solvent:copper at 2 K

5.7.1.6. 32:1 Solution:Copper Oxide

There are several important observations to be made about these copper oxide samples. The first is that the magnetisation of these samples is an order of magnitude lower than the equivalent copper samples. The second point is that the copper oxide samples also display the same magnetic ordering dependence on Pyr i.e. samples with little Pyr are paramagnetic while samples only containing only Pyr and copper oxide are superparamagnetic. This supports the idea that the Pyr is interacting with the copper in the copper oxide. The final observation is that the 16:16:1 P:W:CuO has a larger magnetisation than the 32:0:1 P:W:CuO at 10000 Oe. A similar effect was seen in the 128:1 solvent:copper sample, as seen in Figure 105. The reason why the 16:16:1 P:W:Cu has a larger magnetisation could be because it had a longer time for any chemical reactions to occur, as this sample undergoes a similar, if not the same, chemical reaction as the copper sample.
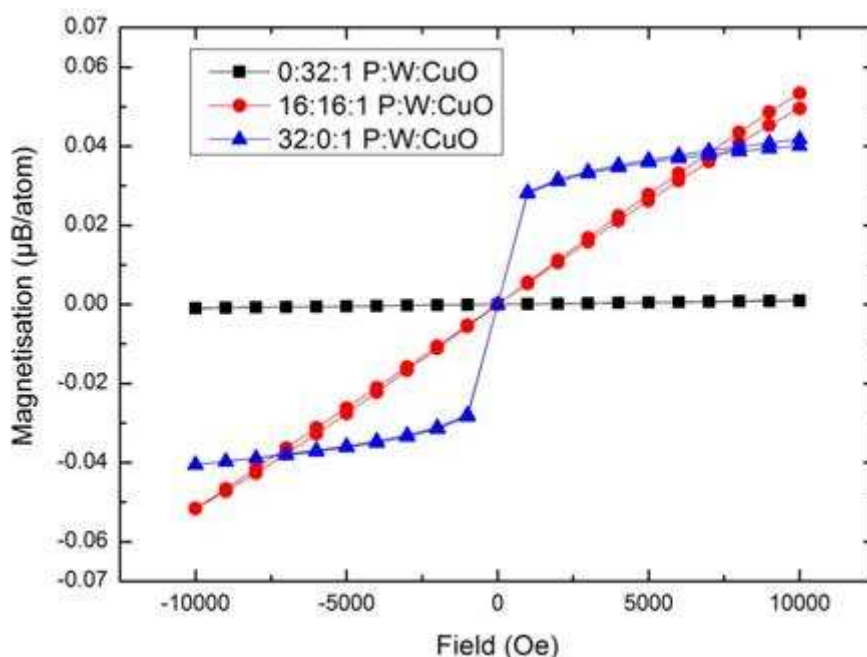
Figure 106: Hysteresis loops for 32:1 solvent:copper oxide at 2 K

5.7.1.7. 64:64:1 Pyr:Water:Copper Oxide

Figure 107 shows the magnetisation of a 64:64:1 Pyr:water:copper oxide evolving over several days. It can be seen that the reaction requires between 2 and 24 hours to reach

completion. This was determined by comparing the magnetisation after different times. The increase in the level of magnetisation in this 24 hour period is around a factor of 3, therefore, demonstrating that the time between sample production and measurement needs to be more strictly controlled.
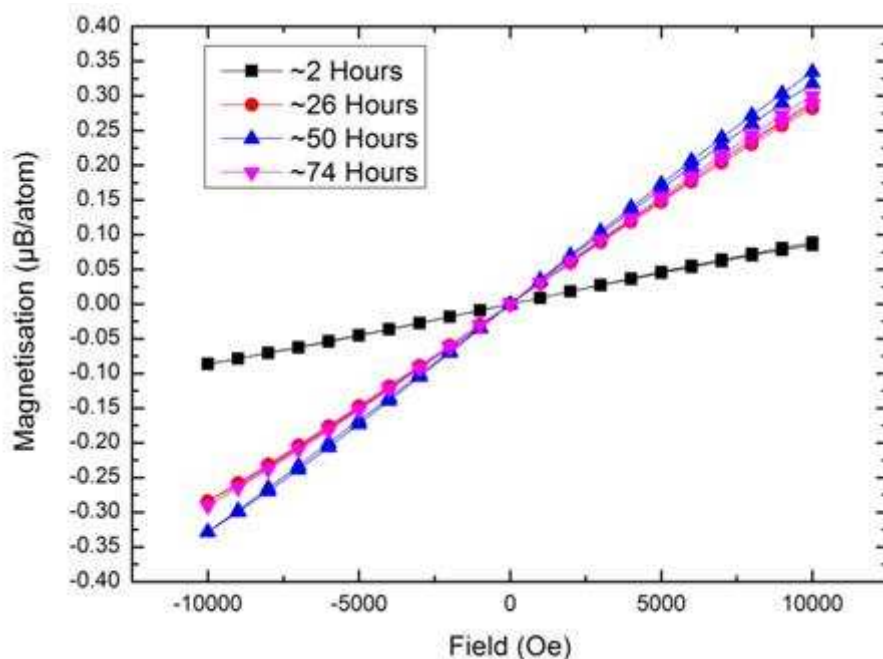
Figure 107: Hysteresis loops for 64:64:1 P:W:CuO at 2 K after different reaction times

5.7.2. *Copper Dilution*

The data collected in this section can be scaled such that the magnetisation of the sample can be compared to the available solvent allowed to mix with the copper. This re-arrangement gives a different perspective of the above data.

5.7.2.1. *Pure Pyr:Copper Samples*

Figure 108 seems to show that the 16:0:1, 32:0:1 and 64:0:1 P:W:Cu samples have very similar magnetisations. It would be expected that the 128:0:1 P:W:Cu sample would also lie near the other curves, however, this is not the case. The reason for the decreased magnetisation in the 128:0:1 P:W:Cu is probably due to a shortened period of time between

sample production and measuring. The lower magnetisation in the 8:0:1 P:W:Cu is because the measurement was taken at 4 K because the SQUID was overloaded at 2 K.
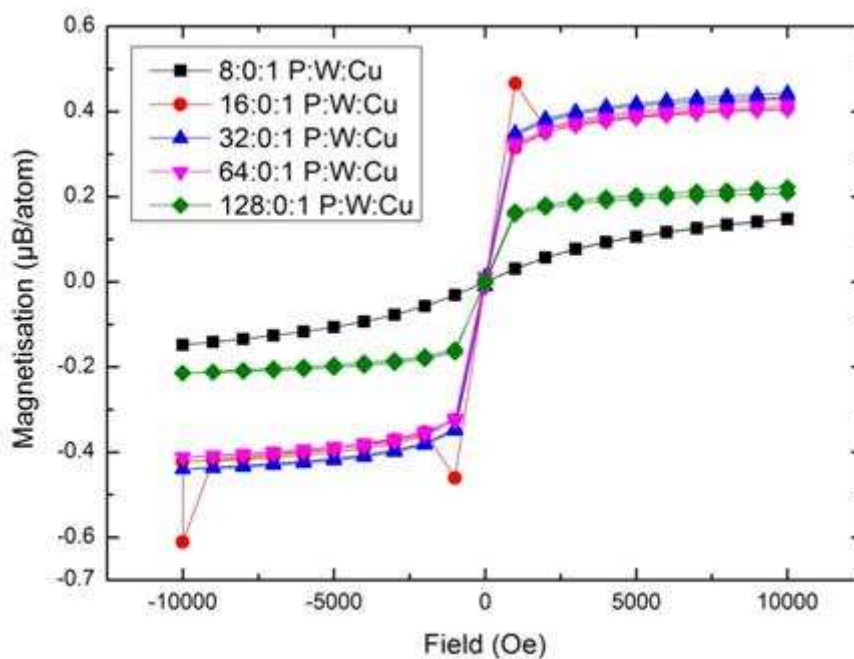
Figure 108: Hysteresis loop for various dilutions of Pyr:copper samples at 2 K, except the 8:0:1 P:W:Cu, which was run at 4 K.

5.7.2.2. 1:1 Pyr:Water Samples

Figure 109 shows that the 16:16:1 P:W:Cu and 64:64:1 P:W:Cu mixed layers sample have similar magnetisations. The green and purple layers of the 64:64:1 P:W:Cu are slightly more magnetic and is probably due to them having extra time for any reactions to conclude, as it was measured over 24 hours after production. The 4:4:1 P:W:Cu is the least magnetic and is probably because of the limited amount of Pyr to react with the copper.
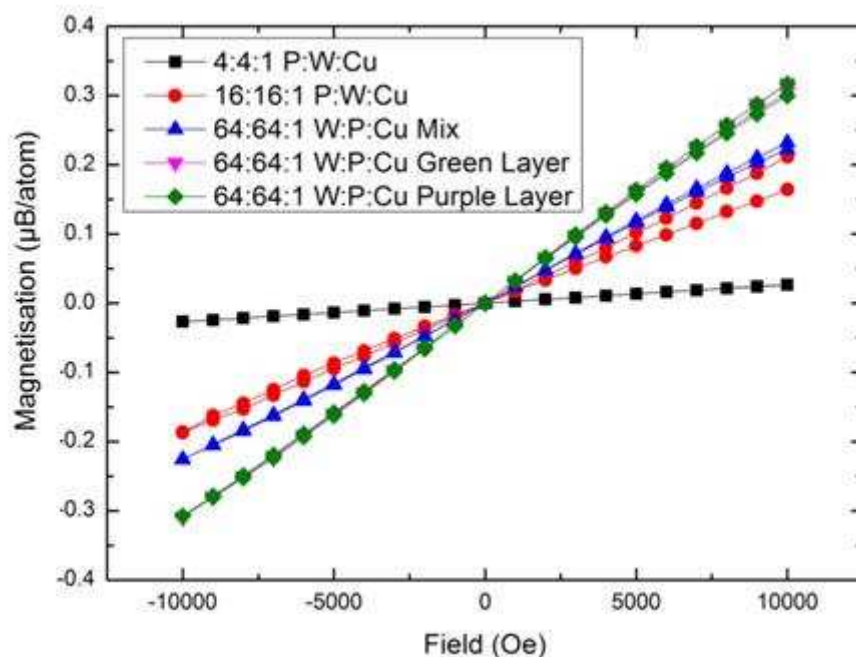
Figure 109: Hysteresis loop for various dilutions of Pyr:water:copper samples at 2K

5.7.2.3. Pure Water Samples

The most striking observation from Figure 110 is that the magnetisation of the 0:128:1 P:W:Cu is an order of magnitude larger than the 0:8:1 and 0:32:1 P:W:Cu. This is a strange outcome as the water:copper samples did not seem to undergo any reaction and therefore should have similar magnetisations. The cause of the heightened magnetisation could be that the sample was contaminated. Another observation is that all of these samples have a larger magnetisation than the dry copper sample, even though it would be expected that the water in the sample, being diamagnetic, would reduce the signal.
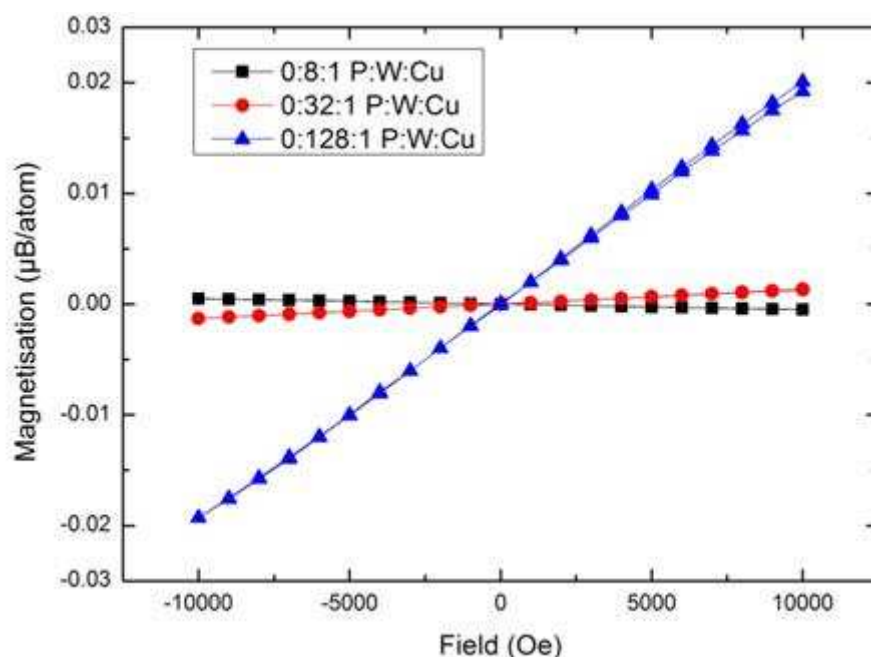
Figure 110: Hysteresis loop for various dilutions of water:copper samples at 4 K

5.7.3. *Summary of Copper, Copper Oxide, Water, Pyruvate Mapping*

Both copper and copper oxide samples, which contain Pry and no water, show high levels of magnetisation, around 60% of the saturation of Nickel, and they also show superparamagnetic behaviour at 2 K (97). Above ~2 K these samples show paramagnetic behaviour. The high level of magnetisation is believed to be due to a chemical reaction between the Pyr and the copper in the samples, this is because a colour change is also observed. The idea of a chemical reaction is supported by the data in Figure 107, which showed that after the 26 hours a copper oxide sample's magnetisation increased by a factor of 3. Some of the anomalies in this section, for example, the 128:0:1 P:W:Cu being less magnetic than the 16:0:1 P:W:Cu, can be explained by the lack of strict time controls between sample production and measurement.

Copper samples which contain both water and Pyr show paramagnetic ordering down to 2 K, with the maximum magnetisation depending on the ratio of Pyr in the sample, as demonstrated in Figure 111. In samples with large quantities of Pyr and water, for example, the 64:64:1 P:W:Cu, the magnetisation is greater than some pure Pyr:copper samples. This is

~ 185 ~

because the pure Pyr:copper samples have a limited quantity of Pyr to react with the copper.
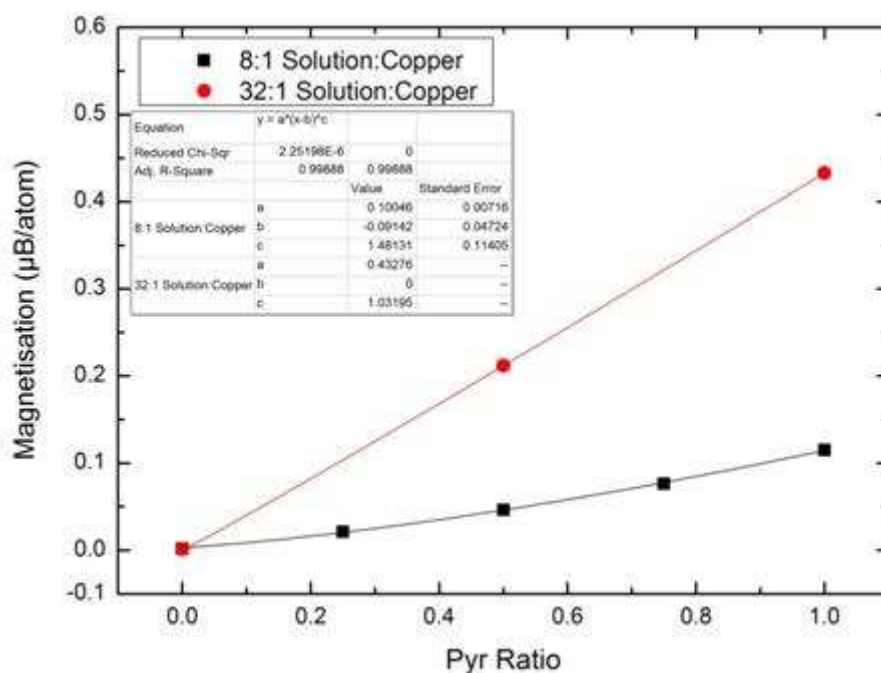
Figure 111: Magnetisation dependence on pyruvic acid in P:W:Cu samples

Another interesting point is that the water:copper samples are more magnetic than the dry copper samples. Figure 86 shows that water is diamagnetic, therefore, it would be expected that the measured magnetisation of the water:copper sample would be smaller than a pure copper sample. However, the water:copper samples are more magnetic, this suggests that the water is interacting with the copper. This raises questions about the WG:copper sample measured in Section 5.6.1. The WG:copper sample showed similar magnetic properties to the dry copper sample, suggesting that the water and glycerol does not react with the copper, while the data from Figure 110 shows otherwise. It could be possible that contaminants have entered the water:copper sample, but due to the reproducibility of these results across several samples, it limits the possibility of a contaminant.

5.8. *Copper and Copper Oxide in Other Solvents*

As there is uncertainty surrounding the measured magnetisation of dry copper, 8:1 WG:copper and 8:1 W:copper (Figure 88, Figure 96 and Figure 110 respectively) further experiments with copper and copper oxide dissolved in various solvents have been conducted. The solvents tested in this section are being used to identify which properties of the solvent are required to obtain high levels of magnetisation, similar to that of the Pry:copper samples. In many of these experiments, the colourations of the samples change, showing that some reaction has taken place.

5.8.1. *1 M Copper Sulphate*

The effects which produced the magnetic properties in the nanoparticles, like quantum confinement, are expected to be at their maximum when the sample contains free ions. A 1 M copper sulphate sample was measured as it shows the magnetisation of free copper ions. This sample is the most paramagnetic material tested in this chapter and is probably because of the free copper ions. Figure 112 shows the hysteresis loops of the 1 M copper sulphate at 2 K, 4 K and 10 K. As these copper ions are very magnetic, even more so than the Pyr:copper samples, it would suggest that the chemical reaction between the Pyr and copper is producing copper ions.
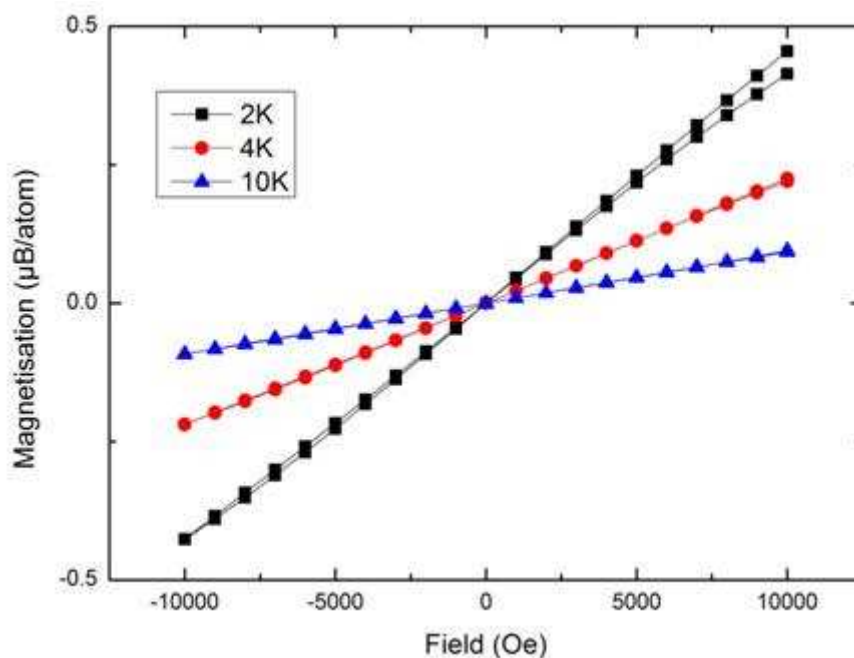
Figure 112: Hysteresis loops of 1 M copper sulphate in water

5.8.2. *8:1 Acetic Acid:Copper*

Acetic acid was tested because it has a similar chemical formula to the Pyr and was expected to produce a very magnetic sample, however, this was not the case. The acetic acid:copper sample has a level of magnetisation between that of the dry copper sample and the water:copper samples. The acetic acid sample demonstrates paramagnetic behaviour, as seen in Figure 113, unlike the Pyr:copper samples which are superparamagnetic. The acetic acid does undergo a reaction with the copper, as it produced a blue solution.
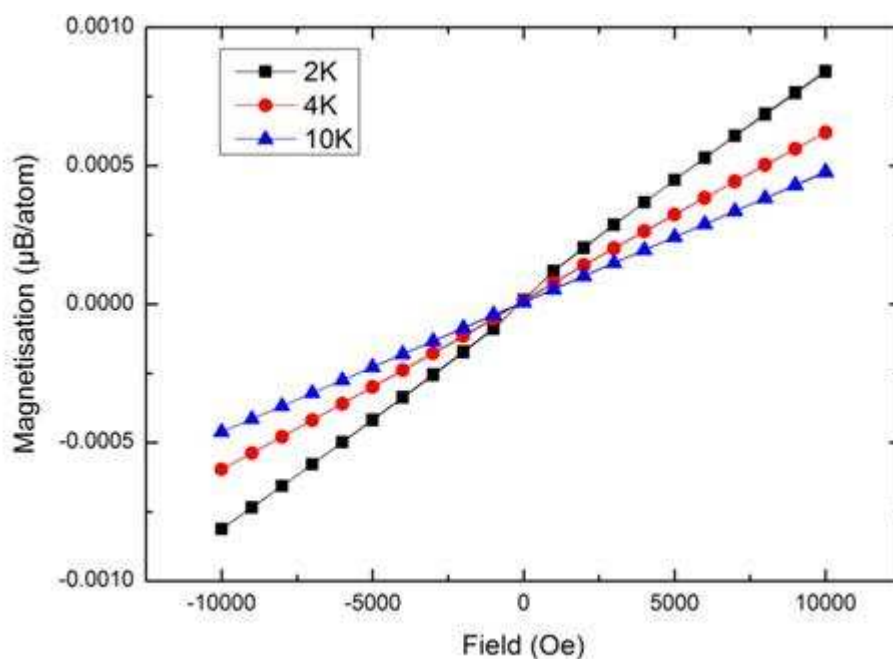
Figure 113: Hysteresis loops for 8:1 acetic acid:copper

The acetic acid has a remarkable field cooling curve, as seen in Figure 114. It does not follow any of the normal magnetisation curves. The decrease in magnetisation, at 250 K, would suggest that the sample is antiferromagnetic or ferrimagnetic below this temperature range. The increase in magnetisation at 50 K and below 6 K, would suggest that there is another source of magnetisation in the sample.

~ 189 ~
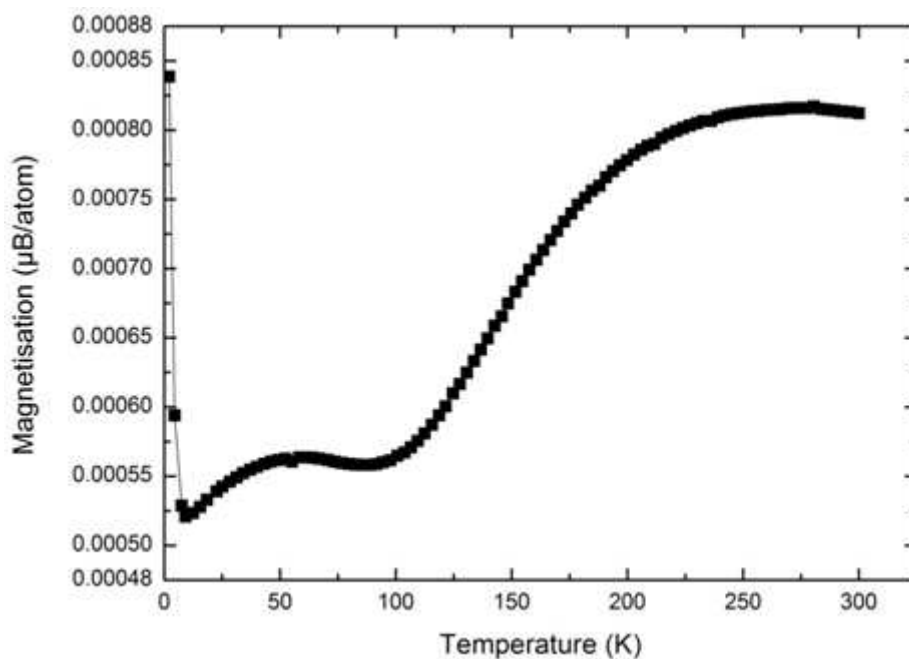
Figure 114: Field cooled 8:1 Acetic acid:copper

5.8.3. *128:1 Acetic Acid:Copper Oxide*

This Acetic acid:copper oxide sample is blue in colour, similar to the 8:1 acetic acid:copper in this section. A higher ratio of acetic acid was used in this sample so that there was no excess copper. This sample is paramagnetic, but slightly less magnetic than the 8:1 acetic acid:copper, as seen in Figure 115. This suggests that the samples are reacting in a similar way to one another.

~ 190 ~
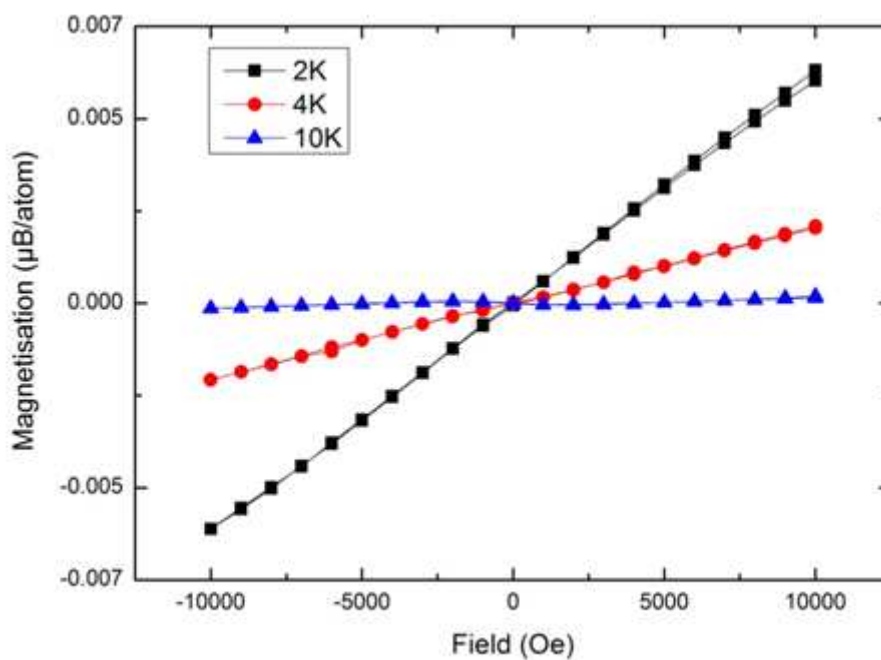
Figure 115: Hysteresis loops of 128:1 acetic acid:copper

5.8.4. *128:1 Acetone:Copper Oxide*

The 128:1 acetone:copper oxide sample is not very magnetic and appears to change magnetic ordering between 10 K and 2 K, as seen in Figure 116. The transition between diamagnetic and paramagnetic ordering is also seen in the field cooled experiment. This transition occurs at 15 K, as seen in Figure 117. The origin of his transition is not known.
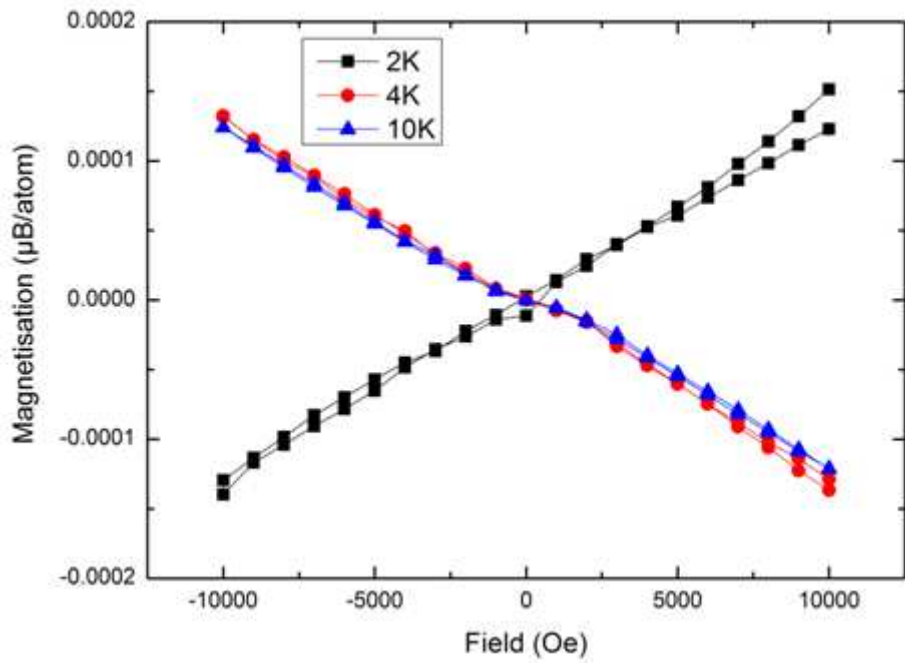
Figure 116: Hysteresis loops of 128:1 acetone:copper oxide
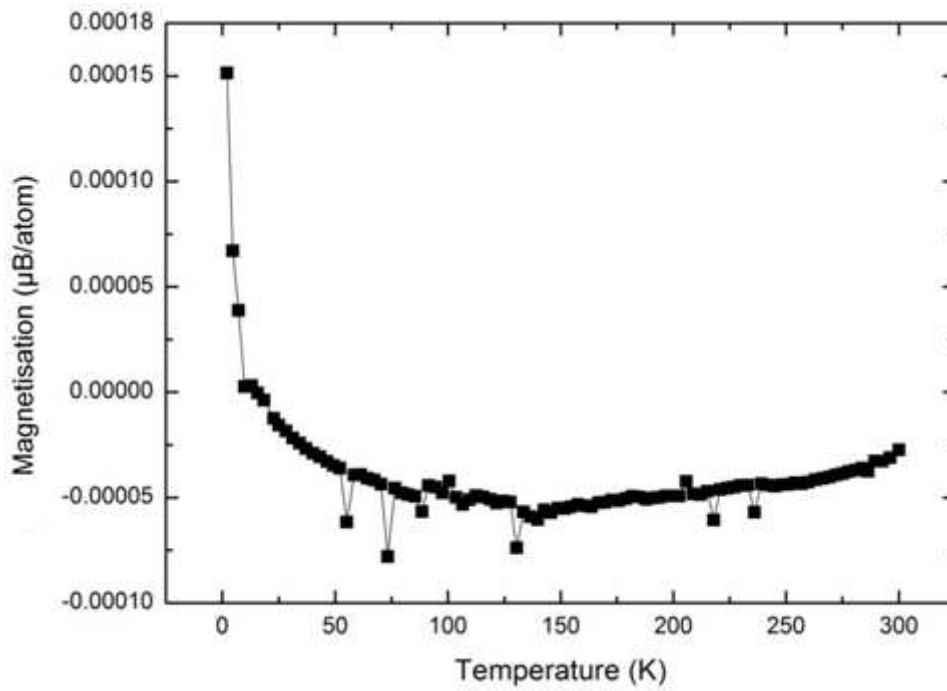
Figure 117: Filed cooling curve of 128:1 acetone:copper oxide at 1 T

5.8.5. *8:1 Buffered Pry:Copper*

A sample of buffered Pyr:copper was produced by adding an appropriate amount of NaOH to the Pyr before mixing it with the copper. The result of the neutralisation has meant that the sample is less magnetic than the earlier tested Pyr:copper samples. The buffered sample does not demonstrate superparamagnetic behaviour and the level of magnetisation is a factor of 30 smaller than the Pyr:copper sample, as seen in Figure 118. The observed colour change is also different compared to other Pyr:copper samples. The colour changes of all of the samples have been documented in Section 5.9.
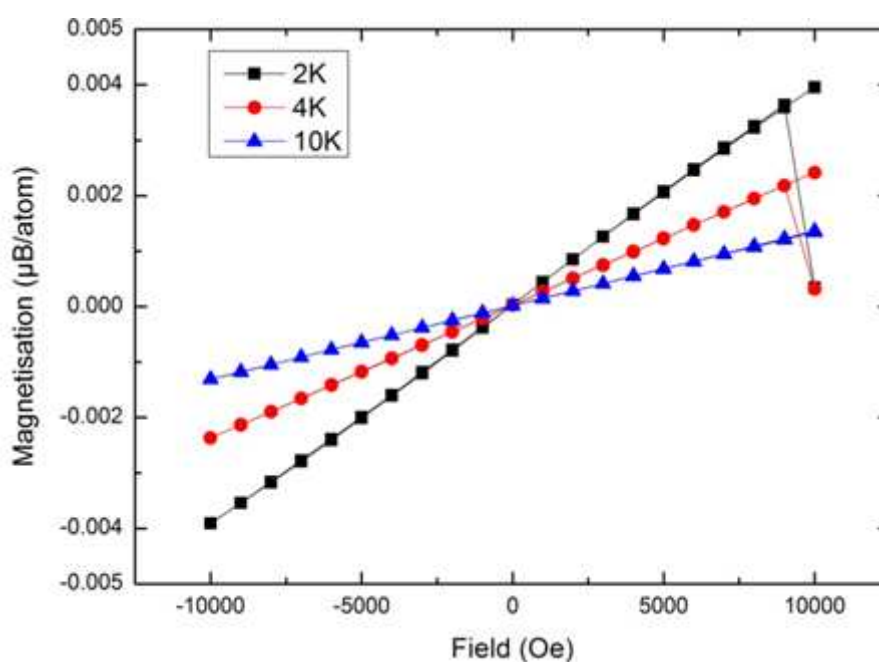
Figure 118: Hysteresis loops of buffered 8:1 Pyr:copper

5.8.6. *128:1 Oxalic Acid:Copper Oxide*

The data from the acetic acid and Pyr samples suggest that the acid group from the solvent is the cause for the increased magnetism. This initiated the idea of using oxalic acid as a solvent because it is a small organic molecule with two acid groups. The magnetisation of oxalic acid:copper oxide sample is higher than most samples, however, is still a factor of

100 less than Pry:copper samples. Figure 119 shows a transformation of the magnetic ordering for this oxalic acid:copper oxide sample, from diamagnetism to paramagnetism between 10 K and 2 K. The oxalic acid clearly reacts with the copper oxide, as a colour change is observed, however, the sample separates into two layers, one is a light blue while the other is clear. The sample was shaken to mix the two layers before these SQUID measurements.
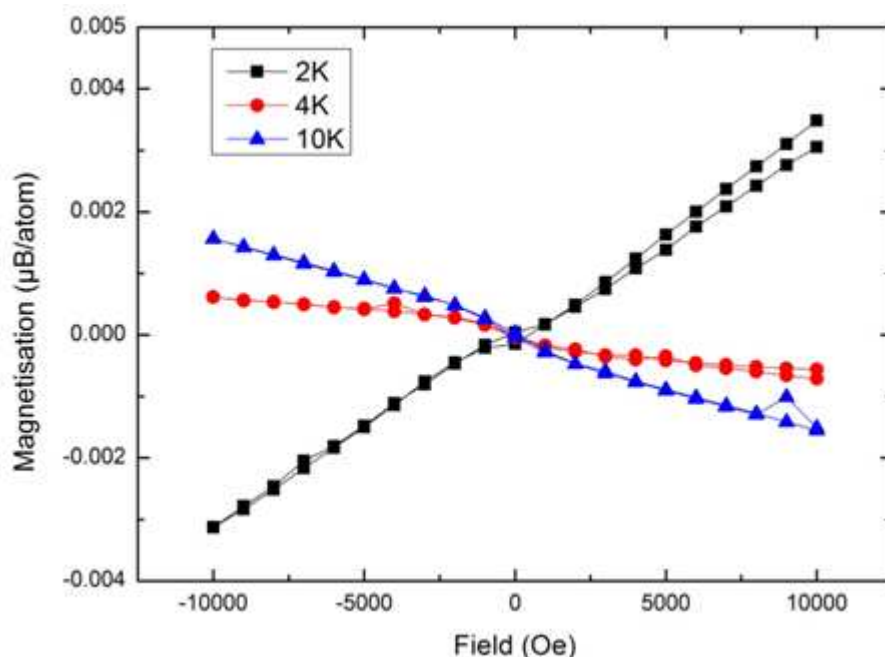
Figure 119: Hysteresis loop for 128:1 oxalic acid:copper oxide

5.8.7. *Summary of Copper and Copper Oxide in Various Solutions*

There is a clear difference in the magnetisation of the samples depending on the solvent used. Samples that contain a solvent with an acid functional group, generally have larger magnetisations than other samples. These samples tend to also experience a colour change, which is a clear indication that there is an interaction between the solvent and the solute. In the cases where there are no colour changes, for example, acetone:copper oxide, the levels of magnetisation are generally much smaller than when an organic acid was used.

The 1 M copper sulphate sample has the largest measured magnetisation from the samples measured in this chapter, it is almost as magnetic as nickel (97). The cause of the

high levels of magnetism in the copper sulphate sample is believed due to it containing free copper ions. In the cases where the copper and copper oxide samples were dissolved in acids, the increased magnetisation could be due to the nanoparticles in the sample being reduced in size, or converted into free copper ions. This would make the copper and copper oxide samples more like the copper sulphate sample and therefore more magnetic.

5.9. *Sample Colours*

In the previous sections it was noted that many of the samples changed colour when exposed to various solvents. A colour change indicates that the sample has undergone a chemical change. This section documents the various colour changes of the samples.

5.9.1. *Copper in Pyr*

Figure 120 shows the colour variations of the Pyr:copper samples. The 128:1 water:copper, the left most sample, shows the colour of all of the copper samples when they are first mixed. Copper samples start out as a black liquid with a viscosity similar to water. The Pyr:copper samples in Figure 120 are a mixture of two layer, the colour of these layers are a dark red/purple, which is probably the copper dominated part of the sample and a yellow/green colour, which is probably the Pyr dominated part of the sample. As two colours are observed, it could suggest that the copper is in two different oxidation states.

Obviously the samples with a small amount of solvent are more viscous, or in some cases, still a powder. However, samples which contain Pyr are more viscous than samples than the equivalent sample which contains water. The 128:1 Pyr:copper has a yellow liquid above the copper, however, moving the sample to take the photo mixed the two layers together.

Figure 120: Various samples of Pyr:Copper. From left to right 1) 128:1 Water:Copper, this is acting as a control colour. 2) 16:1 Pyr:Copper. 3) 32:1 Pyr:Copper. 4) 64:1 Pyr:Copper. 5) 128:1 Pyr:Copper.

Figure 121 shows the various dilutions of solvent:copper with equal parts, by volume, of water and Pyr. As the absolute volume of water and Pry are increased, the quantity of sample, which is green, increases, suggesting that the green part of the sample is the Pyr. It should be noted that the 64:64:1 Pyr:water:copper sample has both a green and purple layer. The green layer is on top of the purple layer, so from Figure 121, it looks as though the 64:64:1 Pyr:water:copper is completely green.

Figure 121: From left to right 1) 4:4:1 water:Pyr:copper 2) 16:16:1 water:Pyr:copper 3) 64:64:1 water:Pyr:copper

5.9.2. *Copper Oxide in Water and Pyr*

The copper oxide samples, which contain Pyr and water, behave in a similar way as the analogous copper sample. The samples with high dilutions of Pyr and water, separate into purple and green layers, similar to the 128:1 Pyr:Cu and 64:64:1 P:W:Cu samples. The

64:64:1 P:W:Cu sample was mixed in Figure 122. The potential chemical reactions for copper and copper oxide samples mixed with Pyr can be found in Section 5.10.

Figure 122: Colouration of 64:64:1 P:W:CuO

5.9.3. *8:1 Buffered Pyruvic Acid:Copper*

The buffered Pry:copper sample underwent a slower reaction, as it took several days before a colour change was observed. The slow colour change would suggest that the sample was not made perfectly neutral.

Another point which should be made, is that even though this sample in Figure 123 has a low dilution, 8:1 solution:copper, the product is still a liquid, unlike an 8:1 Pyr:copper sample, for example, which is more like a paste.

Figure 123: Colouration of 8:1 buffered pyruvic acid:copper

5.9.4. *1 M Copper Sulphate*

It is well known that copper sulphate solutions are blue and Figure 124 has been added as a reference. The blue colouring of the copper sulphate sample comes from the copper making a complex with the water in the sample.

Figure 124: Colouration of 1 M copper sulphate solution

5.9.5. *8:1 Acetic Acid:Copper*

The sample of 8:1 acetic acid:copper forms a dry powder, with various shades of blue and black. The blue powder is probably copper acetate and probably has a similar chemical pathway as the Pyr:copper sample explained in Section 5.10. The black powder is probably unreacted copper.
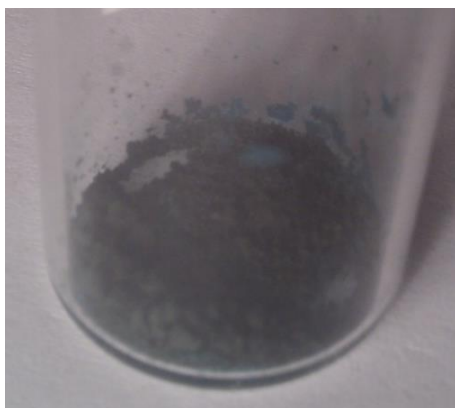
Figure 125: Colouration of 8:1 acetic acid:copper

5.9.6. *128:1 Acetic Acid:Copper Oxide*

The copper oxide has reacted with the acetic acid to make a blue solution in a similar way to the 8:1 acetic acid:copper. Again the resulting sample is expected to contain copper acetate.

Figure 126: Colouration of 128:1 acetic acid:copper oxide

5.9.7. *128:1 Oxalic Acid:Copper Oxide*

The copper oxide has reacted with the oxalic acid, this produces a much lighter blue colour than the equivalent acetic acid sample and it should be noted that there are two layers to the solution. The lower layer is the light blue, presumably a copper oxalate precipice, while the upper layer is clear, which is presumably excess oxalic acid.

Figure 127: Colouration of 128:1 oxalic acid:copper oxide

5.9.8. *Summary of Colour Changes*

The copper and copper oxides react with Pyr, and other organic acids, in a similar fashion to one another. A suggested mechanism for the reaction can be found in Section 5.10. The buffered Pyr:copper sample also demonstrated a colour change, even though the acid group has been neutralised. The colour change of the buffered Pyr:copper sample might be due to an imperfect neutralisation of the Pyr.

The colour changes of the sample take several hours before becoming apparent, indicating that the reaction rates of these samples are relatively slow, in the order of hours or longer. It has been shown in Figure 107 that the magnetic properties of a Pyr:copper oxide sample is related to the reaction time before measurement.

5.10. *Overview*

Within this chapter there have been several sets of magnetisation experiments. The first set were performed on the dry nanoparticles, these experiments give an indication of the purity of the samples. The second set of experiments were conducted on samples that are analogous to the NMR samples used in Chapter 4. These experiments were undergone to link the magnetic and NMR properties of the sample. The Final set of experiments were conducted to determine the conditions required to make the samples more magnetic.

The dry nanoparticles were not very magnetic compared to the copper-nickel alloy control sample. The magnetic ordering displayed by the dry nanoparticles were generally paramagnetic. There were a few examples of diamagnetic and ferromagnetic ordering at 2 K. The most notable ferromagnetic sample was the dry copper oxide, this is because it was ferromagnetic at room temperature, this matches data within the literature (15).

The metal oxides, silver and graphene supplied by Skyspring, were all diamagnetic at high temperatures and become paramagnetic at around 25-50 K. It is suspicious that all of these samples behave similarly to one another. There are three possible explanations for why these samples are similar; the first is that for some reason the background subtraction used in these samples was incorrect. If this was the case, sample supplied by other

manufacturers would also have displayed similar properties. Another explanation is that there is a paramagnetic impurity in the samples. It is possible that a small impurity can change the observed magnetisation of the sample. The final possibility is that these samples are just coincidently similar, which seems unlikely. From there three possible explanations, the most likely is that the sample have been contaminated.

The nano copper, which was supplied by Skyspring, may also be contaminated, however, as the copper is already paramagnetic, the impurity could be masked by the copper's own paramagnetic signal. Repeating these tests using nanoparticle samples from another supplier would determine if there the samples supplied by SSnano were contaminated.

The data collected in this chapter also demonstrates that the size of the particles also effects their magnetic properties. These size dependences can be seen when comparing the magnetic properties of nano-sized and micron-sized copper in Section 5.5.2. and the free copper ions found in the copper sulphate sample in Section 5.8.1. The smaller the particle size, the more magnetic the sample. A similar comparison can be made when comparing the micron-sized and nano-sized aluminium samples in Section 5.5.2.

As an aside, bulk aluminium is known to be a superconductor at around 1.2 K (100,101). Although the measurements in the susceptometer are conducted at 2 K and higher, there are times in the dilution fridge where the aluminium nanoparticles could become superconducting, for example during thermal mixing. Further investigations would be required to determine to see if superconducting aluminium has an effect on the T_1 times of the protons in a sample.

A concern with the samples from Chapter 4 was that the nanoparticles had oxidised with the oxygen in the atmosphere as both copper and copper oxide samples had similar proton T_1 times. The production of stable, monodisperse copper nanoparticles has been proven difficult in the literature because of the oxidation of nano copper which further justifies this concern (103). It is well known that increasing the surface area to volume ratio of a material increases the reaction rate of chemical reactions, therefore, it is plausible that the nanomaterials could react with the air. To determine if the copper sample was oxidised, its magnetic properties were compared to a copper oxide sample. The result is that the copper and copper oxide samples have different magnetic properties, as seen in Section 5.5.2. therefore, can be defined as being different samples i.e. the copper has not become fully

oxidised. The same measurements were also conducted on aluminium and aluminium oxide, again showing that the aluminium and aluminium oxide are independent samples.

Three samples, which are identical to samples used in the NMR experiments in Chapter 4, also had their magnetic properties measured. From the three WG samples, it has be deduced that more magnetic samples are better NMR relaxation agents, however, the data set is currently very limited. If high levels of magnetisation are desirable, then it would be suggested that copper sulphate should be tested as a relaxation agent in future work as it was the most magnetic sample measured in this chapter. The negative effects of using the more magnetic samples is that they have broader peaks in the NMR spectra. This might not be a concern as the samples will be measured at room temperature in the final application. At these high temperatures the samples will be much less magnetic, therefore, maintain narrow peaks in the NMR spectra. It should be mentioned that experiments on a wider variety of samples are required to gain a better understanding between the magnetic and NMR properties of the nanoparticles.

The most interesting result in this chapter is the vast increase in magnetisation of the copper and copper oxide samples, due to the addition of pyruvic acid. The magnetic ordering of these samples becomes superparamagnetic when the samples are cooled to 2 K. Since superparamagnetism only occurs in samples with single domains, and coupled to the fact that a chemical reaction is occurring between the copper and the Pyr, it would follow that the chemical reaction is reducing the size of the copper nanoparticles. The decrease in the copper particle size can also explain the increase in magnetisation in the sample. If the copper is being broken down into smaller particle, or single ions, it would be expected to behave in a similar way to the copper sulphate sample, hence have a large magnetisation. These large magnetisations are seen in the Pyr:copper samples so it is a reasonable assumption that the Pyr is reducing the size of the copper nanoparticles.

To produce the copper ions, one might expect a reaction between the organic acid and the metal to produce a salt and hydrogen gas. A similar reaction chain can be produced for metal oxides. This is important as the Pyr:copper oxide samples also undergo a similar colour and magnetisation change.

$$Metal + Acid \rightarrow Salt + H_2$$

$$Metal\ oxide + Acid \rightarrow Salt + Water$$

As the pyruvic acid is a weak acid, the reaction is expected to occur very slowly. However, the large surface area of the copper and copper oxide nanoparticle might allow for the reaction to occur at an observable rate. The overall reaction scheme with a weak acid is conceptually identical to above, and is shown here for the example of pyruvic acid and copper:

The reaction can be monitored by observing the change colour, and measuring the magnetic properties of the sample. From Figure 107 it can be seen that the reaction requires around 24 hours to reach completion. Further evidence for a reaction can be seen in Figure 105, as the 64:64:1 P:W:Cu separates into two layers. In Figure 105 the mixture of the two layers was measured several hours after the sample was produced, while the individual green and purple layers were measured 24 hours and 48 hours after, respectively. The individual layers were more magnetic than the mixture, therefore suggesting that the copper and the Pyr was still reacting throughout the first 24 hours. The fact that both layers in the 64:64:1 P:W:Cu sample have the same final magnetisation also suggests that the reaction had finished after ~24 hours.

Although observing a colour change does indicate that a chemical reaction has occurred, it does not indicate the anything about the magnetic properties of the product. The reverse is also true, the lack of a colour change does not necessarily mean that the samples are not interacting with the solvent. For example, water:copper samples, which does not show any signs of a reaction, have been shown to be more magnetic than the dry copper sample, as seen in Figure 100 and Figure 88 respectively. The enhance magnetisation in the water:copper sample is counter intuitive as pure water has been proven to be diamagnetic in Figure 86. Thus, it would be expected that a water:copper sample would have a reduced apparent magnetisation. The cause for this increase in magnetisation in the water:copper sample is not known.

A full summary of the magnetisation of each sample at 2 K, with notes, can be seen in Table 14. It should be noted that samples which are diamagnetic for the majority of the field

cooling experiment, before showing paramagnetic ordering at the lower temperatures, will be denoted by an asterisk (*) and the data point displayed in Table 14 will be the magnetisation of the diamagnetic sample at the lowest temperature before the paramagnetic component is apparent.

Sample	Magnetisation per atom at 1T 2K (Bohr magneton)	Magnetic Ordering	Notes
Gold 6nm	-0.0259*	D	Point taken at 75 K, Paramagnetic component below 50 K
Gold 30nm	-0.0217*	D	Point taken at 75 K, Paramagnetic component below 50 K
Gold 12nm	-0.0101*	D	Point taken at 75 K, Paramagnetic component below 50 K
128:1 Oxalic acid:CuO	-1.18E-3*	D	Paramagnetic component below 20 K
128:1 Acetic acid:CuO	-7.60E-4*	P	Diamagnetic above 4 K
ZnO Nano	-1.62E-4*	D	Point taken at 75 K, Paramagnetic below 50 K
Al2O3 Nano	-1.49E-4*	D	Point taken at 75 K, Paramagnetic below 50 K
8:1 WG:Ag	-1.04E-4*	D	Point taken at 75 K, Paramagnetic below 50 K
SnO2 Nano	-1.02E-4*	D	Point taken at 75 K, Paramagnetic below 50 K
8:1 WG:Al	-1.01E-4	D	
Graphene Nano	-8.11E-5*	D	Point taken at 75 K, Paramagnetic below 50 K
8:1 P:Al	-7.36E-5	D	
0:32:1 P:W:CuO	-6.36E-5*	D	Paramagnetic component below 50 K
Pyruvic acid	-4.933E-5*	D	Paramagnetic component below 20 K
Ag Nano	-4.37E-5*	D	Point taken at 75 K, Paramagnetic below 50 K
Al Nano	-4.26E-5	D	Paramagnetic component below 50 K
MgO Nano	-3.89E-5*	D	Point taken at 75 K, Paramagnetic below 50 K
Water	-1.64E-5	D	
0:32:1 P:W:Cu	9.81E-6*	D	Paramagnetic component below 50 K
Cu Micron	4.09E-5	F	
Al Micron	1.24E-4	P	
128:1 Acetone:CuO	1.51E-4	P	Noisy field cooling curve
8:1 WG:Cu	3.41E-4	P	
Cu Nano	3.91E-4	P	

Pt Nano	6.21E-4	P	
CuO Nano	6.32E-4	F	
8:1 Acetic acid:Cu	8.39E-4	Unknown	Unusual 1 T cooling plot as seen in Figure 113
0:8:1 P:W:Cu	2.01E-3	P	
8:1 Buffered P:Cu	3.95E-3	P	
0:128:1 P:W:Cu	0.02	P	
2:6:1 P:W:Cu	0.022	P	
32:0:1 P:W:CuO	0.042	SP	
4:4:1 P:W:Cu	0.047	P	
16:16:1 P:W:CuO	0.053	P	
CuNi Control	0.062	F	Curie temp ~150 K
6:2:1 P:W:Cu	0.076	P	
64:64:1 P:W:CuO Day 1	0.089	P	
8:0:1 P:W:Cu	0.134	SP	The sample was only measured down to 4 K
16:16:1 P:W:Cu	0.212	P	
128:0:1 P:W:Cu	0.222	SP	
64:64:1 P:W:Cu mix	0.232	P	
64:64:1 P:W:CuO Day 2	0.291	P	
64:64:1 P:W:CuO Day 4	0.300	P	
64:64:1 P:W:Cu Purple	0.317	P	
64:64:1 P:W:Cu Green	0.317	P	
64:64:1 P:W:CuO Day 3	0.335	P	
64:1 P:Cu	0.405	SP	
16:1 P:Cu	0.407	SP	
32:0:1 P:W:Cu	0.433	SP	
1.07molar copper sulphate	0.455	P	
Nickel	0.579	F	Calculated from (97)
Iron	2.18	F	Calculated from (97)

Table 14: Summary of the magnetisation data. The Magnetic ordering has been abbreviated to D is diamagnetic, F is ferromagnetic, P is paramagnetic and SP is superparamagnetic.

5.11. *Conclusion*

The magnetic properties of the nanoparticle samples depend on several parameters, including the size of the nanoparticles and the solvent used to dissolve the nanoparticles. Unfortunately this limits the usefulness of the SQUID measurements of the dry samples. The magnetic properties of the dry samples can only be used as a measure of purity of the sample.

A chemical reaction occurs between organic acids and the copper or copper oxide nanoparticles; this is observed as a colour change in the sample and an increase in magnetisation. These chemical reactions take several hours to reach completion and are believed to reduce the size of the nanoparticle. It could be possible that the nanoparticles are being reduced to the point that they become individual ions. The idea that the nanoparticles are being reduced in size correlates with the large magnetic properties found in the copper sulphate sample. This is because the magnetic properties of the copper sulphate are believed to be due to the sample containing single copper ions.

As the copper and copper oxide samples are undergoing a chemical reaction with organic acids, the final sample may not be useful. Ideally, the solvent should be extracted from the nanoparticles, so that the resulting sample is pure for in vivo applications. However, if a chemical reaction is occurring, then it might be impossible to extract the solvent. If samples which have undergone a reaction cannot be used, then other nanoparticles which are inert should be considered. From proton data, taken in Chapter 4, platinum should be considered as a relaxation agent as it should be inert and has favourable relaxation properties.

In samples where the solvents are not organic acids, acetone or water for example, there is no clear indication that there is an interaction between the solvent and the nanoparticles; however, the levels of magnetisation can increase compared to their dry counterpart. In the 128:1 acetone:copper oxide sample, for example, the level of magnetisation increases, however, for the 8:1 WG:copper sample, the magnetisation decreased compared to its dry counterpart. In both cases the sample does not show any indication of physical change.

Finally, the three samples that were identical to samples used in the NMR experiments in Chapter 4, showed that a more magnetic samples are better relaxation agents. Unfortunately the data set is limited and many more experiments would need to be conducted to confirm this conclusion.

Chapter 6. Overall Conclusions

Chapters 3, 4 and 5 contain large quantities of data and information that need to be combined. To summarise the data this chapter has been broken down into three subsections. These are:-

- A general overview of the results contained within chapters 3, 4 and 5
- A section discussing the interconnections between data
- A short conclusion explaining the data and results mean

6.1. *Overview Summary*

6.1.1. *Lanthanide NMR*

The electron spin flip time is the key parameter that determine if the lanthanide additive will cause an enhanced relaxation rate. Lanthanides are effective relaxation agents when the electron spin flip time is equal to the inverse Larmor frequency. Both Dy-DTPA and Ho-DTPA were shown to be effective relaxation agents at around 10 K in Figure 20. It has also been shown that a 6 mM Dy-DTPA sample can produce a shorter proton T_1 than an undoped sample at temperatures as low as 0.1 K; however, the T_1 times of the 6mM Dy-DTPA sample are still too long at millikelvin temperatures to take advantage of the brute force polarisation.

The level of polarisation enhancement under typical polarising conditions (1.5 K and 10 T) is significant, but not enough to be considered for clinical applications, as DNP systems can produce enhancement factors of ~100 greater for protons than the brute force method at these polarising conditions. With this in mind the brute force method, with a lanthanide relaxation agent, has limited applications.

6.1.2. *Nanoparticle NMR*

The addition of copper and copper oxide nanoparticles has been proven to make the brute force method effective down to the millikelvin temperature regime, as seen in Figure 36 and Figure 38 respectively. With the sample becoming polarised in a more extreme physical environment, the absolute polarisation of the protons and ^{13}C in the sample become comparable with samples polarised via DNP.

The reason why the copper and copper oxide nanoparticles are superior to other tested nanoparticles is not fully understood; however, it is believed to be because another relaxation mechanism is involved. The extra mechanism seems to be due to the magnetisation of the nanoparticles, though much more detailed work is required to confirm this idea.

As the copper and copper oxide nanoparticles do have a sufficiently short $T_{1/2}$ time at the conditions required to achieve polarisations comparable to DNP, therefore, it would be recommended that these samples are considered for further research, with the possibility that they could be used in clinical studies if the sample can be filtered.

The samples which contain copper or copper oxide in an organic acid seem to undergo a chemical reaction, this could mean these samples are impossible to filter. Therefore, it is suggested that other nanoparticles should be used as the relaxation agent for these organic acids. Data from this research would suggest that platinum would be a feasible relaxation agent, as it sufficiently reduces the proton $T_{1/2}$ in the millikelvin regime while maintaining a longer $T_{1/2}$ at several Kelvin; it should also be relatively unreactive in pyruvic acid and other similar solvents.

6.1.3. *Thermal Mixing*

Thermal mixing was tested on samples of 2 M NaAc WG containing Dy-DTPA at 4 K, and on samples of 2 M NaAc WG containing copper nanoparticle samples at ~16 mK. In these experiments all the nuclei (^{13}C and ^{31}P), except the protons, were saturated before going to close, or through, a zero B_0 field. The B_0 field was then returned to the resonance field of the target nuclei for measurement. The measured polarisation of the saturated nuclei (^{13}C and

[31]P) increased, this is because the spin temperatures of all of the nuclei have tended towards an equilibrium. It should be noted that this method of polarisation transfer is only around 75 % efficient, due to losses arising from being at the low field for a significant time.

A study of thermal mixing on a pure Pyr sample was also conducted (Section 4.5.3.) in order to optimise the thermal mixing technique. The optimisation was conducted by varying the mixing field and mixing time of the thermal mixing step. From these optimisation experiments, it would seem that it is more important to select the correct mixing field, rather than the correct mixing time. The optimal mixing conditions for the pure Pyr were a field of 0.005 T and a mixing time of 50 ms.

6.1.4. B_0 Field Ramping

There was an expectation that ramping the B_0 field could cause relaxation in the nanoparticle samples. The B_0 field oscillations were expected to induce local field fluctuations in the nanoparticles within the sample, in a similar manner to that of the lanthanides measured in Chapter 3. Although this was proven incorrect, it did lead to the discovery of a polarisation transfer technique that was attributed to the transfer of polarisation between ^{23}Na to ^{13}C. The understanding of the mechanism is poor; however, it seems to be a high field version of thermal mixing. The similarity in the gyromagnetic ratios of ^{23}Na and ^{13}C allow for the resonance lines to overlap at high fields, therefore, the spin temperature of the ^{13}C and ^{23}Na to equilibrate.

If ramping B_0 can pass polarisation from one long lived nucleus to another, it could be possible for a hyperpolarised state to be replenished, therefore allowing for signal averaging. This is advantageous, as hyperpolarised NMR experiments are generally single shot experiments. If this B_0 ramping technique is like thermal mixing, it will probably only work in the solid state, therefore, has limited uses.

6.1.5. Nanoparticle Magnetism

It has been shown in this research that the nanoparticles mainly displayed paramagnetic, superparamagnetic and ferromagnetic ordering at 2 K. Many samples from

SSnano showed diamagnetic ordering above ~25 K before showing a paramagnetic component. As the magnetic properties from the nanoparticles supplied by SSnano were very similar, it would indicate that there could be an impurity in these samples, therefore, further investigations of these nanoparticles are required.

High level of magnetisation are observed in copper and copper oxide sample that contain a solvent, the most notably example are samples that contain Pyr. In these cases a colour change was observed, this is an indication that a reaction is taking place. The magnitude and magnetic ordering of the copper and copper oxide also changed, above 2 K the samples were paramagnetic, while at 2 K some of the samples became superparamagnetic. The magnetisation of these samples increased by a factor of 1000. The time required for these chemical reactions to reach completion is in the order of several hours, as seen in Figure 107.

The addition of solutions, including solutions which are not organic acids, change the magnetisation of the samples, therefore, the dry sample data cannot be compared with the NMR data collected in Chapter 4. This drastically reduces the number of samples whereby the magnetic measurements and NMR measurements can be compared.

6.2. *Interconnections*

The interconnections between the work presented in Chapters 3, 4 and 5 are highlighted in this section.

6.2.1. *Pyr Magnetism and Line Broadening*

The Pyr:copper samples in Chapter 4 showed a line broadening effect at temperatures below 1 K. Figure 46 shows the FWHM as a function of temperature for a Pyr:water:copper sample. The line broadening would imply that the sample itself is becoming magnetic as the temperature is lowered, this is confirmed in Figure 103. It should be noted that the measurements in the SQUID are limited to 2 K and 1 T, while the NMR experiments were conducted at 2.45 T and at temperatures as low as 15 mK, which means the data has to be extrapolated to get a full sense of the level of magnetisation the sample in the polariser.

6.2.2. *Relationship between Magnetisation and $T_{1/2}$ Times*

The correlation between the measured level of magnetisation and the value of the proton $T_{1/2}$ time of a sample is not as clear as anticipated. There are several reasons why it is difficult to relate the magnetisation data with the NMR data; the main reason is the unexpected interaction between the solution and the nanoparticles. These interactions have meant that only a limited number of samples have both NMR and SQUID measurements that can be compared. These samples WG:copper, WG:aluminium and WG:silver. This limited data set would suggest that larger magnetisations result in shorter proton $T_{1/2}$ time, however, more experiments should be conducted to confirm this result.

NMR data and SQUID data for Pyr:copper samples are also difficult to compare, due to the line broadening effect of the NMR signal. The calculation used to produce the expected infinity values does not account for the line broadening effect. If the infinity values are not well known, the $T_{1/2}$ values are also not well known, therefore comparing the magnetisation to the $T_{1/2}$ time is impossible without more data.

The most effective way of correlating the magnetic properties of the nanoparticle samples to the proton $T_{1/2}$ times would be to measure more WG:nanoparticle samples in the SQUID magnetometer and compare it to the other NMR data within this research.

6.3. *Take Home Message*

The brute force method can be used, when in conjunction with a relaxation agent, to obtain high levels of polarisation. If a system is required to only produce a modest enhancement to the signal, simple polariser with polarising conditions of 1.5 K and 10 T can be used. Such a system would probably not require the addition of a relaxant to achieve an adequately polarised state. Such a system would be inexpensive if only moderate signal enhancements are required. This system would not be suitable for clinical studies because it is preferable to use a small quantity of highly polarised sample, than a large quantity of sample with a lower polarisation.

If a system is required to produce the largest possible polarisation on a sample then DNP, or brute force using a nanoparticle relaxant, is more suitable. The separating factor between these two methods is scalability and time required to polarise a sample.

DNP systems, such as the GE Spin lab, are currently limited to polarising four samples simultaneously, though the polarisation time is around 30 minutes, this means that many samples can be produced. These samples achieve higher levels of polarisation in the polariser than in the brute force method. The short polarisation time of the spin lab makes DNP systems useful for research groups, where changing samples is a regular occurrence.

A brute force system is more useful in an environment where samples are routinely being used. A brute force system can polarise as many samples as will fit into the high field, low temperature environment. This means that even though each individual sample takes hours to polarise, there should be one ready when required due to the vast number of samples being polarised simultaneously.

The brute force method does offer several advantages, for example, it can potentially polarise all of the nuclei in a sample, when combined with thermal mixing, which could lead to multi-nucleus experiments. Alternatively, if many nuclei in a sample are polarised, there is a possibility of repolarising a target nucleus by using the field ramping technique discussed in Section 4.6.3. though this may be limited to samples which are in the solid state. An example could be a sample containing both polarised ^{23}Na and ^{13}C. A single shot ^{13}C measurement can be conducted, followed by field ramping. The field ramping could allow for transfer of the ^{23}Na polarisation to the ^{13}C, so that a second measurement can be conducted. The brute force method may also be able to retain more of its polarisation for the measurement due to it being ejected in a cold state.

Before implementing the brute force method, further research is required. One concern is that some of the solutions react with the nanoparticles, which may make the samples unusable. There is also a great deal of research required to producing a dissolution step for a brute force system, even if the current DNP dissolution system is used as a template, though some of this work has been done by M. Hirsch, et al.

The final points to be made are regarding the magnetic properties of the nanoparticle samples. To the first order, it would appear that having a non-diamagnetic material seems to decrease the protons $T_{1/2}$ time. The proton polarisation can then be transferred to ^{13}C via

thermal mixing. This allows for the ^{13}C in the sample can be polarised in a time similar to that require to polarise the protons in the sample. After the ^{13}C is polarised, the sample would be ready for use, so long as the nanoparticles are filtered out of the sample.

Although copper is an effective relaxation agent for samples containing NaAc, it is less useful for Pyr samples, as the chemical reaction between the Pyr and the copper is likely to make the sample unusable; therefore, other nanoparticles should be studied to find a suitable replacement. It is possible that other interesting molecules, such as glutamate, would also undergo a similar chemical reaction with some of the nanoparticles which would be undesirable. A replacement relaxant to the copper nanoparticles should be chemically inert, while still being an effective relaxation agent. This means that it would produce a short proton T_1 at the millikelvin temperatures while retaining a suitable long proton T_1 at the higher temperatures. The work in this thesis would suggest that platinum nanoparticles could potentially replace the copper nanoparticles, though further studies would have to be made.

Chapter 7. Works Cited

1. Chierotti, M. R., Gobetto, R. *Solid-State NMR Studies on Supramolecular Chemistry*. John Wiley & Sons, Hoboken, DOI 10.1002/9780470661345 (1996).

2. Cavalli, A., Salvatella, X., Dobson, C. M., Vendruscolo, M. Protein Structure Determination from NMR Chemical Shifts. *PROCEEDINGS OF THE NATIONAL ACADEMY OF SCIENCES* **104 (23)**, 9615-9620 (2007).

3. Nelson, S. J., Kurhanewicz, J., Vigneron, D. B., Larson, P. EZ., Harzstark, A. L., Ferrone, M., Criekinge, M. V., Chang, J. W., Bok, R., Park, I., Reed, G., Carvajal, L., Small, E. J., Munster, P., Weinberg, V. K., Ardenkjaer-Larsen, J. H., Chen, A. P., Hurd, R. E., Odegardstuen, L. I., Robb, F. J., Tropp, J., Murray, J. A. Metabolic Imaging of Patients with Prostate Cancer Using Hyperpolarized [1-13C] Pyruvate. *SCIENCE TRANSLATIONAL MEDICINE* **5 (198)** (2013).

4. Ardenkjaer-Larsen, J. H., Jóhannesson, H., Petersson, J. S., Wolber, J. Hyperpolarized Molecules in Solution. In : *In Vivo NMR Imaging*. Humana Press, New York City, DOI 10.1007/978-1-61779-219-9_11 205-226, (2011).

5. Griffin, R. G., Prisner, T. F. High Field Dynamic Nuclear Polarization—The Renaissance. *PHYSICLA CHEMISTRY CHEMICAL PHYSICS* **12 (22)**, 5737-5740. (2010).

6. Krjukov, E. V., O'Neill, J. D., Owers-Bradley, J. R. Brute Force Polarization of 129Xe. *JOURNAL OF LOW TEMPERATURE PHYSICS* **140 (5-6)**, 397-408 (2005).

7. Owers-Bradley, J. R., Horsewill, A., Peat, D. T., Goh, K. S. K., Gadian, D. G. High Polarization of Nuclear Spins Mediated by Nanoparticles at Millikelvin Temperatures. *PHYSICAL CHEMISTRY CHEMICAL PHYSICS* **15 (25)**, 10413-10417 (2013).

8. Golman, K., Olsson, L. E., Axelsson, O., Månsson, S., Karlsson, M., Petersson, J. S. Molecular Imaging Using Hyperpolarized C-13. *THE BRITISH JOURNAL OF RADIOLOGY* **76**, S118-S127 (2003).

9. Carr, D. H., Brown, J., Bydder, G. M., Steiner, R. E., Weinmann, H. J., Speck, U., Hall, A.

Chapter 7. Works Cited

S., Young, I. R. Gadolinium-DTPA as a Contrast Agent in MRI: Initial Clinical Experience in 20 Patients. *AMERICAN JOURNAL OF ROENTGENOLOGY* **143 (2)**, 215-224 (1984).

10. Runge, V. M., Clanton, J. A., Lukehart, C. M., Partain, C. L., James Jr, A. E. Paramagnetic Agents for Contrast-Enhanced NMR Imaging: A Review. *AMERICAN JOURNAL OF ROENTGENOLOGY* **141 (6)**, 1209-1215 (1983).

11. Lauffer, R. B. Paramagnetic Metal Complexes as Water Proton Relaxation Agents for NMR. *CHEMICAL REVIEWS* **87 (5)**, 901-927 (1987).

12. Solomon, I. Relaxation Processes in a System of Two Spins. *PHYSICAL REVIEW* **99 (2)**, 559 (1955).

13. Anderson, A. G., Redfield, A. G. Nuclear Spin-Lattice Relaxation in Metals. *PHYSICAL REVIEW* **116 (3)**, 583 (1959).

14. Walstedt, R. E., Hahn, E. L., Froidevaux, C., Geissler, E. Nuclear Spin Thermometry Below 1K. *PROCEEDINGS OF THE ROYAL SOCIETY OF LONDON: SERIES A. MATHEMATICAL AND PHYSICAL SCIENCES* **284 (1399)**, 499-530 (1965).

15. Gao, D. J. Z., Zhu, J., Qi, J., Zhang, Z., Sui, W., Shi, H., Xue, D. Vacancy-Mediated Magnetism in Pure Copper Oxide. *NANOSCALE RESEARCH LETTERS* **5 (4)**, 769-772 (2010).

16. Garitaonandia, J. S., Insausti, M., Goikolea, E., Suzuki, M., Cashion, J. D., Kawamura, N., Ohsawa, H., Muro, I. Gd., Suzuki, K., Plazaola, F., Rojo, T. Chemically Induced Permanent Magnetism in Au, Ag, and Cu Nanoparticles: Localization of the Magnetism by Element Selective Techniques. *NANO LETTERS* **8 (2)**, 661-667 (2008).

17. Makarova, T. L. Nanomagnetism in Otherwise Nonmagnetic Materials. *ARXIV PREPRINT ARXIV* **0904 (1550)** (2009).

18. Abragam, A. *The Principle of Nuclear Magnetism*. Clarendon Press, Oxford, ISBN 019852014X, (1961).

19. Abragam, A., Proctor, W. G. Spin Temperature. *PHYSICAL REVIEW* **109 (5)**, 1441 (1957).

Chapter 7. Works Cited

20. Gadian, D. G., Panesar, K. S., Linde, A. J. P., Horsewill, A. J., Köckenberger, W., Owers-Bradley, J. R. Preparation of Highly Polarized Nuclear Spin Systems Using Brute-Force and Low-Field Thermal Mixing. *PHYSICAL CHEMISTRY CHEMICAL PHYSICS* **14 (16)**, 5397-5402 (2012).

21. Bloch, F. Nuclear Induction. *PHYSICAL REVIEW* **70 (7-8)**, 460 (1946).

22. Levitt, M. *Spin Dynamics: Basics of Nuclear Magnetic Resonance.* John Wiley & Sons, Chichester, ISBN 1118681843, (2001).

23. Ernst, R. R., Anderson, W. A. Application of Fourier Transform Spectroscopy to Magnetic Resonance. *REVIEW OF SCIENTIFIC INSTRUMENTS* **37 (1)**, 93-102 (1966).

24. Peat, D. T., Horsewill, A. J., Köckenberger, W., Linde, A. J. P., Gadian, D. G., Owers-Bradley, J. R. Achievement of High Nuclear Spin Polarization Using Lanthanides as Low-Temperature NMR Relaxation Agents. *PHYSICAL CHEMISTRY CHEMICAL PHYSICS* **15 (20)**, 7586-7591 (2013).

25. Kuhns, P. L., Hammel, P. C., Gonen, O., Waugh, J. S. Unexpectedly Rapid F19 Spin-Lattice Relaxation in CaF2 Below 1 K. *PHYSICAL REVIEW B* **35 (10)**, 4591 (1987).

26. Comment, A., Rentsch, J., Kurdzesau, F., Jannin, S., Uffmann, K., van Heeswijk, R. B., Hautle, P., Konter, J. A., van den Brandt, B., van der Klink, J. J. Producing Over 100 ml of Highly Concentrated Hyperpolarized Solution by Means of Dissolution DNP. *JOURNAL OF MAGNETIC RESONANCE* **194 (1)**, 152-155 (2008).

27. Witte, C., Schröder, L. NMR of Hyperpolarised Probes. *NMR IN BIOMEDICINE* **26 (7)**, 788-802 (2013).

28. Overhauser, A. W. Polarization of Nuclei in Metals. *PHYSICAL REVIEW* **92 (2)**, 411 (1953).

29. Karabanov, A., Kwiatkowski, G., Köckenberger, W. Quantum Mechanical Simulation of Cross Effect DNP Using Krylov–Bogolyubov Averaging. *APPLIED MAGNETIC RESONANCE* **43 (1-2)**, 43-58 (2012).

30. Hu, K. N., Yu, H. H., Swager, T. M., Griffin, R. G. Dynamic Nuclear Polarization with

Biradicals. *JOURNAL OF THE AMERICAN CHEMICAL SOCIETY* **126 (35)** (2004).

31. Golman, K., Axelsson, O., Jóhannesson, H., Månsson, S., Olofsson, C., Petersson, J. S. Parahydrogen-Induced Polarization in Imaging: Subsecond 13C Angiography. *MAGNETIC RESONANCE IN MEDICINE* **42 (1)**, 1-5 (2001).

32. Hübler, P., Giernoth, R., Kümmerle, G., Bargon, J. Investigating the Kinetics of Homogeneous Hydrogenation Reactions Using PHIP NMR Spectroscopy. *JOUNRAL OF THE AMERICAN CHEMICAL SOCIETY* **121 (22)**, 5311-5318 (1999).

33. Walker, T. G., Happer, W. Spin-Exchange Optical Pumping of Noble-Gas Nuclei. *REVIEWS OF MODERN PHYSICS* **69 (2)**, 629 (1997).

34. Appelt, S., Baranga, A. B. A., Erickson, C. J., Romalis, M. V., Young, A. R., Happer, W. Theory of Spin-Exchange Optical Pumping of 3 He and 129 Xe. *PHYSICAL REVIEW A* **58 (2)**, 1412 (1998).

35. Babcock, E., Nelson, I., Kadlecek, S., Driehuys, B., Anderson, L. W., Hersman, F. W., Walker, T. G. Hybrid Spin-Exchange Optical Pumping of 3He. *PHYSICAL REVIEW LETTER* **91 (12)**, 123003 (2003).

36. Beckmann, P., Clough, S., Hennel, J. W., Hill, J. R. The Haupt Effect: Coupled Rotational and Dipolar Rrelaxation of Methyl Groups. *JOURNAL OF PHYSICS C: SOLID STATE PHYSICS* **10 (5)**, 729 (1977).

37. Horsewill, A. J. Quantum Tunnelling Aspects of Methyl Group Rotation. *PROGRESS IN NUCLEAR MAGNETIC RESONANCE SPECTROSCOPY* **35 (4)**, 359-389 (1999).

38. Tomaselli, M., Degen, C., Meier, B. H. Haupt Magnetic Double Resonance. *THE JOURNAL OF CHEMICAL PHYSICS* **118 (19)**, 8559-8562 (2003).

39. Saunders, M. G. *Enhancing the Sensitivity of NMR by Dynamic Nuclear Polarisation*, Dissertation, University of Birmingham (2011).

40. Crabb, D. G., Higley, C. B., Krisch, A. D., Raymond, R. S., Roser, T., Stewart, J. A. Observation of a 96% Proton Polarization in Irradiated Ammonia. *PHYSICAL REVIEW LETTERS* **64 (22)**, 2627 (1990).

41. Jannin, S., Bornet, A., Melzi, R., Bodenhausen, G. High Field Dynamic Nuclear Polarization at 6.7 T: Carbon-13 Polarization Above 70% Within 20min. *CHEMICAL PHYSICS LETTERS* **529**, 99-102 (2012).

42. Niendorf, H. P., Laniado, M., Semmler, W., Schörner, W., Felix, R. Dose Administration of Gadolinium-DTPA in MR Imaging of Intracranial Tumors. *AMERICAN JOURNAL OF NEURORADIOLOGY* **8 (5)**, 803-815 (1987).

43. Bernheim, R. A., Brown, T. H., Gutowsky, H. S., Woessner., D. E. Temperature Dependence of Proton Relaxation Times in Aqueous Solutions of Paramagnetic Ions. *THE JOURNAL OF CHEMICAL PHYSICS* **30 (4)**, 950-956 (1959).

44. Vander Elst, L., Roch, A., Gillis, P., Laurent, S., Botteman, F., Bulte, J. W., Muller, R. N. Dy-DTPA Derivatives as Relaxation Agents for Very High Field MRI: The Beneficial Effect of Slow Water Exchange on the Transverse Relaxivities. *MAGNETIC RESONANCE IN MEDICINE* **47 (6)**, 1121-1130 (2002).

45. Bloembergen, N., Purcell, E. M., Pound, R. V. Relaxation Effects in Nuclear Magnetic Resoannce Absorption. *PHYSICAL REVIEW* **73 (7)**, 679 (1948).

46. Cheung, T. T. P. Spin Diffusion in NMR in Solids. *PHYSICAL REVIEW B* **23 (3)** (1981).

47. Suter, D., Ernst, R. R. Spin Diffusion in Resolved Solid-State NMR Spectra. *PHYSICAL REVIEW B* **32 (9)**, 5608 (1985).

48. Blum, H., Cusanovich, M. A., Sweeney, W. V., Ohnishi, T. Magnetic Interactions Between Dysprosium Complexes and Two Soluble Iron-Sulfur Proteins. *JOURNAL OF BIOLOGICAL CHEMISTRY* **256 (5)**, 2199-2206 (1981).

49. Hirano, S., Suzuki, K. T. Exposure, Metabolism, and Toxicity of Rare Earths and Related Compounds. *ENVIRONMENTAL HEALTH PERSPECTIVES* **104 (1)**, 85 (1996).

50. Alsaadi, B. M., Rossotti, F. J., Williams, R. J. Hydration of Complexone Complexes of Lanthanide Cations. *JOURNAL OF THE CHEMICAL SOCIETY* **11**, 2151-2154 (1980).

51. Atsarkin, V. A., Demidov, V. V., Vasneva, G. A., Odintsov, B. M., Belford, R. L., Radüchel, B., Clarkson, R. B. Direct Measurement of Fast Electron Spin-Lattice Relaxation: Method

and Application to Nitroxide Radical Solutions and Gd3+ Contrast Agents. *THE JOURNAL OF PHYSICAL CHEMISTRY A* **105 (41)**, 323-9327 (2001).

52. Hendrick, R. E., Haacke, M. E. Basic Physics of MR Contrast Agents and Maximization of Image Contrast. *JOURNAL OF MAGNETIC RESONANCE IMAGING* **3 (1)**, 137-148 (1993).

53. Murata, K. I., Tanaka, H. Liquid–liquid Transition Without Macroscopic Phase Separation in a Water–Glycerol Mixture. *NATURE MATERIALS* **11 (5)**, 436-443 (2012).

54. Moeller, T., Thompson, L. C. Observations on the Rare Earths—LXXV(1): The Stabilities of Diethylenetriaminepentaacetic Acid Chelates. *JOURNAL OF INORGANIC AND NUCLEAR CHEMISTRY* **24 (5)**, 499-510 (1962).

55. Korringa, J. Nuclear Magnetic Relaxation and Resonnance Line Shift in Metals. *PHYSICA* **16 (7)**, 601-610 (1950).

56. Narath, A., Fromhold Jr, A. T., Jones, E. D. Nuclear Spin Relaxation in Metals: Rhodium, Palladium, and Silver. *PHYSICAL REVIEW* **144 (2)**, 428 (1966).

57. Knight, W. D. Nuclear Magnetic Resonance Shift in Metals. *PHYSICAL REVIEW* **76 (8)**, 1259 (1949).

58. Moriya, T. The Effect of Electron-Electron Interaction on the Nuclear Spin Relaxation in Metals. *JOURNAL OF THE PHYSICAL SOCIETY OF JAPAN* **18 (4)**, 516-520 (1963).

59. Walstedt, R. E. *The NMR Probe of High-Tc Materials*. Springer Science & Business Media, Berlin Heidelberg, ISBN 3540755640, (2008).

60. Kuzmany, H. *Solid State Spectroscopy: An Introduction*. Springer, Heidelberg, ISBN 3642014798, (2009).

61. Bedanta, S. *Supermagnetism in Magnetic Nanoparticle Systems,* Dissertation, Universität Duisburg-Essen (2007).

62. Brya, W. J., Wagner, P. E. Direct, Orbach, and Raman Relaxation in Dilute Cerous Magnesium Nitrate. *PHYSICAL REVIEW* **147 (1)**, 239 (1966).

63. Bierig, R. W., Weber, M. J., Warshaw, S. I. Paramagnetic Resonance and Relaxation of

Chapter 7. Works Cited

Trivalent Rare-Earth Ions in Calcium Fluoride. II. Spin-Lattice Relaxation. *PHYSICAL REVIEW* **134 (6A)**, A1504 (1964).

64. Scott, P. L., Jeffries, C. D. Spin-Lattice Relaxation in Some Rare-Earth Salts at Helium Temperatures; Observation of the Phonon Bottleneck. *PHYSICAL REVIEW* **127 (1)**, 32 (1962).

65. Van Vleck, J. H. Paramagnetic Relaxation and the Equilibrium of Lattice Oscillators. *PHYSICAL REVIEW* **59 (9)**, 724 (1941).

66. Orbach, R. Spin-Lattice Relaxation in Rare-Earth Salts. *PROCEEDINGS OF THE ROYAL SOCIETY OF LONDON: SERIES A. MATHEMATICAL AND PHYSICAL SCIENCES* **264 (1319)**, 458-484 (1961).

67. Poole, C. P., *Relaxation in Magnetic Resonance: Dielectric and Mossbauer Applications*. Academic Press, New York, ISBN 0323151825, (1971).

68. Chen, H., Müller, M. B., Gilmore, K. J., Wallace, G. G., Li, D. Mechanically Strong, Electrically Conductive, and Biocompatible Graphene Paper. *ADVANCED MATERIALS* **20 (18)**, 3557-3561 (2008).

69. Ruoff, R. S., Lorents, DC. Mechanical and Thermal Properties of Carbon Nanotubes. *CARBON* **33 (7)**, 925-930 (1995).

70. Guimaraes, A. P. *Principles of Nanomagnetism*. Springer, Heidelberg, ISBN 3642014828, (2009).

71. Dutta, P., Pal, S., Seehra, M. S., Anand, M., Roberts, C. B. Magnetism in Dodecanethiol-Capped Gold Nanoparticles: Role of Size and Capping Agent. *APPLIED PHYSICS LETTERS* **90 (21)**, 213102-213102 (2007).

72. Bloembergen, N., Pound, R. V. Radiation Damping in Magnetic Resonance Experiments. *PHYSICAL REVIEW* **95 (1)**, 8 (1954).

73. Hoult, DI., Ginsberg, N. S. The Quantum Origins of the Free Induction Decay Signal. *JOURNAL OF MAGNETIC RESONANCE* **148 (1)**, 182-199 (2001).

74. Pöschko, M. T., Schlagnitweit, J., Huber, G., Nausner, M., Horničáková, M., Desvaux, H., Müller, N. On the Tuning of High-Resolution NMR Probes. *CHEMPHYSCHEM* **15 (16)**, 3639-3645 (2014).

75. Crooker, S. A., Rickel, D. G., Balatsky, A. V., Smith, D. L. Spectroscopy of Spontaneous Spin Noise as a Probe of Spin Dynamics and Magnetic Resonance. *NATURE* **431 (7004)**, 49-52 (2004).

76. Kempf, JG., Hirsch, ML. Personal Communication..

77. Gallagher, F. A., Kettunen, M. I., Day, S. E., Hu, DE., Karlsson, M., Gisselsson, A., Lerche, M. H., Brindle, K. M. Detection of Tumor Glutamate Metabolism in Vivo Using 13C Magnetic Resonance Spectroscopy and Hyperpolarized [1-13C]Glutamate. *MAGNETIC RESONANCE IN MEDICINE* **66 (1)**, 18-23 (2011).

78. Kurhanewicz, J., Vigneron, D. B., Brindle, K., Chekmenev, E. Y., A. Comment, C. H. C., DeBerardinis, R. J., Green, G. G., Leach, M. O., Rajan, S. S., Rizi, R. R., Ross, B. D., Warren, W. S., Malloy, C. R. Analysis of Cancer Metabolism by Imaging Hyperpolarized Nuclei: Prospects for Translation to Clinical Research. *NEOPLASIA* **13 (2)**, 81-97 (2011).

79. Kohler, S. J., Yen, Y., Wolber, J., Chen, A. P., Albers, M. J., Bok, R., Zhang, V., Tropp, J., Nelson, S., Vigneron, D. B., Kurhanewicz, J., Hurd, R. E. In Vivo 13Carbon Metabolic Imaging at 3T With Hyperpolarized 13C-1-Pyruvate. *MAGNETIC RESONANCE IN MEDICINE* **58 (1)**, 65-69 (2007).

80. Stefanita, C. G. *From Bulk to Nano: The Many Sides ot Magnetism,* Volume 117. Springer Series in Material Science, Heidelberg, ISBN 3540705481, (2008).

81. Ulrich, M., García-Otero, J., Rivas, J., Bunde, A. Slow Relaxation in Ferromagnetic Nanoparticles: Indication of Spin-Glass Behavior. *PHYSICAL REVIEW B* **67 (2)**, 024416 (2003).

82. Moriggi, L., Cannizzo, C., Dumas, E., Mayer, C. R., Ulianov, A., Helm, L. Gold Nanoparticles Functionalized With Gadolinium Chelates as High-Relaxivity MRI Contrast Agents. *JOURNAL OF THE AMERICAN CHEMICAL SOCIETY* **131 (31)**, 10828-10829 (2009).

Chapter 7. Works Cited

83. Cardinal, J., Klune, J. R., Chory, E., Jeyabalan, G., Kanzius, J. S., Nalesnik, M., Geller, D. A. Noninvasive Radiofrequency Ablation of Cancer Targeted by Gold Nanoparticles. *SURGERY* **144 (2)**, 125-132 (2008).

84. Jiles, D. C. *Introduction to Magnetism and Magnetic Materials*. CRC press, Boca Raton, ISBN 0412798603, (1998).

85. Sheahen, T. P. *Introduction to High-Temperature Superconductivity*. Plenum Press, New York, ISBN 0306470616, (1994).

86. Iwasa, Y. *Case Studies in Superconducting Magnets: Design and Operational Issues*. Springer-Verlag New York Inc., New York, ISBN 0306470624, (2009).

87. Binder, M., Weber, A., Mosendz, O., Woltersdorf, G., Izquierdo, M., Neudecker, I., Dahn, J. R., Hatchard, T. D., Thiele, J. U., Back, C. H., Scheinfein, M. R. Magnetization Dynamics of the Ferrimagnet CoGd Near the Compensation of Magnetization and Angular Momentum. *PHYSICAL REVIEW B* **74 (13)**, 134404 (2006).

88. Nealon, G. L., Donnio, B., Greget, R., Kappler, J. P., Terazzi, E., Gallani, J. L. Magnetism in Gold Nanoparticles. *NANOSCALE* **4 (17)**, 5244-5258 (2012).

89. Gréget, R., Nealon, G. L., Vileno, B., Turek, P., Mény, C., Ott, F., Derory, A., Voirin, E., Rivière, E., Rogalev, A., Wilhelm, F., Joly, L., Knafo, W., Ballon, G., Terazzi, E., Kappler, JP., Donnio, B., Gallani, JL. Magnetic Properties of Gold Nanoparticles: A Room-Temperature Quantum Effect. *CHEMPHYSCHEM* **13 (13)**, 3092-3097 (2012).

90. Henkel, M., Pleimling, M., Sanctuary, R. Ageing, Rejuvenation and Memory: The Example of Spin-Glasses. In : *Ageing and the Glass Transition*. Springer, Berlin Heidelberg, ISBN 3540696830, (2007).

91. Mathieu, R., Hudl, M., Nordblad, P. Memory and Rejuvenation in a Spin Glass. *EUROPHYSICS LETTERS* **90 (6)**, 67003 (2010).

92. Sahoo, S., Petracic, O., Kleemann, W., Nordblad, P., Cardoso, S., Freitas, P. P. Aging and Memory in a Superspin Glass. *PHYSICAL REVIEW B* **67 (21)**, 214422 (2003).

93. Sasaki, M., Jönsson, P. E., Takayama, H., Mamiya, H. Aging and Memory Effects in

Superparamagnets and Superspin Glasses. *PHYSICAL REVIEW B* **71 (10)**, 104405 (2005).

94. Bedanta, S., Eimüller, T., Kleemann, W., Rhensius, J., Stromberg, F., Amaladass, E., Cardoso, S., Freitas, P. P. Overcoming the Dipolar Disorder in Dense CoFe Nanoparticle Ensembles: Superferromagnetism. *PHYSICAL REVIEW LETTERS* **98 (17)**, 176601 (2007).

95. Jaklevic, R. C., Lambe, J., Silver, A. H., Mercereau, J. E. Quantum Interference Effects in Josephson Tunneling. *PHYSICAL REVIEW LETTERS* **12 (7)**, 159 (1964).

96. Drung, D., Assmann, C., Beyer, J., Kirste, A., Peters, M., Ruede, F., Schurig, T. Highly Sensitive and Easy-to-Use SQUID Sensors. *APPLIED SUPERCONDUCTIVITY* **17 (2)**, 699-704 (2007).

97. Crangle, J., Goodman, G. M. The Magnetization of Pure Iron and Nickel. *PROCEEDINGS OF THE ROYAL SOCIETY OF LONDON A: MATHEMAICAL, PHYSICAL AND ENGINEERING SCIENCES* **321 (1547)**, 477-491 (1971).

98. Kaufmann, A. R., Starr, C. Magnetic Properties of Solid Solutions. III. The Paramagnetic Alloys of Copper and Nickel. *PHYSICAL REVIEW* **63 (11-12)**, 445 (1943).

99. Castro, E. V., Peres, N. MR., Stauber, T., Silva, N. AP. Low-density Ferromagnetism in Biased Bilayer Graphene. *PHYSICAL REVIEW LETTERS* **100 (18)**, 186803 (2008).

100. Matthias, B. T., Geballe, TH., Compton, VB. Superconductivity. *REVIEWS OF MODERN PHYSICS* **35 (1)**, 1 (1963).

101. Eisenstein, J. Superconducting Elements. *REVIEWS OF MODERN PHYSICS* **26 (3)**, 277 (1954).

102. Jungermann, E., Sonntag, NOV. *Glycerine: A Key Cosmetic Ingredient*. CRC Press, Boca Raton, ISBN 0824784650, (1991).

103. Mott, D., Galkowski, J., Wang, L., Luo, J., Zhong, C. J. Synthesis of Size-Controlled and Shaped Copper Nanoparticles. *LANGMUIR* **23 (10)**, 5740-5745 (2007).